The Charge Management System for LISA and LISA Pathfinder

Daniel Hollington
High Energy Physics Group

Department of Physics
Imperial College London

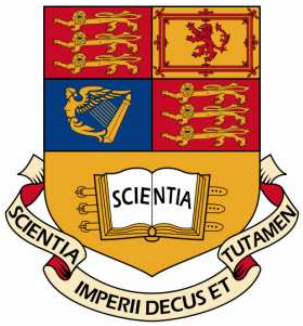

Thesis submitted for the Degree of Doctor of Philosophy to
Imperial College London

· 2011 ·

Abstract

The test masses at the heart of the Laser Interferometer Space Antenna (LISA) and LISA: Pathfinder experiments will experience charging caused by incident ionising radiation. This thesis describes work carried out in developing, testing and understanding the performance of the hardware used to characterise and counteract this test mass charging.

Work will be presented that describes the simulation and testing of a radiation monitor to be flown on board Pathfinder. The Charge Management System will then be introduced and the results from testing at the Trento torsion pendulum facility discussed. Several measurements of individual properties that affect discharging are made and these are then incorporated into simulations of the discharging system as a whole. Finally, initial studies are conducted into the suitability of UV-LEDs as the discharging light source for LISA, with particular focus on their spectral stability.

For my Mum, Dad and Sister.

Contents

List of Tables

List of Figures

Declaration and Copyright

This thesis is my own work, except where explicitly indicated in the text.

Daniel Hollington
2011

Acknowledgments

This thesis would not have been possible without the help and support from a number of people. A special thanks goes to my supervisor Tim for giving me the opportunity to study for this PhD in the first place. As a supervisor he has provided a good balance between being there to offer help when needed while at the same time giving me room to learn for myself. I would also like to thank my second supervisor Henrique for providing advice and constructive criticism when needed.

Since I first started at Imperial and throughout my PhD, the LISA postdocs have been there to answer my endless questions and offer advice. A big thanks to Simon, Markus, Diana and Peter, I would not have been able to finish without your help. During the course of my work I have also had the pleasure of visiting several groups of people across Europe. Thank you to our collaborators in Trento, Barcelona and Coimbra.

One of the best things about studying for a PhD at Imperial has been getting to know the other postgrads. They have provided hours of interesting conversation and have made the last few years fly-by. I have to mention by name Jonathan, Shyam, Harsit and Mitesh who have all been good fun to be around. The table tennis table is our legacy to the astro-group. I would also like to thank my friend Shahin who has been great to chat to when I needed to take a break from work.

Finally, I would like to thank my Mum, Dad and sister Emma. They have always been there with love and support. Thank you.

Chapter 1

Ripples in Space-Time

Introduction

In 1916, Albert Einstein's general theory of relativity revolutionised the way in which we think about the Universe. It is based on the concept of a malleable space-time where the presence of matter and energy cause space-time to curve, and the curvature of space-time then influences the movement of matter. A consequence of this relationship between matter, energy and space-time is that certain astrophysical systems can generate self-sustaining waves which propagate out through the universe, analogous to ripples on a pond. By studying the properties of these ripples in space-time itself, one may learn about the sources that created them as well as observationally test general relativity. However, the waves are extremely challenging to detect and to date only indirect evidence for their existence has been found. Nevertheless, due to technological advances the first direct detections are expected within the next decade and with them a new era of gravitational wave astronomy will begin.

This thesis describes the development and testing of technology that will be vital for a planned space-based gravitational wave detector called the Laser Interferometer Space Antenna, or LISA.

1.1 Gravitational Waves

A prediction of general relativity, gravitational waves are oscillations in space-time which travel away from their source at the speed of light. Like any waves they have a frequency and an amplitude, determined by the properties of the source generating them. They are produced by accelerating masses in analogy with electromag-

netic waves, which are produced by accelerating charges. Also like electromagnetic waves, gravitational waves are transverse with space alternately being stretched and compressed perpendicularly to their direction of motion. However, unlike electromagnetic waves where the lowest-order contribution is from an oscillating charged dipole, gravitational waves lowest-order contribution is produced by a time-varying mass quadrupole.

Until now, the vast majority of what we have learned about the Universe has been inferred from observing electromagnetic radiation. Due to their properties gravitational waves will both compliment these observations as well as offering insight into new areas. This is predominantly due to the fact that gravity interacts relatively weakly with matter. While electromagnetic waves can be scattered and attenuated by matter as they propagate through the Universe, gravitational waves are barely affected. This means that gravitational waves can be observed to vast astronomical distances and also probe regions of high matter densities. But a consequence of their weak interaction with matter also makes gravitational waves incredibly challenging to directly detect.

Gravitational waves have another advantage over electromagnetic observations, where the measured quantity is usually energy flux which falls off with distance from the source at $1/r^2$. As will be shown, the measured quantity of a gravitational wave is a strain amplitude which falls off at $1/r$, giving sensitivity to larger distances.

General relativity predicts that gravitational waves will have two polarisations, labelled '+' and '×'. One may visualise the effect of each polarisation by imagining a ring of test particles, Figure 1.1. A '+' polarised gravitational wave propagating perpendicularly to such a ring would cause the ring to be alternately stretched and compressed, vertically and horizontally. A '×' polarised wave would be the same, but rotated 45°. One should note that the area within the ring stays constant and that there is no motion in the direction the wave propagates.

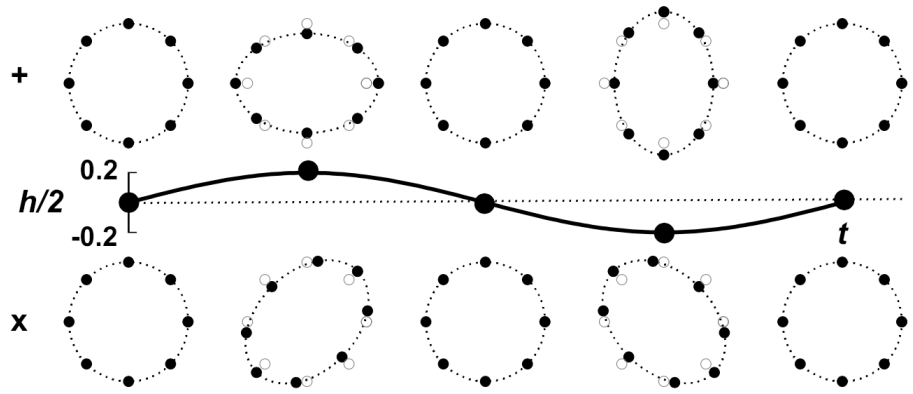

Figure 1.1: The effect of both '+' and '×' gravitational wave polarisations on a ring of test particles. Figure from Schutz and Ricci (2010).

Figure 1.1 shows the observable effect of a gravitational wave which is the strain amplitude. Denoted as h, the dimensionless strain amplitude is given by $h = \frac{\Delta l}{l}$, where l is the proper distance between two opposite test particles at $t = 0$ and Δl is the maximum change in proper distance caused by the gravitational wave. The examples in Figure 1.1 show a greatly exaggerated effect, with a strain amplitude of $h \approx 0.2$. Real world amplitudes would be incredibly small but one may estimate the strains produced by a source with a highly asymmetric mass distribution, like a binary system, using, (Camp and Cornish, 2004):

$$h \sim \frac{2G^2M^2}{rRc^4} \tag{1.1}$$

where G is the gravitational constant, M is the total mass of the system, r is the distance to the system, R is the radius of the system and c is the speed of light. Clearly, a strong source of gravitational waves will be massive, compact and astronomically nearby. One such example is a white dwarf binary system recently discovered by Brown et al. (2011). This system is within our Galaxy and is around 1 kpc from Earth. It is composed of two white dwarfs with masses of 0.55 $M_\odot$ and 0.25 $M_\odot$, and radii of 0.0132 $R_\odot$ and 0.0353 $R_\odot$ respectively. They orbit each other at an average radius of just $\sim 1.5 \times 10^5$ km. Using Equation 1.1:

$$h \approx \frac{2(6.7 \times 10^{-11})^2(1.6 \times 10^{30})^2}{(1.5 \times 10^8)(3.1 \times 10^{19})(3.0 \times 10^8)^4} \approx \frac{2.3 \times 10^{40}}{3.8 \times 10^{61}} \approx 6.0 \times 10^{-22}$$

This is typical of the amplitude scale of most predicted gravitational waves reaching Earth and explains why they are so difficult to directly detect.

1.2 Predicted Sources

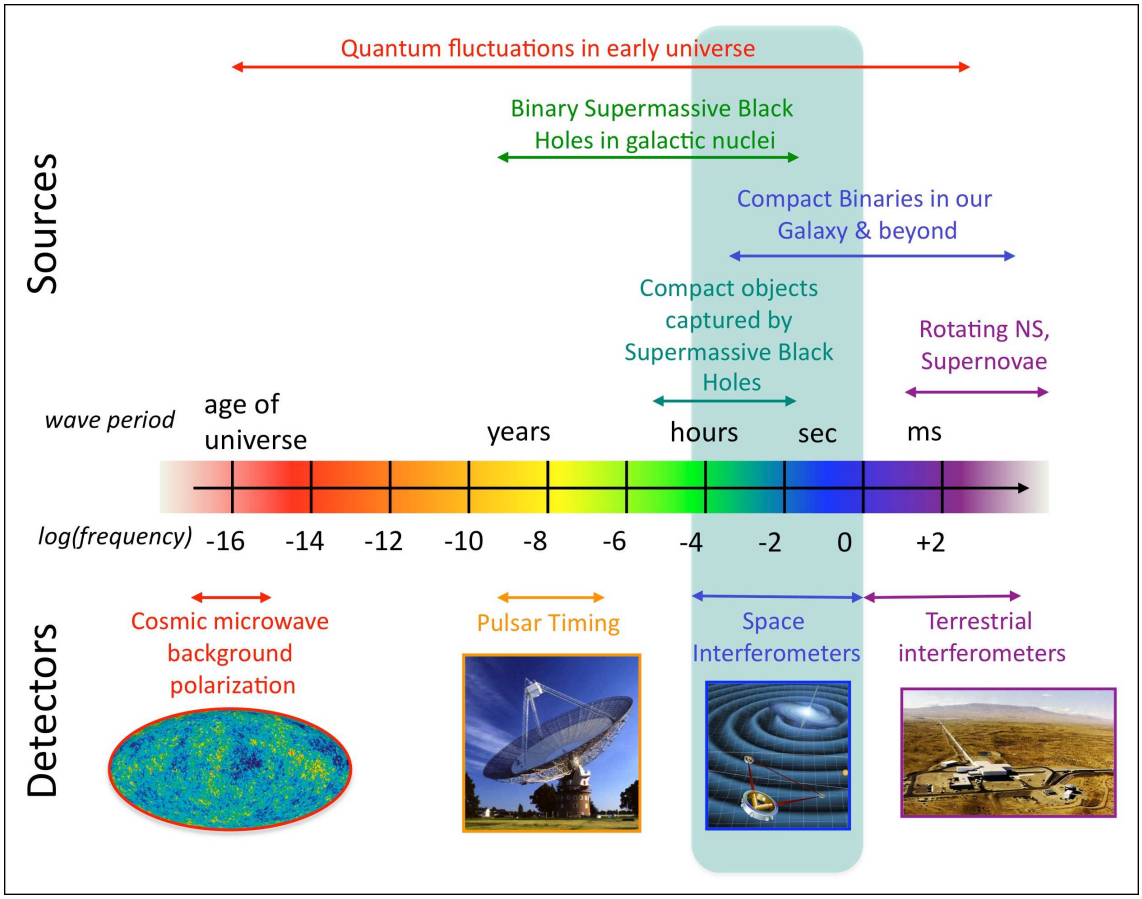

Figure 1.2: A diagram showing a range of predicted gravitational wave sources and the methods capable of detecting them. Note the huge range in frequency from $\sim 10^{-18}$ to $> 10^{3}$ Hz. Figure courtesy of NASA (2011).

In addition to the possibility of unknown sources of gravitational waves, our current knowledge of astrophysics, cosmology and theoretical physics allows us to predict a range of objects capable of producing them. These sources span a huge range in frequency requiring different techniques to study them. These are shown in Figure 1.2 and demonstrate that the predicted sources can be broadly separated into four regimes. These are extremely low frequency ($\sim 10^{-18}$ to $\sim 10^{-15}$ Hz), very low frequency ($\sim 10^{-9}$ to $\sim 10^{-7}$ Hz), low frequency ($\sim 10^{-4}$ to $\sim 10^{0}$ Hz) and high frequency ($\sim 10^{1}$ to $\sim 10^{4}$ Hz), (Camp and Cornish, 2004).

Extremely low frequency gravitational waves are thought to have been created during the period of inflation, when quantum fluctuations were amplified and now form part of a gravitational wave background in the Universe. This stochastic background would span the entire gravitational wave spectrum but at the extremely

low frequency end its affect could be observed in the Cosmic Microwave Background, or CMB. In addition to several ground based experiments, the European Space Agency's *Plank* mission hopes to detect such an affect, (Efstathiou and Gratton, 2009).

Moving into the next frequency region, very low frequency gravitational waves are predicted to arise from a variety of theoretical mechanisms including phase transitions in the early universe, collisions between vacuum bubbles and topological defects like cosmic strings and domain walls. One predicted astrophysical source of gravitational waves in this frequency range are pairs of supermassive black-holes (mass $> 10^{10}$ $M_{\odot}$) as they inspiral towards merger.

1.2.1 Low Frequency Gravitational Waves

The low frequency region between $\sim 10^{-4}$ and $\sim 10^{0}$ Hz is predicted to contain a diverse range of sources, (Bishop and Maharaj, 2002). These sources are of particular interest here as they include the ones LISA is designed to study.

The most numerous type of source is expected to be stellar mass binaries composed of white dwarfs, neutron stars or black holes. Indeed, there are thought to be so many binary white dwarf systems within our Galaxy, around 10^7, that they will form an unresolved background below ~ 2 mHz, (Ruiter et al., 2009). Above this frequency it is predicted that several thousand systems will be close and bright enough to be individually resolved. The parameters describing the properties of a small subset of around ten have already been characterised through electromagnetic observations, like the previously mentioned Brown et al. (2011) system. These so called 'verification binaries' should produce predictable signals in a space based detector like LISA and can be used to calibrate the instrument, (Stroeer and Vecchio, 2006).

The strongest gravitational waves are predicted to originate from the inspiral and mergers of supermassive black-holes in the mass range $10^4 - 10^7$ $M_{\odot}$. For LISA, such mergers could be detected with signal to noise ratios of $> 10^3$, (Baker et al., 2007). With such a clear signal, subtle features of the waveform can be studied and general relativity tested. In addition these sources can be detected out to vast astronomical distances, $z > 20$, allowing the merger history through time to be examined, (Arun et al., 2009). This in turn will aid understanding of galaxy formation and evolution. However, there is considerable uncertainty regarding the rate of mergers ranging from ~ 1 to > 100 per year, (Sesana et al., 2009).

Another source of low frequency gravitational waves are extreme mass ra-

tio inspirals, or EMRIs. These systems arise when a supermassive black hole ($10^5 - 10^7$ $M_\odot$) at a galactic centre captures a roughly stellar mass object ($1 - 1000$ $M_\odot$) like a white dwarf, neutron star or black hole. The gravitational waves resulting from the inspiral and merger would produce a very clean waveform allowing for a precise test of general relativity. However, a signal could be complicated due to the presence of multiple inspiralling objects, though the occurrence of such complex systems is expected to be low. Again, the event rates for EMRIs are fairly uncertain with current estimates of those detectable by LISA at several hundred per year, (Gair et al., 2004).

1.2.2 High Frequency Gravitational Waves

The group of astrophysical systems predicted to produce gravitational waves in the high frequency range, between $\sim 10^1$ and $\sim 10^4$ Hz, are of particular interest for ground based detectors. High frequency sources generally need to be highly relativistic and have a mass less than approximately 1000 $M_\odot$. These include: Coalescing binary systems composed of neutron stars (~ 1.4 $M_\odot$) or stellar mass black holes ($\sim 1-10$ $M_\odot$) in the last few hours before merger; rapidly rotating non-axisymmetric neutron stars, for example neuron stars accreting matter from a companion star; and collapsing stars (supernova) but only if the collapse is sufficiently non-axisymmetric (Barish, 2000; Cutler and Thorne, 2002).

1.3 Detection Methods

Given the incredibly small strain amplitudes of predicted gravitational waves, direct detection is extremely challenging and has so far proved elusive. However, strong indirect evidence has been found via the orbital decay of a binary pulsar system and a direct detection is expected to be made in the coming years. This section will discuss the various methods that are being employed to make such a direct detection. Depending on the detection technique, in addition to the gravitational waves strain amplitude and frequency, several other properties of the waves can be measured including their polarisation and evolution in time as well as the direction and number of the sources creating them. This would provide a great deal of insight into the sources that generated them and could be combined with separate electromagnetic observations to provide further information.

1.3.1 Pulsar Timing

Until now no gravitational waves have been directly detected, though their existence has been inferred from timing pulsars. Detecting the regular radio pulses produced by pulsars allows them to be used as stable clocks. By modelling a pulsar system one can accurately predict the time-of-arrival of future pulses. Such a technique, called the pulsar timing method, was used to obtain the first observational evidence of gravitational waves. This won the 1993 noble prize for Hulse and Taylor and involved precisely measuring the orbital period of the pulsar binary system named PSR B1913+16. The subsequent orbital decay matches predictions of energy loss due to gravitational waves, as shown in Figure 1.3. This strong agreement between theory and observation is taken as convincing evidence for the existence of gravitational waves, (Weisberg and Taylor, 2005).

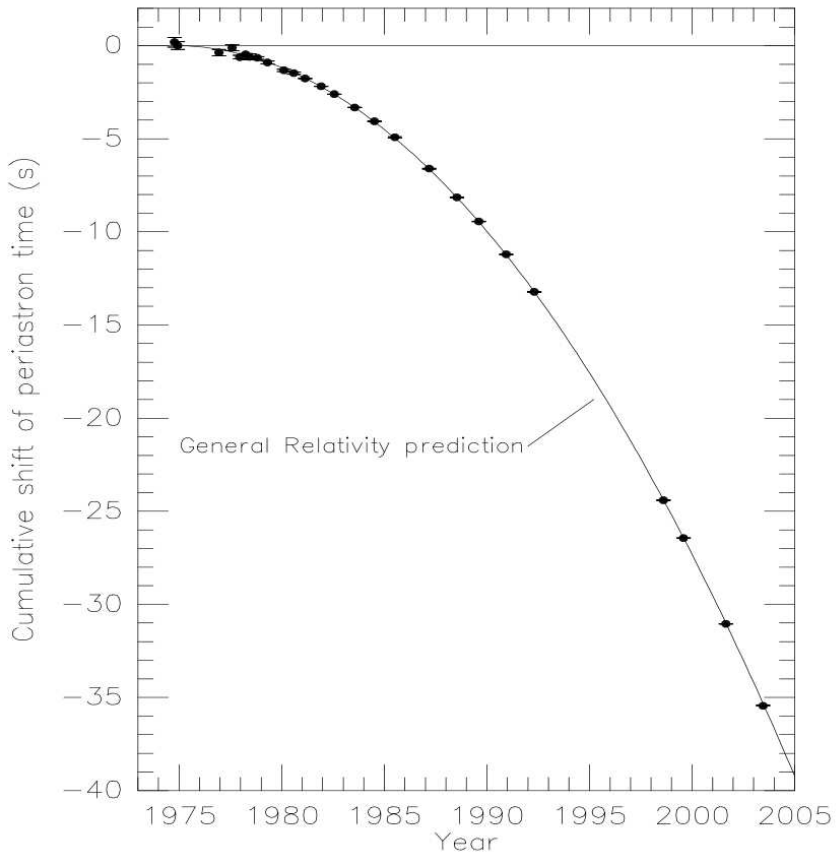

Figure 1.3: Comparison between the orbital decay predicted by general relativity via the emission of gravitational waves and actual observations made over thirty years of the PSR B1913+16 binary system. Figure from Weisberg and Taylor (2005).

Using a similar technique pulsars are also being used to try and make a direct detection of gravitational waves. The idea is to monitor the time-of-arrival from a collection of millisecond pulsars within our galaxy, (Hobbs, 2011). A propagating gravitational wave will cause the proper distance between the Earth and a pulsar to alternately increase and decrease, shifting the time-of-arrival in a cyclical way. It is possible that other effects could cause such a signal from a single pulsar therefore the time-of-arrival from many pulsars are measured allowing a correlated gravitational wave signature to be obtained. This method is sensitive to gravitational waves in the very low frequency range, between $10^{-8} - 10^{-9}$ Hz, therefore detectable sources include supermassive black hole mergers and the gravitational wave background. The International Pulsar Timing Array collaboration hopes to make such a detection within the next 5 to 10 years, (The IPTA Collaboration, 2010).

1.3.2 Spacecraft Doppler Tracking

Similar to the pulsar timing method, spacecraft Doppler tracking effectively treats the Earth and a distant spacecraft as free test masses. A ground station on Earth sends a monochromatic microwave signal, ν_0, to the spacecraft which is coherently transponded back. The difference in the Doppler shifted returned frequency is given by $\Delta\nu$ and is related to the relative velocity between the Earth and the spacecraft, Δv, by $\frac{2\Delta v}{c} = \frac{\Delta\nu}{\nu_0}$, (Armstrong, 2006). In an idealised system at particular frequencies there should be no change in the time-series of the dimensionless relative velocity $\frac{2\Delta v}{c}$. Therefore if a gravitational wave were to perturb the system it could be observed in this time-series data. However, several sources of noise including fluctuations in the density of the solar wind and Earth's atmosphere limit the sensitivity of such measurement. This Doppler tracking technique has most recently been used with the *Cassini* spacecraft to place an upper limit of $h < 2 \times 10^{-15}$ for the gravitational wave background at ~ 0.3 mHz, (Armstrong et al., 2003). This is still several orders of magnitude above the expected strains produced by even the strongest sources. Nonetheless, it is currently the most sensitive measurement made in this frequency range.

1.3.3 Resonant Bar Detectors

The earliest attempt at direct gravitational wave detection involved resonant bar detectors or 'Weber bars', (Weber, 1960). While these have been in operation since the late 1960's and despite several claimed detections by Weber himself, which were later disproven, they are only now approaching sensitivities capable of detecting the

strongest sources of gravitational waves. The idea is that a long cylindrical metal bar resonates on the passage of a gravitational wave of the appropriate frequency. The bars are designed to have a resonant frequency that is thought to be of astrophysical interest in the the high frequency range between 500 and 1500 Hz. However, this type of detector is only sensitive in a narrow frequency band of $\sim$ 5 to 50 Hz. Several bar detectors are currently in operation, such as the cryogenically cooled *EXPLORER* and *NAUTILUS* experiments, (Astone et al., 2008). These detectors are operated at $\sim$ 3 K and have reached strain sensitivities of $\sim 3.4 \times 10^{-19}$, but only in a frequency range of $\sim$ 30 Hz, centred at $\sim$ 930 Hz.

1.3.4 Interferometers

The most promising method for not only detecting gravitational waves but also performing detailed scientific studies is by using laser interferometry. First described in detail by Weiss (1972), the idealised case involves splitting a beam of laser light and sending it down two perpendicular, equal length arms. Free test masses at the end of each arm act as mirrors, reflecting the light back towards the origin where an interference pattern from the two beams is observed. If a gravitational wave were to pass perpendicularly through the interferometer the proper length of the arms would alternately increase and decrease. This time-varying change in relative arm length will then be observed in the shifting interference pattern as the path length of the two beams varies.

Unlike resonant bars, interferometers are broadband detectors and are sensitive to gravitational wavelengths that are comparable to the length of the arms. It should also be kept in mind that such detectors simultaneously detect all gravitational waves in its sensitivity range and individual signals need to be separated later. Predicting the waveforms from theoretical sources, so called 'source modelling' greatly aids in this and there is a large ongoing effort in this area, (Sathyaprakash and Schutz, 2009).

Several ground-based laser interferometers are already in operation. The two most advanced experiments are LIGO (Laser Interferometer Gravitational-Wave Observatory, (Abramovici et al., 1992; The LIGO Collaboration, 2009)) in the USA, with arms 4 km in length, and VIRGO (named after the 'Virgo' cluster, (Bradaschia et al., 1990; The VIRGO Collaboration, 2010)) in Italy, with arms 3 km in length. They are sensitive to high frequency gravitational waves from $\sim$ 10 Hz to $\sim$ 10 kHz and both detectors have achieved peak sensitivities at $\sim$ 100 Hz of $h \approx 10^{-21}$, each performing several science runs over a number of years. To date no detections have

been made though given the current sensitivities and the distance out to which they could detect a source leads to theoretical predictions of at best one detectable event per year, (Cutler and Thorne, 2002). Planned upgrades of both LIGO (Advanced LIGO) and VIRGO (Advanced VIRGO) in the next few years will increase sensitivity and increase the distance out to which they can detect sources. This will theoretically increase the number of possible detections to several thousand per year, (Cutler and Thorne, 2002).

An intrinsic limitation of these ground-based detectors is that their frequency range is confined to between ~ 10 Hz and ~ 10 kHz which in turn restricts the type, and number of sources that they can observe. There are several factors that limit this range, one example being their arm lengths as lengths beyond a few kilometres are impractical. Noise also limits ground based detectors; terrestrial vibrations (anthropomorphic and seismic) and shot noise of the detected light. While it is possible that future technologies will overcome these limitations, an absolute limit will be reached below ~ 1 Hz, (Hughes and Thorne, 1998). Both man-made and natural gravity-gradient noise and local disturbances in the Newtonian gravitational field, for example the variation in the atmospheric mass above the detector, will produce noise. These sources of noise will be larger than expected gravitational wave amplitudes at lower frequencies and impossible to shield against. In order to observe sources within the low frequency band it is necessary to move the interferometer into space. While this approach allows longer arm lengths, no terrestrial noise and a more stable gravitational field, it also brings many new challenges.

1.4 LISA

The Laser Interferometer Space Antenna (LISA) is a planned ESA mission that aims to use laser interferometry to detect and study gravitational waves. Currently being considered for a tentative launch date of around 2022, the current design has a frequency window of 0.1 mHz to 0.1 Hz, where it will be optimal in the $1-10$ mHz range. Hopefully, by the time LISA launches direct detections of gravitational waves will have been made with ground detectors as well as using pulsar arrays. However, analogous to observing the Universe at different electromagnetic wavelengths, LISA (low frequency) and ground based interferometers (high frequency) are complimentary rather than competitive as they observe different astrophysical sources, as discussed previously and shown in Figure 1.4. LISA has the potential to open a completely new window on the Universe.

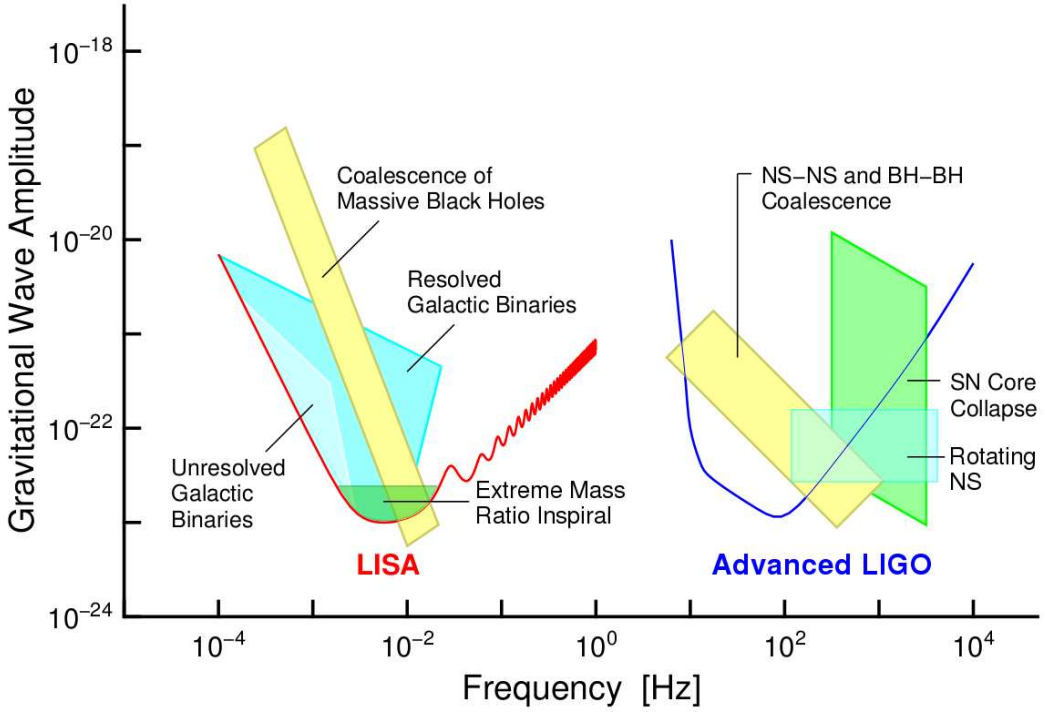

Figure 1.4: A comparison between the sources that LISA and Advanced LIGO will hope to study. The figure demonstrates the complimentary nature of space based and ground based detectors. Adapted from Danzmann and Rüdiger (2003).

A detailed description of the LISA experiment is provided by The LISA Collaboration (2011). To summarise, it will consist of three identical spacecraft flying in an approximately equilateral triangle formation at ~ 1 AU from the sun. This constellation will trail the Earth's orbit by 20° and be inclined to the ecliptic plane by 60°, as shown in Figure 1.5. The spacecraft will form three semi-independent interferometers, each with arm lengths of approximately 5×10^6 km. In this way each craft acts as the centre of an interferometer supplying the interfering light from a 1 W infra-red Nd-YAG laser, while simultaneously acting as one of the mirrors for each of the other two interferometers.

The interferometer mirrors themselves are actually 46 mm cubic test masses made from a $Au_{0.7}Pt_{0.3}$ alloy. This alloy was chosen due to its low magnetic susceptibility but the test mass is also coated with a 1 μm layer of pure gold to provide a reflective mirrored surface. There are six such test masses, two within each spacecraft. For LISA to successfully detect gravitational waves these test masses need to maintain almost pure geodesic motion as stray forces can create acceleration noise, masking any gravitational wave signals. They are shielded from the external space environment by the surrounding spacecraft with the test masses floating freely

within. The space craft then manoeuvre around the test masses using micro-newton thrusters forming a so called 'drag-free system'. However, as there are two test masses per spacecraft they can only truly be free in one axis each, which is used for the interferometry measurements. Forces need to be applied in the other axes to keep the test masses in their nominal positions.

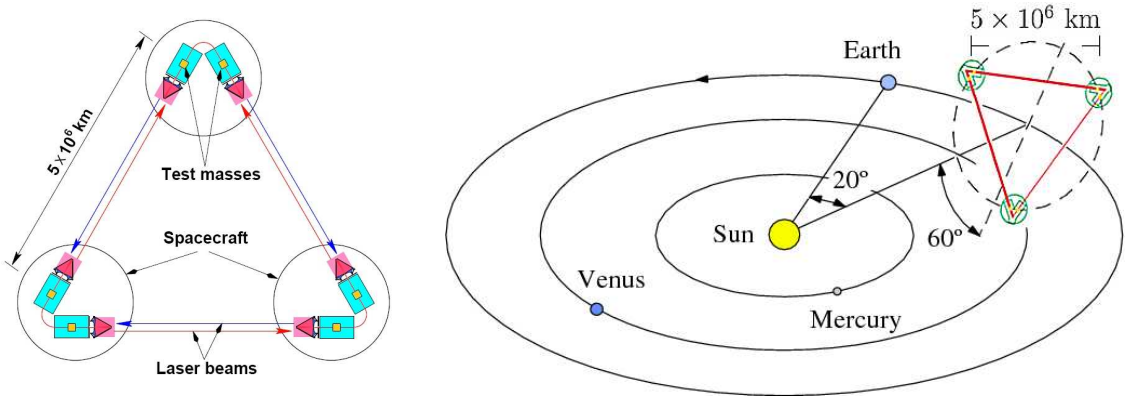

Figure 1.5: *Left:* LISA's nominal configuration. *Right:* The LISA constellation. Note that with the chosen orbit the LISA constellation will rotate around its centre once per year. This rotation of the interferometers will allow the sky position of particular sources to be deduced. Adapted from Camp and Cornish (2004).

1.4.1 Inertial Sensor

To achieve drag free control, each test mass floats within its own independent housing, which has walls lined with a series of capacitive sensors, their layout shown in Figure 1.6. The housing structure is constructed from molybdenum while the electrodes are made from sapphire, both gold coated like the test mass. There are twelve sensing electrodes and also six injection electrodes that apply a 5.4 V, 100 kHz AC bias to the test mass in order to produce a 0.61 V AC potential on the test mass. As the test mass moves within the housing the gaps between the test mass and each sense electrode varies; which in turn causes the measured capacitances from the sense electrodes to change. By taking combinations of these measurements it is possible to determine both the translational and rotational position of the test mass. When a test mass is centred, there is a gap between it and the housing of 4.0, 2.9 and 3.5 mm in x, y and z respectively.

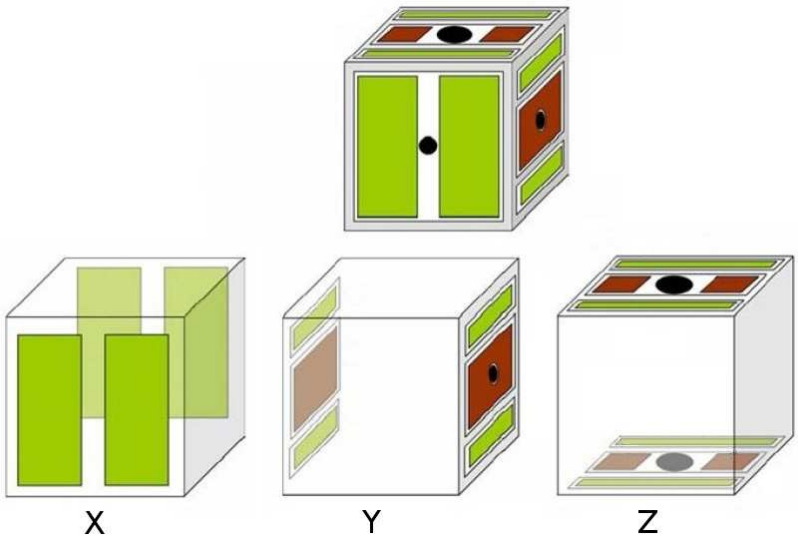

Figure 1.6: A diagram of the inertial sensor's electrode layout. The sense electrodes are shown in green while the injection electrodes are shown in red. The test mass floats freely within and interferometry is performed in the x axis. Adapted from Schulte (2007).

The capacitive sensors also play another important role. By applying DC voltages of a few volts to the sense electrodes it is possible to actuate a test mass. Depending on the combination of applied voltages the test mass can be translated or rotated within the housing. This is necessary not only at the start of the experiment in order to position the test masses but also to periodically move them in the non-interferometry axes in order to prevent the two test masses within each spacecraft from drifting apart.

1.4.2 Interferometry

The interferometry actually performed using LISA will be a considerable departure from the basic case outlined in Section 1.3.4. For example, LISA's interferometer arms are at 60° to one another rather than the optimal 90°, which introduces a $\sqrt{3}/2$ decrease in sensitivity. Additionally, and in contrast to ground based detectors, LISA's arms are neither equal nor constant in length. Due to the orbital dynamics of the LISA constellation there is a variation of the $\sim 5 \times 10^6$ km long arms by up to 2 %, leading to relative velocities between spacecraft that can be up to ± 15 m s^{-1}, (Folkner et al., 1997). It is initially surprising that one can measure the sub-atomic sized variation in length caused by gravitational waves with such a dynamic system. Fortunately, these variations in arm length are periodic over time

scales of months during the planned LISA orbit, with corresponding frequencies well below the scientific sources that LISA is interested in. This variation in arm length only causes a problem when the frequency fluctuations in the interferometry laser light are considered.

Noise in the laser frequency is not a problem in a standard Michelson interferometer with fixed, equal length arms, as any variation in frequency cancels when the two beams are interfered. If, like in the LISA case, the split laser light travels non-equal distances the variation in the initial frequency causes a shift in phase and therefore a phase noise is introduced. LISA plans to overcome this problem by using a technique called time delay interferometry (TDI), (Armstrong et al., 2003). This involves measuring the phase of the incoming light separately by combining it with a reference beam. By then taking different linear combinations of the interferometer measurements the effect of the shift in phase due to the laser frequency can be removed in post-processing.

There is a further complication for LISA interferometry caused by the long arm lengths. Even though the initial laser beam is highly collimated there is still some beam divergence. By the time the beam has travelled 5×10^6 km it is spread over an area 20 km in diameter, with only a few hundred pico-Watts of the original 1 W of laser power being received by the second spacecraft. The light would be undetectable if it were simply reflected back, continuing to diverge on the return journey. It is thus necessary to phase-lock the incoming light with the laser of the secondary craft and return it at full power, a system known as an active mirror.

With all these factors taken into account the interferometry measurement for a single arm can be broken down into three separate interferometry stages. Step one is to measure the distance between the optical bench on the first craft, and the test mass on board the first craft. Step two is to measure the distance between the optical benches on-board the spacecrafts at each end of the arm. The final step is to measure the distance between the optical bench on the second spacecraft, and the test mass on board that craft. These are then combined to produce the final required measurement of the test mass separation distance, which varies in time.

1.4.3 Sensitivity Requirements

The high level of sensitivity required for LISA means that spurious test mass acceleration noise must be kept to a minimum. While the spacecraft and inertial sensor housing shield the test masses from the space environment, they also interact with it. Unwanted forces acting on the test mass can overpower the weak gravitational

wave signal, therefore it is necessary to define an upper limit for the residual test mass acceleration noise:

$$S_a^{\frac{1}{2}} < 3 \times 10^{-15} \left[1 + \left(\frac{f}{3 \times 10^{-3} Hz} \right)^2 \right] ms^{-2} Hz^{-\frac{1}{2}} \tag{1.2}$$

which is valid in the frequency range of 0.1 mHz to 0.1 Hz. There are many sources of acceleration noise for LISA, some of which will be discussed in the following sections. By now it should be clear that the level of test mass isolation required presents an extreme scientific and technical challenge.

1.5 Pathfinder

The precision with which gravitational free-fall needs to be maintained for the test masses prompted a technology demonstration mission, LISA: Pathfinder. Pathfinder will give an opportunity to test many of the key LISA technologies in a space environment, some of which are impossible to test on Earth. Technologies related to achieving this goal include: the inertial sensors, the drag-free altitude control system and performing precision laser interferometry in space. The mission will act as a scaled down version of LISA with the performance requirement relaxed by an order of magnitude:

$$S_a^{\frac{1}{2}} < 3 \times 10^{-14} \left[1 + \left(\frac{f}{3 \times 10^{-3} Hz} \right)^2 \right] \mathrm{ms}^{-2} \mathrm{Hz}^{-\frac{1}{2}} \tag{1.3}$$

in a reduced bandwidth of 1 mHz to 30 mHz, (Lobo et al., 2006). Currently scheduled for launch towards the end of 2013, the craft will orbit at the L1 Lagrange point instead of the more complex orbit envisioned for LISA. Pathfinder will consist of just a single spacecraft housing two test masses each surrounded by an inertial sensor. While one of the test masses will be used as a reference the other will be kept in gravitational free fall and an internal interferometer between the two will be used to measure the level of any disturbances. This effectively shrinks one of the LISA arms to 30 cm and creates a set-up similar to that of LISA. It should be stressed that Pathfinder is not capable of detecting gravitational waves but is designed to test the technologies required for their detection.

Design, manufacture and testing of the Pathfinder hardware has been ongoing for a number of years and is nearing completion. This process involves each instrument or sub-system passing through nine 'Technology Readiness Levels', beginning with studies into basic physical principles and technology concepts and culminating

in being successfully operated during a mission.

Given the interrelated nature of many of the Pathfinder sub-systems, as the design of one has evolved the changes have fed into the design of others. For example, the design of the caging mechanism which secures the test mass during launch. Initially the caging system consisted of two retractable 'plungers' in contact with the centre of the upper and lower test mass faces. However, during testing at a fairly advanced stage of this systems development it was discovered that just two plungers were insufficient to reliability secure a test mass during launch like conditions. It was necessary to add eight additional retractable 'fingers' to grip the test mass on the upper and lower corners. This change in turn affected the design of the sensor housing and test mass as well as other systems that depend on their geometry. Figure 1.7 shows photographs of the early test mass and sensor housing design. It will later be discussed in detail how the flight geometries differ and how these changes affect other systems.

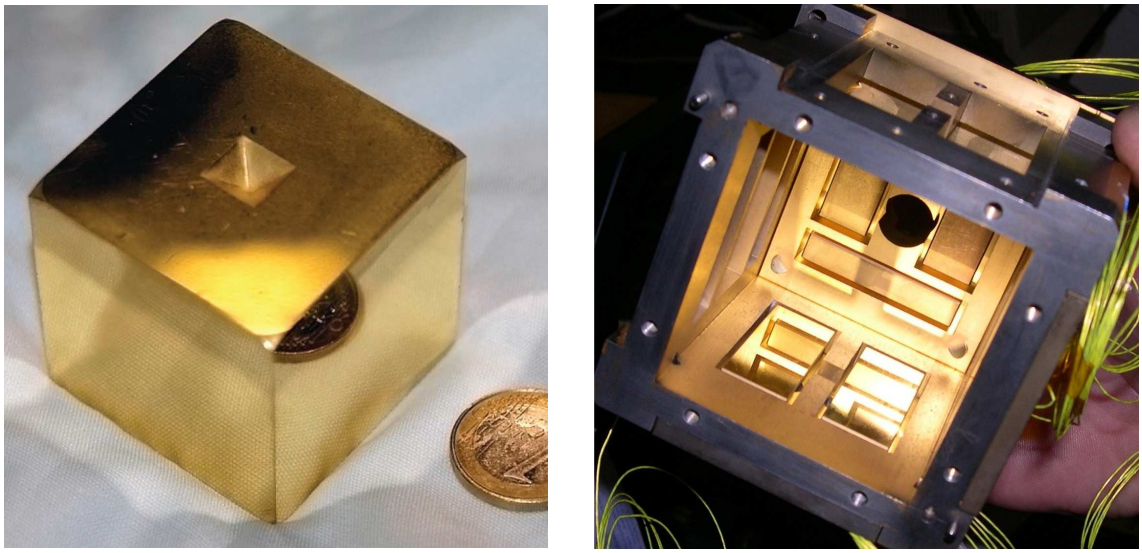

Figure 1.7: *Left:* A photograph of an early test mass design. Notice the central recess where one of the caging plungers is designed to hold the test mass. *Right:* A photograph of the engineering model inertial sensor with the upper Z-face removed. All the internal surfaces are gold coated and the capacitive sensor electrodes are visible. During the experiment the cubic test mass will float freely within the inertial sensor with a gap of 2.9 to 4.0 mm between the housing and test mass. Notice the circular hole in the lower Z-face through which one of the caging plungers is retracted after launch. Photograph courtesy of UTN.

1.6 Acceleration Noise

The key to LISA's success will be in its ability to accurately measure the variation in proper distance between pairs of isolated, distant test masses. At the frequencies of interest, the measured variation in proper distance will be formed by the combination of three components; the gravitational wave signal itself, the noise in the optical path measurement and noise due to spurious forces acting on the test masses. These two groups of noise can produce fake path difference with each dominating at opposite ends of LISA sensitivity. The noise in the optical measurements will be the limiting factor at frequencies above ~ 5 mHz while below this test mass acceleration noise will dominate, (Sylvestre and Tinto, 2003). The main source of optical noise is shot noise, particularly in the main interferometer beam where a large proportion of the initial light is not received at the secondary spacecraft due to beam divergence. Additional sources of optical noise include master clock noise, residual laser phase noise, laser beam pointing instabilities and scattered light effects.

An important part of the Pathfinder mission will be to study the various noisy forces that can act on a test mass, which will dominate the noise budget for LISA at frequencies below ~ 5 mHz. Many of these are dependant on the test mass position with respect to the spacecraft and walls of the inertial sensor. While the drag-free system aims to keep the test mass centred it is obviously imperfect and noise in the test mass position can couple with position dependent forces to create acceleration noise in the LISA band. For example, while every effort is made to balance the distribution of mass within the spacecraft, gravity gradients will still couple with test mass position.

Other sources of acceleration noise will include various thermal effects. For example, temperature fluctuations within the inertial sensor will create time varying radiation pressures in addition to thermal activated outgassing and radiometer effects. Also, the interplanetary magnetic field or magnetic fields originating from within the spacecraft can couple to a test mass's small magnetic moment and add to the acceleration noise. In order to better understand effects like these Pathfinder will include instruments to generate controlled noise sources and then observe the result on test mass position. For example, heaters will be used to induce temperature gradients, while magnetic coils will create non-uniform magnetic fields.

1.6.1 Electrostatic Interactions

Noise also arises from electrostatic interactions between the test mass and the surrounding electrode housing. Indeed, it is via such interactions that the position of a

test mass is determined and fed into the drag-free control loop. Both the sensing and actuation of the test mass using applied biases can inadvertently produce spurious accelerations of low frequency in the sensitive x axis. One can treat the individual surfaces of the electrode housing and their adjacent regions on the test mass as a group of i parallel plate capacitors. The electrostatic force on the test mass in the direction κ can then be approximated as:

$$F_\kappa = \frac{1}{2}\sum_i \frac{\partial C_i}{\partial \kappa}(V_{TM} - V_i)^2 \tag{1.4}$$

where C_i is the capacitance between the housing surface i and the test mass, κ is the distance between the ith surfaces in either x, y or z, V_{TM} is the test mass potential and V_i is the potential of the ith housing surface. It is this electrostatic force that is used to actuate the test mass by applying biases to the sense electrodes. However, note that it depends on the test mass potential, V_{TM}, which is given by:

$$V_{TM} = \frac{q}{C_T} + \sum_i \frac{C_i V_i}{C_T} \tag{1.5}$$

where q is the net test mass charge and C_T is the total capacitance of all i surfaces. For the isolated test masses used for LISA and Pathfinder the net charge will vary in time due to incident cosmic rays. A charged test mass will then interact via the Coulomb force with the sensor housing, also coupling with test mass position and noise in the applied voltages. The charged test mass will also interact via the Lorentz force with both the interplanetary magnetic field and magnetic fields present within the spacecraft. The total noise associated with test mass charging is dependant on the fluctuating charging events and Shaul et al. (2005) have produced noise estimates for both LISA and Pathfinder. For LISA the total noise associated with test mass charging was predicted to be between $2.52 - 3.62 \times 10^{-16}$ ms^{-2}Hz$^{-\frac{1}{2}}$ while for Pathfinder between $1.14 - 2.14 \times 10^{-16}$ ms^{-2}Hz$^{-\frac{1}{2}}$, compared to a noise budget allocated for charging of 11×10^{-16} ms^{-2}Hz$^{-\frac{1}{2}}$ and 15×10^{-16} ms^{-2}Hz$^{-\frac{1}{2}}$ for LISA and Pathfinder respectively. Of course the total net charge on the test mass needs to be kept below a specified threshold, which is 10^7 individual charges (The LISA Collaboration, 2011).

1.7 Sources of Test Mass Charging

The distance to the LISA and Pathfinder orbits from Earth, 50×10^6 and 1.5×10^6 km respectively, will place them far from the protective nature of the Earth's magne-

tosphere. They will therefore be exposed to the interplanetary charged particle environment. Detailed charging simulations have been carried out for both LISA, (Araújo et al., 2005), and Pathfinder, (Wass et al., 2005). Using accurate models of the experimental geometries the simulations showed that only incident particles with energies greater than $\sim$ 100 MeV can penetrate the spacecraft and reach the test masses.

At these energies there are two main sources of charged particles in the solar system; Galactic Cosmic Rays, or GCRs, and Solar Energetic Particles, or SEPs. GCRs form a permanent isotropic background flux originating from outside the solar system. The GCRs are composed of $\sim$ 98 % nuclei and $\sim$ 2 % electrons and positrons. Of the nuclei $\sim$ 87 % are hydrogen, $\sim$ 12 % are helium and $\sim$ 1 % are heavier nuclei, (Simpson, 1983). The flux of the GCR background varies during the eleven year solar cycle due to the Sun's varying magnetic field which shields the solar system. GCR flux is maximal at solar minimum and reduced at solar maximum. Figure 1.8 shows the spectra of several GCR components and how they vary during the solar cycle. To give some sense of the GCR flux, at energies greater than $\sim$ 100 MeV the proton flux varies between $\sim 2 - 4$ cm^{-2}s^{-1} during solar minimum and maximum.

SEP events on the other hand are transient and short lived, originating from solar eruptions. Their properties vary from event to event and last between a few hours to a few days but can temporarily increase the cosmic ray flux by several orders of magnitude. Events that can significantly increase test mass charging rates are only predicted to occur a few times a year at solar maximum and less than once a year at solar minimum, (Wass et al., 2005). Even then, only the largest events are expected to create test mass acceleration noise in excess of the allocated budget.

The simulations by Araújo et al. (2005) predict test mass charging rates for LISA resulting from incident GCRs of $\sim +50$ es^{-1} at solar minimum and $\sim +20$ es^{-1} at solar maximum. Simulations by Wass et al. (2005) for Pathfinder obtained similar charging rates. The same studies suggest large SEP events, occurring perhaps only once during a solar cycle, can produce increased charging rates of $\sim +70000$ es^{-1}. However, smaller SEP events produce increased charging rates of $\sim +100$ es^{-1} and can occur a few times a year at solar minimum.

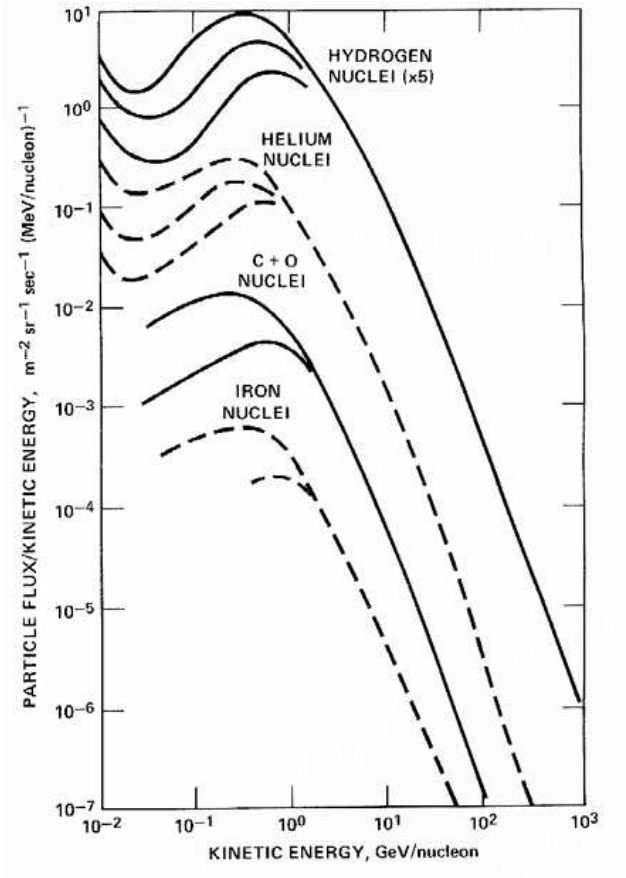

Figure 1.8: The spectra of the most abundant GCR components. For each species the variation observed during the solar cycle is shown. Note the hydrogen spectrum has been multiplied by 5 to offset it from the helium spectrum. Adapted from Meyer et al. (1974).

1.8 Managing Test Mass Charge

It is vital for the success of the LISA and Pathfinder experiments that the inevitable charging of the isolated proof masses can be counteracted. This is achieved using a non-contact method, so as not to disturb the free falling test masses, and involves illuminating either a test mass or its surrounding housing with ultraviolet (UV) light in order to generate a current of photoelectrons. By controlling the intensity of the UV light this discharging current can be used to counteract the charging caused by cosmic rays. However, there are many complications to this simple idea. The entire thesis relates to monitoring and counteracting test mass charging, initially for Pathfinder but then looking forward to improvements for LISA.

Chapter 2

The Pathfinder Radiation Monitor

Introduction

As discussed in the previous chapter, ionising radiation incident on the spacecraft will act to charge the test masses used in both the LISA and Pathfinder experiments. This radiation is predominately in the form of protons while a small but significant fraction, $\sim 10\%$, comes in the form of alpha particles, (Simpson, 1983). Particles originating from the sun are referred to as Solar Energetic Particles, or SEPs, while those produced outside the solar system are known as Galactic Cosmic Rays, or GCRs. Noise due to test mass charging is dependant on the flux and energy spectrum of the incident radiation both of which will vary in time as well as with the source.

With this in mind the Pathfinder data and diagnostics sub-system will include a radiation monitor to characterise the radiation environment in addition to systems designed to study the ambient magnetic and thermal conditions. As well as measurements from the inertial sensor providing the average test mass charging rate, the radiation monitor will offer an independent measure of both the flux and energy spectra of the ionising radiation which causes the charging. The combined data can then help to find correlations between the measured radiation environment and test mass charging itself. Also, the radiation monitor will help to validate existing charging models for Pathfinder and build confidence in those for LISA.

The radiation monitor employs a simple design which was initially developed by our group at Imperial College London. Its hardware has since been further developed and built by a Barcelona based collaboration consisting of NTE-SENER, the Institut d'Estudis Espacials de Catalunya (IEEC) and the Institut de Fisica d'Altes Energies (IFAE). Given our groups knowledge of test mass charging and simulation experience, Imperial College London has also been involved with testing of the instrument since its inception. This chapter describes the results from proton

beam testing of the flight model radiation monitor and simulations designed to aid analysis.

2.1 Hardware Design

There were several important factors driving the design and development of the Pathfinder radiation monitor. It needed to be as small and lightweight as possible, and have a low power consumption. In addition, it was desirable that it was based on a simple, reliable technology that had a space heritage. With these considerations in mind, a system based on silicon PIN (positive-intrinsic-negative) diodes was determined to be the best option. Similar detectors have been flown on many previous missions, (Buhler et al., 1996; Mohammadzadeh et al., 2003; McKenna-Lawlor et al., 2003; Dettmann et al., 2007), as using PIN diodes as ionising detectors allow both the flux and energy of the incident radiation to be measured.

The key idea behind any radiation monitor design is that a charged particle travelling through a material deposits energy. On average for a silicon PIN diode, every 3.66 eV of energy deposited within the intrinsic region frees a charge carrier which can then be collected by reverse biasing the PIN diode, (Knoll, 1979). The charge signal can be amplified and its amplitude is thus proportional to the energy deposited within the intrinsic region of the diode.

It is also necessary to understand the relationship between the amount of energy deposited and the initial energy of the incident particle. For protons and atomic ions, but not electrons, the average amount of energy a charged particle deposits per unit length as it travels through a material is given by the Bethe formula, (Poenaru and Greiner, 1997):

$$-\frac{dE}{dx} = \frac{4\pi e^4 z^2}{m_0 v^2} nZ \left[\ln \frac{2m_0 v^2}{I} - \ln\left(1 - \frac{v^2}{c^2}\right) - \frac{v^2}{c^2} \right] \tag{2.1}$$

where e is elementary charge, z, m_0 and v are the atomic number, rest mass and velocity of the charged particle respectively, n, Z and I are the number density, atomic number and mean excitation potential of the absorber material respectively, and c is the speed of light in a vacuum. When $\frac{v}{c} \ll 1$ the energy a charged particle deposits per unit length becomes proportional to $\log(E)/E$. For a given type of incident particle and absorber, the amount of energy deposited increases as the particles energy decreases. The total amount of energy deposited within an absorber will also be dependant on the path length of the charged particle through the material. This would create a problem for a single PIN diode detector as there

would be no way of distinguishing between a higher energy particle that travelled through the thickest dimension of the silicon or a slower one that passed through the thinnest dimension. This problem can be alleviated by using two PIN diodes in a telescopic arrangement and only recording the deposited energy of particles that deposit energy in both, thus limiting the angular acceptance. This in turn greatly reduces the range of possible path lengths through the diodes.

The Pathfinder radiation monitor uses two diode packages which are identical to those used by the Fermi Gamma-ray Space Telescope (FGST). The Large Area Telescope instrument on-board FGST uses 1600 of these diode packages and supplied the ones used for the radiation monitor from the many space qualified flight-spares they possessed. Each package consists of two silicon diodes mounted on a 0.8 mm thick ceramic substrate with a 1.0 mm thick resin window. For the radiation monitor only the larger of the two silicon regions is used from each package. This sensitive region has a nominal area of 10.5×14.0 mm, is nominally 300 μm thick, has its edge bordered by a 1.15 μm thick aluminium light shield and is encased by the silicone resin window, Figure 2.1.

Figure 2.1: A production photograph of one of the PIN diode packages mounted on one of the copper shield walls, temporarily held in place with *Kapton* tape. To prevent oxidation, the copper shield pieces are coated with a silver layer several microns thick. Note the sensitive silicon part of the diode (black) is laterally offset from the centre of the substrate. Photograph courtesy of IEEC.

The two diodes packages themselves are mounted in a telescopic configura-

tion, 20 mm apart, within a 6.4 mm thick copper shield. The copper shield is a 43.4×40.8×36.1 mm cuboid with rounded corners that is mounted within an aluminium flight box which also contains the associated electronics, Figure 2.2. The copper shield is designed to prevent protons with an incident energy less than 70 MeV reaching the diodes. Previous simulations showed that only particles above 100 MeV had sufficient energy to penetrate the inertial sensor and cause test mass charging, (Wass et al., 2005).

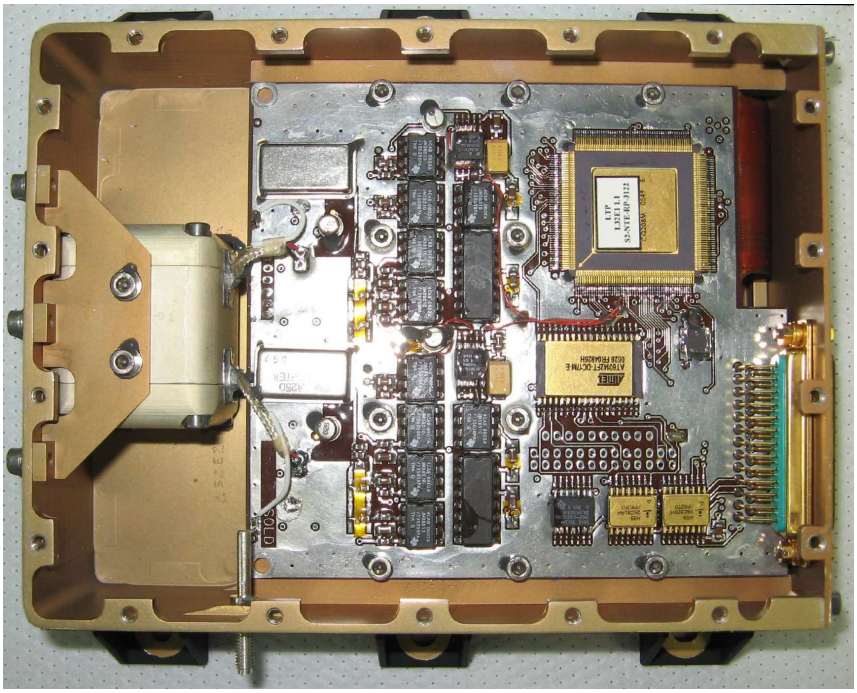

Figure 2.2: A photograph viewing the inside of the aluminium flight box with the lid removed. The radiation monitor electronics can be seen on the right while the copper shield containing the PIN diodes is shown on the left. Photograph courtesy of IEEC.

2.2 Data Acquisition

The radiation monitor electronics are designed to keep a count of any events which deposit more than 60 keV in either the front or rear diode. These are known as single events. In addition, if both diodes are triggered within 525 ns of each other, the energy deposited in the rear diode is recorded. These are referred to as coincidence events. The singles counting is done independently and therefore any coincident events are also counted as two singles events. Energy deposited during a coincident event is stored in a 1024 bin histogram. The deposited energy dynamic range for

the radiation monitor was chosen to be 0-5 MeV giving each bin a $\sim$ 4.88 keV width in energy. During the mission, the coincident spectra will be built up over 10 minute periods while the number of single events will be counted in 10 second periods. Given that the data transfer budget for the radiation monitor is limited to just over 18 bits per second, it was necessary to carefully allocate memory usage, Figure 2.3.

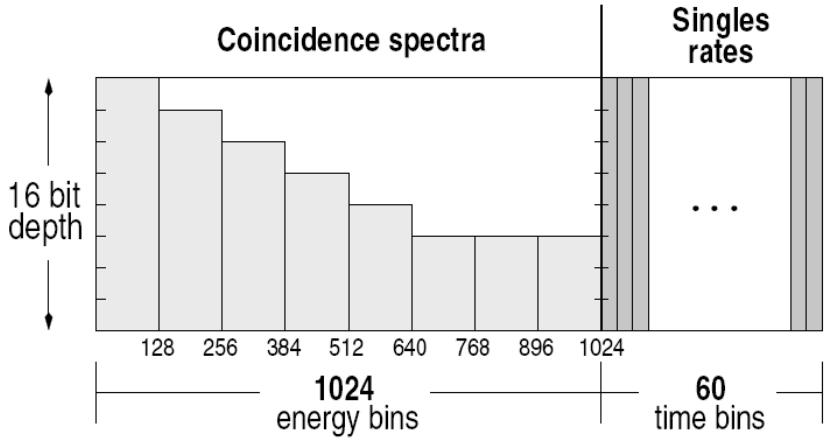

Figure 2.3: Allocation of data transfer budget. During a 10 minute period the coincident spectra can store, $128 \times (16+14+12+10+8+6+6+6) = 9984$ bits, while the singles count can store $60 \times 16 = 960$ bits. This leads to the required average data rate of $\frac{10944}{600} = 18.24$ bits per second. This figure was adapted from one found in Cañizares et al. (2009).

For the coincidence data more bits have been allocated to the lower energy bins as these are predicted to have higher counts. The highest count possible in the first 128 energy bins is $2^{16} = 65536$ while in the last 384 bins a maximum count of $2^6 = 64$ is possible. Above these levels the bins would become saturated. Depending on the energy of the incident radiation, this leads to a maximum coincident count rate of > 5000 counts per second. The maximum singles count rate is $\sim$ 6500 counts per second. Simulations predict that these maximum rates should be more than sufficient as a large SEP event should produce coincident rates of $\sim$ 100 counts per second and singles rates of $\sim$ 1500 counts per second, while the GCR background will produce coincident rates of $\sim$ 0.4 counts per second and singles rates of $\sim$ 4 counts per second, (Wass et al., 2005).

2.3 Beam Test

The flight model radiation monitor was built by the Barcelona collaboration and underwent final space qualification testing during the autumn of 2010. Representing Imperial College London, I attended the proton beam testing along with members from the Barcelona group. As we had been heavily involved with simulating and analysing the data from similar tests performed on the prototype radiation monitor, my role was to analyse the data collected and, with the aid of my own simulation, demonstrate the radiation monitors performance.

The tests were performed at the Proton Irradiation Facility (PIF) at the Paul Scherrer Institute in Switzerland, and were split into three parts. The first part involved irradiating the radiation monitor at various incident proton energies in order to test that the radiation monitor was recording the deposited energy spectrum as expected, Section 2.6.3. The second part involved irradiating the radiation monitor with a fixed proton energy but with increasing flux to determine the maximum count rate capacity of the radiation monitor, Section 2.6.4. The third part involved irradiating the radiation monitor at various proton energies and at various incident angles in order to check the effectiveness of the copper shield and the angular acceptance of the diodes telescopic configuration, Sections 2.6.5.2 and 2.6.5.3.

At the PIF, protons are delivered to the exposure site after first being accelerated by the COMET cyclotron to 250 MeV with a σ $\sim$0.25 MeV and an approximately Gaussian energy profile. The beam was set during the tests to have a uniform circular spacial profile with a diameter of 90 mm. The incident beam energy can be reduced using seven local copper degraders of varying thickness, between 0.5 mm and 38 mm. By raising and lowering these copper degraders into and out of the initial proton beam quasi-continuous energies can be achieved down to $\sim$10 MeV. Also present within the beam line was a flat, air-filled ionisation chamber and an x-y wire chamber, both having thin, $\sim$1.0 mm, *Kapton* windows. While neither of these devices were in use during the tests their *Kapton* windows do act to degrade the incident beam by a small amount. A 70 mm thick, circular copper collimator was placed after the degraders to restrict the angular spread of protons arriving at the target area. It had an outer diameter of 180 mm and the inner aperture diameter of 40 mm was large enough to allow the entire diode area to be exposed equally. A plastic scintillator, with a sensitive area of approximately 1 cm^2, was placed upstream just below the collimator aperture, in order to measure the flux of the beam.

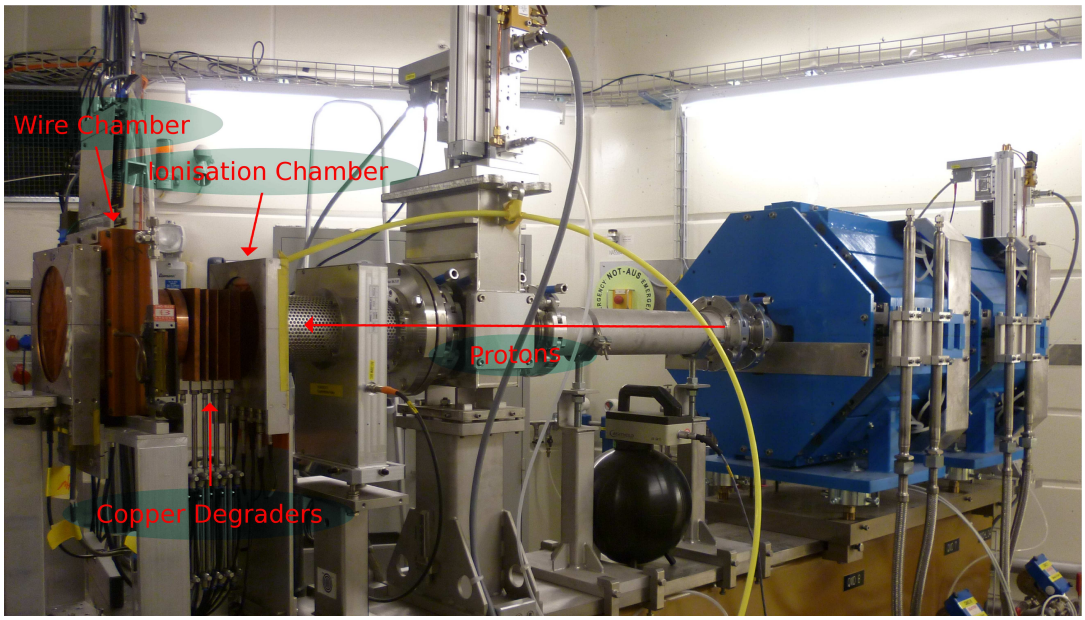

Figure 2.4: A photograph of the PIF beam line where the proton beam travels from right to left. The seven copper degraders in the up position can be seen to the left of the image. Also visible are the unused but present, ionisation and wire chambers. The photograph was taken prior to the circular copper collimator and radiation monitor being added.

The radiation monitor itself was mounted on a rotary table at the end of the beam line, which allowed a minimum stepper motor rotation of 0.1° with respect to the beam. The radiation monitor was carefully aligned so that the telescopic diode arrangement was parallel with respect to the beam and the diode centres with the beam centre. The beam line is shown in Figure 2.4 and the radiation monitor mounted on the rotary table in Figure 2.5. After the radiation monitor had been positioned and aligned the testing room was sealed and the beam settings and rotary table were controlled remotely from a separate room. Each set of data was taken during a 60 second exposure to the proton beam and except for the maximum count rate test, with a flux which was nominally around 1000 protons s^{-1} cm^{-2}.

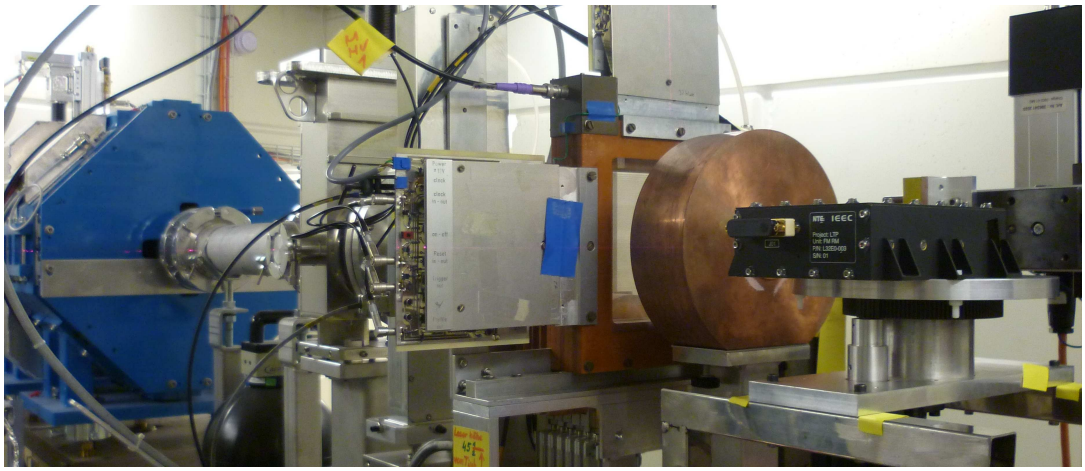

Figure 2.5: A photograph of the PIF beam line in its final configuration. The radiation monitor mounted and aligned on the rotary table can be seen to the right of the image.

2.4 Geant4

Geant4 is a freely available software tool kit that is designed to simulate the passage of particles through matter. Written in C++ and designed with an object orientated philosophy, it uses Monte Carlo techniques and a wide range of models to accurately describe physical processes. Originally designed for use by the high energy physics community it is now used within a range of areas including nuclear, accelerator, medical and space physics. The software is maintained and improved by a world wide collaboration of physicists and software developers and regular updates are available on-line, (The Geant4 Collaboration, 2003).

The underlying aim of Geant4 is to provide the user with a framework in which to design and build their simulation. It provides a wide range of classes, functions and models that can be used as tools and combined to create something specific. By using the Geant4 structure it is possible to build fairly complex simulations in a relatively short space of time. The user can concentrate on the details of their particular problem rather than having to write the entire simulation from the ground up. At the same time Geant4 is flexible enough to allow the user to change or add to the default functionality by altering the source code themselves.

In addition to the *main* function a Geant4 simulation normally consists of three distinct parts. A geometry file defines the volumes that make up the system, their dimensions and composition as well as their position with respect to one another. The Geant4 framework provides several ways of representing a volume, one of which

is using so called Constructive Solid Geometry (CSG) solids like spheres, cuboids, cylinders and many more. These solids can then be combined using boolean operations by adding, subtracting and intersecting to create more complex geometries. A second file which describes how primary events are generated is also required. This file describes the type of particle, or particles, that will initially be generated in the system, their energy, direction and initial position as well as additional relevant properties like their polarisation. Again, Geant4 provides several classes and functions to aid in this process, or the user can write their own from scratch.

The third part of a standard Geant4 simulation is a file that describes all the particles and physical processes to be used. Geant4 provides classes that describe common particles like protons, electrons, neutrons and gammas in addition to many others from the particle zoo. Over one hundred types of particle are provided by Geant4 and the user has the option of defining their own. The same file also contains the physical processes that describe how the particles interact with materials within the system. By default Geant4 provides general transportation, electromagnetic, hadronic, decay and optical processes, which are further broken down into specific processes relating to different particle types. Many of the processes also have several implementations and the user is free to choose the model that suits their needs, for example if speed or accuracy is more desirable. It is also within this file that production cuts are defined. While all generated particles are tracked to zero range, only those above an optional user supplied threshold are produced. This threshold is defined as the possible range of any particle produced within the material. Geant4 also allows different productions cuts to be applied in different regions. This has the advantage of allowing a smaller threshold in regions where greater accuracy is beneficial while not effecting performance elsewhere in the system.

2.5 Simulating the Beam Test

To aid the radiation monitor qualification, the beam tests were simulated in Geant4. The simulation provided additional confidence that the radiation monitor was performing as expected and help understand the characteristics of the system itself. In addition, an accurate simulated model of the radiation monitor can be used in future Geant4 simulations of the entire spacecraft. This can then be used to understand measured data from Pathfinder and study the connection between test mass charging and the radiation environment measured by the monitor. The simulations described here are based on source code originally written by Peter Wass during similar work with the prototype, (Wass et al., 2006a). However, the code was almost

completely rewritten by myself to include differences in the beam line set-up, the aluminium flight box and a much more detailed model of the diode packages. Due to changes with Geant4 itself since the previous work was carried out, the structure of the physics models and visualisation was also completely changed.

2.5.1 Simulation Description

The simulated geometry included the eight degrader plates, the wire and ionisation chambers, plastic scintillator, collimator, rotary table base plate, aluminium flight box, copper shield and a detailed model of the two silicon diode packages, Figure 2.6. The incident proton beam was simulated as described in Section 2.3. A Geant4 production cut of 1 mm was applied globally but a cut of 10 μm was used inside the aluminium flight box region. This reduced the simulation run time by not tracking particles that did not have sufficient energy to penetrate the shield while providing increased accuracy within the sensitive diode regions.

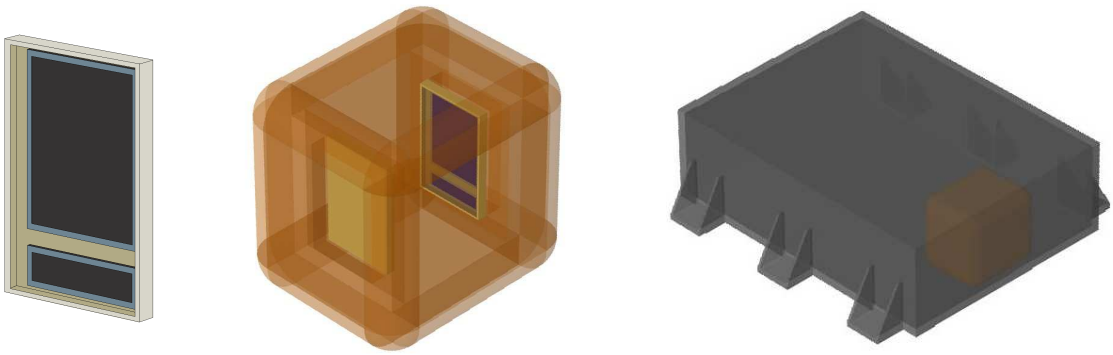

Figure 2.6: The simulated Radiation Monitor. *Left*: The diode package, including the offset silicon regions, aluminium light shields and resin window. *Middle*: The two diodes mounted within the copper shield. *Right*: The copper shield mounted within the aluminium flight box.

The diodes were modelled in greater detail than the rest of the simulation geometry in order to achieve results that were as accurate as reasonably possible, Figure 2.6. While creating the new simulation, it was realised that the sensitive silicon regions do not lie exactly at the centre of the ceramic substrate and are in fact laterally offset by 0.5 mm. This can be seen clearly in Figure 2.1. As it is the ceramic substrates that are aligned within the copper shield, and both diodes face each other, this exacerbates the problem so that the sensitive regions are actually laterally offset by 1.0 mm with respect to each other. Considering the sensitive

regions are only 10.5×14.0 mm this leads to a subtle but measurable effect, discussed in Section 2.6.2.2.

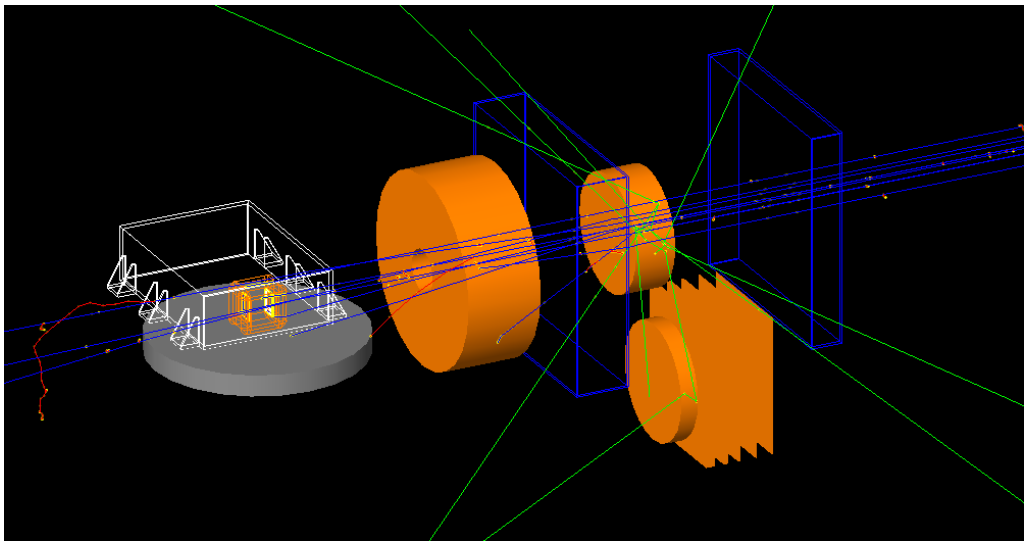

Figure 2.7: The simulated beam line showing the degrader settings for nominally 150 MeV protons and ten accumulated events. The flight box is mounted on the rotary table and the diodes are at 0° with respect to the beam.

With a few exceptions the physics list used within the simulation was the same as that used by Araújo et al. (2005), and is described in detail therein. The list includes hadronic, electro-nuclear and decay physics models and many of these have been physically validated through previous work, (The Geant4 Collaboration, 2006). While most of these processes only apply to energies much higher than required they were left in so as not to inadvertently break the complex list structure while trying to remove the unused physics. Protons in the energy regime of interest, less than 250 MeV, predominately lose energy through inelastic interactions with atomic electrons in the material being traversed, via both ionisation and excitation. The most important models for this simulation were therefore those that describe the electromagnetic physics, and these were completely updated to the new modular format used by Geant4. For the rest of the work discussed the standard electromagnetic physics module was used. As a cross check, the Livermore and Penelope electromagnetic physics modules were tried and the results found not to vary.

In order to easily obtain the amount of energy the incident protons deposited within the diodes, the use of what are known as sensitive detectors were required. In the Geant4 framework by defining a sensitive detector, in this case the larger silicon layers in the diode packages, various quantities can be extracted from the simulation specific to the sensitive area. During a run, for any incident proton depositing energy

in the sensitive regions, the initial energy of the particle, the deposited energy in the front and rear diodes and the position of the initial incidence in the diodes were recorded by the simulation. The output was in the form of an ASCII file and these data were then converted via a MATLAB script to the same form as the radiation monitor measured data by adding a Gaussian noise of $\sigma = 17$ keV to mimic the effect of the electronics and detector noise, and implementing a 60 keV detection threshold as was the case for the real monitor. The choice of 17 keV for the noise is discussed in Section 2.5.3.

2.5.2 Beam Properties

The PIF initial beam was simulated using a Gaussian energy profile with a peak energy of 250 MeV and a spread in energy of $\sigma = 0.25$ MeV, which were its nominal properties and well defined. The pre-degrader beam had a uniform circular spatial profile and although the actual beam had a 90 mm diameter, the simulation used a 42 mm diameter. This was because it was found that due to the collimator limiting the final beam to 40 mm anyway, it vastly reduced the run time without effecting the results. Table 2.1 shows the beam settings for each nominal incident energy while Figure 2.8 shows the resulting beam energy distributions from simulation.

Nominal Energy (MeV)	Copper Thickness (mm)	Initial Number	Mean Energy (MeV)	Sigma (MeV)
250	0.0	1.0×10^6	247.06	0.36
200	19.5	1.0×10^6	197.98	1.35
150	38.0	2.0×10^6	144.16	2.13
100	50.0	3.0×10^6	100.19	3.01
90	52.0	3.0×10^6	91.43	3.35
80	54.0	4.0×10^6	81.23	3.52
70	56.0	4.0×10^6	71.05	3.90

Table 2.1: The calculated incident beam properties from simulation. Note that the actual mean energies were not expected to be exactly the same as the nominal values. The affect of the *Kapton* windows in degrading the beam is observed at 250 MeV.

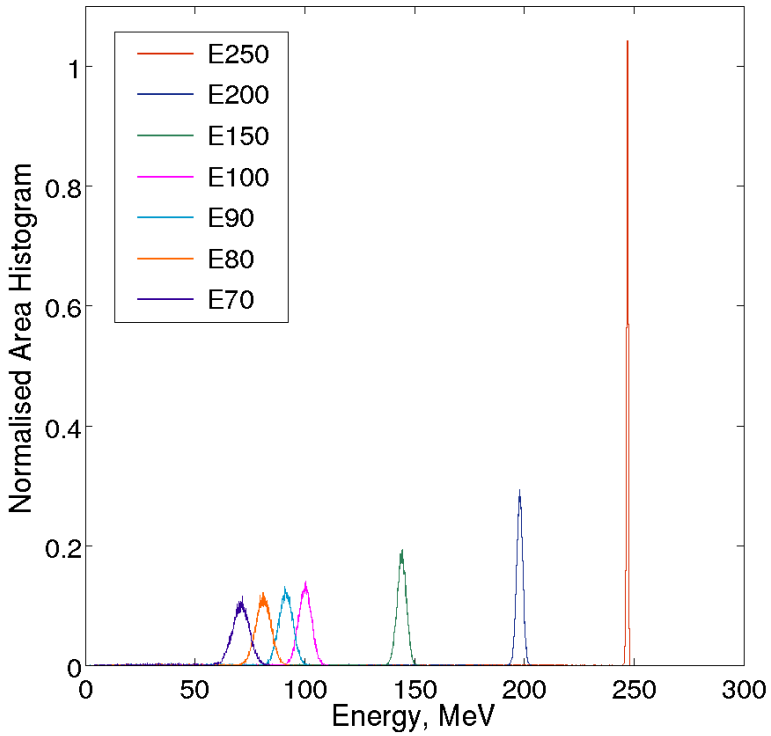

Figure 2.8: The incident energy spectra with areas normalised to one, calculated from the simulation. As the initial 250 MeV beam is degraded in order to reach lower energies, the width in the beams energy increases.

2.5.3 Parameter Tuning

A decision was made to vary as few of the potentially large number of free parameters as possible in the simulation. With this in mind the nominal values were taken and only the diode silicon thickness, level of electronics noise and the thickness of the ionisation and wire chamber *Kapton* windows were varied. The silicon thickness was nominally 300 μm but it quickly became clear that it needed to be greater than this in order to adequately fit the observed data. Varying the silicon thickness varied the position of the spectral peak and for reasonable values, 300$\pm$50 μm, had a greater affect at higher energies. While studying the literature for the GLAST diodes a document by Serma Technologies was discovered that described a detailed study of the engineering model diodes composition, with cross-sections and an X-ray inspection, (Aude et al., 2002). This study found the silicon thickness to be 320 μm which gives much improved simulation results, Figure 2.9. For the remainder of work discussed, a value of 320 μm was taken for the silicon thickness.

As previously mentioned, a value of σ = 17 keV for the Gaussian electronics

noise was found to give the best results and was used throughout this work. The measured value was ∼13 keV but this was made at ∼ 22°C whereas the PIF temperature was ∼ 30°C, so an increase was expected as the electronics noise is strongly temperature dependent. Varying the σ of the electronics noise affected how broad the spectra appeared and for reasonable values, 13±8 keV, had a greater effect at higher incident energies.

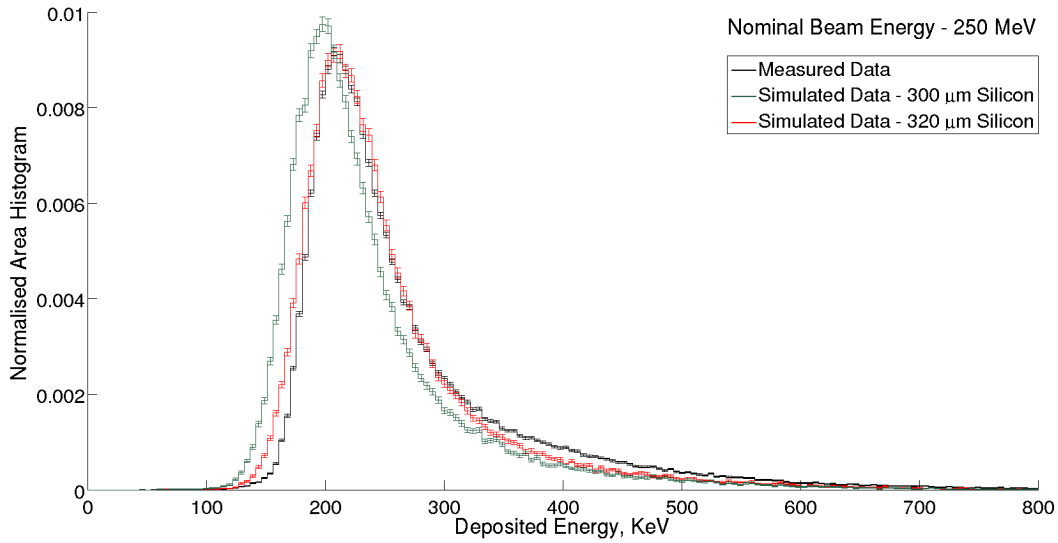

Figure 2.9: Shows the improvement in the simulated spectra at 250 MeV when the silicon thickness is increased from 300 μm to 320 μm.

The only other parameter that was tuned was the thickness of the *Kapton* windows for the ionisation and wire chambers. It was not possible to accurately measure them as they were part of a sealed unit, but they appeared to be approximately ∼1 mm thick. From the simulation, a window thickness of 1.25 mm was found to give the best results. The *Kapton* thickness acted to slightly degrade the incident beam energy and for reasonable values, 2.0±1.5 mm, had a greater affect at lower incident energies. The effect of tuning additional parameters is discussed further in Section 2.6.3, but with just these three variable parameters and everything else taking nominal values, good agreement between simulation and measured data was achieved.

2.6 Results

2.6.1 Background Counts

Background counts were measured when the radiation monitor was in the control room prior to the tests, and a couple of times after it had been set-up at the target position in between the tests. With the proton beam turned off, the radiation monitor was left to record data for at least twenty minutes. In the control room, a single count background rate of 1.10 ± 0.38 counts s^{-1} was measured and in the beam room the rate was found to be 1.59 ± 0.36 counts s^{-1} and 1.85 ± 0.47 counts s^{-1}. For most of the beam test measurements, the single count rates were approximately fifty times greater than the background levels so the effect of the background was minimal, though was considered in the analysis. The same measurements showed a coincident background of less than one event per minute, and this was ignored in the analysis.

2.6.2 Angular Calibration of the Rotary Table

2.6.2.1 Angular Offset

It was important to check that the copper shield, PIN diodes and the radiation monitor as a whole, were in correct alignment. As the angle of the incident proton beam increases with respect to the radiation monitor, the path length through the shielding increases, and the energy of the protons is reduced. The lower energy protons then deposit more energy in the silicon diodes. Additionally, the protons path length through the silicon itself rises, again increasing the energy deposited. If the radiation monitor is correctly aligned, and the telescopic diode arrangement is perpendicular to the beam, the peak in the energy deposited in the diodes should be at a minimum for a particular incident energy. To study this effect the radiation monitor was exposed to nominally 250 MeV protons at orientations with respect to the beam of between -40° and +4.5°. The limited range of the positive angles was due to a reluctance to risk rotating the protruding radiation monitor too close to the collimator.

To perform the analysis it was necessary to accurately determine the position of peak energy deposited. It is important to remember that the Bethe formula, Equation 2.1, describes the average energy loss for a charged particle. For a thin layer of silicon, like the ~ 300 μm diodes used in the radiation monitor, fluctuations about this mean value are significant and non-Gaussian, with tails extending to higher losses for the deposited energy spectra recorded within the diodes. Although

small energy transfers are more likely, for a thin layer there are fewer interactions, and some deposit large amounts of energy resulting in the tails. This distribution was first described by Landau (1944). Were the thickness of the layer increased, the number of interactions would also increase, and the deposited energy distribution would approach a Gaussian distribution.

Given Landau's distribution is defined by a complex integral, the analysis was simplified by using an approximation developed by Moyal (1955), given by:

$$n(E) \approx Ae^{\left(-\left(\frac{E-\mu}{\beta}\right)-e^{-\left(\frac{E-\mu}{\beta}\right)}\right)} \tag{2.2}$$

where E is the deposited energy, β is related to the energy spread, μ is the peak position of the distribution and A is a normalisation constant. In order to obtain the peak energy deposited in the radiation monitor for a particular angle of incidence, the parameters β, μ and A were varied while minimising $\chi^2 = \sum_{i=1}^{n} \frac{(O_i - E_i)^2}{\sigma_i^2}$, where O_i is the observed value, E_i is the expected value from the model for a particular set of parameters and σ_i is the error in the observed value. The reduced χ^2 values for the best fits were typically between 2 and 7, which was considered acceptable given Equation 2.2 is only an approximation of the deposited energy spectrum. The peak energy deposit was well defined for angles less than ~ 20 °, while at greater angles it was too broad to be used accurately. The results of varying peak position with incident angle are shown in Figure 2.10.

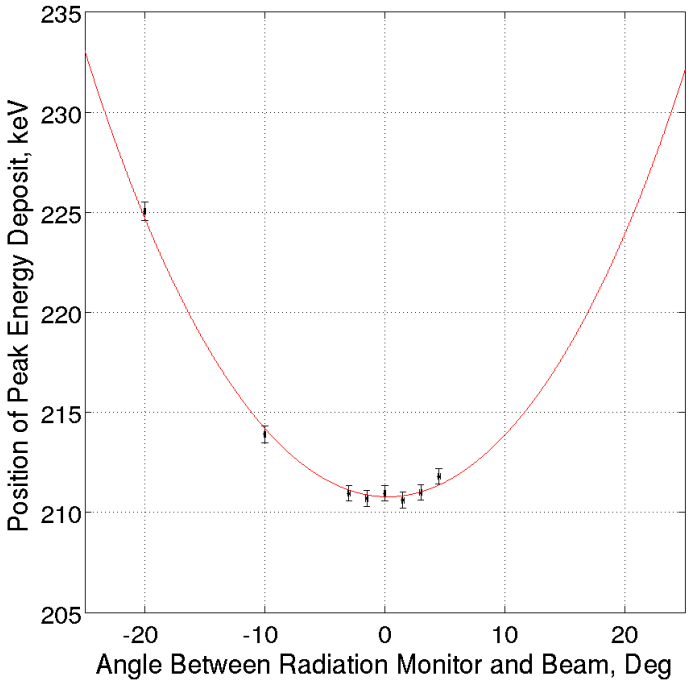

Figure 2.10: Position of the peak energy deposit in the silicon diode for a given rotary table angle. The fit obtained using Equation 2.3 is also shown in red, and had a reduced χ^2 value of 1.1.

Given the position of the peak deposited energy is proportional to the incident protons path length through both the shield and the diode, and the path length is proportional to the cosine of the beam angle with respect to the radiation monitor:

$$E_{peak} = \frac{K}{\cos(\theta - \theta_{angular})} \tag{2.3}$$

where E_{peak} is the position of the peak energy deposit, K is a constant, θ is the nominal angle between the beam and the radiation monitor and $\theta_{angular}$ is a measure of any angular offset present. By using Equation 2.3 and again minimising χ^2 for the data in Figure 2.10, a value of $\theta_{angular} = +0.3° \pm 0.3°$, where the error is the 1σ confidence interval. This was considered small enough to allow any angular offset to be ignored for the rest of the analysis and show that the radiation monitor was well aligned.

2.6.2.2 Linear Offset of Diodes

A further effect can be studied using the same data, but this time considering the ratio of single to coincident counts for a given rotary table angle. This should be

minimal when the the total areas of the sensitive silicon in both diode packages are in the same line of sight with respect to the proton beam. When the sensitive areas are well aligned with respect to the beam the number of coincident events is relatively high, while the number of singles is relatively low. As they move out of alignment, the number of singles increases while the number of coincident events decrease. Both the angular offset of the radiation monitor and the linear offset between the diodes themselves, as mentioned in Section 2.1, cause the minima to move away from 0° and should take the form, $\theta_{ratio} = \theta_{linear} + \theta_{angular}$. The result of plotting this ratio with respect to radiation monitor is shown in Figure 2.11.

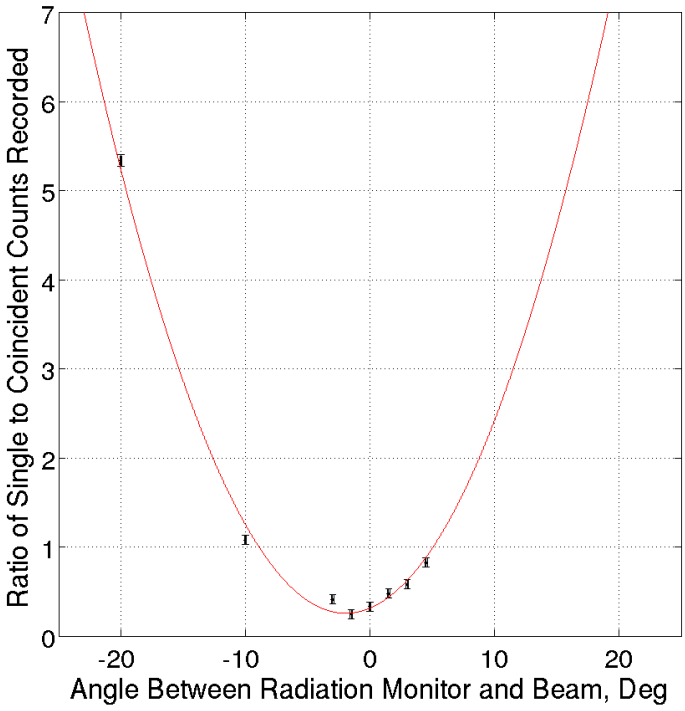

Figure 2.11: Shows the affect of the diodes linear and angular offset on the position of the minima when plotting the ratio of single to coincident counts for a given angle. The fit obtained using a quadratic is also shown in red, and had a reduced χ^2 value of 5.7.

The diodes linear offset of 1.0 mm ± 0.2 mm from each other and a separation distance of 20.0 mm ± 2.0 mm gives $\theta_{linear} \approx \arctan\left(-\frac{1}{20}\right) = -2.9° \pm 0.6°$. The position of the minima from Figure 2.11 was obtained by fitting a quadratic to the data while minimising χ^2, which gave $\theta_{ratio} = -1.9° \pm 0.3°$. Using this, another estimate of the the radiation monitor angular offset can be obtained, $\theta_{angular} = +1.0° \pm 0.7°$. This is in fair agreement with the previous method and is again small enough to suggest that the radiation monitor was well aligned with respect to the beam. While

any small angular offset was ignored in the simulation, the diodes linear offset was included.

2.6.3 Deposited Energy Spectra Test

In order to ensure the radiation monitor was measuring the deposited energy spectra correctly, runs were performed at various incident energies with a rotary table angle of 0°. Measurements were made nominally at 250 MeV, 200 MeV, 150 MeV, 100 MeV, 90 MeV, 80 MeV and 70 MeV. The results were then compared to simulation. Using the parameters described in Section 2.5.3, good agreement was found between the measured data and simulation, as can be seen in Figures 2.12 to 2.15. The agreement could be improved further by, possibly arbitrarily, varying additional parameters like the degrader's thickness, Figure 2.14. Given the quality of the agreement between simulated and real data already these adjustments were not made.

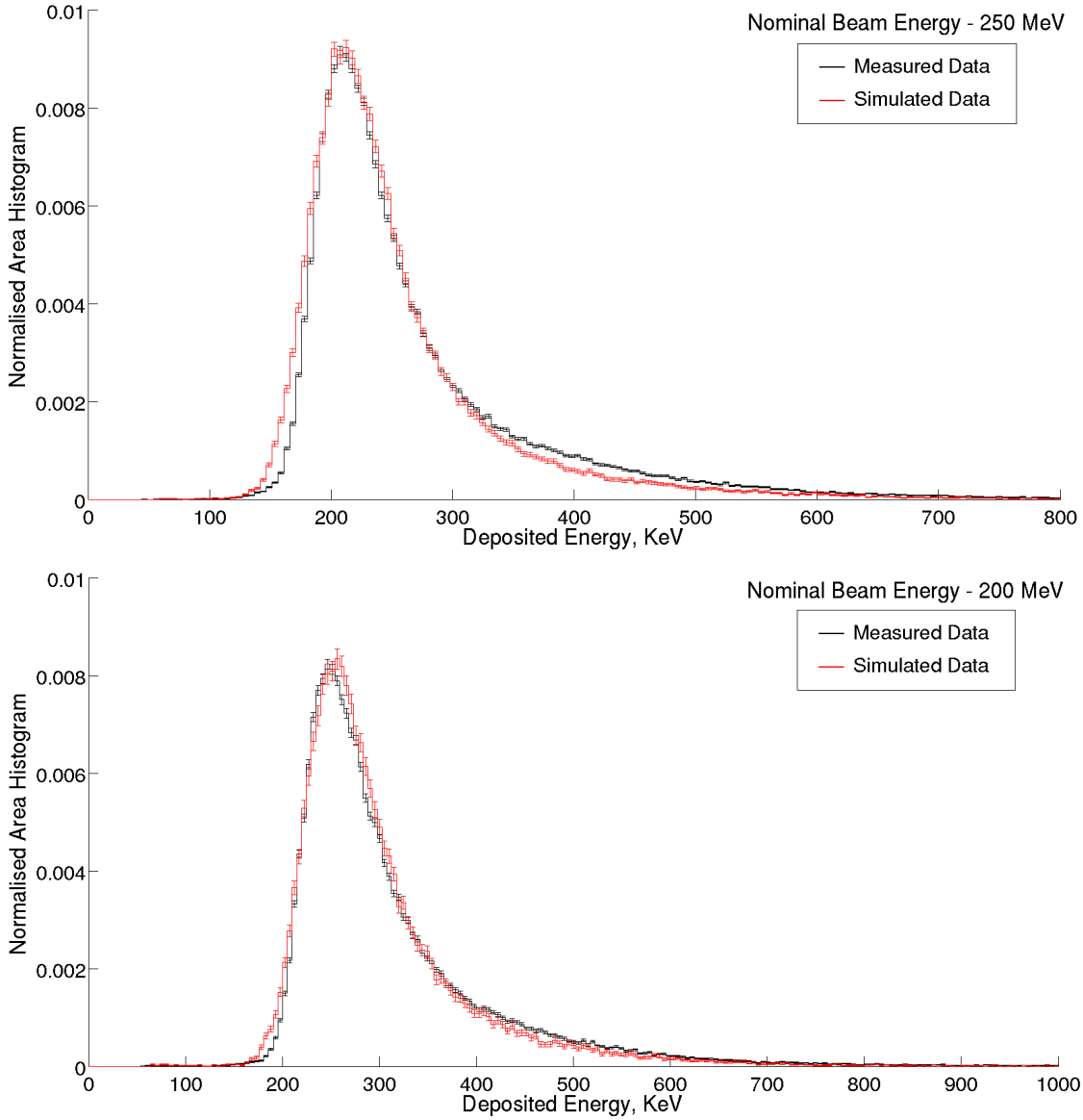

Figure 2.12: Comparison of deposited energy spectra from simulation and measured data for incident protons with 250 MeV (*Top*) and 200 MeV (*Bottom*) nominal energy.

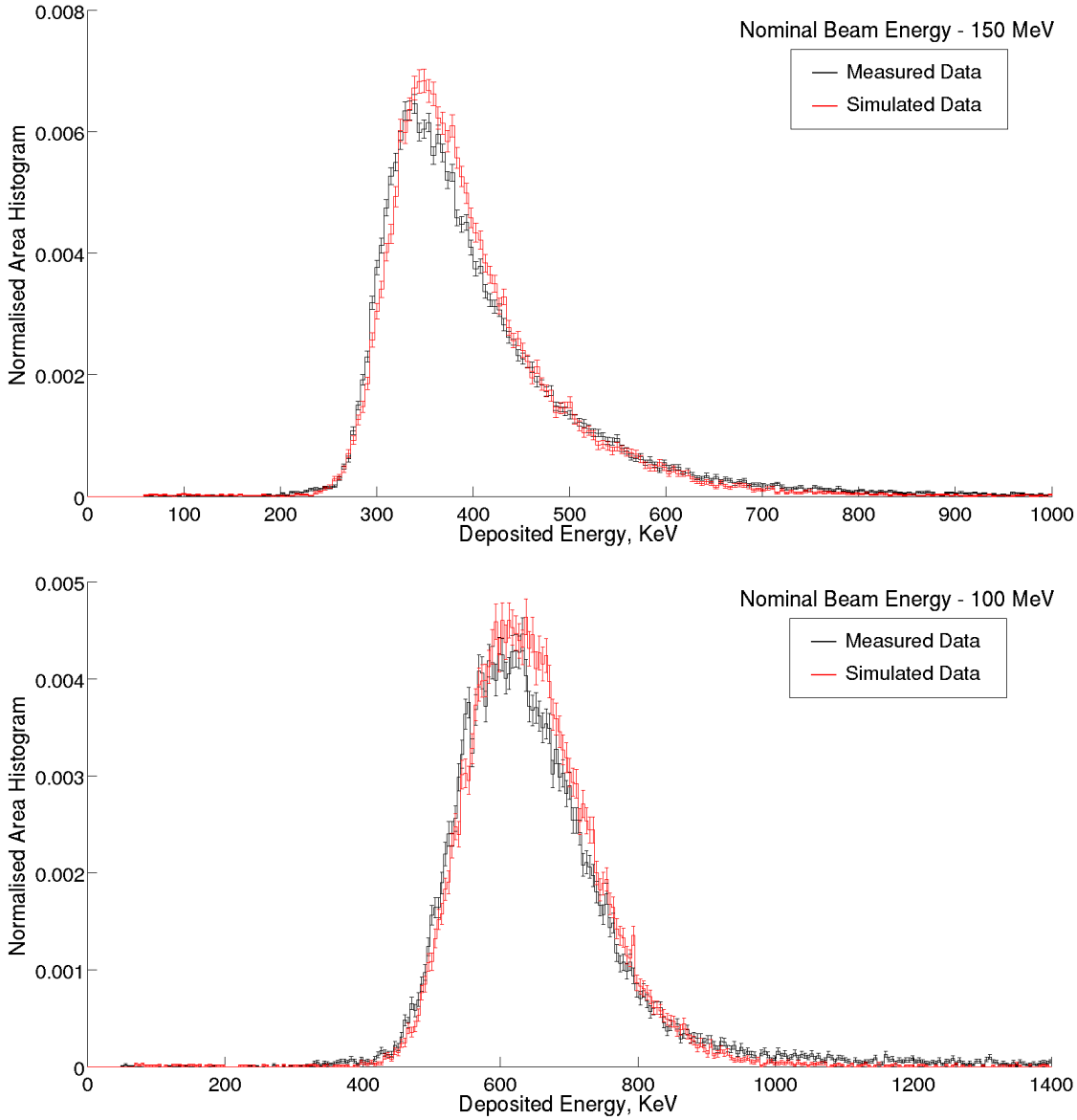

Figure 2.13: Comparison of deposited energy spectra from simulation and measured data for incident protons with 150 MeV (*Top*) and 100 MeV (*Bottom*) nominal energy.

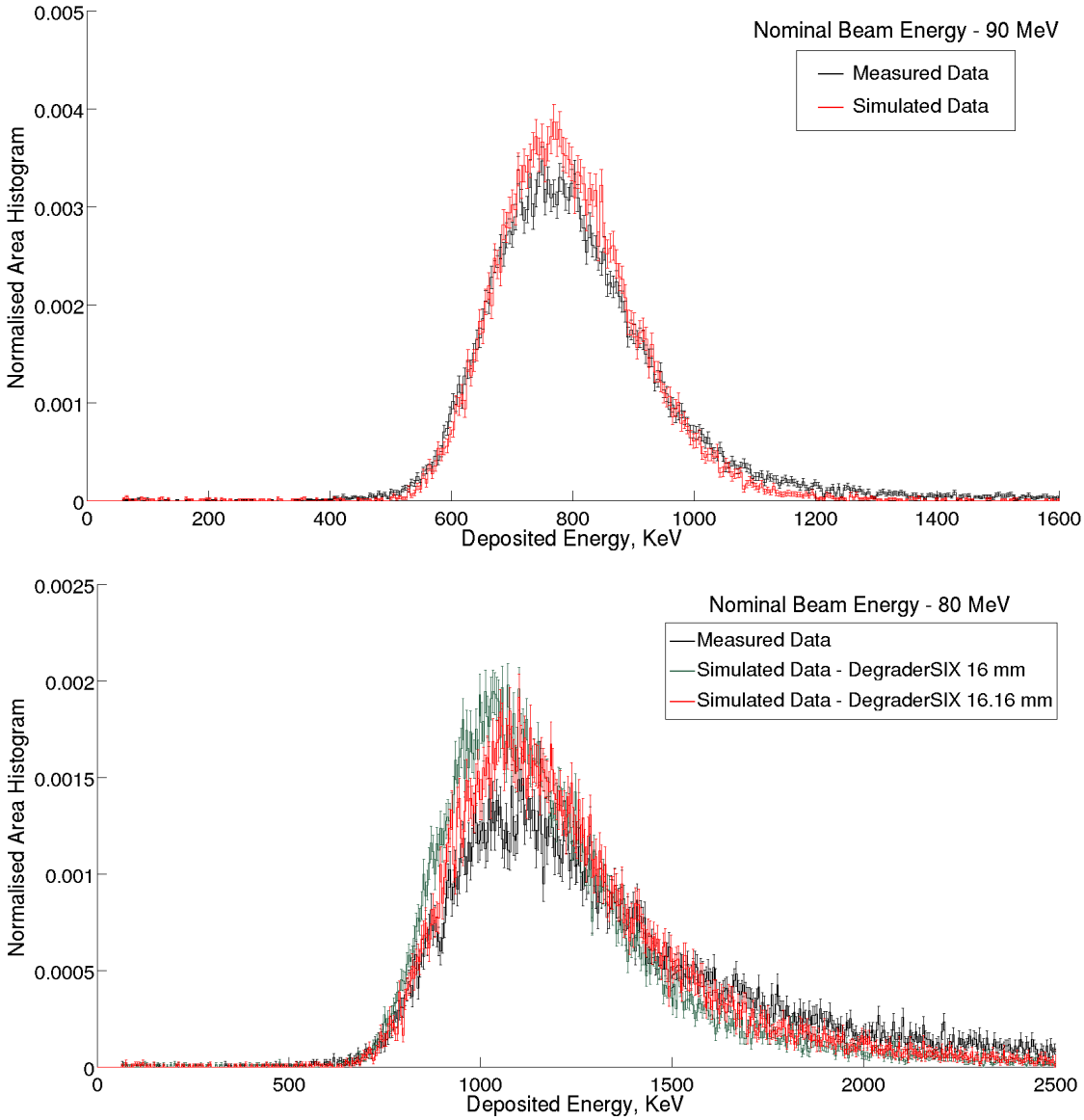

Figure 2.14: Comparison of deposited energy spectra from simulation and measured data for incident protons with 90 MeV (*Top*) and 80 MeV (*Bottom*) nominal energy. Also shown is the effect within the simulation of changing the thickness of degrader plate six by only 1 %. Note that for 200 MeV and 70 MeV this plate was also used but the spectra show no visible change.

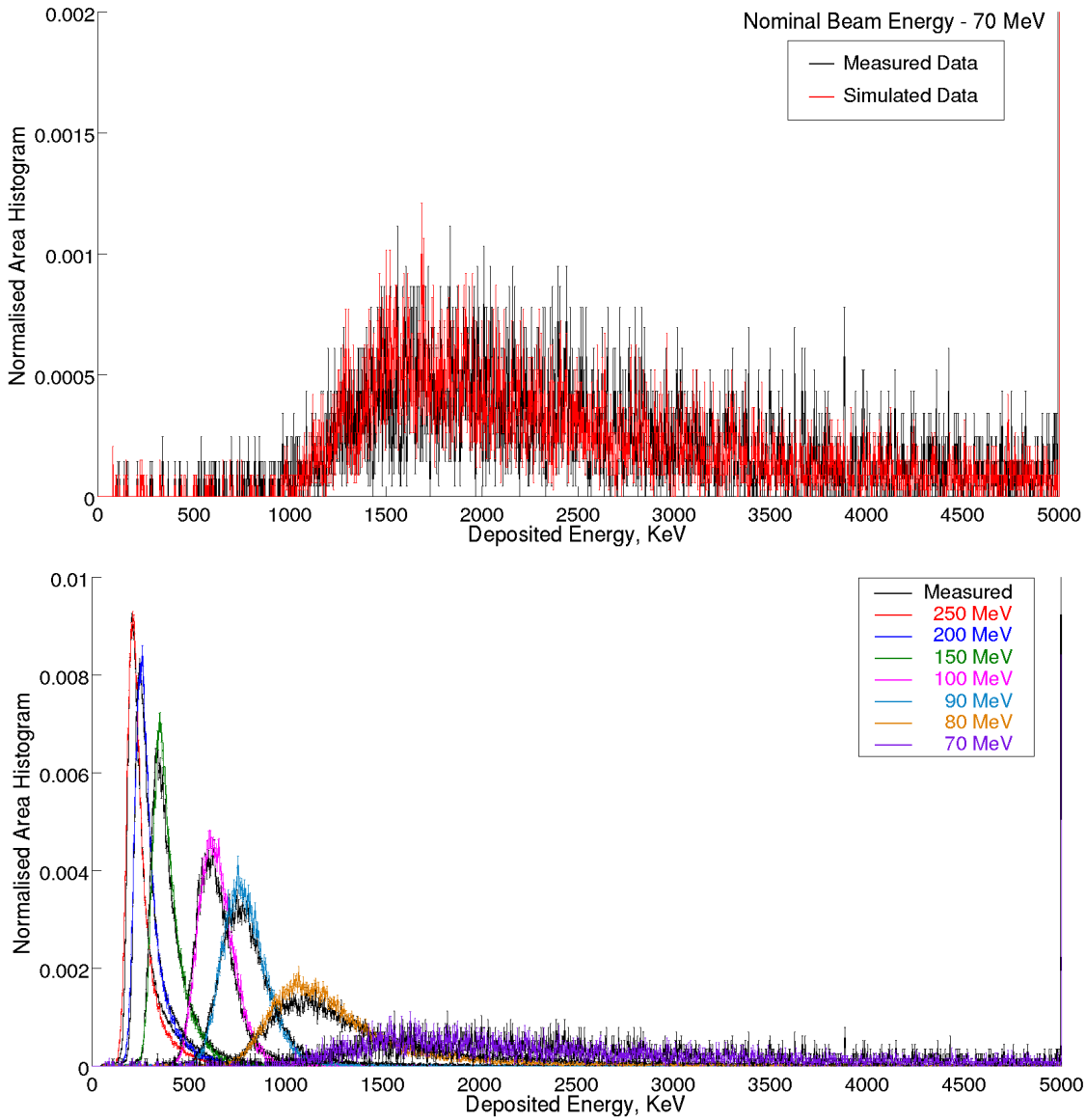

Figure 2.15: Comparison of deposited energy spectra from simulation and measured data for incident protons with 70 MeV (*Top*) nominal energy. Also shown is data for all incident energies (*Bottom*).

2.6.4 Maximum Count Rate Test

In order to examine the maximum count rate the radiation monitor is capable of before dead time in the electronics becomes an issue, a series of measurements at a nominal energy of 100 MeV and a rotary table angle of 0° were made. These were performed with an increasing flux from $\sim$ 500 protons s^{-1} cm^{-2} to $\sim$ 7500 protons s^{-1} cm^{-2}. An upper limit for the maximum count rate for the radiation monitor can be found by plotting the flux measured by the PIF plastic scintillator against the count rates measured by the radiation monitor and then examining at what point the linear relationship between the two breaks down. Figure 2.16 shows this relationship and suggests a good linear agreement up to around $\sim$ 2000 protons s^{-1} cm^{-2} in the plastic scintillator equating to around $\sim$ 3000 protons s^{-1} total counts in the radiation monitor. In space, even the most violent SEP events are expected to produce single count rates of less than $\sim$ 2000 protons s^{-1} in the radiation monitor while the GCR background should produces less than $\sim$ 10 protons s^{-1}, (Cañizares et al., 2009).

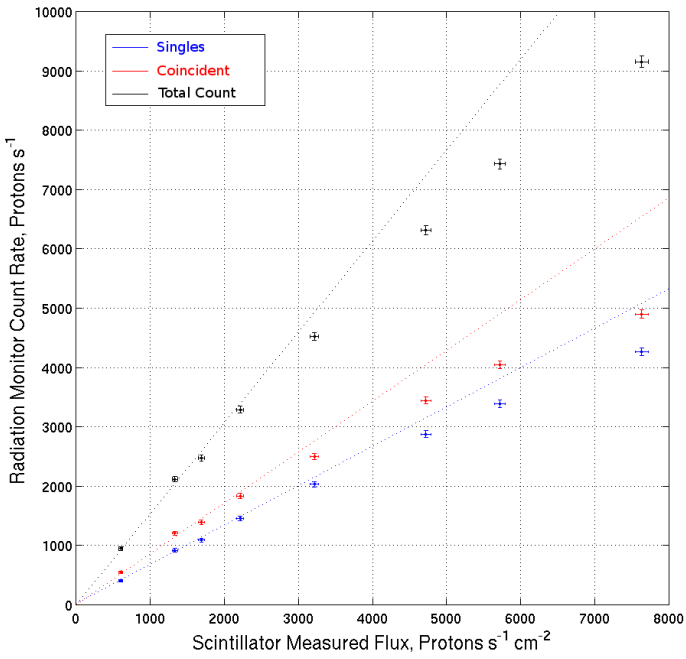

Figure 2.16: Demonstrates the linear relationship between the PIF scintillator flux measure and the radiation monitor count rate at fluxes less than $\sim$ 2000 protons s^{-1} cm^{-2}. Above this dead time in the radiation monitor electronics begin to have a significant effect.

2.6.4.1 Estimating Radiation Monitor Dead Time

It is possible to estimate a lower limit for the dead time in the radiation monitor electronics if one assumes the dead time for the plastic scintillator is negligible. The dead time in the radiation monitor is certainly greater than that of the scintillator as can be seen in Figure 2.16 by the way the radiation monitor count rate is underestimated. As expected, Figure 2.16 also shows that the effective dead time is different for coincident and single detections. There is a fairly complex relationship between the dead time in the radiation monitor electronics and the effect on the coincident and single count rates. This is due to the possibility of a single count in one diode, and the ensuing dead time, causing a coincident event to be counted as another single. Even so, the effective dead time in both cases can be approximated by assuming a non-paralysable dead time of the form, (Turner, 2007):

$$n = \frac{m}{1 - m\tau} \tag{2.4}$$

where m is the recorded count rate, τ is the dead time and n is the true count rate. From this a dead time of $\tau_{CE} \approx 55$ μ s for coincident events and $\tau_{SE} \approx 40$ μ s for single events was found. By correcting for this effect the count rates continue to be linear up to ~ 7000 protons s^{-1} cm^{-2} and above, as shown in Figure 2.17. Although this is a fairly crude estimate, it agrees fairly well with the predicted dead time for the radiation monitor of 35 ns. It should also be noted that it is very unlikely that the radiation monitor will be required to measure counts at anything close to the levels where dead time becomes significant.

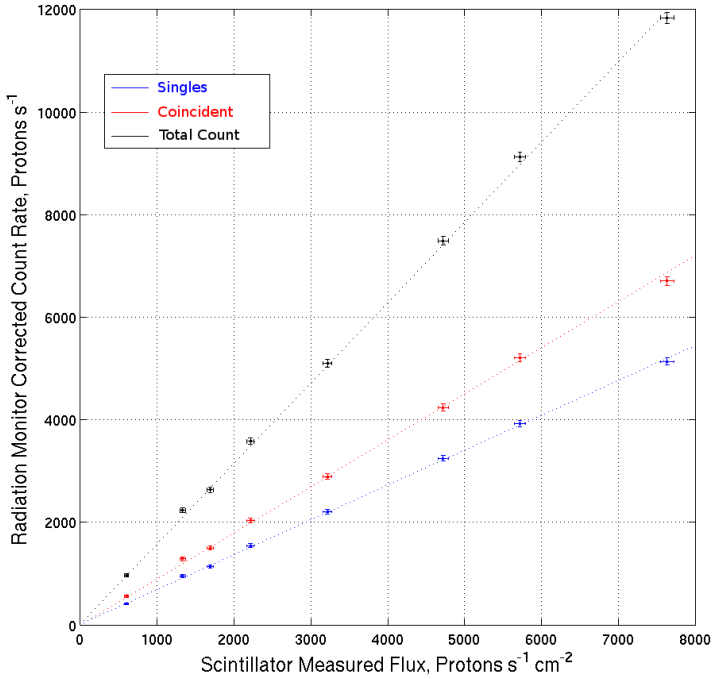

Figure 2.17: Shows the corrected count rates if one assumes a non-paralysable dead time and $\tau_{CE} \approx 55$ μ s and $\tau_{SE} \approx 40$ μ s.

2.6.5 Count Rate Tests

In order to check both the low energy cut-off caused by the radiation monitor shielding and the angular acceptance of the diodes telescopic configuration, beam measurements were made at 250 MeV, 200 MeV, 150 MeV, 100 MeV, 90 MeV, 80 MeV and 70 MeV with the rotary table angle set at -40°, -35°, -30°, -25°, -20°, -15°, -10°, -5° and 0°. Then, using the coincident count rate in the radiation monitor, normalised by the flux measured by the PIF plastic scintillator and the approximate diode area, allowed the low energy cut-off and angular acceptance to be studied when plotted against varying incident energy or table angle.

2.6.5.1 Scintillator Calibration Problem

When a full analysis of the results were made after the tests had been conducted, it became clear that there had been a problem with the count rate tests. Strangely, while measurements made at 100 MeV or less gave results consistent with expectation results at 150 MeV and above were nonsensical. As shown in Figure 2.18, the radiation monitor seemed to be detecting counts at a rate up to seven times higher than the plastic scintillator suggested, with the problem increasing for inci-

dent energies of 150 MeV and above. The problem had not affected the previous maximum count rate tests as they had been performed at 100 MeV. There seemed to be two possibilities; either the radiation monitor was over-estimating the flux or the PIF plastic scintillator was under-estimating it, but only at 150 MeV and above. Given the quality of the results for the other measurements and the way the radiation monitor electronics work, it was very difficult to imagine a mechanism that would explain this anomaly if it was caused by the radiation monitor. On the other hand, the flux levels required for these tests ($\sim$ 1000 protons s^{-1} cm^{-2}) were at the lower limits of the facilities capabilities and the plastic scintillator was set-up and calibrated specifically for these tests. To give further context to the situation, the proton accelerator used was shared with a separate facility that treated cancer patients during the day. As such the tests had to be performed at the weekend and throughout the night. The scintillator calibration itself took place late on a Saturday evening, under considerable time pressure. It therefore seemed more likely that the problem was with the plastic scintillator calibration rather than the radiation monitor.

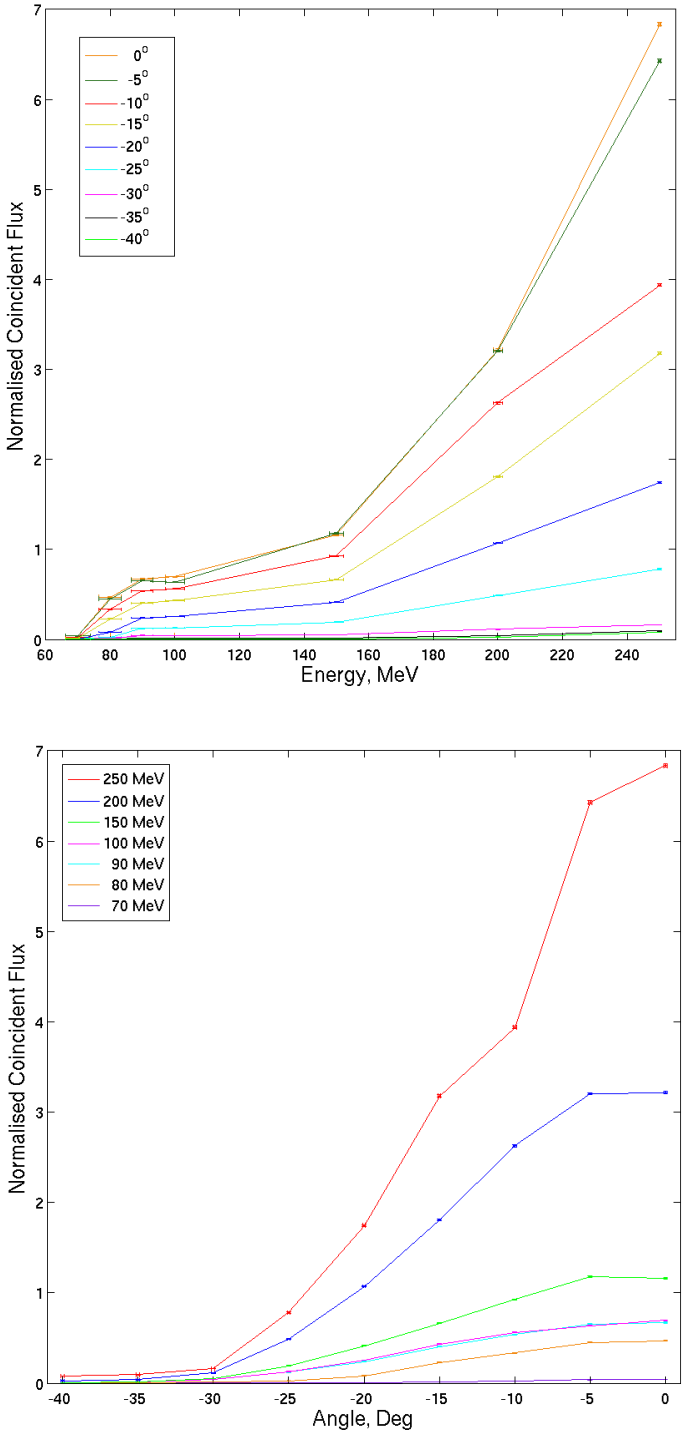

Figure 2.18: *Top*: The effect on the normalised measured coincident flux caused by varying the nominal energy of the incident proton beam. *Bottom*: The effect on the normalised measured coincident flux caused by varying the table angle. Note the nonsensical results for 250 MeV, 200 MeV and 150 MeV, where the normalised flux should be below one.

After the fact, we contacted the PSI technicians and explained our concerns with the plastic scintillator data. After checking their logs, they agreed there had been a significant error with the way they obtained the calibration factor used to calculate the flux measured by the scintillator. This calibration factor was calculated automatically by combining several measurements made along the beam line and varied with incident energy. The calibration factor was then applied to the measurements made by the plastic scintillator to give a measure of the flux at the exposure site. Although they were unable to identify the exact source of the problem, they did suggest an approximate fix. In their experience, the calibration factor should increase linearly with increasing incident energy, Figure 2.19. As suspected, the calibration factor was indeed linear at incident energies less then 150 MeV but for an unknown reason moved increasing away from this line at higher energies. If one corrects for this problem so that the calibration factors at high energy lie along this line, the fluxes measured by the plastic scintillator become $\sim 1.44\times$ greater at 150 MeV, $\sim 3.48\times$ greater at 200 MeV and $\sim 6.59\times$ greater at 250 MeV. This correction brings the normalised flux measurements back to realistic levels and is used in the following sections. At the same time a different method of studying the radiation monitor behaviour independently of the plastic scintillator measurements will be discussed.

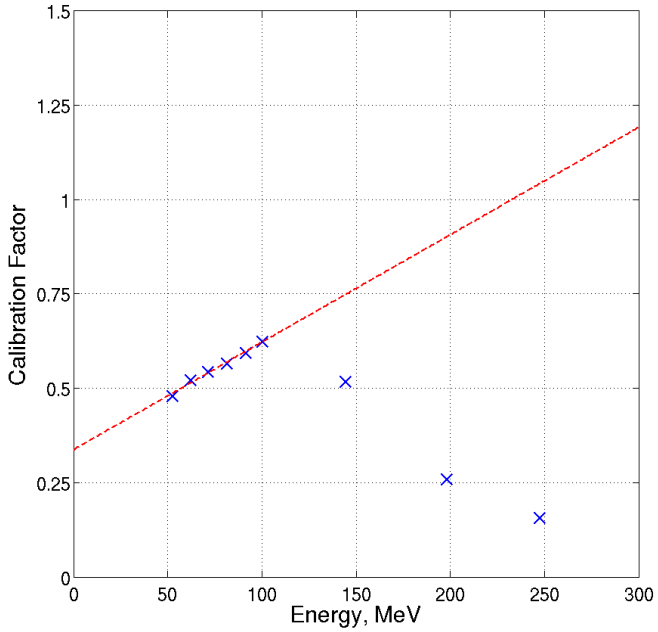

Figure 2.19: The calibration factor varying with increasing incident energy. The blue crosses show the factors initially used and how they moved away at higher energies from the linear relationship one would expect.

2.6.5.2 Low Energy Cut-Off Test

The aim of the low energy cut-off test was to verify that the radiation monitor shielding is effective at preventing incident radiation with an energy less than ∼70 MeV being detected. The test involved irradiating the monitor with nominally 250 MeV, 200 MeV, 150 MeV, 100 MeV, 90 MeV, 80 MeV and 70 MeV protons and also varying the angle of incidence from 0° to -40° in steps of -5°. The number of coincident counts recorded within the monitor can then be studied to determine at what energy the radiation monitor ceases to make coincident detections. Although at each setting the irradiating flux should have been ∼ 1000 protons s^{-1} cm^{-2}, due to the calibration issue discussed, the flux was considerably higher at higher energies.

A comparison with simulation was also made using the same settings as before. In both the simulated and measured case the coincident counts within the monitor were converted to a detected flux measurement and then normalised by the actual incident flux. For the simulation the incident flux is obtained by counting the number of protons entering a 1 cm^2 area at the target position with the radiation monitor removed, but simulating the same number of initial protons. The results for both cases are shown in Figure 2.20. The horizontal error bars in both figures are the 1σ spread in the beams energy calculated from simulation, Section 2.5.2. The vertical error bars are the counting errors added in quadrature with the measured data also including an assumed 5 % error in the scintillator flux. This is fairly approximate but is an attempt to quantify the main source of error in the measurement.

While the overall form of the results agree well there are some deviations. There seems to be a systematic disagreement at 250 MeV where apart from at 0° and -5° the measured data dips down. This is likely caused by the poorly calibrated scintillator data. What is particularly pleasing in both the measured and simulated data is that the results for 0° and -5° appear the same. This is because of the diodes linear offset, discussed in Section 2.6.2.2, which causes the optimal diode alignment to occur at ∼ -2.5 °. This causes the measurements at 0° and -5° to be equally misaligned.

Irrespective of any problems caused by the poorly calibrated scintillator readings, the shielding is clearly effective and agrees quite well with simulation. A steep decline in the number of coincident protons detected is indeed observed between 70 MeV and 100 MeV at all angles as expected. Further confirmation of the shields effectiveness came from an additional measurement made at 60 MeV and 0° which measured only ∼ 1 coincidence event per second compared to ∼ 100 per second at 70 MeV, both with an incident flux ∼ 1000 protons s^{-1} cm^{-2}.

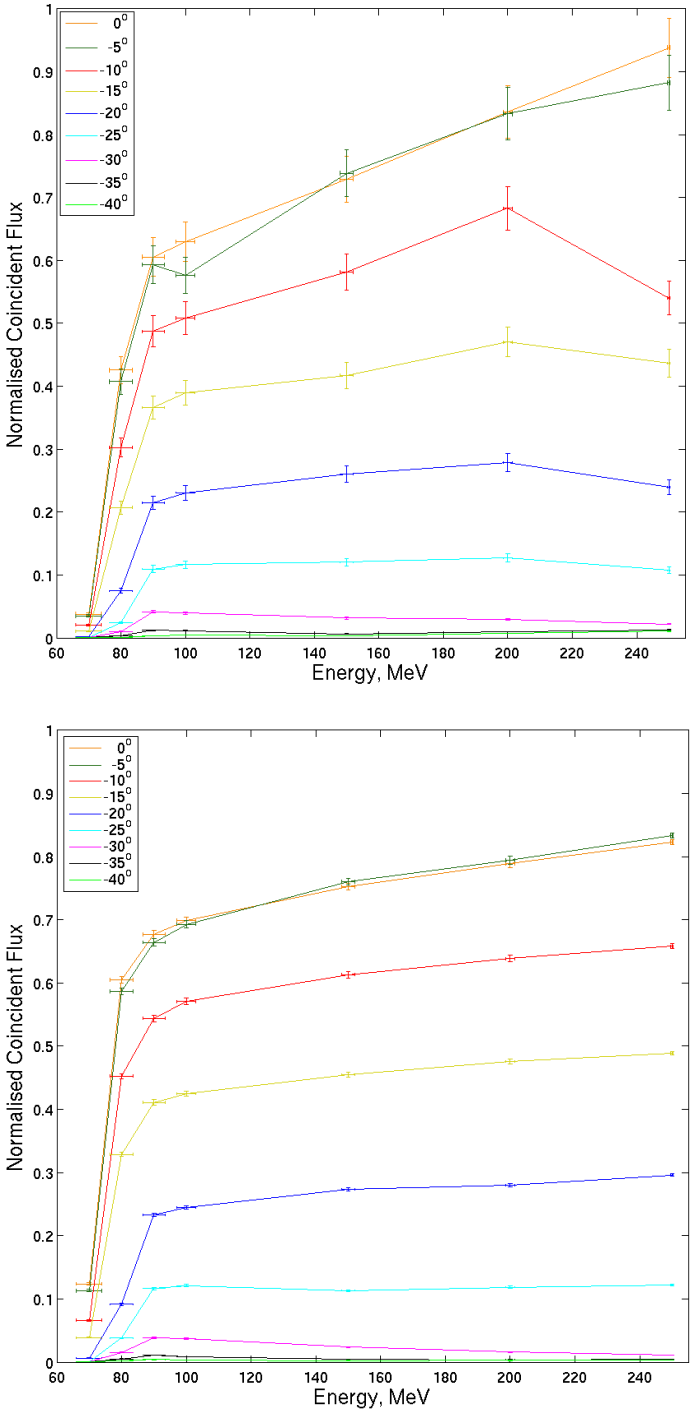

Figure 2.20: Normalised flux varying with incident energy for different angles. *Top*: Measured data including calibration correction. *Bottom*: Simulated data.

Given the uncertainties with the plastic scintillator flux measurements, it seemed prudent to further verify the radiation monitors performance by comparing the measured results to simulation, but in a way that did not involve the scintillator flux. This was achieved by instead considering the ratio obtained from the number of coincident detections over the total number of detections recorded in the radiation monitor. Figure 2.21 shows these results and excellent agreement is observed between measurement and simulation. The overall scale and shape at all energies and angles agree well, with the features around ~ 90 MeV being particularly impressive. This agreement is taken as further confirmation that it was indeed the scintillator measurements that were at fault rather than the radiation monitor.

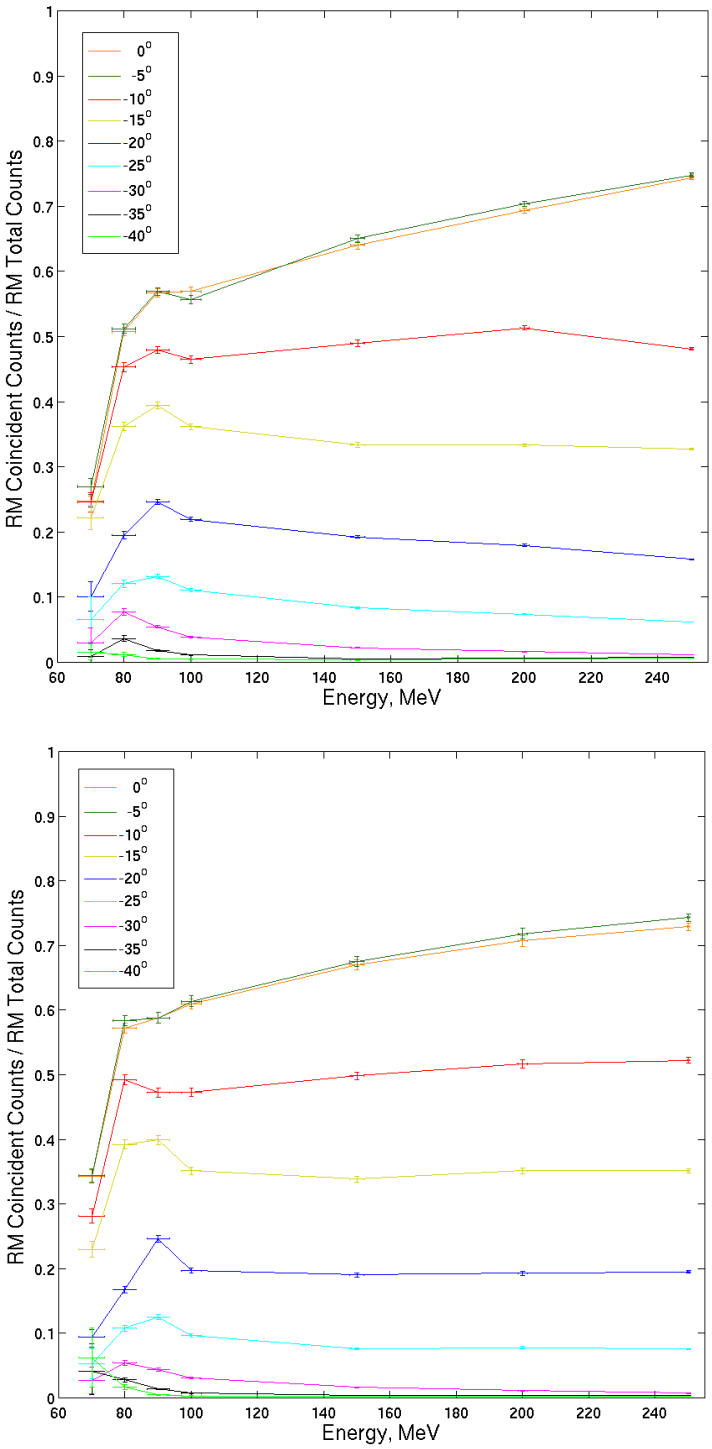

Figure 2.21: The ratio of coincident counts to total counts detected by the radiation monitor, varying with incident energy for different angles. *Top*: Measured data. *Bottom*: Simulated data.

2.6.5.3 Angular Acceptance Test

By re-plotting the same data from the previous section, but in terms of normalised flux with varying angle, we are able to study the angular acceptance of the radiation monitor. From a purely geometrical consideration the angular cut-off for the diodes telescopic configuration should be, $\theta_{cutoff} \approx -90 + \arctan\left(\frac{20}{10.5}\right) \approx -27.7°$. The true acceptance angle will be slightly larger in magnitude, as protons are scattered back toward the two diodes from more extreme angles, which is what Figure 2.22 shows. The simulated results show good agreement with the measured data at angles between -15 ° and -40 ° but less so at lower magnitude angles. In this range, although the form and order of the curves are the same the normalised fluxes are quite different. The poorly calibrated scintillator may again play a part here, though it is not clear. None the less, as expected, both the measured and simulated data show an angular acceptance of ∼-30°, which is in agreement with theory.

As before, in order to work around the scintillator problem, the ratio of the coincident counts to total counts were studied, Figure 2.23. Again, these show a better agreement between measured and simulated results than the normalised fluxes, which reinforces that it was the scintillator at fault.

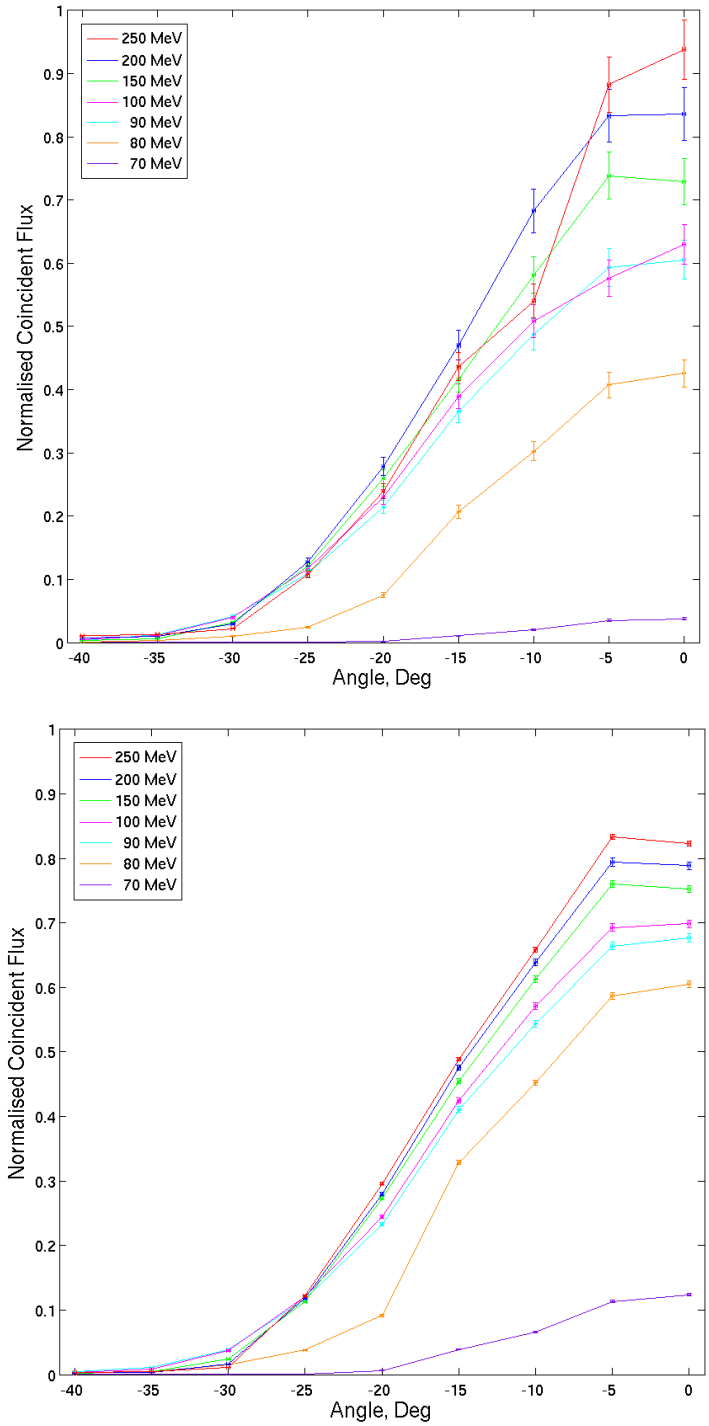

Figure 2.22: Normalised flux varying with angle for different incident energies. *Top*: Measured data including calibration correction. *Bottom*: Simulated data.

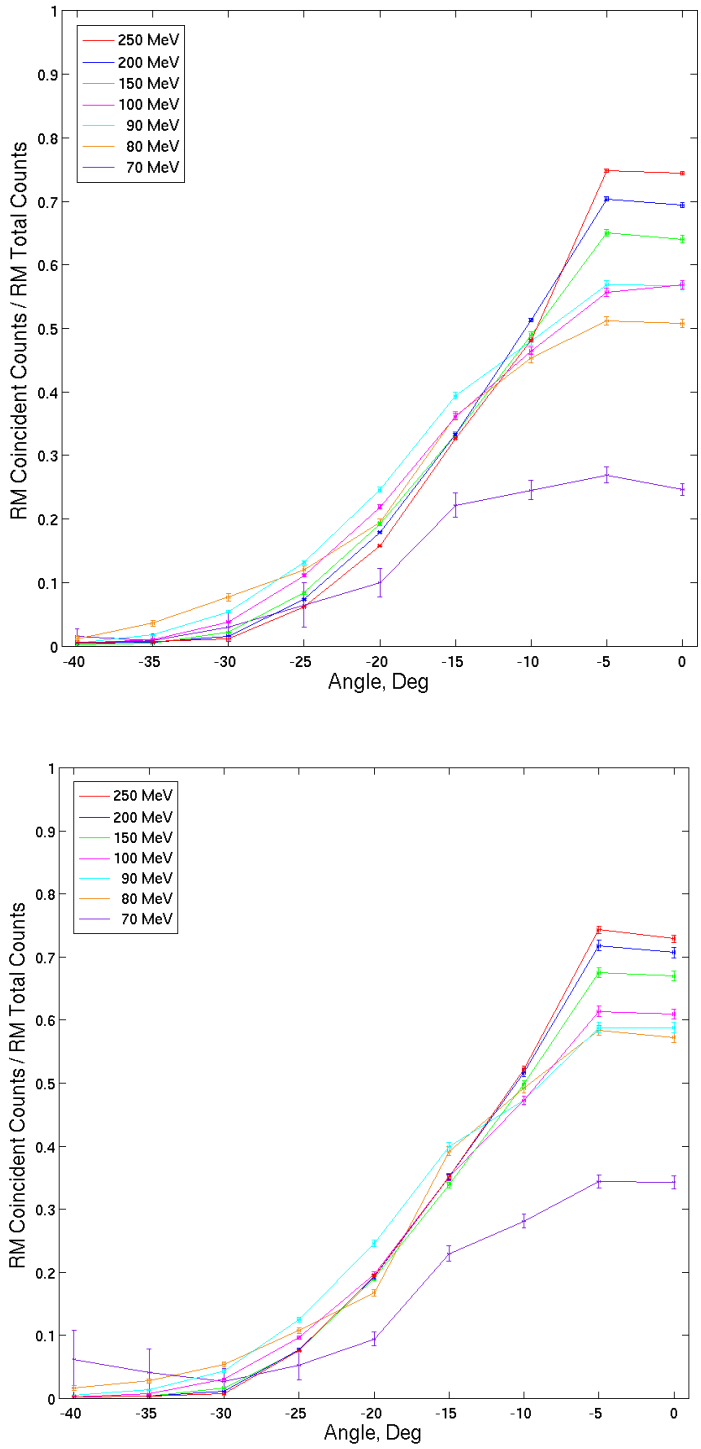

Figure 2.23: The ratio of coincident counts to total counts detected by the radiation monitor, varying with angle for different incident energies. *Top*: Measured data. *Bottom*: Simulated data.

2.7 Conclusions

A radiation monitor, which was initially designed by our group and whose hardware has been developed and built by a Barcelona based collaboration, will be flown on-board Pathfinder. It will be able to characterise both the flux and energy spectra of the radiation environment responsible for test mass charging. From the beginning, our group at Imperial College London has been closely involved with the design and testing of the instrument. This involvement culminated in attending the proton beam flight model qualification testing carried out at the Paul Scherrer Institute in Switzerland. My role was to help conduct the beam tests, analyse the data collected and, with the aid of simulations, demonstrate the radiation monitors performance. The radiation monitor passed every test and results from it were in good agreement with both theory and simulation. In summary these were:

- The simulations show good agreement with measured data across all incident energies and table angles.
- A linear offset of 1.0 mm between the diodes was found during the analysis causing a small but measurable effect.
- The range for the deposited energy in the radiation monitor (0 to 5 MeV) was shown to be sufficient to capture the entire spectra for incident protons down to 70 MeV.
- The maximum count rate before dead time in the electronics became significant was found to be $\sim$ 3000 protons s^{-1} total counts in the radiation monitor.
- The PIF plastic scintillator flux measurements were almost certainly incorrect for data measured at 250 MeV, 200 MeV and 150 MeV.
- Simulated and measured data agree with the expectation of an approximately 70 MeV cutoff in energy for the copper shield.
- Simulated and measured data agree with the expectation of an approximately $\pm 30^{\circ}$ cutoff in angular acceptance for the diodes telescopic configuration.
- The data collected and the simulation outputs will aid analysis of the flight data from Pathfinder.

Chapter 3

Charge Management

Introduction

So far this thesis has discussed how the free falling test masses, to be used at the heart of both Pathfinder and LISA, become charged due to incident ionising radiation. In the previous chapter the radiation monitor was presented which will fly on board Pathfinder in order to help characterise the radiation environment present. In this chapter the system used to actually counteract this charging is introduced. Over a number of years the Charge Management System for Pathfinder has been designed, developed, built and tested by our group at Imperial College London. Its key concept is to illuminate the gold surfaces of the test mass or the surrounding electrode housing with ultra-violet light. This causes electrons to be emitted via the photoelectric effect and allows the charge on the isolated test mass to be controlled. The many complications to this simple idea will be discussed and the various components that make up the Charge Management System described. Results from testing the system at the University of Trento's torsion pendulum facility are also presented, which will later be simulated in Chapter 5.

3.1 The Charge Management System

Due to the extremely pure level of gravitational free fall required, the method of neutralising any accumulated charge on the isolated test masses has to be non-contact. This is achieved by exploiting the photoelectric effect in order to generate a net flow of electrons either towards or away from the test mass. In its most simplistic form this means illuminating the inner housing to add negative charge to the test mass or illuminating the test mass itself in order to remove negative charge.

In the original design, changes to which will be discussed later, the entire test mass as well as all the electrode and housing surfaces were gold coated. Therefore the energy of the illuminating photons had to be above the work function of gold, the minimum energy required to completely remove an electron from the surface. The work function for pure gold, deposited in an ultra-high-vacuum and measured *in situ*, is given as 5.2 eV in the literature, (E. E. Huber, 1966). But as will be discussed in Chapter 4, surface contamination resulting from exposure to air semi-permanently reduces it, typical to around $\sim$ 4.2 eV, (Saville et al., 1995). This means an illuminating wavelength of considerably less than $\sim$ 300 nm, or greater than $\sim$ 4.1 eV, is required for discharging, which is in the mid-ultra-violet region. Ideally, the illuminating wavelength will be as short as possible, not only to ensure that the energy is above the work function threshold but also to generate increased numbers of photoelectrons. This is because in an ideal case the quantum yield, the ratio of photoelectrons produced to the number of photons absorbed, is related to the energy of the incident photons and takes the form, (Eastman, 1970):

$$Y(\nu) \propto (h\nu - \phi)^2 \tag{3.1}$$

where Y is the quantum yield, h is the Planck constant, ϕ is the work function and ν is the frequency of the incident light. It is therefore desirable to choose a wavelength as short as possible but technical limits determine how short one may go and a compromise has to be made. These compromises will be discussed in the following Sections, but the 254 nm spectral line produced by a mercury vapour lamp was chosen. Figure 3.1 shows a schematic diagram illustrating the basic concept behind test mass discharging.

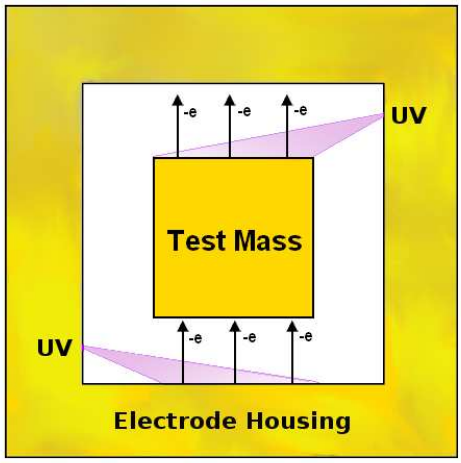

Figure 3.1: A schematic showing the basic concept behind controlling the test mass charge. By exploiting the photoelectric effect with the use of 254 nm UV light, illuminating the housing nominally causes the test mass to charge negatively while illuminating the test mass nominally causes it to charge positively.

There are three main complications to the simple concept of discharging presented so far. The first is the inevitable absorption of reflected light by unintended surfaces. For example, if one were attempting to discharge a negative test mass by illuminating it with UV light, a certain fraction of the light would be reflected and absorbed by the surrounding housing. This would then create photoelectrons that would act against the intended direction of discharge. At 254 nm, the intrinsic reflectivity of gold is $\sim 35\%$ at normal incidence but increases to 100% as the angle of incidence approaches 90°. It is possible that the reflection properties of a surface or the angle of the initial UV light can conspire to prevent discharging in one direction.

The second complication to discharging is the possibility of significantly different photoelectric properties between adjacent surfaces, even if they are nominally identical. Again, one could attempt for example to discharge a negative test mass by illuminating it with UV light. If the reflection properties are ideal the test mass may absorb around 70% of the total light and the housing only 30%. If the photoelectric properties of the two surfaces are then fairly similar, a net flow of photoelectrons will be produced travelling from the test mass to the housing, as intended. But if there is a significant difference in the quantum yields, say the yield is three times higher for the housing than the test mass, then bipolar discharge will again not be possible as the net photocurrent will be in the wrong direction.

The third complication is the presence of local electric fields between the test mass and the electrodes or housing. One will recall from the description of the inertial sensor in Chapter 1 that there are 18 separate electrodes embedded within the housing walls that surround the test mass. Both AC and DC biases are applied to these electrodes in order to sense a test mass's position and actuate it when necessary. Indeed, as will be described in Section 3.3.2, the charge on the test mass itself is measured by applying an AC voltage to the bias electrodes and measuring the positional response in the test mass which is related to its charge. Crucially, the maximum energy of the photoelectrons is typically less than 1 eV while potential differences between the test mass and housing or electrodes can be up to several volts. This means that photoelectrons can be strongly affected by the electric fields and the flow in either direction can be partially or completely, enhanced or suppressed. As will be discussed, it can even be used to one's advantage in order to enhance the discharge rate in a desired direction by applying a DC bias to the appropriate electrodes. Depending on the polarity and combination of the applied biases, the test mass potential to the grounded housing can also be changed.

It should be clear that not only are the actual properties of the electric fields important but also the position of where the photoelectrons themselves are emitted

as different regions can experience different electric fields. The origins of the emitted photoelectrons are determined by where the UV light is absorbed which depends not only on the geometry of the system and the reflection profiles of the illuminated surfaces but also the distribution of the UV light as it first enters the inertial sensor.

As will be explored in Chapters 4 and 5, the relationship between these three complications are interconnected and fairly complex. To begin with though the Charge Management System hardware will be described and the results of its testing at a torsion pendulum facility presented. The measurements made during testing aid understanding of the discharging system as a whole and will also be used in this thesis to help verify simulations.

3.1.1 UV Light Unit

The first component in the Charge Management System is the UV Light Unit, or ULU. It is essentially a box which contains the mercury lamps that provide the UV light source used for discharging as well as their associated electronics. The initial design contained eight mercury lamps but following descoping was reduced to just six. Three lamps are used with each inertial sensor, with two pointing at the housing and one at the test mass. This is due to previous simulations by Araújo et al. (2005) and Wass et al. (2005) suggesting the test masses will always charge positively in the space environment, therefore being more likely to require discharging negatively. Each individual lamp is controlled separately and is pulse-width modulated at $\sim$ 1 kHz in order to adjust the output power with an 8-bit resolution and a dynamic range in output power of $\sim$ 330. The light from each lamp passes through an attached optics barrel which filters the light before focusing it into an optical fibre. The fibre then routes the UV light to the inertial sensors. Figure 3.2 shows the fully constructed flight ULU.

If possible, two different operational modes for the discharge system will be tested during the Pathfinder mission. In continuous discharge mode a very low UV intensity will be used to produce a small net photocurrent, $\sim 10 - 100$ e s^{-1}, to continuously counteract charging and keep the test mass charge below $\sim 10^5$ individual charges. This nominal mode of discharging would be done while the experiment is still taking low noise interferometry science data. As such no DC biases can be applied to aid discharging, requiring the discharge system to be capable of bipolar discharging with no applied DC fields. This method of discharge is preferable as it would reduce the net charging rates which were shown by Shaul et al. (2004) to produce acceleration noise in excess of the LISA noise budget over long signal

integration times.

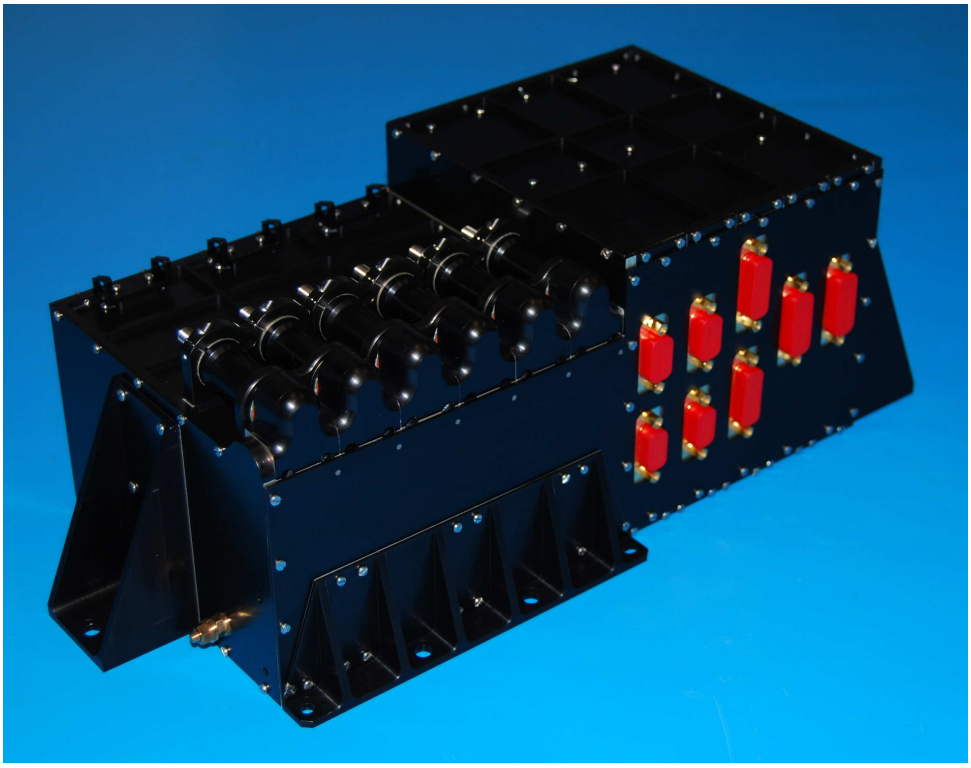

Figure 3.2: A photograph of the flight ULU which contains the six mercury lamps and their drive electronics. The six lamp holders and their attached optics barrels are seen on the left. The red covers on the right protect the electronic connectors. To meet thermal specifications the ULU is black-anodised.

The second mode of operation is to allow the charge on the test mass to build up to a relatively high level over a few days, $\sim 10^7$ individual charges, then discharge at a very high UV intensity producing a net photocurrent of $\sim 10^4$ e s^{-1} until the test mass charge is brought below $\sim 10^5$ individual charges, taking approximately twenty minutes. With this mode of operation the experiment would leave science mode allowing a DC bias to be applied in order to enhance the discharge rate. Although the intrinsic dynamic range of the mercury lamps is only ~ 330, the two modes of operation require an effective dynamic range of ~ 1000. This is achieved using multiple lamps at once or by applying DC biases to enhance or suppress the discharge rate, increasing the effective dynamic range of the Charge Management System.

3.1.1.1 Mercury Lamps

The UV light source for Pathfinder are commercial mercury discharge lamps, Model 11SC-1, supplied by UVP. The bare lamps consist of a 5.4 cm long quartz pencil bulb filled with low pressure mercury vapour and require a voltage of $\sim$ 1000 V to initially strike but thereafter an operating voltage of $\sim$ 500 V, with a drive current of tens of milli-amperes. The electrical discharge between two electrodes within the bulb ionises the mercury vapour allowing free electrons to be accelerated by the electric field between the electrodes. These accelerated electrons can then collide with the mercury atoms in vapour form, causing further ionisation or raising a bound electron to an excited state. When an excited electron relaxes it emits a photon characteristic of the transition. As such the low pressure mercury lamps emit a spectrum of light at discrete wavelengths, the most intense being at 254 nm, (Sansonetti et al., 1996). It is these photons that are used in the discharging system with the rest being filtered out, particularly another spectral line at 185 nm, which would damage the optical fibres used to transport the light. The 254 nm photons are ideal in that they have an energy of 4.88 eV, which is energetic enough to liberate photoelectrons from gold while limiting damage to the optical fibres used to transport the light.

In addition to producing a wavelength of light suitable for discharging, mercury lamps were also chosen for Pathfinder as they are a very mature, well understood technology. Furthermore, they have a space heritage having already been used in a mission called ROSAT, (Adams et al., 1987). Operating for over eight years between 1990 and 1999, ROSAT was a space based X-ray telescope consisting of several instruments. One of its instruments, the Wide Field Camera, required regular calibration throughout the missions duration. As such a calibration system was produced by a group at Imperial College London which generated a grid image of 185 nm light spots. The system's light source was a mercury lamp of the same type as chosen for Pathfinder, meaning they had already proved capable of passing the stringent space qualification testing required for space based experiments.

3.1.1.2 Flight Hardware Production

The ULU flight hardware was assembled in a class 1000 clean room at Imperial College London. Prior to this, the six mercury lamp units contained within the ULU were produced in the same facility. This involved a highly controlled procedure with every stage being documented and photographed. I personally manufactured half of the flight lamp units as well as several flight spares. The process is shown pictorially in Figure 3.3.

Figure 3.3: **A**: A set of raw flight lamp components: titanium holder, mercury lamp bulb and thermistor. **B**: The mercury lamp bulb wrapped with heater wire. **C**: The lamp after *Stycast* coating of heater wires and attached thermistor. **D**: The mercury lamp potted in its holder using red RTV at bulb end. **E**: The lamp holder back filled with *Arathane* to fully secure lamp and wires. **F**: The finished flight lamp.

The raw components of each mercury lamp unit were a bare Model 11SC-1 bulb, a custom made titanium holder, a thermistor and a heater coil, (**A**). The thermistor and heater coil are necessary to both measure the lamp temperature and, if required, heat the lamp before it is turned on. This is because below ~ 25 °C the quantity of mercury in vapour form decreases and the voltage required for the lamps to initially strike increases. To ensure this does not cause a problem the heater coil allows the lamps to be heated before being turned on as the ambient spacecraft temperature is expected to be below 25 °C. Once running the operational temperature of the lamps creates a self sustaining level of mercury vapour.

The first production stage (**B**) was to hand wind the heater wire around the base of the lamp bulb. This was an incredibly awkward process as the wire was not allowed to overlap and had a tendency to slip. Once the coil was complete it was temporarily held in place using aluminium tape where the coil joined the attached leads. The next stage (**C**) involved covering the base of the lamp bulb in *Stycast*, a black epoxy. This was done in several coats so that the heater coil could first be secured in place before removing the aluminium tape. Then the lamps high voltage leads could be added and the thermistor embedded at the base of the lamp. With each coating, outgassing was performed under a ~ 1 mbar vacuum before the layer was cured in an oven at 50 °C for several hours.

The lamps were then potted in their titanium holders using a room temperature vulcanizing silicone rubber, RTV, which only covered the base of the quartz bulb, (**D**). The RTV also required outgassing and took about a day to cure at room temperature. The rubber like quality of the RTV allows for thermal expansion as well as cushioning the delicate bulb. The holders were next back filled at the lead end with *Arathane*, a grey electrically insulating adhesive compound, outgassed, and left to cure at room temperature for about a day, (**E**). Finally, a tight fitting white PTFE washer was added to cover the exposed RTV, (**F**). At several points during production an independent mandatory inspection was carried out by external personnel to ensure the quality and consistency of the flight lamp units. If for any reason a lamp failed, a new unit was started from scratch.

3.1.2 Fibre Optic Harness

The second component in the Charge Management System is the Fibre Optic Harness, or FOH, which routes the 254 nm UV light from the ULU to the inertial sensor. The path from each lamp to the inertial sensor varies between two and four metres and requires several bends as well as a joint. Indeed, a strong factor in the FOH

design was the need for fairly tight bends of < 2 cm in radius. This was a challenge as a ~ 1 mm diameter single core fibre capable of delivering the intensity of UV photons necessary for discharging would have a minimum bend radii of ~ 10 cm. To overcome this problem a multi-core fibre, made up of a bundle of 19 individual 200 μm diameter cores was chosen. The bundle is held together in a polyether-ether-keytone, or PEEK, sleeve and its multi-core design allows the minimum bend radii requirement to be met while still being capable of transmitting the required intensity of photons.

Another important requirement for the fibre was it needed to be radiation hard. Generally a fibre's attenuation of 254 nm light increases with exposure to UV and space radiation. Extensive testing was therefore carried out at Imperial College London on fibres from a number of manufacturers in order to find a fibre where these effects were minimised. Finally, fibres manufactured by Fibre Guide were chosen which have high purity silica cores and a high OH content in addition to fluorine doped silica cladding. An end on photograph of the multi-core fibre is shown in Figure 3.4.

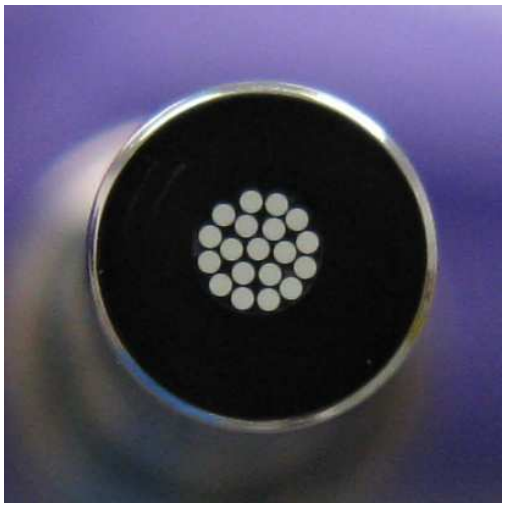

Figure 3.4: A photograph taken of the end of the flight FOH. The 19 individual fibres that make up the bundle are clearly visible, each being 200 μm in diameter, giving the bundle a diameter of approximately 1 mm.

3.1.3 Inertial Sensor UV Kit

The final component in the Charge Management System is the Inertial Sensor UV Kit, or ISUK. It channels the 254 nm UV light from the FOH and injects it into the inertial sensor, towards either the test mass or electrode housing surfaces. With the inertial sensor housed in a vacuum chamber the ISUKs are essentially 1 mm diameter, 67.3 mm long optical fibres housed within vacuum feedthroughs. However, in order to minimise potential test mass disturbances from magnetic impurities it is custom-made from titanium. A photograph of an ISUK is shown in Figure 3.5.

Figure 3.5: A photograph of an ISUK which consists of a 1 mm diameter optical fibre mounted within a custom-made titanium vacuum feedthrough.

The design for Pathfinder has three ISUKs for each inertial sensor, with two pointed at the electrode housing and one at the test mass. They are all aimed at the lower z faces entering the inertial sensor directly through the intersection of the outer x and y sides. They were originally inclined $\pm 8^\circ$ with respect to the z plane but as will be shown in Chapter 4, gold is fairly reflective at this angle of incidence of 82°. Indeed, about 70% of 254 nm light is reflected, so a decision was later made to change the angle to $\pm 20^\circ$ in order to increase the amount of absorption at the primarily illuminated surface. Even so, at this angle of incidence of 70° about 50% of 254 nm light is still reflected. Unfortunately, due to constraints from the inertial sensor geometry any further increase in the entrance angle is not possible.

3.2 Torsion Pendulum Testing

As discussed in Chapter 1, the aim for LISA is to keep the residual acceleration noise of the test masses below $\sim 3 \times 10^{-15}$ ms^{-2}Hz$^{-\frac{1}{2}}$ in the frequency band between 0.1 mHz and 0.1 Hz, (Carbone et al., 2005). Likewise, Pathfinder will also have very stringent limits on test mass acceleration noise, though an order of magnitude higher than LISA and in a reduced bandwidth between 1 and 30 mHz. To reach these goals a detailed understanding of possible test mass disturbances is required to aid the experimental design. With this in mind a torsion pendulum facility has been developed over a number of years by a group at the University of Trento, Italy. There have been several iterations of pendulum experiments but they all involve using a replica electrode housing, with a test mass suspended within, to study disturbances originating from within the inertial sensor itself.

The torsion pendulum experiments also offer an ideal opportunity to test the performance of the discharge system and two such test campaigns have so far been carried out. The first, in 2006, used an engineering model charge management system and were carried out with the single-mass pendulum experiment which had an early inertial sensor design. Over the last couple of years an ongoing campaign has made measurements with a system closer to that of flight and were carried out with the four-mass pendulum experiment. Here the two measurement campaigns are presented.

3.3 Single-Mass Pendulum

A free-falling test mass is obviously not practical for ground testing so a torsion pendulum instead allows the test mass to be rotationally 'free' via suspension from a torsion fibre. The single-mass setup is able to characterise sources of noise that induce net torques on the test mass around the z axis. The inertial sensor varies from the flight design for Pathfinder with the differences relevant to discharging discussed in the following sections. Figure 3.6 shows a photograph of the test mass used and a diagram describing the single-mass setup.

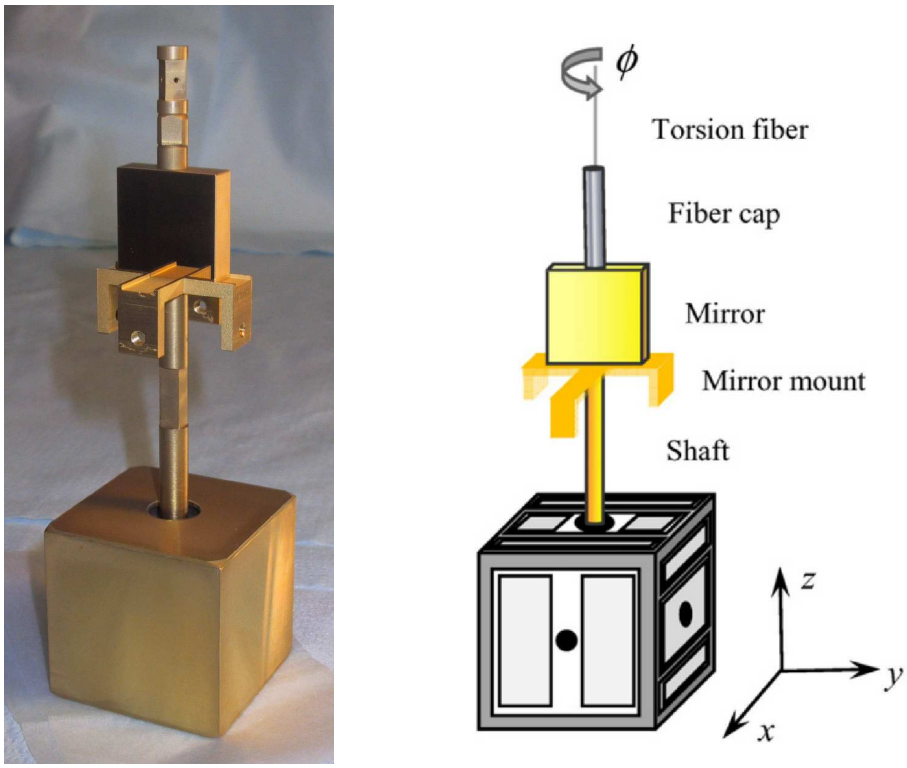

Figure 3.6: *Left*: A photograph of the hollow test mass attached to the shaft. The quartz ring that electrically isolates the test mass is just visible, attached to the inner surface. Photograph courtesy of UTN. *Right*: A diagram of the single-mass torsion pendulum showing the test mass within the electrode housing, suspended from the torsion fibre. The position of the mirror used for the autocollimator measurements and a balancing mass are shown. Adapted from Cavalleri et al. (2009a).

The single-mass torsion pendulum experiment is described in detail by Carbone et al. (2007) and Cavalleri et al. (2009a). In summary, it consists of a cubic test mass with sides 46 mm in length, suspended from a 25 μm thick, 1 m long tungsten torsion fibre. A truly representative test mass at $\sim$ 2 kg would be too heavy to be suspended by a fibre thin enough to achieve the desired experimental sensitivity. Instead a hollow aluminium test mass is used which has a 700-800 μm thick gold coating and is attached to the torsion fibre via an aluminium, 7 mm diameter shaft, which is also gold coated. The test mass is electrically isolated from the grounded shaft by a 1.4 mm thick fused quartz ring attached to the inner test mass surface with the shaft connecting via a 12 mm diameter hole on the top test mass surface. Measurements have shown that discharge through the quartz ring is unmeasurable in 10^6 s giving a resistance greater than $R > 10^{16}$ Ω.

The test mass is suspended within the electrode housing and its angular deflec-

tion can be independently measured with either the capacitive sensors that line the housing, like in flight, or with a commercial autocollimator and a mirror mounted on the pendulum shaft. The two methods give approximately the same accuracy but for the results discussed here the autocollimator measurements were used. The inertial sensor is housed within a vacuum chamber and the entire apparatus is mounted on a vibrationally isolated platform.

3.3.0.1 Single-Mass Sensor Geometry

Both the electrode housing and test mass used with the single-mass pendulum differ from the flight geometry in several important ways. Here we only discuss differences capable of affecting the discharging properties. Firstly, the electrodes are made of gold coated *Shapal* rather than gold coated sapphire, as is the case in flight. Given both are gold-plated in the same way this should not effect the discharging properties directly, but the underlying substrate could affect the quality of the finish, affecting the roughness. This will change the distribution of the reflected UV light within the sensor, which could in turn affect the discharging behaviour. The gold coated housing is made from molybdenum, as in flight, but is missing features associated with the test mass caging mechanism. These are essentially four holes on each z face where fingers that hold the test mass during launch are retracted. A further departure from the flight geometry is the presence of the shaft and this is exasperated by the UV light entering the sensor on the same upper z face.

The test mass also differs from those to be used in flight. While the fact the test mass is hollow should not affect discharging the finish of the test mass's gold coating is reported to give a rather diffuse appearance (Weber et al., 2006). This is a departure from the flight test masses as they will be required to have an extremely smooth finish, giving specular properties at 254 nm. This again will alter the distribution of the reflected UV light within the sensor, possibly affecting the discharging behaviour. The test mass used with the single-mass torsion pendulum also lacks the complex corner features related to the caging system that will be present in flight. The differences in both the electrode housing and test mass geometries are significant and the affect they have on discharging will be discussed in the following chapters.

3.3.1 Single-Mass Charge Management System

The discharging results for the single-mass pendulum used an engineering model charge management device, very similar to the flight model described in Section

3.1. The same type of mercury lamps were used as well as the same optics barrel configuration. The lamps could be turned on and off and their power set with 8-bit resolution, with the units electronics sent commands via a PC running a custom written Labview program. Only two lamps were employed, the output from one aimed at the test mass and the other at the electrode housing.

There was however a departure from the flight configuration in the way the UV light was routed to the inertial sensor. Firstly, the light travelled from the ULU to the sensor via a 1 m long, single core, 600 μm diameter fibre, whereas in the flight case a multi-core fibre will be used as described in Section 3.1.2. The way in which the UV light was injected into the sensor was also rather different. Rather than use a custom made ISUK, like in flight, the light entered a standard ConFlat feedthrough with a 1 mm diameter fibre which led to a $\sim$ 20 cm long, 600 μm diameter fibre on the vacuum side. The fibre was terminated as it entered the inertial sensor with a 4 mm cylindrical fibre head. In a further deviation from the flight setup, the light entered the system at 8° to the horizontal rather than 20°, as will be the case in flight. These differences are significant and the affect they have on discharging will be discussed in the following chapters.

3.3.2 Measuring Test Mass Charge

The method of measuring test mass charge for the single-mass pendulum is analogous to that which will be applied for Pathfinder, (Weber et al., 2006). A low frequency 'dither' voltage is applied to the x electrodes which produces a response in the test mass which is related to the test mass charge. For Pathfinder the polarity of the applied voltages are such that a translation in produced, but given that in the torsion pendulum case the test mass is rotationally free, the polarities are chosen so as to produce a rotation. By measuring the rotation ϕ with the autocollimator, the frequency dependant torque $N(f)$ can be obtained via the pendulum transfer function:

$$N(f) = I(2\pi f)^2 \left(1 - (fT_0)^2 - \frac{i}{Q}\right) \phi(f) \tag{3.2}$$

where I is the moment of inertia, T_0 is the pendulum's free period and Q is the quality factor of the torsion fibre. I was calculated to be 4.31×10^{-5} kg m^2, T_0 was measured and varied from 564 to 600 s and Q was measured to be 2880. To obtain a coherent torque N_{MOD}, a sinusoidally varying voltage with an amplitude of V_{MOD} and a frequency of f_{MOD} is applied to the four x sense electrodes. This torque is then proportional to the test mass potential V_{TM}, and for a centred test mass is

given by:

$$N_{MOD} = -4\left|\frac{\partial C}{\partial \phi}\right|\left(V_{TM} - \frac{\sum_{j(x)}\delta V_j}{4}\right)V_{MOD}\sin\left(2\pi f_{MOD}t\right) \tag{3.3}$$

where $\left|\frac{\partial C}{\partial \phi}\right|$ is the partial derivative of the x electrodes capacitance with respect to the rotation and δV_j is any stray DC voltages on the x electrodes. The charge on the test mass is finally related to V_{TM} by:

$$V_{TM} = \frac{q}{C_T} + \sum_i \frac{C_i \delta V_i}{C_T} \tag{3.4}$$

where q is the free charge on the test mass, C_i is the capacitance between the housing surface i and the test mass, C_T is the total capacitance of all i housing surfaces and V_i is the potential of the ith housing surface. For the measurements discussed here $V_{MOD} = 1$ V and $f_{MOD} = 3$ mHz, which led to a measurement error of approximately 5000 elementary charges per 333 s measurement cycle. In addition to the dither voltages a 4.47 V, 100 kHz AC injection bias, V_{Inj}, was applied to the y and z injection electrodes. In some of the tests, DC biases were also applied to the z sense electrodes, V_{ZBIAS}, in order to either enhance or suppress certain photoelectric currents. The polarity of the applied dither and injection voltages as well as the DC biases are shown in Figure 3.7.

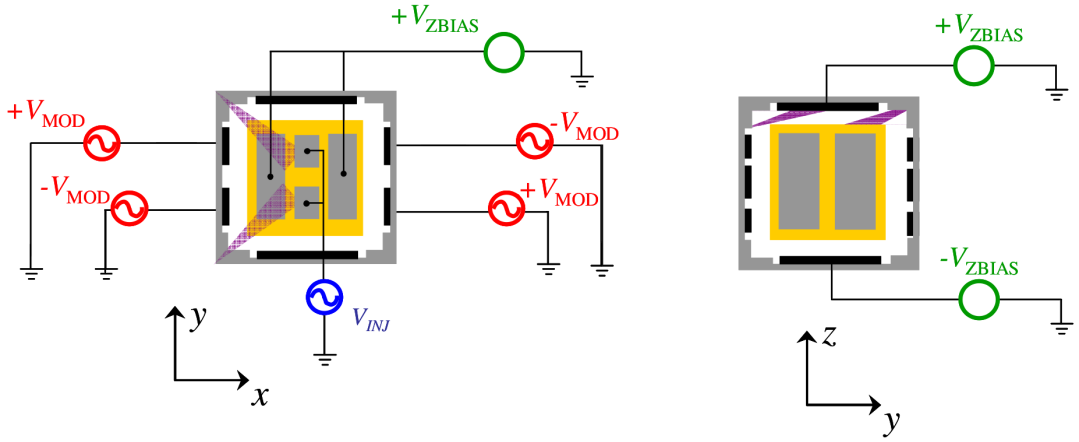

Figure 3.7: A diagram showing the AC and DC voltages that were applied while measuring test mass charge. Also shown in purple is the UV illumination of both the test mass and upper z electrodes. Adapted from Weber et al. (2006).

3.3.3 Results

Using the setup described, the engineering model Charge Management System was tested with the engineering model inertial sensor at the single-mass torsion pendulum facility, during 2006. The results of the testing are discussed in detail in Wass et al. (2006b) and Weber et al. (2006). Here, a summary of their findings are presented.

After measuring the output power from the two lamps being used for the testing, the level of attenuation by the optical fibres were measured. The throughput for the fibre system delivering UV to the test mass was measured as 0.005 and for the electrode housing as 0.012. The cause of such a large proportion of the initial light being lost was later found to be poor coupling between fibre connections and has been significantly improved since to values ~ 0.5. The test mass was then charged alternately positive/negative by illuminating either the test mass or electrode housing, allowing the discharging rate around $V_{TM} = 0$ to be calculated. This was repeated for several lamp powers with $V_{ZBIAS} = 0$ and the results are shown in Figure 3.8.

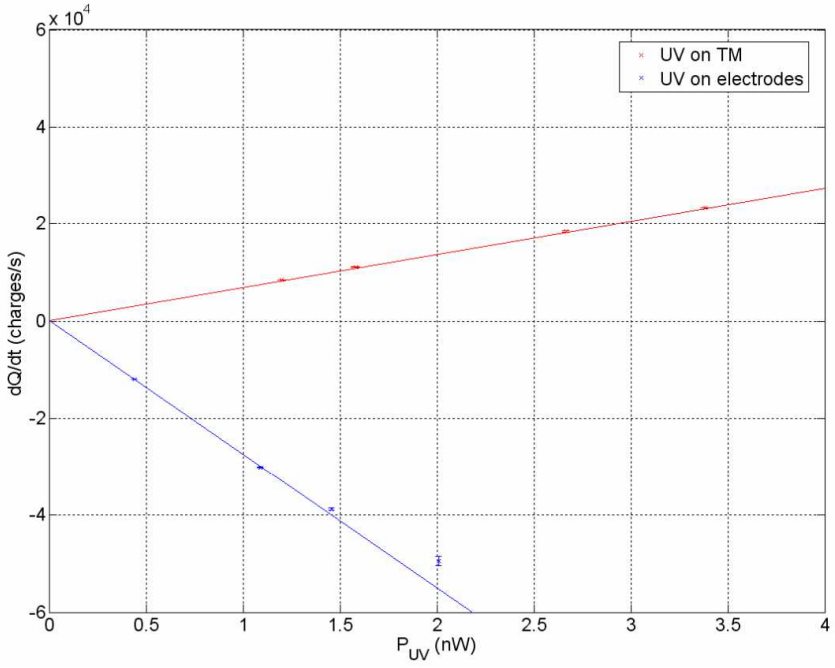

Figure 3.8: A plot showing the measured discharge rates at $V_{TM} = 0$ for both test mass illumination (Red) and electrode housing illumination (Blue). No V_{ZBIAS} was applied and as expected both illuminations show a linear relationship. Figure taken from Weber et al. (2006).

As expected, a linear relationship between the UV power and the discharging rate was found. There was also a clear asymmetry between the discharging rates

for test mass illumination and electrode housing illumination which was quantified by fitting s straight line to each set of data. A value of $6830 \pm 15\ e^{-1}\ s^{-1}\ nW^{-1}$ was calculated for test mass illumination and $-27460 \pm 140\ e^{-1}\ s^{-1}\ nW^{-1}$ for the electrode housing illumination. This asymmetry is thought to be due to the different geometries, surface reflectivities and photoelectric properties of the illuminated surfaces. Nevertheless, the charge management device was observed to be capable of bipolar discharge.

The next test involved discharging in one direction until a test mass equilibrium potential, V_{EQ}, was reached. The test mass is only at an equilibrium potential if one integrates over an entire injection bias cycle. An equilibrium is reached because as the test mass potential increases the photoelectric flow in the dominant direction is gradually suppressed. Eventually no net photocurrent flows and an equilibrium potential is therefore reached. This typically took 1 to 2 hours and was repeated for various V_{ZBIAS}. The results for both illuminations are shown in Figure 3.9.

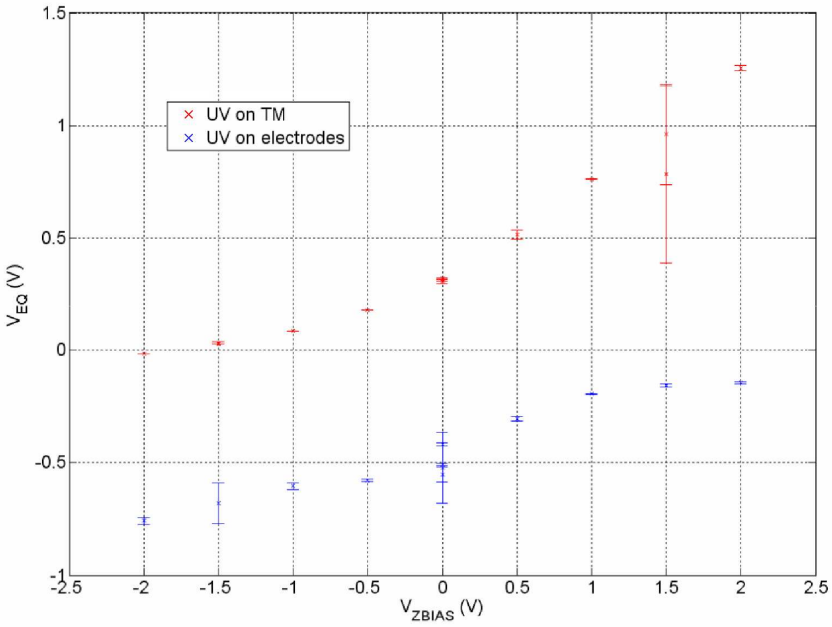

Figure 3.9: A plot showing the test mass equilibrium potential reached for different applied V_{ZBIAS} for both test mass illumination (Red) and electrode housing illumination (Blue). Note the negative equilibrium reached upon test mass illumination with $V_{ZBIAS} = -2$. Figure taken from Weber et al. (2006).

The results demonstrate the effect that the applied V_{ZBIAS} has in either enhancing or suppressing the photoelectric current and show that at least some absorption took place in the z sense electrode regions. The measurements again show an asymmetry between both illuminations. Of particular interest is the reading made with

$V_{ZBIAS} = -2$ for the test mass illumination which shows a negative V_{TM} equilibrium was reached. This means that with this setup bipolar discharge is possible using a single lamp and an appropriate applied bias.

A continuous discharge experiment was also carried out. This involved having both lamps turned on simultaneously and adjusting the lamp powers so that the photoelectric currents match in both directions. This allowed the test mass potential to be held near zero while simulating the situation expected in flight. One current acted to 'charge' the test mass, in analogy with the radiation environment in space, while the other acted to 'discharge'. Four separate tests were performed with the test mass potential held near zero, to within 10 mV or $\sim 10^6$ individual charges, for between one and two days. The pendulum torque noise was then analysed during this time and no detectable excess noise was seen in the Pathfinder bandwidth. This was despite the fact that the magnitudes of the photoelectric currents were 100 times larger than are expected in flight.

3.3.4 Conclusions

The testing of the engineering model Charge Management System with the single-mass pendulum was deemed a complete success. The system showed it was capable of discharging in either direction and at the rates required for Pathfinder. A simple demonstration of the systems capability of continuous discharging was also shown. However, as stated in Sections 3.3.0.1 and 3.3.1, the setup studied had many, possibly significant, departures from the flight system. Later measurements with a four-mass pendulum experiment had a setup more representative of flight.

3.4 Four-Mass Pendulum

Like the single-mass, the four-mass pendulum is primarily designed to study sources of test mass acceleration noise. Rather than observe net torques though, it can make direct measurements of translational forces acting along the sensitive x axis. It achieves this by suspending four connected test masses from a torsion fibre, each displaced from the centre by about 11 cm, thus forming a cross-shaped structure. Figure 3.10 shows a photograph of the configuration.

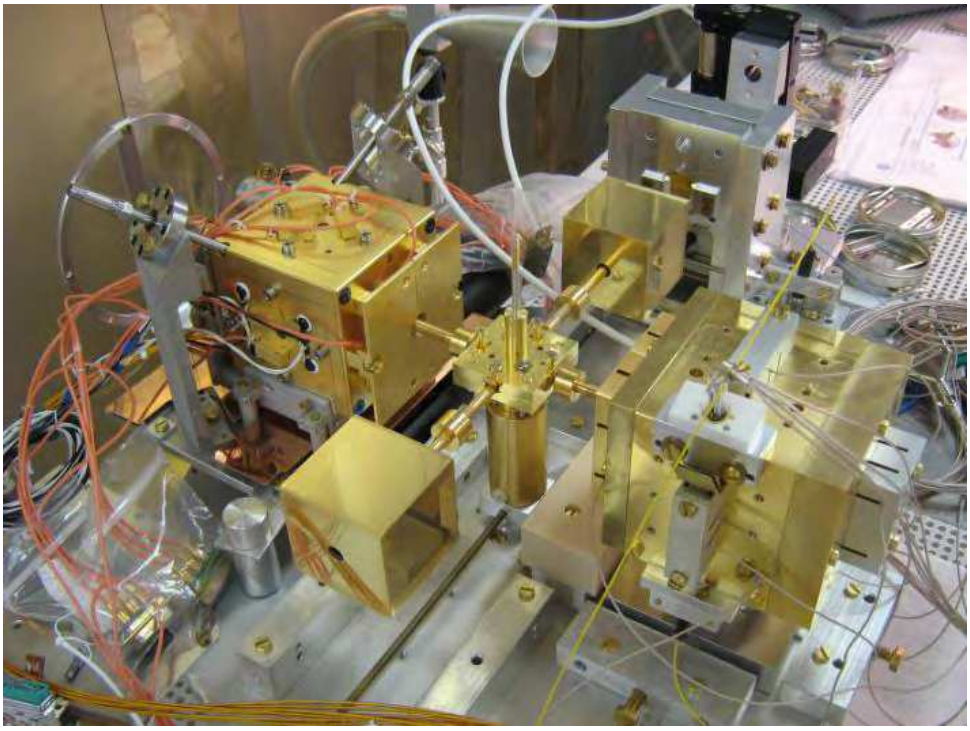

Figure 3.10: A photograph of the four-mass torsion pendulum experiment. The test mass of interest can be seen on the left with the two ISUKs used for discharging visible, entering from above. Photograph courtesy of UTN.

As is seen in Figure 3.10, of the four test masses only one is surrounded by a Pathfinder like electrode housing, which is effectively on its side so that the shaft can still enter in the z plane. The adjacent test mass is also enclosed but by a custom built, simplified sensor which can be used to counteract forces introduced by the inertial sensor. During operation the entire system is enclosed within a vacuum chamber and, similar to the single-mass, the test mass position can be measured with either the capacitive sensors or an optical autocollimator with two degrees of freedom. A full description of the four-mass torsion pendulum experiment is given by Cavalleri et al. (2009b). Here, only details relevant to discharging are discussed.

3.4.1 Differences to Single-Mass Setup

In terms of discharging, the setup of the four-mass experiment is significantly different to that used with the single-mass pendulum and much closer to the flight system. It uses flight replica ISUKs, as described in Section 3.1.3, to inject the UV light into the sensor. As will be the case in flight, these are inclined at $\pm 20°$ to the z plane, unlike the $\pm 8°$ used in the single-mass. Furthermore, the ISUKs illuminate the z faces of the test mass and electrode housing that are on the opposite side to where

the pendulum shaft is located. Again, this is an improvement on the single-mass case.

For the results presented, the inertial sensor is also much closer to the flight design. It includes the holes through which the test mass caging fingers will enter and the test mass also has the corner features related to the caging mechanism. This is significant as the UV light used for discharging is expected to be initially incident in these regions. Finally, the gold coatings of the test mass faces have highly specular reflection properties, as will be the case in flight. One should keep in mind that even with this setup there are still several departures from the flight case which could effect discharging. A full discussion of these differences will be given in Chapter 5, where the system will be simulated.

3.4.2 Results

To date, three different test masses have been studied with the four-mass experiment. The first, TM1, had a geometry which was the same as the single-mass test mass as it lacked corner caging features. Initial measurements with TM1 agreed qualitatively with the single-mass results. As one would expect, illuminating the electrode housing caused the test mass to charge negatively while illuminating the test mass caused it to charge positively. This was the case for any applied V_{ZBIAS}. Unfortunately, while a bake-out of the system was being performed, glue joints within the hollow test mass failed causing damage beyond repair.

The four-mass pendulum was remounted with a second test mass, TM2. This test mass had a flight like geometry, including corner caging features. It showed a significant departure from the behaviour displayed by the single-mass system and TM1. Illuminating either the electrode housing or the test mass caused the test mass to charge positively, even after bake-out. The results seemed to show that the test mass had a much higher quantum yield than the housing with the reflected light absorbed by TM2 producing a larger photocurrent than that from the housing. An inspection of the TM2 surface revealed discolouration of the z face and defects were observed in the gold coating, possibly explaining the anomalous results. It should also be noted that both TM1 and TM2 were cleaned with isopropyl alcohol before integration, possibly affecting the photoelectric properties. A full description of the results obtained for TM1 and TM2 can be found in Wass et al. (2010).

The results presented here were obtained using a test mass closest to the flight model, called TM3. It has the same flight like geometry as TM2 but a superior flight like surface finish, with no visible defects. TM3 was also installed as re-

ceived, with no cleaning taking place prior to installation. Unfortunately, TM3 has shown behaviour qualitatively similar to TM2 in that with no applied biases, the test mass charges positively no matter which illumination is used. Measurements were made before and after the system was baked-out (110 °C for one week), with the discharging properties improving and stabilising post bake-out. This was presumably because the bake-out process acted to remove surface contamination and leave a more uniform system. Here a selection of the post bake-out findings shall be discussed with full details being found in Antonucci et al. (2010, 2011).

3.4.2.1 Test Mass Equilibrium Potential

As has been discussed previously, when a lamp is left to illuminate the system the test mass eventually reaches an equilibrium potential. This is because the initial net photocurrent in a particular direction is gradually suppressed as the test mass charge increases until there is no net current, giving an equilibrium potential. This idea is complicated slightly by the presence of the 100 kHz AC injection bias which causes the test mass potential to oscillate around the equilibrium position. One might naively expect this injection bias to have no effect on the actual equilibrium potential reached as during its cycle it alternately suppresses the flow in one direction and then the other. While this is true, the number of photoelectrons being emitted from the test mass and housing is not the same in both directions leading to a net flow during an injection cycle, shifting the equilibrium potential. Figure 3.11 shows measurements made with TM3 of the test mass equilibrium position varying with the magnitude of the 100 kHz AC injection voltage.

The unexpected discharging properties of TM3 are shown clearly in Figure 3.11, being significantly different to the results obtained with the single-mass pendulum. The desired behaviour is for a negative test mass equilibrium potential to be reached upon illuminating the housing. This is not what was observed with the nominal science mode injection voltage amplitude of 5.4 V nor at lower injection voltages of 0.54 or 0.054 V. The results also show the dependence of the equilibrium potential on the magnitude of the injection voltage. As one would expect, the larger the injection voltage the higher the test mass potential reached.

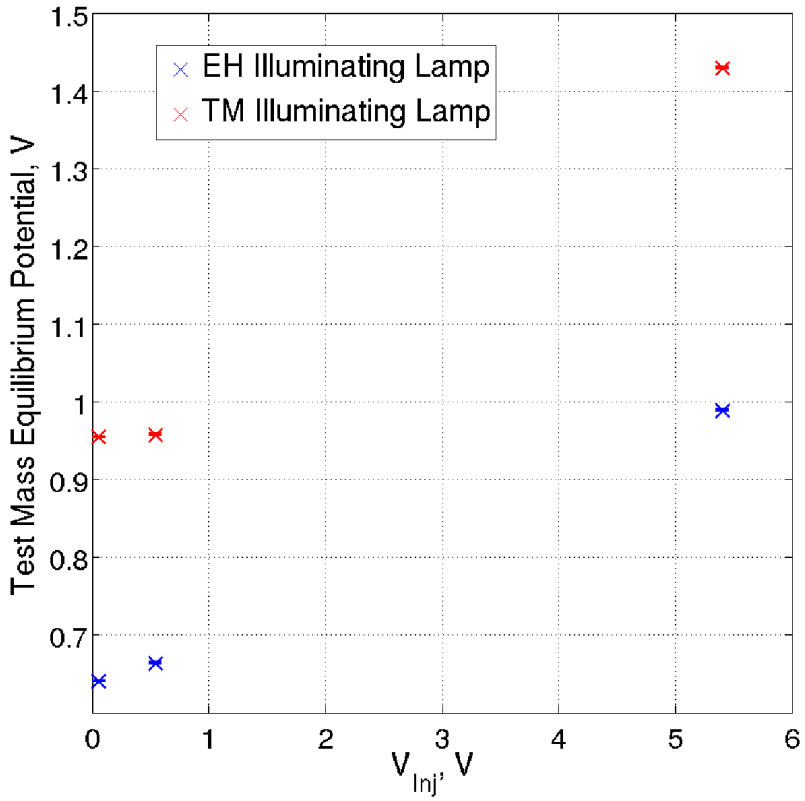

Figure 3.11: Measurements made with TM3 of the equilibrium potential reached with 100 kHz AC injection voltages, V_{Inj}, of 0.054, 0.54 and 5.4 V. Note the unexpected behaviour when illuminating the electrode housing. Nominally, the test mass should reach a negative equilibrium potential upon illuminating the housing but this is not the case at any injection bias. This Figure was created from data taken from Antonucci et al. (2011).

3.4.2.2 Effect of Applying Bias

An investigation was carried out to discover the minimum potential the test mass could be brought to by employing appropriate DC biasing of the sense electrodes. It was found that by applying positive DC voltages to all but the lower z sense electrodes a negative test mass equilibrium potential could be reached. For a neutral test mass these applied biases raise the test mass to a positive potential with respect to the grounded housing and the lower sense electrodes. The inertial sensor was then illuminated, with photoelectrons originating from the test mass being suppressed while those from the housing being enhanced. This brought the test mass to a lower positive potential until an equilibrium was reached. Illumination was then stopped and the positive DC biases turned off, leaving the test mass at a negative potential. Measurements were made with +4.5 V applied to all the x sense electrodes, +5.0 V

to all the y sense electrodes and +4.5 V to just the upper z sense electrodes. Using a 0.054 V, 100 kHz AC voltage on all the injection electrodes a test mass equilibrium potential of -0.614 ± 0.001 V was reached when illuminating the electrode housing.

While this discharging method is not ideal, it could not be used for continuous discharging while Pathfinder science data is being taken, it does offer an alternative discharging method for discontinuous discharging out of science mode. It also allowed TM3 to be brought to negative potentials giving an opportunity to study the discharging behaviour more thoroughly.

3.4.2.3 Apparent Yield

Being able to discharge the test mass in either direction allowed the apparent yields at different test mass potentials to be studied. It is important here to make a clear distinction between the quantum yield and the apparent yield. As previously mentioned, the quantum yield is an intrinsic property of an individual surface and is defined as the ratio of photoelectrons produced to the number of photons absorbed. The apparent yield on the other hand is a property of the entire inertial sensor and varies depending on the state of the system. At a particular test mass potential the apparent yield is the net number of electrons exchanged with the test mass per UV photon entering the inertial sensor. It is not possible to measure individual quantum yields within the sensor directly, instead apparent yields are measured and it will be shown in Chapter 5 how these can be used to estimate the surfaces quantum yields.

The apparent yields were obtained by first measuring the test mass potential, V_{TM}, using a similar method to that described in Section 3.3.2. Either the test mass or electrode housing was then illuminated for a short time. The UV light power entering the system during this illumination was known following measurements with a calibrated photodiode of the ISUK output. Finally the test mass potential was remeasured allowing the net number of electrons exchanged with the test mass during illumination to be calculated, leading to the apparent yield values. All apparent yield measurements were taken with a 100 kHz AC injection voltage of 0.054 V, which is small enough to not significantly alter the results. The apparent yields observed at various test mass potentials for both illuminations are shown in Figure 3.12.

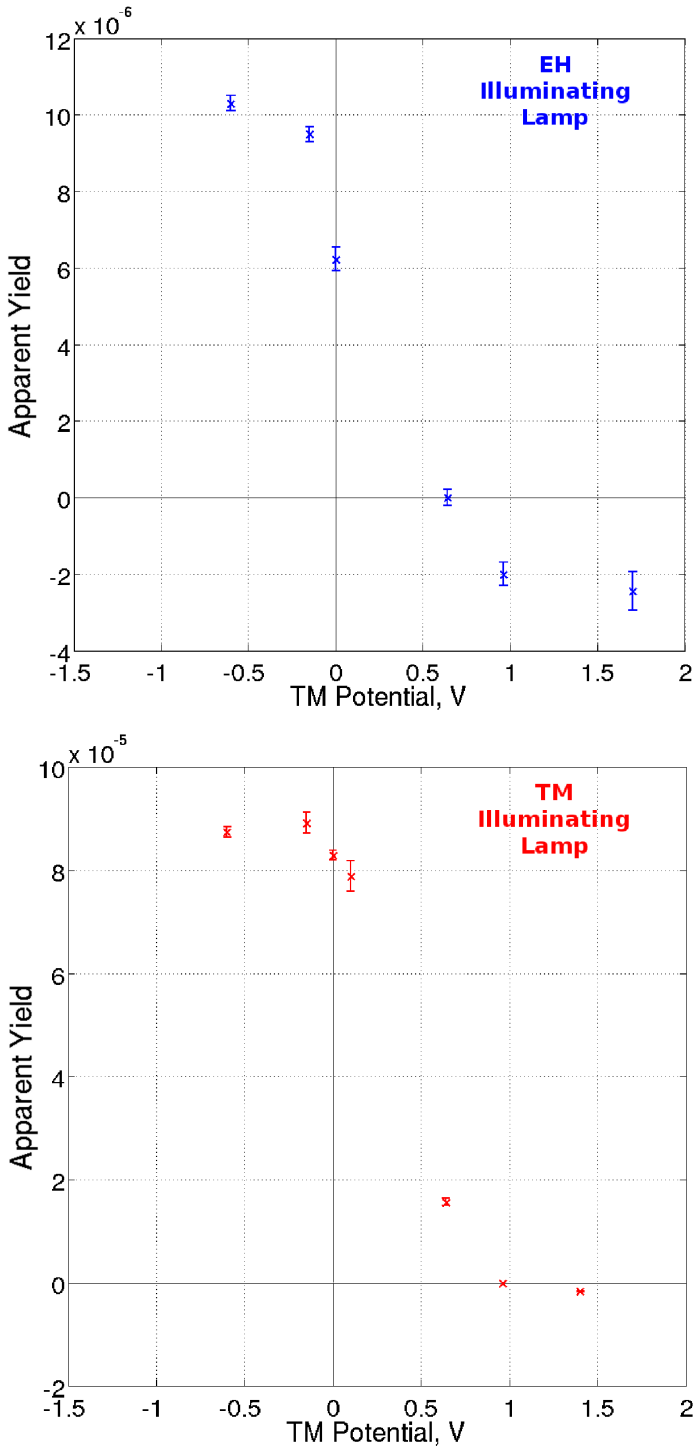

Figure 3.12: The results from measuring the apparent yields at different test mass potentials, for both illuminations. As expected, both appear to show asymptotic behaviour as each photocurrent saturates. It is also important to note the order of magnitude difference in the yield scales, with the test mass producing significantly more photoelectrons. This Figure was created from data taken from Antonucci et al. (2011).

As one would expect, both illuminations show asymptotic behaviour. This is because at either extreme there is a point where the test mass potential completely suppresses the photocurrent in one direction while the photocurrent in the opposite direction flows completely unopposed and therefore saturates. The point where the apparent yield is zero gives the test mass equilibrium potential previously discussed. It is clear from Figure 3.12 that the number of photoelectrons originating from the test mass is much greater than from the housing. This is due to a combination of the two surfaces quantum yields but also the fraction of UV light each surface absorbs for a given illumination.

For the housing illumination the maximum apparent yields were approximately $+1.03 \pm 0.02 \times 10^{-5}$ e/photon and $-2.4 \pm 0.5 \times 10^{-6}$ e/photon. Likewise, for the test mass illumination the maximum apparent yields were approximately $+8.8 \pm 0.1 \times 10^{-5}$ e/photon and $-1.7 \pm 0.1 \times 10^{-6}$ e/photon. To obtain the actual quantum yields of the electrode housing and test mass from these apparent yields one needs to know the amount of UV light absorbed by either surface for each illumination. This will be calculated in Chapter 5 with the aid of a ray trace simulation.

One can also obtain an estimate of the surfaces work functions from Figure 3.12. The energy of the illuminating UV photons is known to be 4.88 eV and the point at which either photocurrent saturates gives the maximum energy of the photoelectrons being emitted in the opposite direction. For the housing illumination the photoelectrons originating from the test mass have a maximum energy of between 1.0 and 1.5 eV while those from the housing have a maximum energy between 0.2 and 0.7 eV. These equate to work functions between 3.4 to 3.9 eV and 4.2 to 4.7 eV respectively. One can do the same for the test mass illumination and are found to be in the same ranges. This is interesting as opposite corners of the sensor are illuminated in each case yet the photoelectric properties of each surface seems to be roughly consistent. This suggests both the housing and test mass have fairly uniform photoelectric properties, though they are significantly different from each other. Again, further work will be carried out regarding the work functions in Chapter 5.

3.4.3 Conclusions

Measurements of the Charge Management System with the four-mass torsion pendulum experiment have shown significant unexpected behaviour. Without the application of applied DC biases the system cannot discharge a positive test mass. This

means that if the space environment charges the test mass positively, as predicted by simulation, and the discharge behaviour is the same in flight, continuous discharge will not be possible. However, discontinuous discharging could still be achieved by allowing the test mass to charge over the course of several days, then leave science data taking mode while the biases required for discharging are applied.

There is no guarantee that the system behaviour will be the same in flight. Indeed, it is unlikely that it will be and could even be worse. The variation after bake-out demonstrates the significance of surface contamination which is unpredictable and difficult to control. In addition, it is not clear why the test mass seems to exhibit photoelectric properties that are significantly different from the housing surfaces. Both are gold coated and have been manufactured and handled in the similar controlled conditions.

3.5 Summary

The design and production of the flight Charge Management System for Pathfinder has been described and testing of the system discussed. The basic concept of discharging involves illuminating the gold surfaces of the test mass or the surrounding electrode housing with UV light. This causes electrons to be emitted via the photoelectric effect and allows the charge on the isolated test masses to be controlled. However, there are three main complications to this basic idea:

- Reflections within the sensor allow unintended surfaces to absorb UV light and emit photoelectrons.
- Both AC and DC electric fields within the sensor can either enhance or suppress photocurrents.
- The discharge behaviour of the entire system is strongly dependent on the work function and quantum yield of individual surfaces.

A combinations of these are thought to account for the unexpected four-mass pendulum discharging results which were significantly different from those obtained during earlier testing with the single-mass pendulum. Given these dependencies, the reflection properties of flight representative gold surfaces, the photoelectric properties of various relevant surfaces and the distribution of the initial UV light are all experimentally measured and discussed in Chapter 4. Using these measurements the the four-mass discharging system is simulated and the possible effect of differences present in the flight system studied in Chapter 5.

Chapter 4

Measuring Properties Relevant to Test Mass Discharging

Introduction

Modelling the discharge processes within the inertial sensor has been a long term goal but was given renewed emphasis when the four-mass torsion pendulum measurements, made at the University of Trento, showed a significant change in behaviour compared to that of the single-mass. To aid simulation and increase confidence in the models used it is important to experimentally measure as many of the individual system properties as possible. As was discussed in the previous chapter, in addition to the geometry and the electric fields present, three aspects of the inertial sensor are of particular importance when it comes to understanding the discharging behaviour.

Firstly, the photoelectric properties of the various surfaces within the inertial sensor, specifically the work functions and quantum yields. Secondly, the reflection properties of the surfaces with both the intrinsic reflectivity and the angular distribution of the reflected light being important. Thirdly, the distribution of the UV light that is emitted from the ISUK as it is injected into the inertial sensor.

Characterising these aspects of the discharge system is an ongoing endeavour and this chapter describes the measurements that have been made to date.

4.1 Surfaces

As was explained in Chapter 3, the surface properties inside the inertial sensor are one of the dominant factors that determine the discharge behaviour. There are three different surface types in the flight inertial sensor, each with several roughness

requirements. Originally, all the internal sensor surfaces were to be gold coated and this was the case with both the single and four-mass torsion Pendulum measurements described in Chapter 3. Although the underlying substrates for the test mass, electrodes and housing are different, gold-platinum alloy, sapphire and molybdenum respectively, they are all sputter gold coated in the same way by a company called Selex. The gold coatings are a few microns thick and each element will be stored and transported in the same way which was thought to give these surfaces similar work functions, quantum yields and reflectivities. The surface finish however is dependant on the underlying substrate meaning that the angular distribution of reflected light will vary between them, dependant on the surface roughness.

Due to problems encountered during development of the test mass caging mechanism there will now be two additional surfaces present in the flight sensor. The redesign includes eight caging fingers that will hold the test mass by the $\pm z$ face corners during launch. They are made of iridium and will be retracted back just ~ 0.6 mm into the housing once the experiment begins. Their position within the sensor means they are likely to experience UV illumination. Tests have shown that the finger tips cannot be gold coated as the gold tends to peel away during decaging. Likewise the specially machined corner areas of the test mass, where the fingers grab it, need to be left uncoated for the same reason. This leaves the underlying $Au_{0.7}Pt_{0.3}$ alloy exposed in an area likely to be illuminated.

4.2 Photoelectric Properties

The literature shows that clean gold, deposited in an ultra-high-vacuum and measured *in situ*, has a work function of 5.2 eV, (E. E. Huber, 1966). Given that the energy of the photons used in the charge management device is 4.88 eV, it is only through surface contamination and/or defects that discharge can occur at all. Upon exposure to air the effective work function for gold is reduced to around 4.2 eV and can remain stable even after repeated exposure to UV (240 to 300 nm) in a 10^{-6} Torr vacuum, (Saville et al., 1995). According to work done by Bajpai et al. (1976); Alloway et al. (2003); Gottfried et al. (2003), surface contamination strongly affects the measured work function of gold with adsorption of water, carbon and hydro-carbons having particular influence. It is also important to note that the work function for iridium found in the literature is between 5.4 and 5.8 eV, (Haynes and Lide, 2010), while for $Au_{0.7}Pt_{0.3}$ alloy the work function has been found to be 5.4 eV, (Bouwman and Sachtler, 1970). There appears to be no work in the literature studying the effect of contamination in either case. To the best of the authors knowledge

there is also no published work relating the quantum yield of any of these surfaces at 254 nm. Unpublished studies on gold, carried out at Imperial College London during the early development of the discharging system, obtained fairly stable work function values of ~ 4.3 eV with quantum yields of $\sim 2\times10^{-5}$ electrons per absorbed 254 nm photon, (Rochester et al., 2003).

4.3 Modena Measurements

In order to better understand the photoelectric properties of the surfaces present in the inertial sensor, the surface science group at the University of Modena, Italy, led by Prof. Nannarone, have been carrying out a series of surface measurements on behalf of the Pathfinder collaboration. These measurements were started in early 2008 and continue as additional relevant surfaces become available. Their as yet unpublished work has been received in the form of several internal project reports. Here a summary and discussion of their findings are presented.

The gold samples examined so far include a spare sense electrode from the same batch as those used in the single-mass torsion pendulum experiment, several gold coated witness samples on sapphire and quartz substrates from the same batch as will be described later in Section 4.4.3, the surface of an actual test mass used at the four-mass torsion pendulum experiment as well as some gold coated aluminium disks and gold coated $Au_{0.7}Pt_{0.3}$ alloy disks. The results are also compared to a gold coated reference sample, supplied by a company called Arrandee rather than Selex. Two uncoated iridium samples have also been measured in addition to two uncoated $Au_{0.7}Pt_{0.3}$ alloy disks.

4.3.1 Techniques

Three techniques have been employed by the Modena group to probe the surface properties; direct photoemission measurements, Ultraviolet Photoelectron Spectroscopy and X-ray Photoelectron Spectroscopy.

4.3.1.1 Direct Photoemission Measurements

First, the photocurrents produced by illuminating a particular surface with 254 nm light from a mercury pencil lamp have been directly measured and used to obtain quantum yield values. These measurements were made in an ultra-high-vacuum (5×10^{-8} mbar) using a Keithley model 6517A electrometer to measure the photocurrent produced upon illumination, with the sample held at a bias with respect

to ground in the -10 to 10 V range. A typical measurement is shown in Figure 4.1.

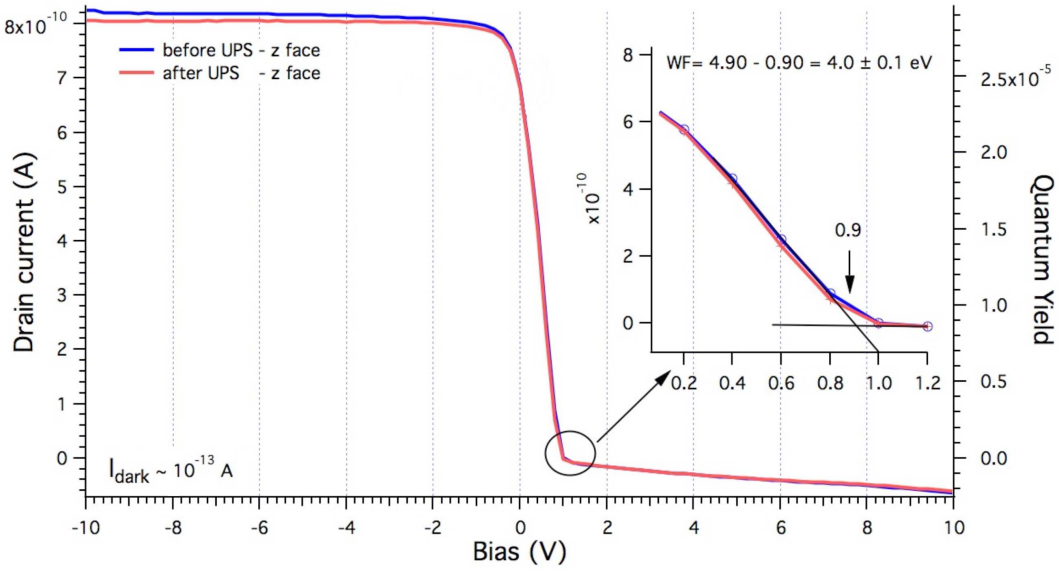

Figure 4.1: Typical photocurrent measurements made at the University of Modena taken before and after a UPS measurement, described later. This Figure shows data obtained from the gold surface of an actual pendulum test mass, TM2. The negative current that flows at large positive bias is interpreted at photoelectrons being produced and then captured from reflected light impinging on other surfaces within the vacuum chamber. Figure courtesy of the University of Modena.

It is possible to use these photocurrent measurements to obtain both the quantum yield for a particular surface and an estimate of its work function. The work function is derived from the positive bias needed to reduce the photocurrent to zero, this being the point at which none of the electrons have sufficient energy to overcome the suppressing potential. The work function is then given by this maximum photoelectron energy minus the incident photon energy. The quantum yield is derived from the saturation photocurrent measured with a large repulsive bias together with knowing the calibrated UV intensity at the surface.

4.3.1.2 Ultraviolet Photoelectron Spectroscopy

Another technique employed by the group at Modena is called Ultraviolet Photoelectron Spectroscopy, or UPS. This measurement involves illuminating the surface in an ultra-high-vacuum with 21.2 eV UV photons and observing the energy and intensity of the emitted electrons. Due to the energy of the incident photons UPS can only liberate valence electrons but offers good energy resolution and can give

a measure of the surfaces work function. This is achieved by subtracting the measured maximum binding energy, relative to the Fermi level, from the 21.2 eV photon energy. Figure 4.2 shows the UPS spectra measured for five, nominally identical, gold coated sapphire substrate witness samples. The presence of defined features (or lack of them) within the measured spectra can also indicate the level of surface contamination. UPS allow the surface to be probed to a depth of a few nanometres.

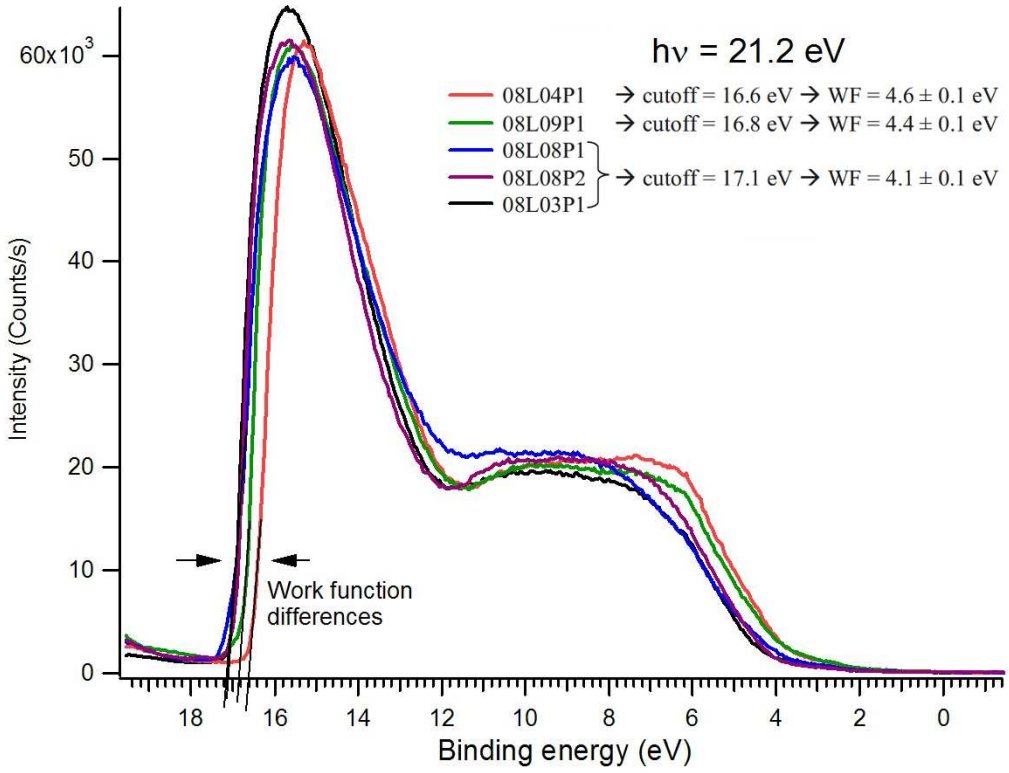

Figure 4.2: UPS measurements made on five separate gold coated sapphire substrates. The work function of each surface can be obtained by subtracting the maximum binding energy, relative to the Fermi level, from the 21.2 eV photon energy. The cause of the variation in the work functions obtained is thought to be due to different levels of surface contamination. Figure courtesy of the University of Modena.

4.3.1.3 X-ray Photoelectron Spectroscopy

A similar technique to UPS, called X-ray Photoelectron Spectroscopy, or XPS was also employed which instead uses 1253.6 eV photons. XPS can give the composition and abundance of additional elements present on the surface. Subtracting the kinetic energy of an emitted electron from the known energy of the incident photon gives the binding energy a particular electron overcame. This allows a spectrum to be built up

from the binding energy of all the emitted electrons. Given that each element has a unique set of possible binding energies, this combined spectrum allows each element to be identified and its relative abundance determined, Figure 4.3. A drawback of XPS is that it can damage organic molecules adsorbed on the the surface, changing the work function. XPS allow the surface to be probed to a depth of ~ 10 nm.

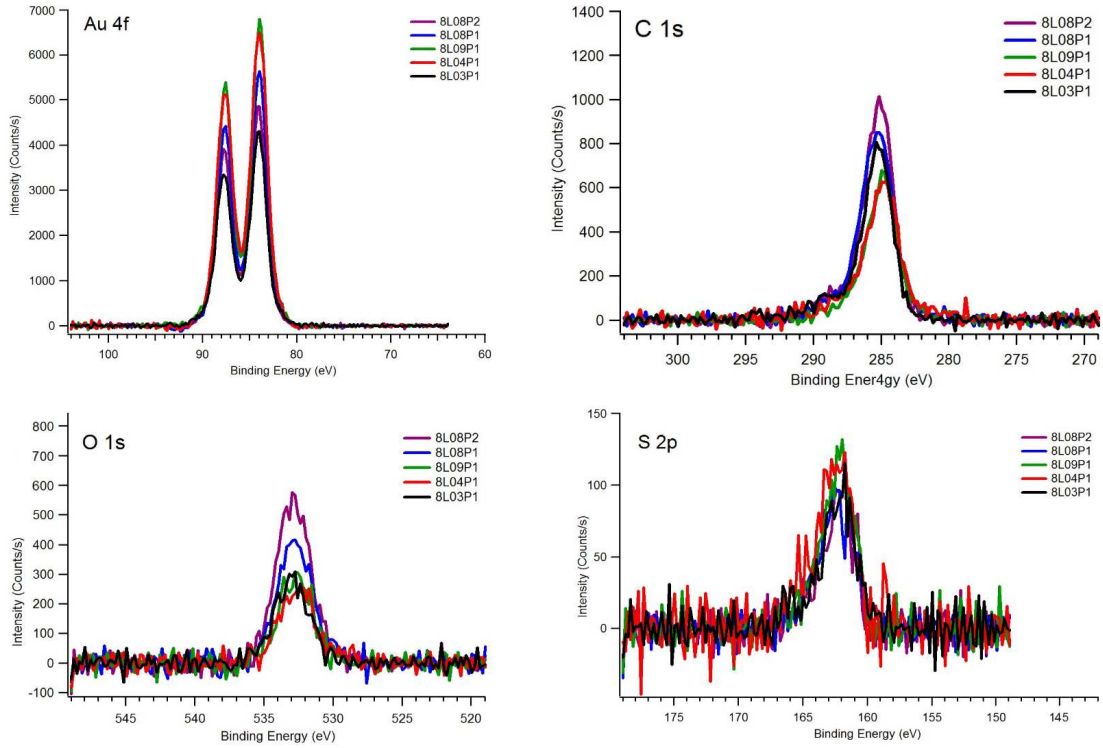

Figure 4.3: XPS measurements made on five separate gold coated sapphire substrates. Spectral features associated with Au, C, O and S were identified on each sample surface, but no other elements were observed. Figure courtesy of the University of Modena.

4.3.2 Work Function and Quantum Yield Results

The work functions and quantum yields obtained using direct photoemission measurements and UPS are collated and summarised in Table 4.1. The results are mainly for gold coated surfaces with two iridium and two $Au_{0.7}Pt_{0.3}$ alloy surfaces also studied. All the gold surfaces studied were coated by the same company (Selex) using the same sputtering technique and should nominally have the same properties. However, the measurements show that the work functions and quantum yields are highly variable, even giving different results at different regions of the same surface. The measured gold work functions vary between 3.6 eV and 5.1 eV, with an aver-

age value of 4.3 ± 0.4 eV. Likewise, the quantum yields measured show even more variation with values between 0.8×10^{-6} and 5.9×10^{-5} being found, a factor of ~ 70 difference. This is a very significant finding as were the test mass and housing to have such a large difference, bipolar discharge without the aid of applied biases would be impossible and continuous discharging could not be performed. The two iridium surfaces were found to have very low quantum yields, less than 4.0×10^{-7}, while the $Au_{0.7}Pt_{0.3}$ alloy samples had measured yields comparable to that of the highest values measured for the gold at 5.0×10^{-5}.

As will be shown in the next section, the variation in properties is thought to be due to surface contamination, either across the surface or in small local regions. This possibly explains some of the more anomalous results. In theory the lower the work function is the higher the yield should be, but this does not always seem to be the case. Indeed, the work functions measured for the gold coated Al witness samples are higher than the incident photon energies yet the surfaces still produce significant quantum yields.

It has been suggested that the range in properties across surfaces was due to isolated contaminated regions. Upon annealing a more uniform contaminated layer would possibly be formed, stabilising the photoelectric properties. This would agree with the four-mass results which seem to show uniform properties after bake-out at 110 °C for one week. Attempts were made at Modena to observe this effect. Generally, while annealing was observed to affect the work function it was not in a controlled or consistent way, with exposure to UV or X-rays during UPS and XPS respectively, having a similar effect. It should be noted that the method of heating was not ideal and further measurements are planned in the future. As would be expected with contamination, sputtering with 2 kV Ar ions for 30 minutes seemed to clean the surface and significantly increase the work function.

Date	Surface	Comment	Work Function (eV)	Quantum Yield
10/03/08	Gold Coated Electrode - Zone 1	As Received.	3.6	-
10/03/08	Gold Coated Electrode - Zone 2	As Received.	3.6	-
10/03/08	Gold Coated Electrode - Zone 3	As Received.	3.6	-
10/03/08	Gold Coated Electrode - Zone 1	Annealed at 130 $^{\circ}$C for 24 hours.	3.8	-
10/03/08	Gold Coated Electrode - Zone 1	Exposed to air again.	3.6	-
10/03/08	Gold Coated Electrode - Zone 1	Annealed at 250 $^{\circ}$C for 24 hours.	3.7	-
10/03/08	Gold Coated Electrode - Zone 1	Sputtered for 30 minutes with 2 kV Ar Ions.	4.6	-
10/03/08	Pure Gold Coated Reference	Flame annealed then cleaned with ethanol.	4.7	-
10/03/08	Pure Gold Coated Reference	Sputtered for 30 minutes with 2 kV Ar Ions.	4.9	-
15/12/08	Gold Coated Sapphire - 8L03P1	As Received.	4.1	-
15/12/08	Gold Coated Sapphire - 8L04P1	As Received.	4.6	-
15/12/08	Gold Coated Sapphire - 8L09P1	As Received.	4.4	-
15/12/08	Gold Coated Sapphire - 8L08P1	As Received.	4.1	-
15/12/08	Gold Coated Sapphire - 8L08P2	As Received.	4.1	-
15/12/08	Gold Coated Sapphire - 8L03P1	After XPS.	4.2	-
15/12/08	Gold Coated Sapphire - 8L04P1	After XPS.	4.4	-
15/12/08	Gold Coated Sapphire - 8L09P1	After XPS.	4.2	-
15/12/08	Gold Coated Sapphire - 8L08P1	After XPS.	4.2	-
15/12/08	Gold Coated Sapphire - 8L08P2	After XPS.	4.2	-
10/05/10	Gold Coated TM2 - z Face	As Received.	4.0	2.8×10^{-5}
10/05/10	Gold Coated TM2 - Side Face	As Received.	4.1	4.1×10^{-6}
19/05/10	Gold Coated Au/Pt Disk - D2	As Received.	4.3	2.0×10^{-5}
19/05/10	Gold Coated Au/Pt Disk - D4	As Received.	4.4	6.2×10^{-6}
18/02/11	Gold Coated Al plate - Zone 1	As Received.	4.7	8.0×10^{-6}
18/02/11	Gold Coated Al plate - Zone 2	As Received.	4.7	6.7×10^{-6}
18/02/11	Gold Coated Al plate - Zone 1	Annealed at 120 $^{\circ}$C for 24 hours.	4.4	5.9×10^{-5}
18/02/11	Gold Coated Al plate - Zone 2	Annealed at 120 $^{\circ}$C for 24 hours.	4.5	4.4×10^{-5}
18/02/11	Gold Coated Al Witness Sample 1	As Received.	5.1	0.8×10^{-6}
18/02/11	Gold Coated Al Witness Sample 2	As Received.	5.0	2.7×10^{-5}
18/02/11	Gold Coated Al Witness Sample 3	As Received.	4.9	1.8×10^{-5}
18/02/11	Gold Coated TM3 Witness Sample	As Received.	-	3.1×10^{-6}
08/07/10	Iridium Sample 1	As Received.	4.2	$< 4.0 \times 10^{-7}$
08/07/10	Iridium Sample 2	As Received.	5.2	$< 4.0 \times 10^{-7}$
25/02/11	Au/Pt Plate - Zone 1	As Received.	4.3	4.5×10^{-5}
25/02/11	Au/Pt Plate - Zone 2	As Received.	-	5.0×10^{-5}

Table 4.1: A summary of the work function and quantum yield results from the University of Modena. Note that both the work function and quantum yield was not measured for all samples, hence gaps in the data.

4.3.3 Surface Composition Results

The surface composition of some of the samples were probed using XPS and the results are collated and summarised in Table 4.2. Only three contaminating elements were detected and for all the samples the percentage of gold, carbon, oxygen and sulphur contained on the surface, to a depth of $\sim$ 10 nm, is shown. All the samples had been exposed to air which caused adsorption, the adhesion of atoms, ions or molecules to the surface, which left the gold covered with carbonaceous contaminants. It is these surface contaminates that are thought to cause the variation in the measured photoelectric properties and there are several clues that suggest this is the case. For example, the gold coated spare electrode measurements show the lowest work functions and also the lowest percentage of gold present in the top $\sim$ 10 nm of the surface. These surfaces were also kept in the least well controlled conditions as they were stored in a normal laboratory environment for a considerable time, over a year, before the measurements were made. Generally the levels of contamination correlate well with the measured work function. The higher the level of contamination the lower the work function.

An interesting observation is the presence of sulphur, but only on the gold coated sapphire witness samples. The small levels of sulphur are likely in the form of organic thiols, compounds containing carbon bonded sulphur. It is not clear why they were only observed on these surfaces. The effect of annealing and sputter cleaning should also be noted. As one would expect the level of contamination is generally reduced and in the case of the gold coated reference sample, supplied by Arrandee rather than Selex, sputter cleaning removed all traces of surface contamination. However, this was not the case for the gold coated electrode where some carbon and oxygen remained. This suggests that contamination was still present in small isolated regions or even within the coating itself. The possibility that the variation seen in the photoelectric properties is in part due to the coating process is being further investigated.

Even if it is discovered that the coatings themselves are contaminated and this problem is solved, surface adsorption from air will certainly still be present. It will also not be possible to completely clean the surfaces once they are in vacuum given that the maximum bake-out temperature for the torsion pendulums and the flight inertial sensor is $\sim$130 °C. Indeed, this is fortunate as without some contamination the 4.88 eV UV photons would have insufficient energy to liberate electrons from the pure gold.

Date	Surface	Comment	Au (%)	C (%)	O (%)	S (%)
10/03/08	Gold Coated Electrode - Zone 1	As Received.	22	64	14	00
10/03/08	Gold Coated Electrode - Zone 2	As Received.	23	65	12	00
10/03/08	Gold Coated Electrode - Zone 3	As Received.	22	63	15	00
10/03/08	Gold Coated Electrode - Zone 1	Annealed at 130 °C for 24 hours.	27	61	12	00
10/03/08	Gold Coated Electrode - Zone 1	Annealed at 130 °C for another 24 hours.	26	63	11	00
10/03/08	Gold Coated Electrode - Zone 1	Annealed at 250 °C for 24 hours.	32	57	11	00
10/03/08	Gold Coated Electrode - Zone 1	Sputtered for 30 minutes with 2 kV Ar Ions.	67	26	07	00
10/03/08	Pure Gold Coated Reference	Flame annealed then cleaned with ethanol.	55	45	00	00
10/03/08	Pure Gold Coated Reference	Sputtered for 30 minutes with 2 kV Ar Ions.	100	00	00	00
15/12/08	Gold Coated Sapphire - 8L03P1	As Received.	26	62	07	05
15/12/08	Gold Coated Sapphire - 8L04P1	As Received.	37	51	06	06
15/12/08	Gold Coated Sapphire - 8L09P1	As Received.	39	49	07	05
15/12/08	Gold Coated Sapphire - 8L08P1	As Received.	28	59	09	04
15/12/08	Gold Coated Sapphire - 8L08P2	As Received.	24	60	12	04
18/02/11	Gold Coated TM3 Witness Sample	As Received.	32	61	07	00

Table 4.2: A summary of the surface composition results from the University of Modena. The percentage of gold, carbon, oxygen and sulphur contained on the surface to a depth of ~ 10 nm is shown.

4.3.4 Photoelectron Energy Distribution

In order to aid the simulations to be presented in Chapter 5, the direct photoemission measurements were used to estimate the form of the photoelectrons energy distributions. This was achieved by first subtracting the dark current from the photocurrents measured at varying applied bias. The opposing bias in V equates to the energy of the photoelectrons able to overcome it in eV and by differentiating the curves one can then obtain an estimate of the photoelectrons energy distribution. These are shown in Figure 4.4.

Although the results are fairly crude, and vary between surfaces, they do demonstrate the general form of the electrons energy distribution, each with a well defined peak. This is in good agreement with the literature where similar, though smoother, distributions have been measured for gold and 4.9 eV illuminating photons, (Vernier et al., 1969; Pauty et al., 1974). Later, these energy distributions will be approximated with triangular functions.

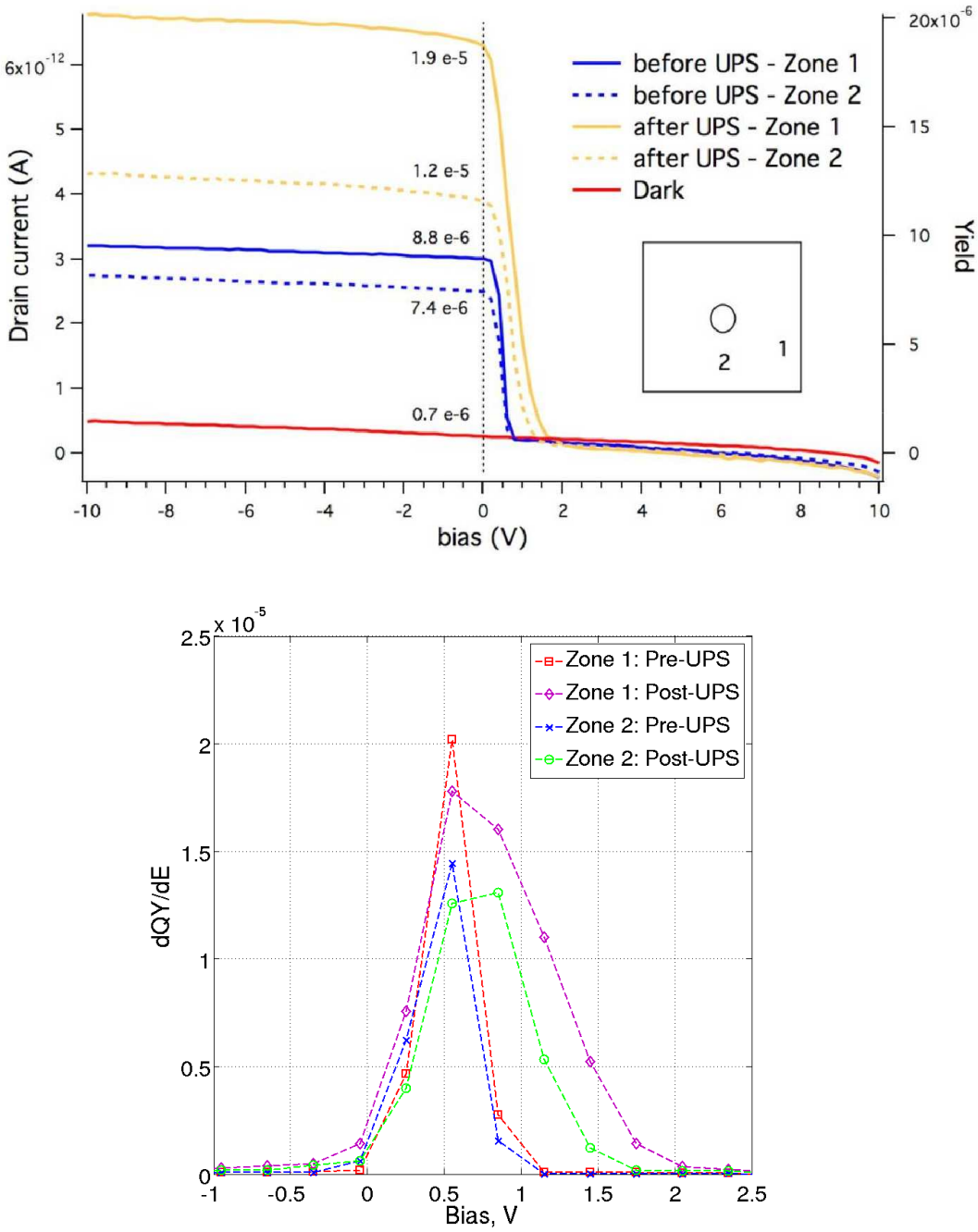

Figure 4.4: *Top*: The photocurrents measured for two regions on the gold coated aluminium plate samples, before and after UPS. Figure courtesy of the University of Modena. *Bottom*: The photocurrent with varying opposing bias was differentiated to obtain the energy distributions.

4.3.5 Conclusions

The results from a series of surface measurements, carried out by the surface science group at the University of Modena, have been collated and discussed. Gold, iridium and $Au_{0.7}Pt_{0.3}$ alloy surfaces were studied and it has been found that:

- Every gold surface produced at least some photoelectrons, even after annealing or exposure to UV or X-rays.
- Iridium was found to produce almost no photoelectrons when illuminated with 254 nm light while the $Au_{0.7}Pt_{0.3}$ alloy was found to have a quantum yield roughly equivalent to gold.
- For the gold surfaces, significant variations in work functions and quantum yields have been observed for surfaces that should nominally be identical.
- The range in the measured gold work functions were 3.6 eV to 5.1 eV and for the quantum yield 0.8×10^{-6} to 5.9×10^{-5}.
- The variable presence of carbonaceous contaminants on the surface, resulting from exposure to air, appear to be the cause.
- The exact photoelectric properties for the flight surfaces will be very difficult, if not impossible to predict, due to the extreme sensitivity to the level and composition of contamination.
- Annealing at 130 °C will not completely clean the surfaces, though will slightly alter the photoelectric properties but not in a controlled or consistent way.
- The amount of variation seen is enough to completely change the behaviour of the discharge system.
- At the time of writing a new test campaign has just begun at the Institut fur Technische Thermodynamik, Stuttgart. The aim is to study the affect of temperature on the quantum yield and perform measurements in a more controlled way than possible at the Modena facility.
- It seems likely this variation is something we will have to live with for Pathfinder and its possible effects will have to be mitigated against.

4.4 Gold Reflection Measurements

Within the current inertial sensor flight design over 97 % of the surfaces will be gold coated while for the two pendulum setups discussed in Chapter 3, all the surfaces were gold coated. In order to better understand the discharging processes and allow for improved modelling of the system, the reflective properties of these gold coatings at 254 nm need to be well understood.

The optical properties of gold are well studied within the literature but few measurements exist at the desired wavelength of 254 nm. The measurements that do exist show some variation and state that the conditions of surface preparation as well as surface roughness can effect the measured optical properties, (Thèye, 1970). The level of surface contamination is also considered to affect the measured optical properties of gold, (Pells and Shiga, 1969). The two measurements that are most relevant for our purposes are those made by Johnson and Christy (1972) and those presented in the handbook of optical constants (Palik and Ghosh, 1998), based on original work by Thèye (1970).

Johnson and Christy (1972) measured the refractive index for gold in the 0.5-6.5 eV spectral range by making reflection and transmission measurements on vacuum evaporated gold films. These films ranged in thickness from 250-500 Å. The thickness range is limited as they state that results become inconsistent below 250 Å and their method of measuring transmission fails above 500 Å. Nevertheless, they reference work by Reale (1970) that shows that thin films above 200-300 Å exhibit the same optical properties as the bulk material. Johnson and Christy (1972) also attempt to examine the effect of surface contamination by repeating the measurements after annealing a gold sample in a nitrogen atmosphere at 150 °C for 9 hours. The results were consistent with the pre-annealed measurements within experimental uncertainties. This should be countered by mentioning Pells and Shiga (1969) who state that for a gold surface to be atomically clean it needs to be heated to 550 °C in an ultra-high vacuum. This will not be possible with the actual inertial sensor surfaces as the maximum bake-out temperature will be approximately 130 °C.

Similar measurements are described by Thèye (1970) for gold in the 0.5-6.0 eV spectral range. This work involved thin, semi-transparent films with a thickness range of 100-250 Å. These measurements lead to a refractive index that is slightly different to that obtained by Johnson and Christy (1972), but as they mention, this could be due to the small thickness of their samples. The samples studied were annealed in a vacuum at $\sim$ 150 °C.

The inertial sensor gold surfaces are exposed to air during assembly and will

spend considerable time in storage; as such some level of contamination is inevitable. This was confirmed by the Modena measurements discussed in Section 4.3. There was concern that the presence of these contaminants could alter the gold's reflection properties. In addition, the sensor gold coatings are several microns thick, which again could cause their properties to deviate from the literature values. Given that the gold surfaces are so important it seemed prudent to experimentally verify their properties. A further benefit of such measurements is they allow the effect of surface roughness on the angular distribution of the reflected light to be examined. With these points in mind I carried out a series of measurements in January 2010 to determine the reflectivity of flight representative gold surfaces.

4.4.1 Experimental Setup

The experimental setup was developed by Dr Claudio Silva at the University of Coimbra, Portugal, and was previously used to measure the reflection properties of Polytetrafluoroethylene, PTFE, that is used within a dark matter particle detector, (Silva et al., 2007). The setup consisted of a large rectangular vacuum chamber approximately 100 cm by 50 cm by 40 cm, which was light sealed from the surrounding environment. For the results described here the vacuum chamber was not evacuated and all measurements were performed in air at room temperature and pressure within a standard laboratory environment. Under these conditions air causes very low attenuation of light from 2200-5500 Å, only ~ 0.2 % is lost at 2500 Å traversing 1.0 m of air at standard temperature and pressure, (Baum and Dunkelman, 1955). The chamber housed the light source, motorised surface mount and motorised photomultiplier tube, PMT, and their configuration is shown in Figure 4.5.

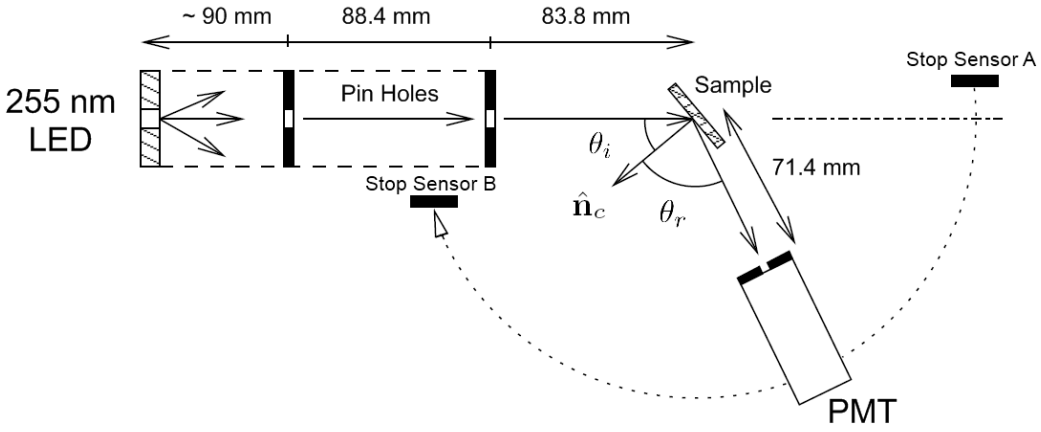

Figure 4.5: The experimental setup that was used for the reflection measurements. A UV LED mounted within a light sealed tube was used as the light source. As the light travelled down the tube it passed through two adjustable pin holes which acted to collimate the beam. The beam was then incident upon the sample and the reflected light detected by the PMT. The angle of the sample with respect to the beam was varied in order to measure different angles of incidence. Note the locations of the stop sensors, which acted as safety precautions for the PMT stepper motor, as well as a positional reference. This figure was adapted from one used in Silva et al. (2009).

A UV LED acted as the light source and a collimated beam was produced using a light sealed tube and two adjustable pin holes. The first pin hole was set to a diameter of 1.6 mm. Initially the second pin hole was set to 1.9 mm but after the first few measurements it was reduced to 1.3 mm in order to reduce the beam diameter. Each pin hole, the light source and the sample holder were mounted on an optical bench within the chamber and the relative heights of each component were varied in order to attain good alignment. The setup also employed three stepper motors; two to adjust the position of the sample and one to vary the position of the PMT. The sample could be moved vertically into and out of the incident beam allowing the beam to be calibrated between measurements. Additionally, the sample's second stepper motor allowed the angle of incidence with respect to the beam to be varied. The PMT was attached to a rigid arm that rotated around the centre of the samples surface and had a slit with a width of 1 mm at its entrance so as to limit the angle of accepted light. The PMT was operated in photon counting mode throughout the measurements described.

The stepper motors were controlled by a program written in C for Virtual Instrumentation (CVI) and run on a desktop PC. This allowed the chamber to be sealed and measurements made at various angles without the need to continually

open the chamber. Other than the sample under investigation, nearly every surface within the chamber was covered with black felt in order to minimise stray reflections.

4.4.2 Light Source

Ideally, the filtered output from one of the mercury lamps used within the charge management device would have been used as the light source for the measurements. Unfortunately due to the construction of the vacuum chamber and the high voltage supply necessary to drive the lamps, this was not possible in the time scale available. Instead, a commercial UV-LED supplied by Seoul Semiconductor Ltd was used. According to its data sheet it has a peak wavelength at 255 nm and a full width half maximum of 15 nm, where Figure 4.6 shows its spectrum. The LED used was the same as those which will be discussed in Chapter 6. The previously discussed literature suggests that the variation in reflectivity of gold at normal incidence for 254 nm and 255 nm is less than $\sim 0.2\%$. Indeed, the literature values themselves vary by $\sim 1.5\%$ at 254 nm. The LED spectrum is broader than the mercury 254 nm line and the literature suggests that gold is $\sim 2\%$ less reflective at 245 nm and $\sim 2\%$ more reflective at 265 nm.

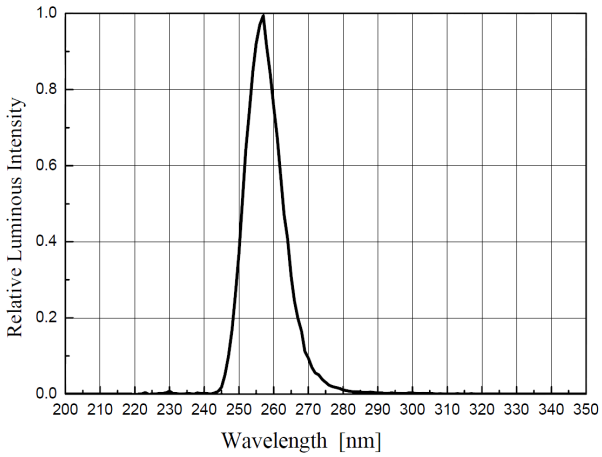

Figure 4.6: Shows the spectrum of the LED used for the measurements at $T = 25°C$ and $I = 20mA$, as given by the LED data sheet, (Seoul Semiconductor Ltd, 2006).

4.4.3 Gold Samples

Two gold coatings were studied at Coimbra, one on a sapphire substrate and one on quartz. They were produced around 18 months prior to the measurements being made as witness samples for the actual coating runs for the replica test mass and housing used at the four-mass torsion pendulum experiment. The same sapphire sample, Lot Number 8L09P1, was measured at Modena. While the electrodes for Pathfinder will have sapphire substrates both surfaces described here should be

representative as the gold coatings are predicted to be of the order of a few microns thick, therefore taking the bulk properties of gold. Although the underlying substrate can effect the surface roughness both are predicted to have a root mean squared surface roughness less than 10 nm which is also a requirement for the flight electrode surfaces.

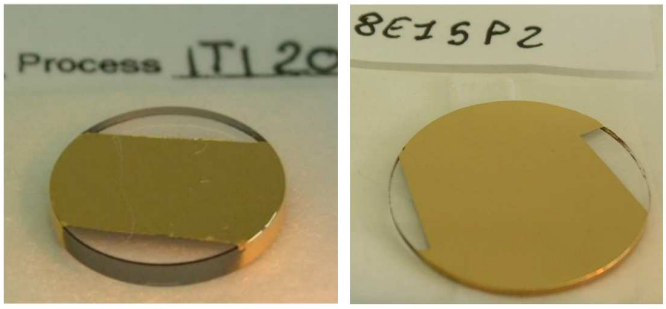

Figure 4.7: *Left*: Gold on sapphire substrate, Lot Number 8L09P1. *Right*: Gold on quartz substrate, Lot Number 8E15P2.

Figure 4.7 shows photos of the two surfaces that were studied. The sapphire substrate had a diameter of 15 mm whereas the quartz substrate had a diameter of 25.4 mm. The samples were both stored and transported in sealed bags of air within a protective optical cloth. A visual inspection of the samples prior to measurement revealed both to appear mirror like. The larger quartz sample had no visually observable defects whereas the sapphire sample had several very minor scratches across the surface. These defects were extremely faint, only covering a small proportion of the total surface, less than a few percent, and were probably caused during transportation or storage rather than manufacture. The samples were each carefully mounted on a rectangular piece of perspex ($\sim$ 40 mm by 30 mm by 10 mm) using double sided *Kapton* tape on the back of the samples. The perspex was in turn mounted within the vacuum chamber on the sample holder. The substrates were handled wearing latex gloves and every care was taken not to touch the actual gold surfaces.

4.4.4 Calibration

Before any measurements could be made the system needed to be aligned and calibrated. The alignment was performed using a red visible laser in place of the UV LED. This made it possible to see the variation in beam size as the two pin holes were adjusted and confirm that the spot size was considerably smaller than the gold surface. It also made it much easier to check that the surface was perpendicular to the beam by making sure the reflected beam was in the same plane as the incident beam. The UV LED was then installed and with the sample raised, background

counts were checked for a range of angles. The background was typically between 1 and 5 photons per second, much lower than the signal to be measured, and seemed to be independent of angle. While the actual measurements were taken, an additional check was performed for large angles of incidence, greater than $\sim 60°$. This involved not only measuring the reflected beam but also scanning behind the sample itself to make sure that the elongated area of beam incidence was not larger than the sample. By doing this a limit on the maximum angle of incidence that could be reliably measured was set at $\sim 80°$ for both samples. The lowest angle it was possible to measure was limited to $\sim 20°$ due to the position of the incident beam and the size of the PMT.

4.4.5 Experimental Method

After the sample was mounted, and the system aligned and calibrated, the chamber was sealed. Before each angular measurement the direct beam properties were measured. This involved raising the sample out of the beam path and scanning the PMT through the un-reflected beam. All measurements described here were taken with PMT steps of 0.5° and data collected for 25 seconds at each PMT position. The angular position of the PMT was measured with respect to stop sensor A, Figure 4.5. The measurement process was automated once the initial commands were sent to the stepper motors and the results were saved in an ASCII file.

Once the direct beam had been measured the sample was lowered into the beam and was rotated to the desired angle of incidence. The PMT then measured the reflected beam in the same way. This set of measurements were then repeated for a range of incident angles and for both samples. By comparing the beam measurements before and after reflection the amount of light absorbed by the surface could be obtained and the sample's optical properties calculated.

4.4.6 Data Analysis

In order to quantify the beam properties a model is introduced which was developed by Silva (2010). It includes several physical parameters and assumes specular reflection. The function used to fit the data arises by considering a uniform circular beam of radius r and that the PMT is only able to view part of this beam through a slit of width ω at a distance from the sample of 71.4 mm, Figure 4.5. The slit width can be defined by its aperture angle η, where $\eta = \arctan\left(\frac{\omega/2}{71.4}\right)$ and the circular beam by its aperture angle ε, where $\varepsilon = \arctan\left(\frac{r}{71.4}\right)$. Integrating between $\pm\eta$ at a given position on the circle gives the intensity I, the PMT detects at a given angular

position:

$$I = \frac{\Phi_i}{\pi\varepsilon^2}\left[\theta\sqrt{\varepsilon^2-\theta^2} + \varepsilon^2 \arctan\left(\frac{\theta}{\sqrt{\varepsilon^2-\theta^2}}\right)\right]_{\theta_{min}}^{\theta_{max}} \tag{4.1}$$

$$\theta_{max} = \theta - \Delta + \eta$$

$$\theta_{min} = \theta - \Delta - \eta$$

where θ is the angle between the stop sensor A and the centre of the PMT slit, Δ is the angle of maximum intensity and Φ_i is the total intensity of the beam. All angles are measured from stop sensor A and are relative to the centre of the sample which the PMT revolves around. For all the measurements described here the slit width was fixed at 1 mm which gives a value of $\eta = 0.4°$. This left three remaining parameters to vary in order to fit Equation 4.1 to the data.

A minimising χ^2 fit was performed on each set of readings with an estimate of the random error in the stepper motor position of $0.05°$ and a $\sqrt{N}$ error in the photon counting. Only data recorded above the background noise was included in the fit as the function goes to zero outside the peak. Figures 4.8 and 4.9 show examples of the fits. There was a slight underestimate in the tails of the distributions but the function generally fits the observed data well for both the incident and reflected beams giving reduced χ^2 values ranging from ~ 0.5 to ~ 12.

While in theory the direct beam parameters should stay the same between measurements this was not always the case. Every time the experiment was turned off, either at night or to make adjustments to the setup, the LED intensity had to be set, leading to variation between measurements. The variation in beam centre and diameter can be put down to adjustments made to the setup during the experiment. For example after the first day the second pin hole was reduced in size and this was seen clearly in the parameter ε obtained for those fits. Allowing for these variations, the direct beam measurements that were taken in the same run show consistent parameter fits, as to be expected. This is especially true for the quartz substrate measurements which were taken after the setup had reached a settled configuration.

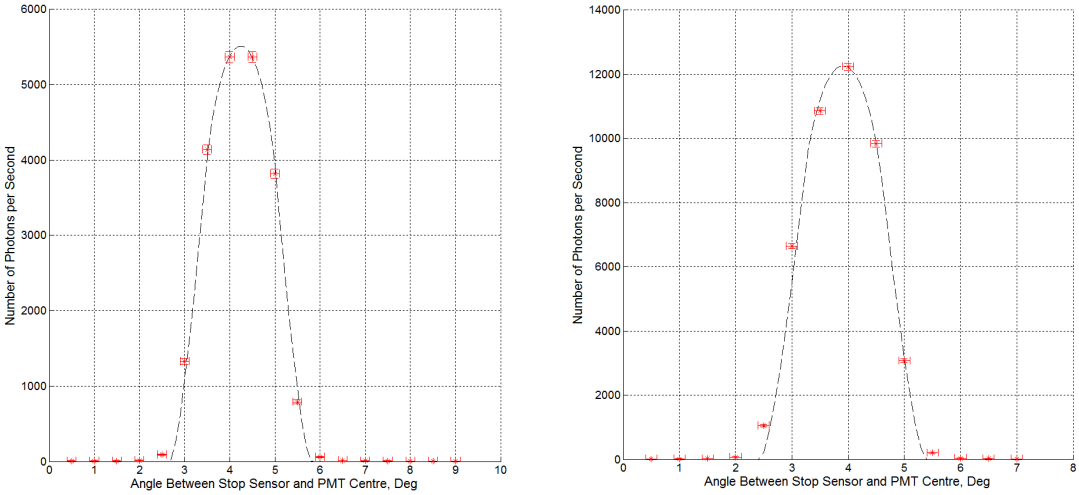

Figure 4.8: Shows two examples of best fits to the direct beam. The variation in beam intensity is because the LED current was set using an analogue dial every time the setup was turned on and off. The position of the peak varied when the experiment was adjusted while setting up and calibrating.

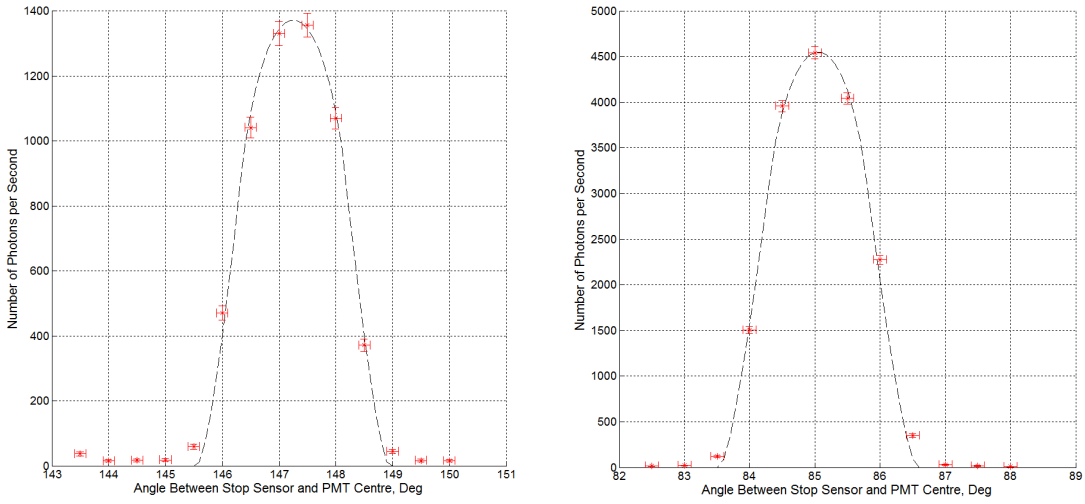

Figure 4.9: *Left*: The reflected beam from the quartz substrate with an angle of incidence of 20°. *Right*: The reflected beam from the quartz substrate with an angle of incidence of 50°. Note in both cases the reflection beam shows very specular behaviour.

Visually, the reflected beam data appeared to be fairly specular but the fitted aperture angles ε showed a small increase between the incident and reflected beam. The average aperture angle obtained for the direct beam measurements for the quartz sample was $1.071 \pm 0.008°$. This gives a beam radius at the PMT of $71.4 \tan \varepsilon = 1.335 \pm 0.010$ mm, just over twice the radius it left the second pin hole with. This suggests that the approximately collimated beam actually spread with an angle of $\sim 0.25°$ which agrees well with a theoretical spread of the beam of $\sim 0.21°$ if the LED is treated as a point source. The reflected beam on the other hand had an average aperture angle of $1.142 \pm 0.021°$ giving a radius of 1.423 ± 0.026 mm. This increase could have been due to the misalignment of the sample causing the reflected beam to travel further than the directly measured beam. As the beam was not perfectly collimated the further the distance the more the spread. Given this small angular spread of the incident beam though, the increased radius of the reflected beam cannot be completely explained by misalignment. Instead, it suggests that reflection from the gold surface was not perfectly specular but the surface roughness must be very small, which is consistent with the predicted root mean squared surface roughness of less than 10 nm. The effect of surface roughness will be discussed further in Chapter 5.

By dividing the total intensity (Φ_i) of the beam after reflection by the total intensity before reflection one can obtain the fraction of light reflected by the surface at a given angle of incidence.

4.4.6.1 Fresnel Equations

The reflection of light as it passes the boundary between two different media is described by the Fresnel equations. As well as being dependant on wavelength, refractive index and angle of incidence, the amount of light reflected is also dependant on polarisation. For s-polarised light the reflection coefficient is given by:

$$R_s = \left[\frac{N_1 \cos(\theta_i) - N_2 \sqrt{1 - \left(\frac{N_1}{N_2} \sin(\theta_i)\right)^2}}{N_1 \cos(\theta_i) + N_2 \sqrt{1 - \left(\frac{N_1}{N_2} \sin(\theta_i)\right)^2}} \right]^2 \tag{4.2}$$

where θ_i is the angle of incidence and N is the refractive index of the medium. For p-polarised light the reflection coefficient is given by:

$$R_p = \left[\frac{N_1 \sqrt{1 - \left(\frac{N_1}{N_2} \sin(\theta_i)\right)^2} - N_2 \cos(\theta_i)}{N_1 \sqrt{1 - \left(\frac{N_1}{N_2} \sin(\theta_i)\right)^2} + N_2 \cos(\theta_i)} \right]^2 \tag{4.3}$$

If the incident light is un-polarised, as the LED light should be, the reflection coefficient is given by combining the two polarisations:

$$R = \frac{(R_s + R_p)}{2} \tag{4.4}$$

The refractive index for air at 254 nm was taken to be $N_1 = 1.00030041$ which is the literature value for dry air at 15 °C, 101.325 kPa and with 450 ppm CO_2 content, (Ciddor, 1996). This value shows very minimal variation at 254 nm for reasonable changes in environmental conditions. It is important to note that for a metal, like the gold surfaces that were studied, the complex index of refraction is used:

$$N_2 = n + i\kappa$$

where n is the refractive index and κ is the extinction coefficient. A χ^2 fit was performed in order to obtain the parameters n and κ for the gold surfaces under consideration. Figure 4.10 shows the fits for both the sapphire and quartz substrates.

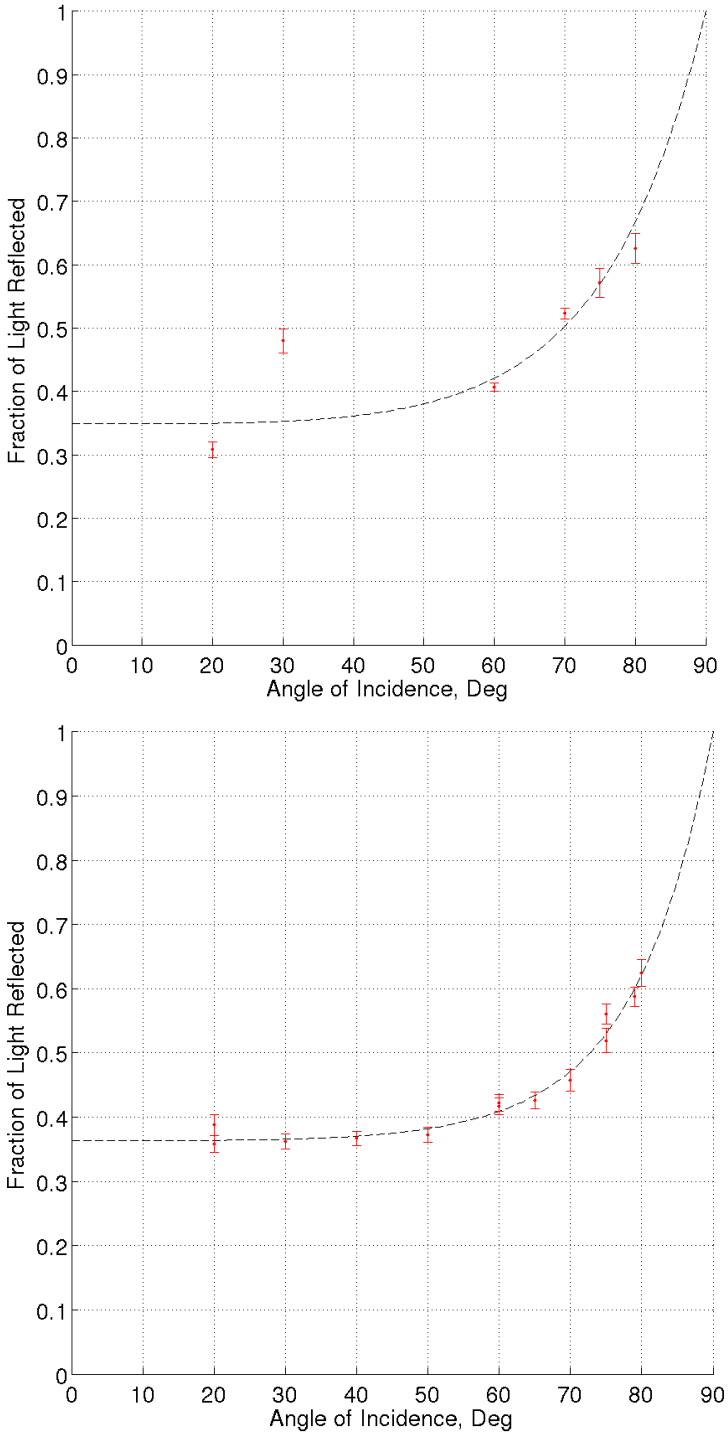

Figure 4.10: *Top*: A χ^2 fit for the sapphire substrate data using the Fresnel equations. *Bottom*: A χ^2 fit for the quartz substrate data using the Fresnel equations. All data points have 1σ error bars derived from fitting Equation 4.1 to the raw data. Problems encountered during the sapphire measurements are discussed in Section 4.4.7.

4.4.7 Results

The fits to the Fresnel equations are excellent for the quartz substrate with a reduced χ^2 value of 1.03, but poor for the sapphire substrate with a reduced χ^2 value of 22.4, Figure 4.10. The individual measurements for the sapphire substrate, particularly at low angles, do not seem to be consistent within the experimental error. At the time there was concern that the incident beam was slightly larger than the gold surface being illuminated for the sapphire substrate, distorting the results. This was due to the smaller surface area of sapphire sample in addition to it being measured at the start of the experiment when the setup was still being adjusted and the size of the beam optimised. The sapphire results also suffer from having fewer measurements which was due to the limited time available, as well as a decision made to concentrate on the quartz sample as its larger surface area offered more reliable results. For what it is worth, the complex refractive index parameters for both fits are in moderate agreement with each other. The refractive index parameters obtained with the quartz measurement agrees within experimental error with the more relevant Johnson and Christy (1972) study. A comparison of results are shown in Table 4.3 and in Figure 4.11.

Source	n	κ
Johnson and Christy (1972)	1.33 ± 0.02	1.688 ± 0.007
Thèye (1970)	1.493	1.707
Sapphire Substrate	0.976 ± 0.027	1.447 ± 0.032
Quartz Substrate	1.296 ± 0.038	1.696 ± 0.027

Table 4.3: Comparison between the measurements made here to previous results. The results also include a 1σ confidence limit on each parameter. Note, no error was provided by Thèye (1970).

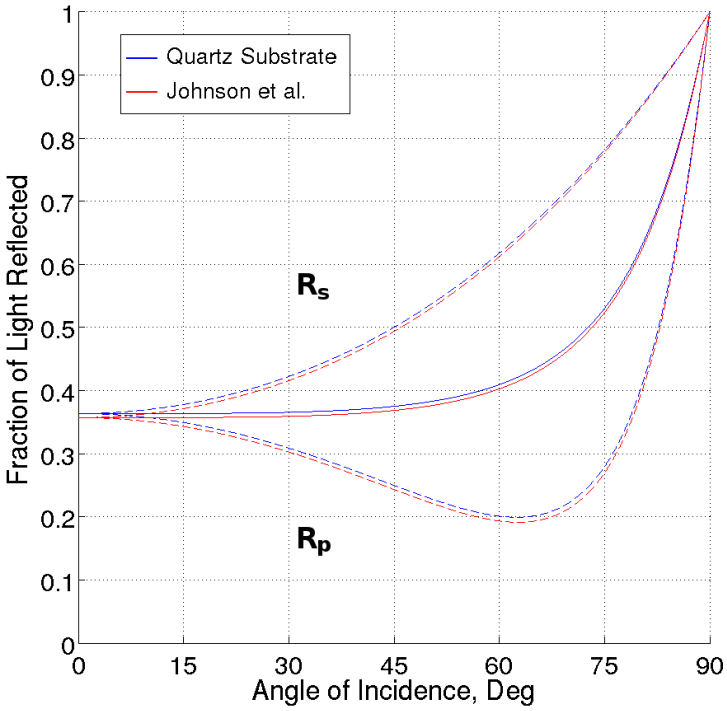

Figure 4.11: Comparison between the 254 nm reflectivity curve obtained from the measurements on the gold coated quartz substrate to those of Johnson and Christy (1972). The curves are generated from the Fresnel equations and the refractive indices given in Table 4.3. The two polarisation components (R_s and R_p) are also plotted.

Given that it is the reflectivity curve for gold that is of interest, it is reassuring to see excellent agreement between the one measured here for the quartz substrate and the results of Johnson and Christy (1972), Figure 4.11. The values given in the handbook of optical constants are originally based on work carried out by Thèye (1970). As discussed previously, these measurements used thin, semi-transparent films which could explain the difference compared to the bulk properties of the measured quartz substrate as well as Johnson and Christy (1972) measurement.

4.4.8 Conclusions

By carrying out reflectivity measurements for flight representative gold coatings, on substrates equivalent to the inertial sensor electrodes, we were able to learn that:

- The production processes for the gold coatings used within the inertial sensor give reflective properties at around 254 nm that are in good agreement with literature values.
- Any surface contamination present does not cause significant variation in the reflection properties.
- The reflected beams were very specular suggesting a small roughness for the flight electrode surfaces, as expected.
- We can be confident in the reflection properties for the electrode and test mass face surfaces which combined make up over 65 % of the total surface area of the inertial sensor.

4.5 ISUK Light Cone Distributions

In order to better understand the discharging behaviour and to aid simulation it was necessary to experimentally measure the output light cone distributions from the ISUKs at 254 nm. Although the ISUKs used at the four-mass torsion pendulum are the same as those that will be used in flight, the fibre optic harness (FOH) that routes the UV light from the mercury lamps to the ISUKs are different. It was suspected that this could lead to differences in the distribution of the light output from the ISUKs and the following describes measurements that I carried out in February 2011 for the two configurations.

4.5.1 Experimental Setup

With the exception of the particular fibre used, the experimental setup was the same for both cases. It consisted of an ISUK, as described previously in Section 3.1.3, which along with the other experimental components, was mounted on an optical bench. The ISUKs are essentially 1 mm diameter, 67.3 mm long optical fibres housed within a custom-made titanium vacuum feedthrough. A clamp which held the ISUK $\sim$220 mm above the optical bench was adjusted so as to align the ISUK output tip with the photodiode used to make the measurements. Theoretically, the light cone emanating from the ISUK should have a angle related to the fibres numerical aperture, which is 0.22 ± 0.02, leading to an emission angle of $\arcsin(0.22) = 12.71\pm1.20°$. This angle is defined in the literature as that which contains 95 % of the the emitted light, (Ghatak and Thyagarajan, 1998).

A mercury lamp of the same type to be used in flight and previously described in Section 3.1.1.1, provided the UV light source. The lamp's light output passed through an optics barrel, again the same as used in flight, which filtered out the non-254 nm spectral lines and then focused the light into the end of the attached optical fibre. The other end of the fibre was attached to the ISUK, both ends using SMA connectors.

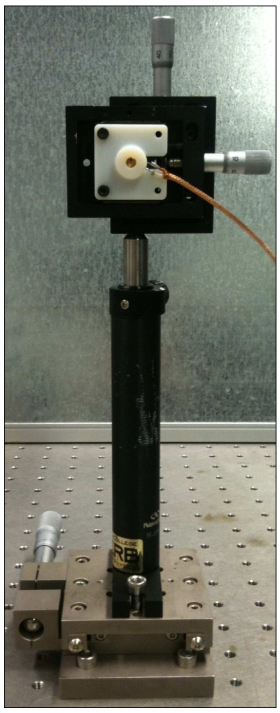

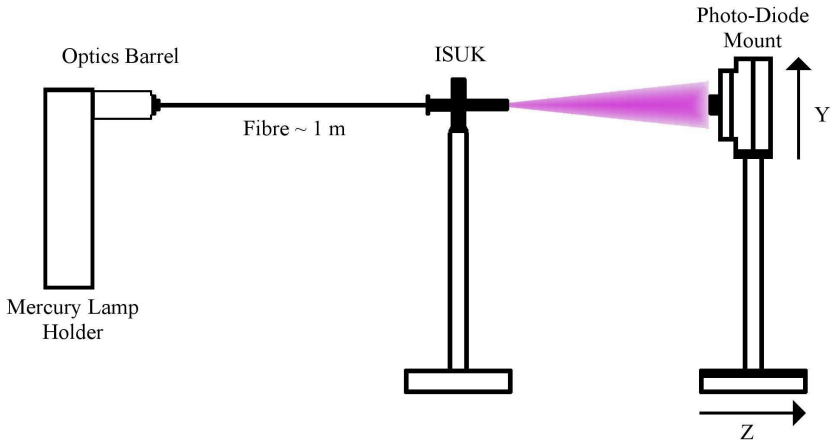

Figure 4.12: *Left*: A photograph of the 3 stage translational mount that held the photodiode, which is also visible. *Above*: A diagram showing the experimental setup used to measure the ISUK light distributions with the single core fibre.

The output UV intensity was measured at a particular position with a commercial silicon carbide photodiode (JEC 0.1S) which had excellent UV sensitivity in the range 210-380 nm, (Laser Components Ltd, 2011). Its small active area of just 0.055 mm^2 made it ideal for these measurements. The photodiode output was fed into an external transimpedance amplifier and then to a PC running a custom LabVIEW program via a 24-bit analogue to digital converter. This allowed the output voltage signal to be recorded as the incoming UV intensity varied with position. The photodiode was mounted on 3 combined translational stages allowing its position to vary in x, y and z, via adjustable spring loaded micrometer screws. An additional photodiode of the same type was mounted within the lamp holder in order to monitor the lamps output. The signal from this fed into LabVIEW in the same way via a separate transimpedance amplifier. Figure 4.12 shows a photograph of the photodiode attached to the translational stages and a diagram showing the position of the rest of the components.

4.5.1.1 Optical Fibres

Two different optical fibres were used in the measurements. The first was the same as that used in the torsion pendulum experiment which is a single, 600 μm diameter core fibre, with a metallic sleeve. The measurements discussed here for the single core fibre were made with the ~1 m long fibre being held completely straight between

the mercury lamp's optics barrel and the ISUK. In addition, a check was made by creating two circular bends in the fibre. Measurements made with bends in the fibre were consistent with the straight fibre results.

The second fibre used was the same as that which will be used in flight, the so called FOH, described in Chapter 3, Section 3.1.2. It is a multi-core fibre made up of a bundle of 19 individual, 200 μm diameter cores, within a polyether-ether-keytone (PEEK) sleeve. In order to make the measurements as flight representative as possible, two separate multi-core fibres were used, connected together via an SMA connector as will be the case in flight. It had a combined length of $\sim$2 m and was attached to a base plate with a bend configuration similar to that of in flight, which is shown in Figure 4.13.

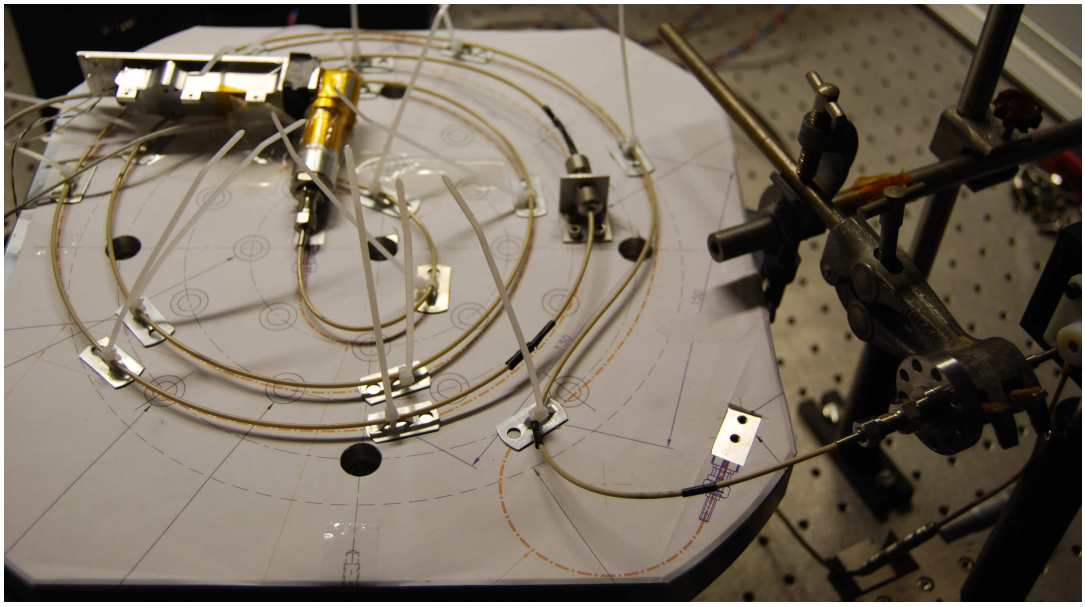

Figure 4.13: A photograph of the configuration used for the multi-core measurements. The holder containing the mercury lamp and the attached optics barrel are seen at the top left with the ISUK at the bottom right.

4.5.2 Experimental Method

Once the setup had been aligned, measurements were taken separately for each fibre. This involved manually scanning through the centre of the UV light cone emitted from the ISUK tip in both x and y. These sets of measurements were repeated at three separate positions in z. The absolute distance between the ISUK tip and the sensitive part of the photodiode was difficult to measure accurately, but for the first set of readings a value of 4.0 ± 0.25 mm was obtained. However, the relative distance

between subsequent measurements was well defined with the z translational stage giving the distance to the nearest ± 0.005 mm.

A small systematic error was present in the experiment because it was the projection of the light cone onto a 2D plane, rather than the intensity at a fixed distance from the source, being measured. Given that 95 % of the emitted light from the ISUK was expected to be within just 12.71°, giving $\cos(12.71) \approx 0.9755$, it should have had a fairly small effect and was ignored during analysis.

4.5.3 Results

The measured light distributions are shown for the single core fibre setup in Figure 4.14 and the multi-core fibre setup in Figure 4.15. The effect of the variation in the mercury lamp's output has not been considered as it was stable between measurements. The error bars for each point are plotted but are too small to see clearly.

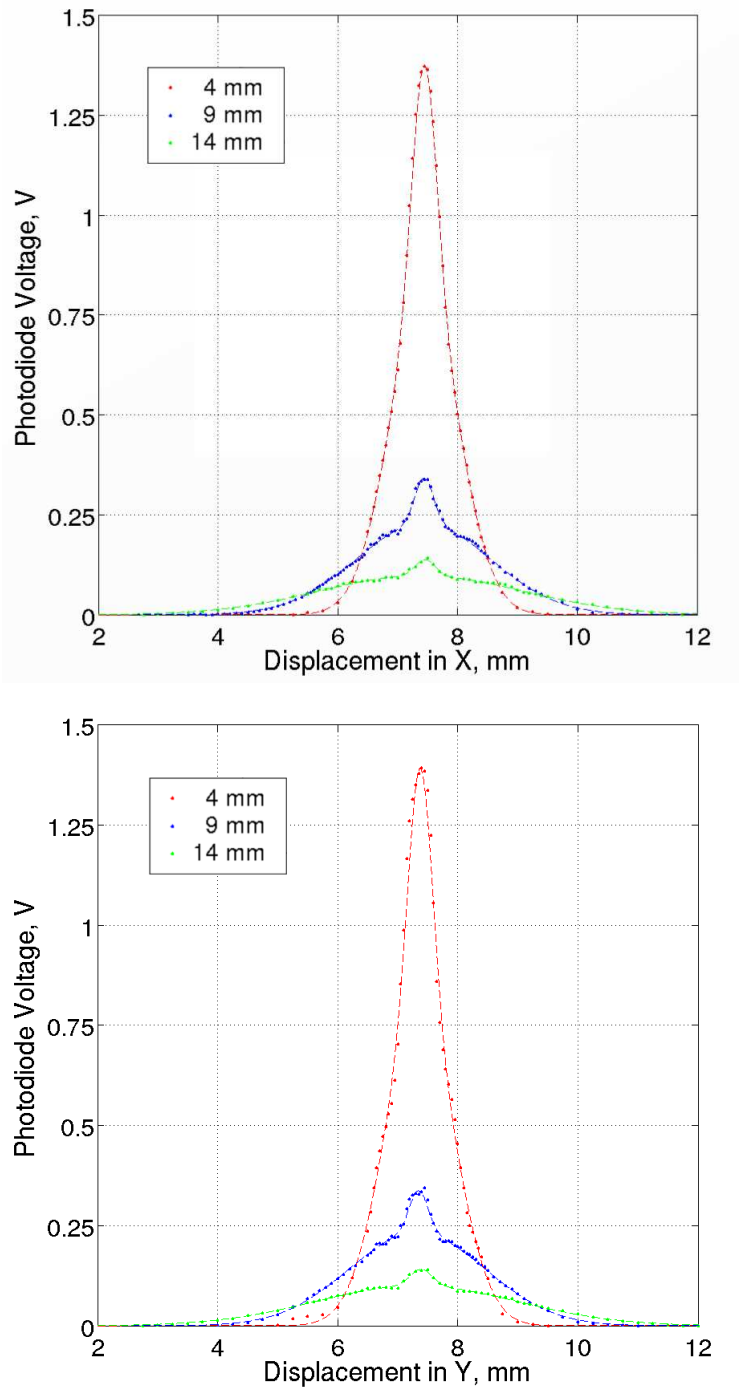

Figure 4.14: The measured light distributions for the single core fibre setup. The horizontal measurements are shown at the top and the vertical ones at the bottom. Measurements were taken with increasing distance from the ISUK tip, each set being 5.000 ± 0.005 mm apart, though as will be discussed, the absolute distance from the fibre could not be measured as accurately. The results of fitting a linear combination of two Gaussians to each curve are also plotted as curves.

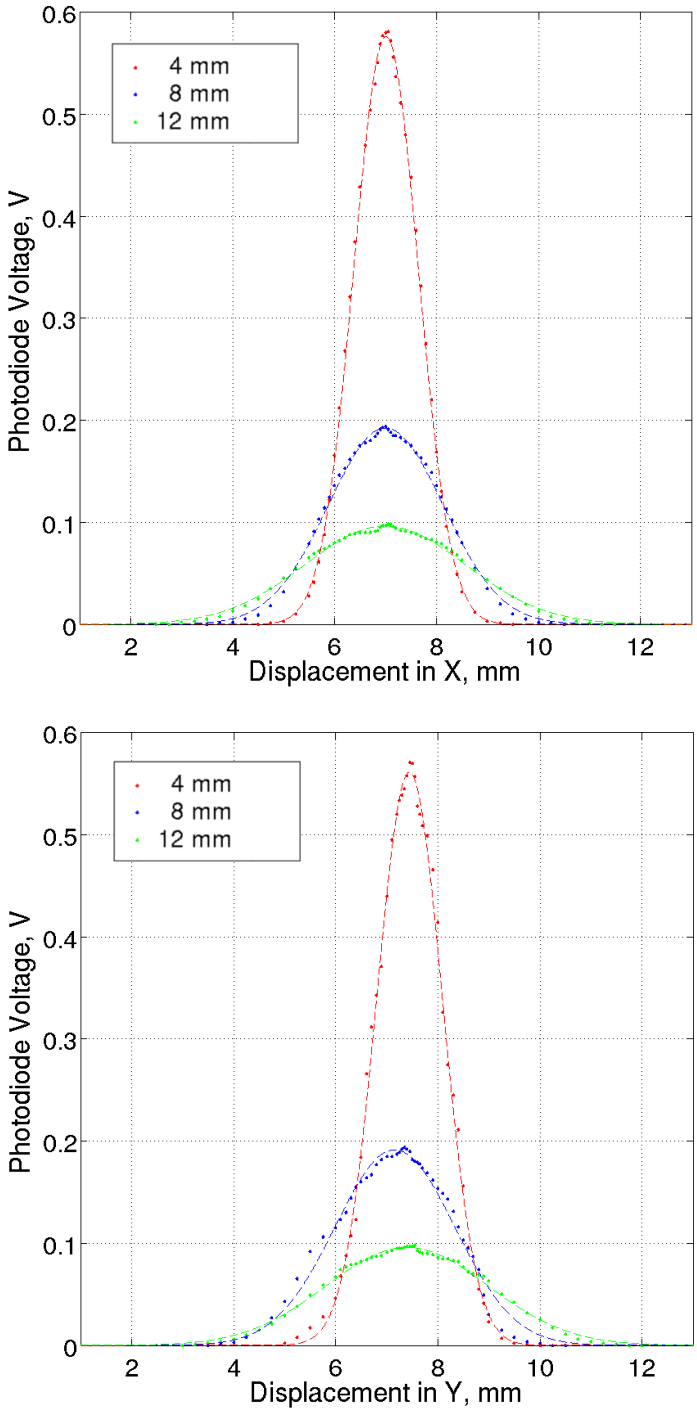

Figure 4.15: The measured light distributions for the multi-core fibre setup. The horizontal measurements are shown at the top and the vertical ones at the bottom. Measurements were taken with increasing distance from the ISUK tip, each set being 4.000 ± 0.005 mm apart, though as will be discussed, the absolute distance from the fibre could not be measured as accurately. The results of fitting a single Gaussian to each curve are also plotted as curves.

4.5.3.1 Single Core Fibre

The measured distributions for the single core fibre setup appeared to consist of two components and it was found that a linear combination of two Gaussians produced good fits to the data. Interestingly, the measured distribution seemed to have a fairly sharp central peak on top of a broader component. This was confirmed by the parameters obtained from performing a minimising χ^2 fit between the data and two Gaussians of the form:

$$f(x) = A_1 e^{-\frac{(x-\mu_1)^2}{2\sigma_1^2}} + A_2 e^{-\frac{(x-\mu_2)^2}{2\sigma_2^2}} \tag{4.5}$$

where A_i is the amplitude, μ_i is the mean and σ_i is the standard deviation. The parameters obtained for the data are shown in Table 4.4.

Distance	Plane	A_1	μ_1	σ_1	A_2	μ_2	σ_2	Reduced χ^2
4 mm	x	0.5845	7.448	0.2021	0.7909	7.443	0.5714	3.88
4 mm	y	0.6076	7.376	0.2002	0.7844	7.361	0.5802	44.25
9 mm	x	0.1125	7.443	0.1542	0.2288	7.438	1.1253	10.71
9 mm	y	0.1049	7.348	0.1578	0.2322	7.329	1.1394	17.37
14 mm	x	0.0401	7.464	0.1621	0.0980	7.394	1.6951	6.35
14 mm	y	0.0412	7.399	0.1805	0.0998	7.317	1.6834	6.05

Table 4.4: The parameters obtained after fitting Equation 4.5 to the single core fibre data.

The μ_i values obtained from the fits suggest good alignment in x, with an average value of 7.438 ± 0.024 mm, as well as in y with a value of 7.355 ± 0.030 mm. This shows the central position of the beam stayed fairly constant as the detector was moved away from the ISUK tip. The other parameters obtained in both x and y are consistent with each other at each position, suggesting a symmetrical beam, as expected. The σ_1 values vary in a small though inconsistent way with increasing distance from the ISUK tip. This is likely due to the fitting algorithm being unable to cleanly separate this component at each distance. Meanwhile the σ_2 values increase steadily and consistently over the same range.

In order to quantify the angular spread of the measured light cone one can plot $2\sigma_2$ against the distance from the ISUK tip. Figure 4.16 shows this relation and as expected it is strongly linear.

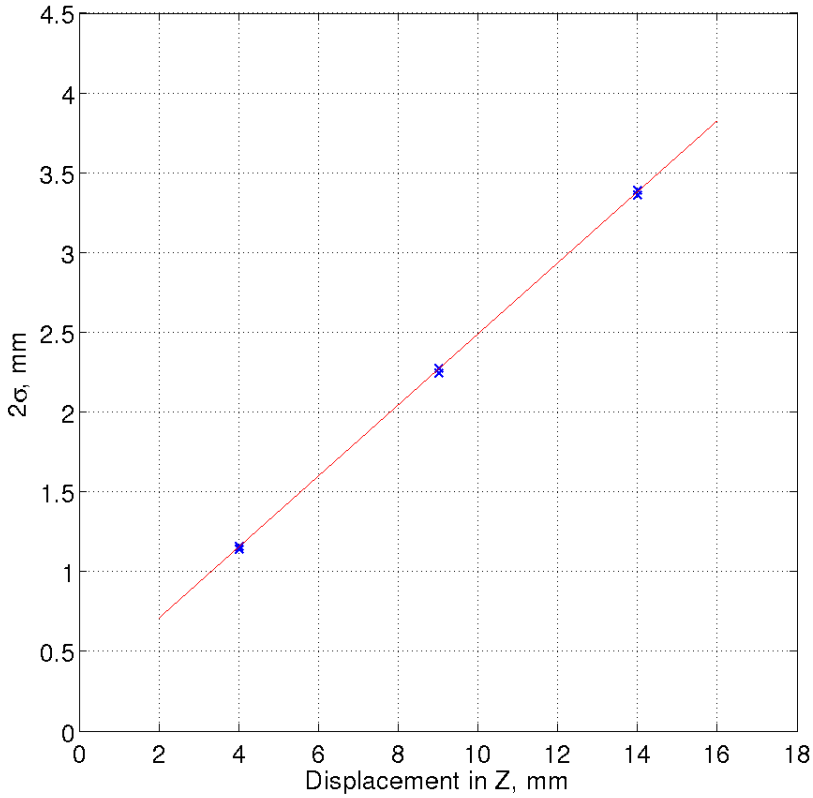

Figure 4.16: The relationship between the beam width and the distance from the ISUK tip for the single core fibre setup. The straight line that was fit to the data is also shown.

A straight line was fit to the data with the parameters found to be $m = 0.2227$ and $C = 0.2604$. This provided the gradient which in turn was used to estimate the emission angle of the beam, $\arctan(0.2227) = 12.55 \pm 0.08°$. This compares well with the theoretical emission angle for the ISUK of $12.71 \pm 1.20°$ discussed earlier. Also worth mentioning is a possible relation between the average width of the sharper component, $2\sigma_1 \approx 0.352 \pm 0.04$ mm and the radius of the single core fibre, 0.3 mm. This may suggest that the sharper component is produced by the optics barrel before the light enters the single core fibre and then propagates through before exiting the 0.5 mm radius ISUK unaffected.

To aid later modelling of the light source the distributions needed to be converted to angle. This was achieved by first using the fitted straight line to obtain an apparent point source for the light cone. This is the point where the line crosses the x axis and was found to be -1.1693 mm. The distance to this point in z was then used to convert each measurement in x and y to an angle θ. Upon normalising the area of each individual distribution to an area of one, the results were combined

and plotted, Figure 4.17.

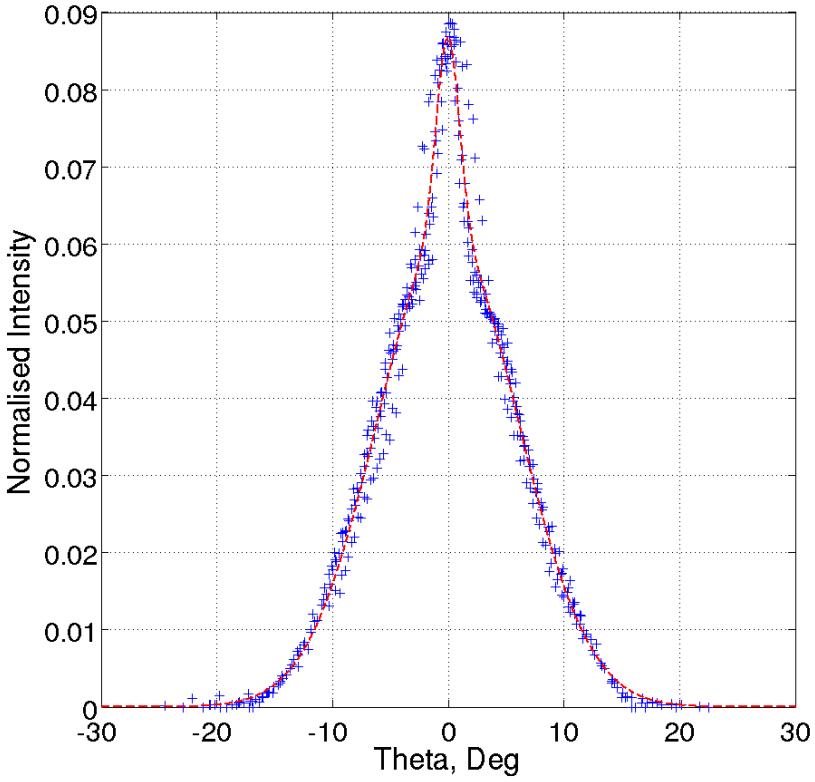

Figure 4.17: A plot of all the single core measurements converted to angle, θ. A linear combination of two Gaussians which was fit to the data is shown in red.

Reassuringly, the six individual measurements in x and y are in fairly good agreement when converted to θ, particularly the broader component. The final step was to fit a linear combination of two Gaussians to this new data, Figure 4.17. The function took the form:

$$f(\theta) = A_1 e^{-\frac{\theta^2}{2\sigma_1^2}} + A_2 e^{-\frac{\theta^2}{2\sigma_2^2}} \tag{4.6}$$

where A_i is the amplitude and σ_i is the standard deviation. The parameters obtained were $A_1 = 0.06157$, $\sigma_1 = 6.064$, $A_2 = 0.02513$ and $\sigma_2 = 0.9856$. A simulated light cone using these parameters will be compared to the measured data in Chapter 5.

4.5.3.2 Multi-Core Fibre

The measured distributions for the multi-core fibre setup are noticeably different to the single core ones but do show similarities, Figure 4.15. Like the single core setup, they are dominated by a disperse component but also show a central feature. This component is much smaller than in the single core case and it is assumed that it relates to the central fibre that makes up the multi-core bundle, which has a radius of just 0.1 mm. This central component was so small that it was felt that the entire distribution could be adequately fit by using a single Gaussian, while ignoring the central bump. The parameters obtained after fitting a single Gaussian to the data, while minimising χ^2, are shown in Table 4.5.

Distance	Plane	A_1	μ_1	σ_1	Reduced χ^2
4 mm	x	0.5766	7.011	0.6323	14.08
4 mm	y	0.5614	7.446	0.6432	48.53
8 mm	x	0.1925	7.005	1.1274	18.17
8 mm	y	0.1915	7.159	1.1722	74.01
12 mm	x	0.0963	7.002	1.5774	5.90
12 mm	y	0.0960	7.405	1.5894	7.44

Table 4.5: The parameters obtained after fitting a single Gaussian to the multi-core fibre data.

Like the single core results, the μ_1 values obtained from the fits suggest good alignment in X, with an average value of 7.006 ± 0.005 mm. The system was less well aligned in y with the measurement at 8 mm being noticeably offset. Subsequent checks, involving the switching of the x and y translational stages, showed that it was caused by the y translational stage sticking slightly. The measurement made in y at 8 mm is ignored in the rest of the analysis. The angular spread of the beam was then calculated in the same way as described before, Figure 4.18.

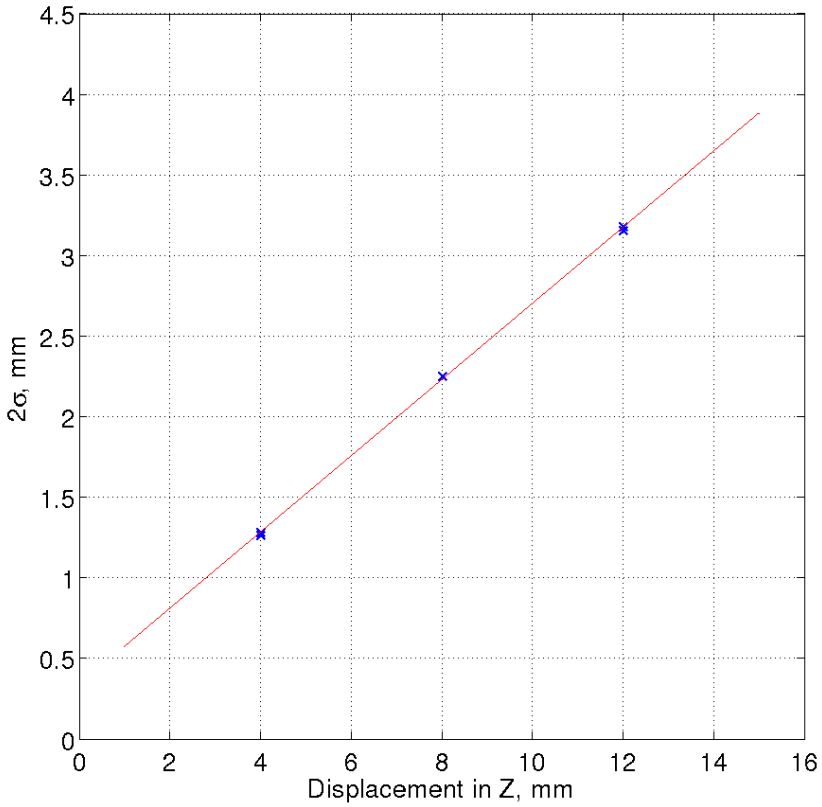

Figure 4.18: The relationship between the beam width and the distance from the ISUK tip for the multi-core fibre setup. The straight line that was fit to the data is also shown.

For the multi-core fibre setup the beams angular spread was calculated as $\arctan(0.2364) = 13.30 \pm 0.15°$. This is in fair agreement with the theoretical value but is probably a slight over-estimate as generally the fitted Gaussians are a little wider than the measured data as can be seen visually in Figure 4.15. Like with the single core measurements, a straight line fit, with $m = 0.2364$ and $C = 0.3365$, allowed the apparent point source position to be calculated as -1.4234 mm. The linear measurements were converted to θ as before and are shown in Figure 4.19.

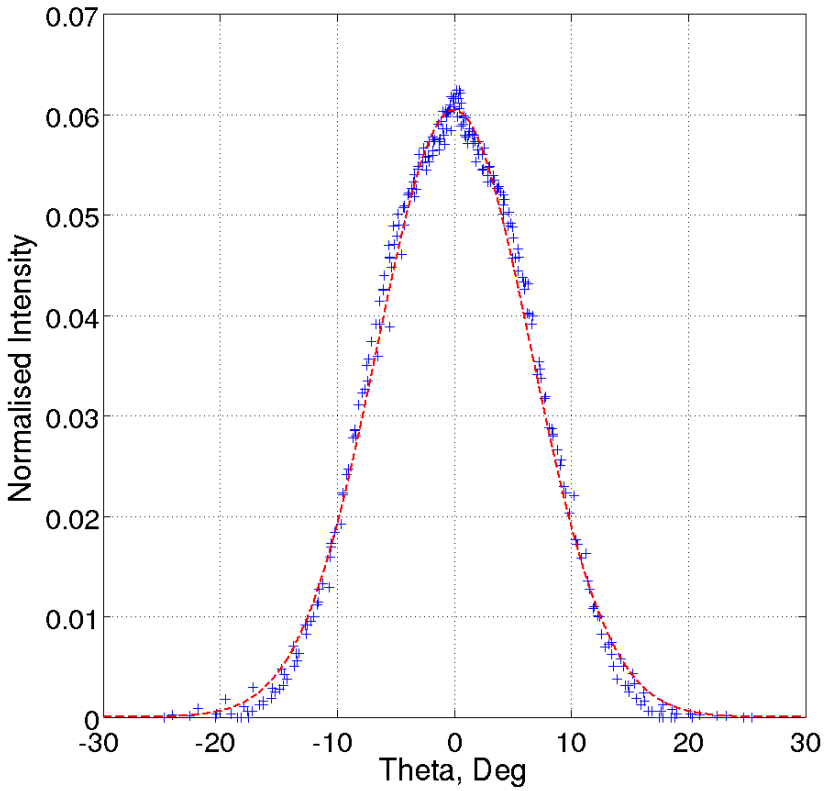

Figure 4.19: A plot of all the multi-core measurements converted to angle, θ. A single Gaussians which was fit to the data is shown in red.

This time a single parameter Gaussian was fit to the data, Figure 4.19. The function took the form:

$$f(\theta) = \frac{1}{\sqrt{2\pi\sigma^2}} e^{-\frac{\theta^2}{2\sigma^2}} \tag{4.7}$$

A value of $\sigma = 6.595$ was found and will be used to simulate the UV distribution in Chapter 5.

4.5.4 Conclusions

Measurements have been made of the distribution of UV light emitted from the ISUKs that deliver the UV light to the inertial sensor system. Knowing their distribution is critical for use in simulation of illumination factors for individual inertial sensor surfaces.

- A setup containing a single core fibre to deliver the light to the ISUK was measured which is the same as that used with the torsion pendulum facility.
- A setup representative of the flight system containing a multi-core fibre was also measured.
- The multi-core distributions was adequately described using one Gaussian function while the single core distributions require the linear combination of two Gaussians.
- The single core distributions were observed to contain a significant, fairly sharp central component in addition to a larger more disperse component.
- The light cone angles measured for both setups were consistent with the theoretical value of the ISUK of $12.71 \pm 1.20°$.
- Both sets of measurements were also converted to distributions in θ, originating at point sources within the ISUK fibre. These will be used within the simulations described in Chapter 5.

Chapter 5

Simulating the Charge Management System

Introduction

As has been shown in previous chapters, the performance of the Charge Management System is dependant on a number of interrelated factors. These include the photoelectric and reflective properties of the inertial sensor surfaces as well as the distribution of the illuminating UV light. In addition, the geometry of the system and the presence of varying electric fields play important roles. In order to better understand the discharging system as a whole simulations have been produced which incorporate all these factors and where possible use experimentally measured parameters to describe them. The simulation has been used to help understand some anomalous four-mass pendulum results and can be used in future to optimise the design of the LISA system.

The simulation consists of two distinct parts. First, a ray trace written in Geant4 models the propagation of the UV light within the inertial sensor which determines the percentage of light absorbed by the various surfaces. The second part is written in MATLAB and uses the calculated absorption ratios to model the flow of the emitted photoelectrons, within region-specific electric fields. This allows discharge rates and the instantaneous test mass potential to be estimated under a variety of operating conditions. Both the four-mass pendulum and Pathfinder sensor geometries have been simulated and the two systems compared. In the case of the four-mass system the models used have been verified by comparing results to those measured at the torsion pendulum. In addition, differences in the flight system have been assessed and their affect on the discharge behaviour for Pathfinder estimated.

5.1 Geant4 Ray Trace

The ray trace part of the simulation was initially written, from scratch, in MATLAB. It included the full 3D sensor geometry and a simple reflection model. Unfortunately, as the design of the caging features evolved it became difficult to include their increasingly complex geometry. To overcome these limitations the ray trace was rewritten in Geant4 which was previously used to model the radiation monitor, described in Chapter 2. While originally created to model the propagation of particles through matter, Geant4 also contains reflection physics models and highly versatile methods for describing complex geometries. Combined with its efficient transportation algorithms, this makes it ideal for ray tracing applications. Figure 5.1 gives an idea of the geometrical complexity of the Geant4 flight model with a fibre-eye-view of the inertial sensor.

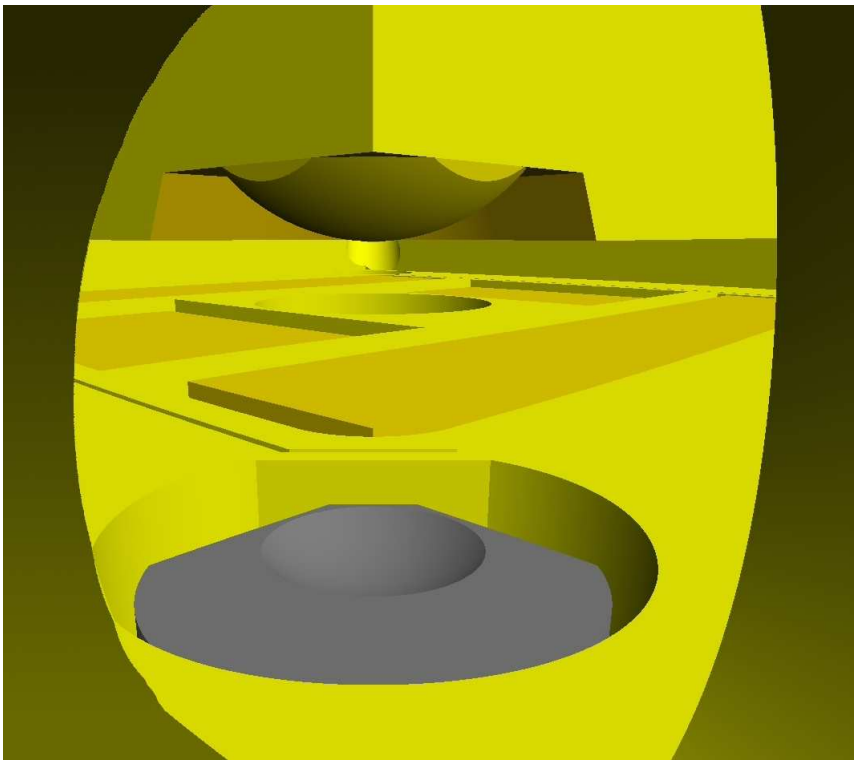

Figure 5.1: A fibre-eye-view of the flight inertial sensor, the image generated from within the hole where the ISUK enters. The retracted caging finger is visible at the bottom (grey) with the corner region of the test mass seen above (dome structure) and the lower z face electrodes in between (orange). The injection electrodes are slightly recessed, as in the real case. Note the unusual shape of the ISUK entry hole is due to the angle of entry as well as it being offset from the intersection of the x and y housing faces.

The Geant4 ray trace can be broken down into three parts. First, there is the system geometry and the composition of each surface. Second is the reflection model used to describe the properties of each surface. Thirdly is the initial distribution of UV light entering the sensor via the ISUK. These three components, and how they differ in the pendulum and flight models, will be described in the following sections. However, both versions of the ray trace follow a common procedure:

- A ray is generated within the ISUK tip with a random polarisation and a direction randomly sampled from the appropriate ISUK light distribution.
- The ray is propagated through the geometry until it is incident with a surface.
- The ray is then either absorbed or reflected, with the likelihood of either event being determined by the reflection properties of the surface, the angle of incidence and the ray's polarisation.
- If the ray is reflected it is given a new direction, dependant on the reflection properties of the surface, then continues to propagate and reflect until it is eventually absorbed.
- This is repeated for a user specified number of rays, typically greater than 10^6.
- The inertial sensor is split into regions and the percentage of light absorbed by each is recorded and outputted to an ASCII file at the end of a run.
- If the user desires, the coordinates of each absorption, or a variety of other properties can also be easily outputted.

5.1.1 Sensor Geometry

One may recall the descriptions of the sensor geometries given in Sections 1.4.1 & 3.4. In particular, Figure 1.6 shows the coordinate system used relative to a central origin. Clearly, the simulated sensor geometry has to be as accurate as possible and with this in mind the technical drawings for the four-mass and flight inertial sensor designs were used to reconstruct the systems within Geant4. Basic structures, like the electrodes, were composed of Constructed Solid Geometry (CSG) solids such as boxes, tubes and spheres. The more complex structures, like the test mass corner regions, were composed of so called boolean solids, essentially formed by adding or subtracting multiple CSG volumes. For example, the housing is formed from a cube with the vacuum filled gap region subtracted out of the middle. Each element was added manually, with each individual addition being checked visually.

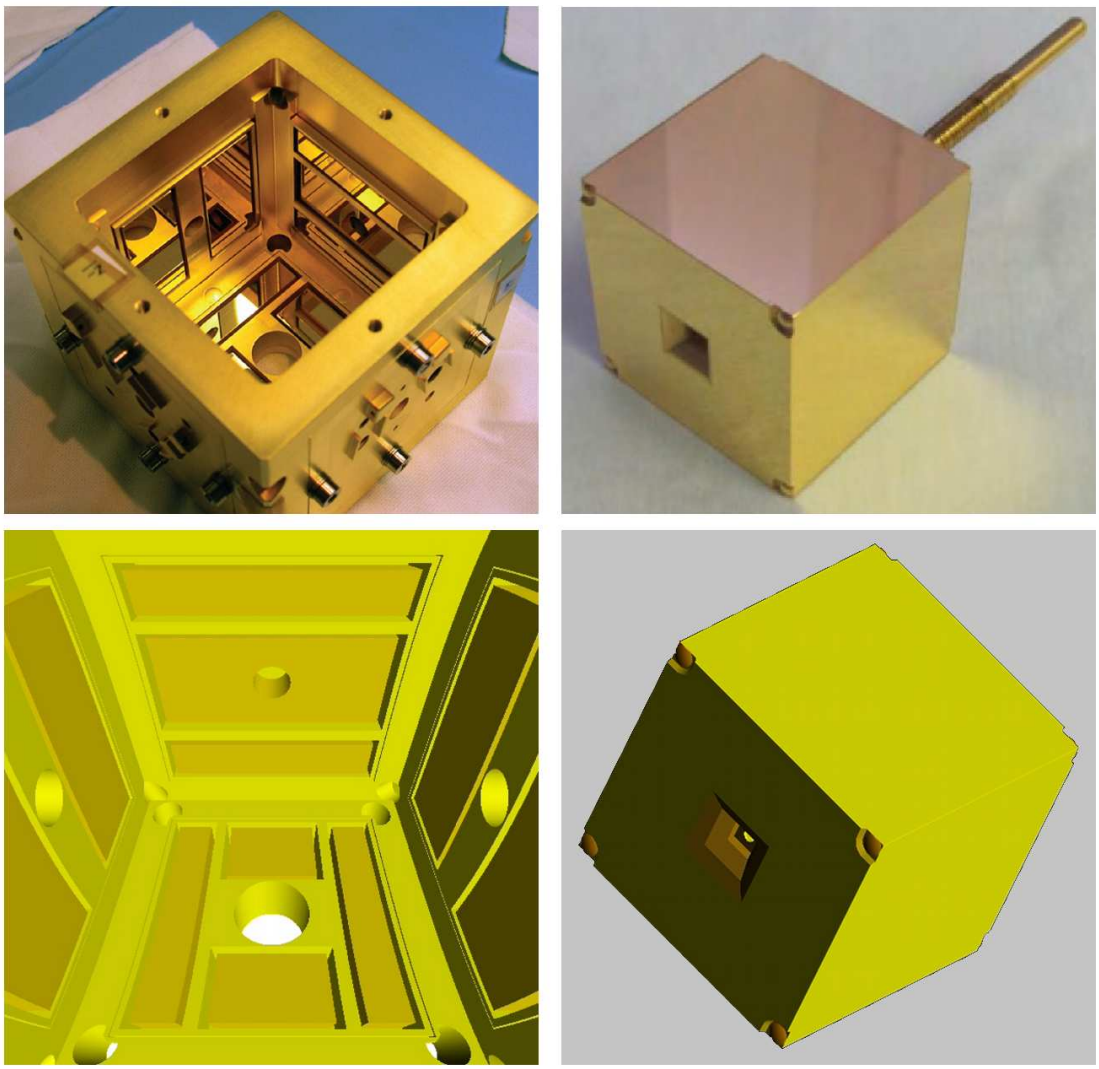

Figure 5.2: *Top Left*: The electrode housing used at the four-mass pendulum, with the lower z face removed. The inner dimensions are 54.0, 51.8 and 53.0 mm in x, y and z respectively. *Top Right*: The 46 mm^3 test mass (TM3) used at the four-mass pendulum. *Bottom Left*: The simulated four-mass electrode housing. *Bottom Right*: The simulated test mass. Photographs courtesy of UTN.

Figure 5.2 shows photographs of the inertial sensor used at the four-mass pendulum and images of the simulated geometry. One should note that with respect to the simulated geometry the electrode housing is upside-down in the photograph, as shown by the ISUK entry holes being visible in the top corners. The photograph also shows the smooth, mirror-like (specular) appearance of the electrodes and test mass faces while the housing appears considerably rougher (diffuse).

5.1.1.1 Geometry Differences

There are several differences between the four-mass and flight inertial sensor geometries and these have been included in the simulations. An obvious difference is the shaft attached to the upper z face of the test mass in the pendulum system which is not present in the flight case. While it is included in the simulation, it should have very little affect when it comes to discharging as hardly any UV light will reach this region, as illumination occurs on the lower z faces. Similarly, the flight test mass includes the central caging recess on both upper and lower z faces but it is only present on the lower face in the four-mass system. Again, this should have little effect on discharging.

Much more significant is the absence of the retracted iridium caging fingers in the four-mass caging holes. These will be present in the flight system and could have a substantial affect on discharging as they are close to the area being illuminated. These differences are included in the simulations as well as a more subtle difference in the geometry around the caging finger recesses. The difference in the simulated geometries are shown in Figure 5.3.

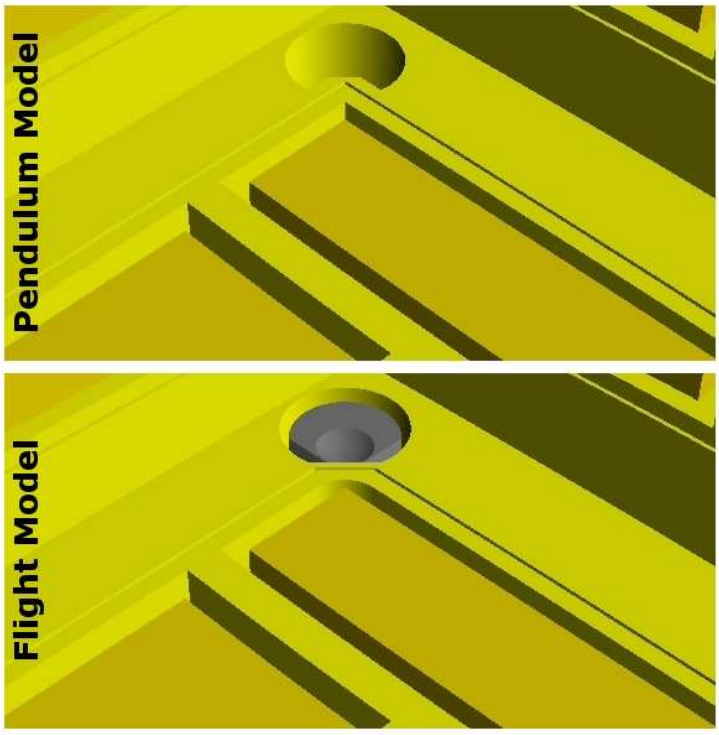

Figure 5.3: A comparison of the simulated four-mass (*Top*) and flight (*Bottom*) geometries. As well as the obvious presence of the retracted caging finger in the flight case, there is also a subtle difference in the shape of the hole.

A further difference between the four-mass and flight systems concerns the caging features on the corners of the test mass. While not geometrically different, the half domes on the corners are gold coated in the four-mass case. Due to the risk of the 1 μm gold layer pealing off during decaging, these regions will remain uncoated in the flight system. This will expose the underlying $Au_{0.7}Pt_{0.3}$ alloy, possibly affecting the discharging behaviour.

5.1.2 Light Sources

As shown in Chapter 4, Section 4.5, the light sources used with the four-mass pendulum and flight system are slightly different. While the ISUKs in both cases are the same the fibres that route the light to them vary, which in turn affects the distribution of the emitted UV. These distributions were measured and it was shown that both cases could be modelled as point sources originating within the ISUK. The light cones produced are symmetrical with the output intensity varying with angle, θ, from the cones central axis. In the case of the multi-core fibre, to be used on Pathfinder, it was shown this variation could be described with a Gaussian and a single parameter, $\sigma = 6.595$. The single core fibre, used with the four-mass experiment, required a linear combination of two Gaussians to fit the observed results. The two Gaussians had amplitudes of $A_1 = 0.06157$ and $A_2 = 0.02513$ with standard deviations of $\sigma_1 = 6.064$ and $\sigma_2 = 0.9856$, respectively.

The two light sources were implemented within the simulations using Geant4's General Particle Source, or GPS. This models the UV light emitted from the ISUKs as a point source and each photon's initial direction is determined randomly with the appropriate weighting. A simple test was performed by using the simulated GPS light sources in Geant4 to recover the experimentally measured distributions. This involved measuring the horizontal variation in intensity at fixed distances, as was the case with the original measurements. The results can be seen in Figure 5.4 and a good agreement was found.

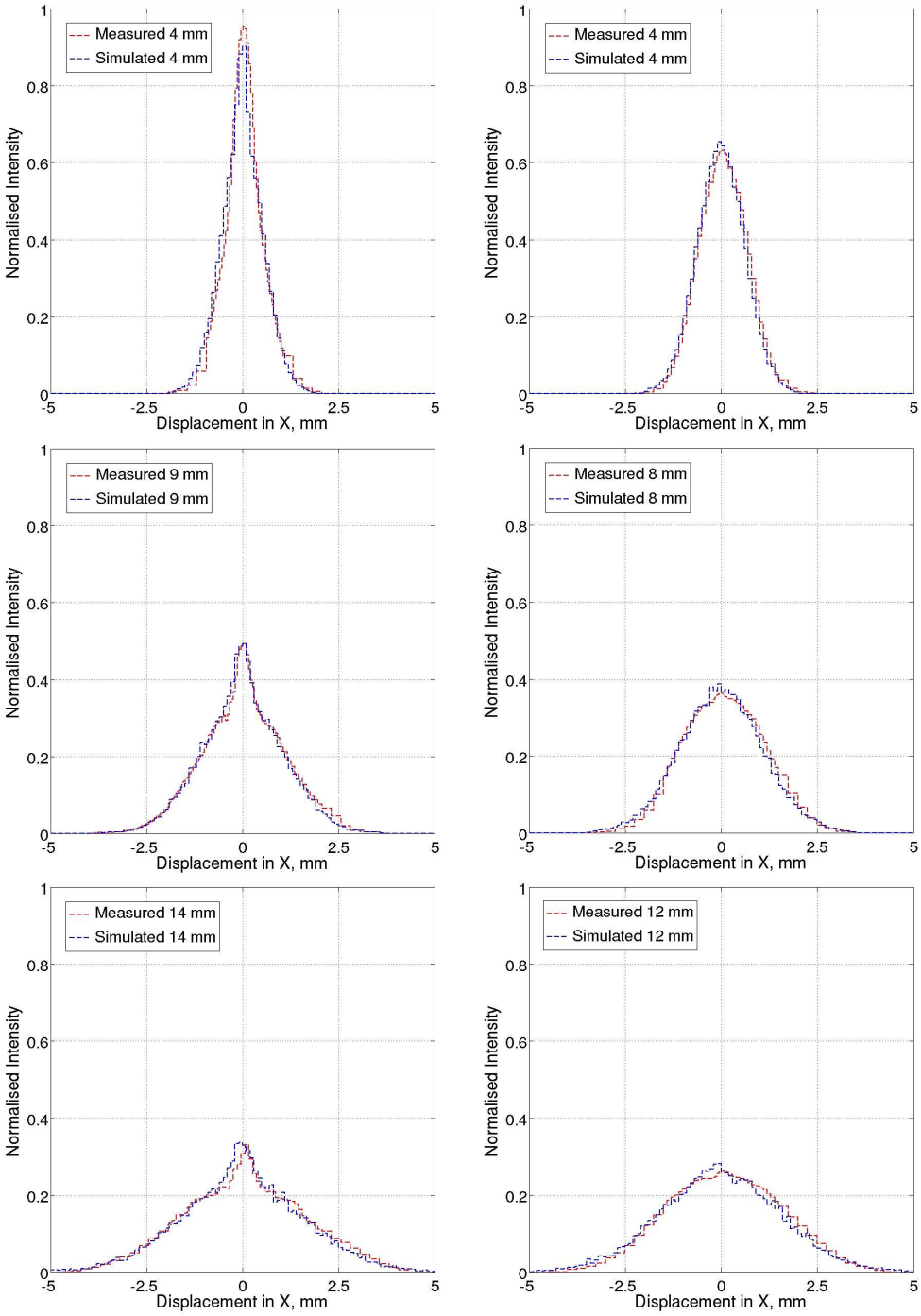

Figure 5.4: Comparison of measured and simulated ISUK light distributions. *Left:* Single core fibre results. *Right:* Multi-core fibre results. The measurements are for increasing distance from the ISUK tip. The simulated light sources show good agreement with the measured data and consistent results with increasing distance.

5.1.3 Reflection Model

Geant4 uses a material's intrinsic optical properties and the concept of surfaces to model reflection. Each volume within Geant4 is composed of a particular material and the user is required to supply the refractive index of said material and the photon energy at which it applies. The probability of a photon being absorbed or reflected at the boundary between two media can then be calculated via the Fresnel equations, described in the previous chapter, Section 4.4.6.1. These equations are dependant on the two refractive indices, the light's polarisation as well as the angle of incidence. Given that the inertial sensor is within a vacuum, one of the boundary materials is always a vacuum, with a value of $n_1 = 1$.

In order to account for the fact that the distribution of reflected light from a material can vary due to surface roughness, Geant4 uses the concept of a surface. A surface determines the distribution of the reflected light and allows materials of the same type, but different surface finishes, to be described within the same simulation. Surfaces come in two forms, one of which is a Logical Skin Surface that can be attached to any geometry volume, effectively surrounding it. Alternatively, a Logical Border Surface can be used which applies to the boundary between two particular volumes. Either surface type can be used, depending on the users requirements, and they act in the same way.

The default model Geant4 uses to describe a surface is called UNIFIED and is described in detail by Levin and Moisan (1996). It uses up to seven parameters to describe each surface which determines the distribution of the reflected light. The reflected light distribution can be made up of four components with the user supplying the weighting of each, making sure that the sum of the four component weights equals one. The four components are a specular spike (R_{ss}), a specular lobe (R_{sl}), a backscatter spike (R_{bs}) and a diffuse lobe (R_{dl}). The four components are shown in Figure 5.5.

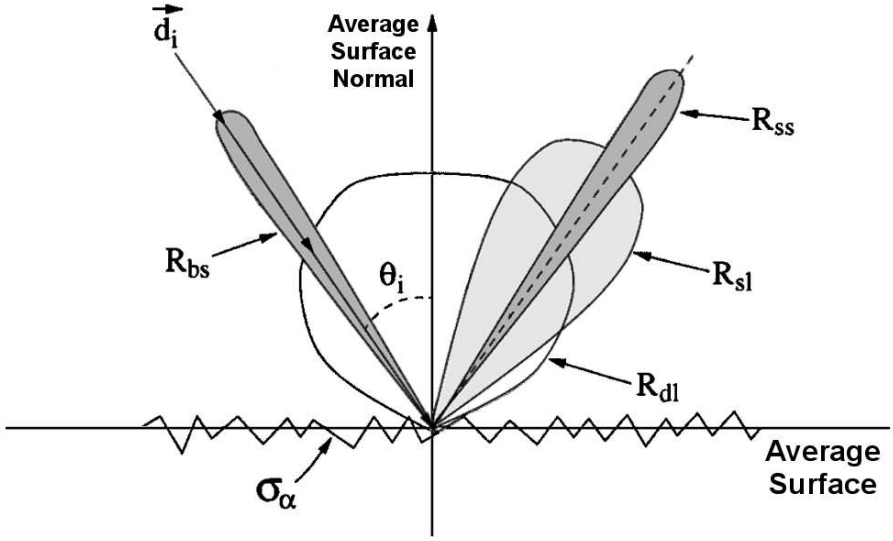

Figure 5.5: Shows the possible ways an incident ray, $\vec{d_i}$, can be reflected in the UNIFORM model. The four possibilities are in a specular spike (R_{ss}), a backscatter spike (R_{bs}), a diffuse lobe (R_{dl}) or a specular lobe (R_{sl}). The shape of the specular lobe is determined by the value of σ_α, which describes the standard deviation in the micro-facet angular distribution. This figure was adapted from one used in Levin and Moisan (1996).

The specular spike describes light reflected at an angle equal to the angle of incidence, with respect to the average surface normal. This is the type of reflection a mirrored surface exhibits. The backscatter spike describes light reflected back in the opposite direction to the incoming light. A very rough surface may exhibit this type of behaviour. The diffuse lobe describes light that is reflected in such a way that the surface appears equally bright, irrespective of the observers viewing angle. Paper exhibits this type of reflection, which is called Lambertian.

Finally, the specular lobe attempts to relate a physical description of a real surface to its reflected light distribution. The shape of the specular lobe is determined by a parameter σ_α. This parameter arises if one considers a surface as being made up of many micro-facets. The angular distribution of these micro-facets, with respect to the average surface normal, is assumed to be Gaussian and has a mean of zero and a standard deviation of σ_α. When a ray is incident with a such surface the micro-facet distribution is sampled and reflection is carried out with respect to this micro-facet's normal, rather than the average surface normal. Two special cases are also considered. First, if a micro-facet is chosen that is not accessible to the incident ray another is selected. The second case is if a reflected ray aims again at the surface then the micro-facet distribution will be sampled once more leading to inter-facet

reflection.

The nice aspect of this model is that σ_α can be measured for a real sample and it also offers a physical explanation of the different reflection distributions that can be observed. As σ_α approaches zero the specular lobe reduces to a specular spike and with an increasing σ_α the specular lobe approaches a diffuse lobe. This is in contrast to the Lambertian diffuse lobe previously described which only considers the average surface normal, leading to non-physical results. It should be kept in mind that the four reflection components can be used individually or combined with a suitable weighting to describe the reflected light distribution of a surface.

In summary, the UNIFIED reflection model requires seven parameters: n_1 and n_2 are the complex refractive indices of the two boundary materials, R_{ss}, R_{sl}, R_{bs} and R_{dl} give the probability of a ray being reflected in each respective way and σ_α is the standard deviation of a Gaussian distribution describing the micro-facet angles with respect to the average surface normal.

5.1.3.1 Refractive Indices

For the inertial sensor used with the four-mass experiment every surface was gold coated. However, this will not be the case in the flight setup with the caging fingers being iridium and the test mass corner domes being left uncoated, exposing the underlying $Au_{0.7}Pt_{0.3}$ alloy. One will recall that the refractive index for flight representative gold surfaces was measured in Chapter 4, Section 4.4. Being a metal, its complex index of refraction is given by a real component, n, and a complex component, κ, which is referred to as the extinction coefficient. For the rest of the work discussed values of $n = 1.296$ and $\kappa = 1.696$, which were measured in Chapter 4, were used within the simulations to describe the gold.

For the additional materials, values were taken from the literature as no suitable flight surfaces were available to measure. Literature values for iridium at 254 nm were found, with $n = 1.13$ and $\kappa = 2.42$, (Palik and Ghosh, 1998). It was not possible to find literature values for $Au_{0.7}Pt_{0.3}$ alloy at 254 nm, so an approximation had to be made. Given that pure platinum has literature values of $n = 1.38$ and $\kappa = 1.85$, (Palik and Ghosh, 1998), that are fairly close to those measured for gold, a simple 70/30 weight was applied to the values of gold and platinum to estimate the $Au_{0.7}Pt_{0.3}$ alloy. The values obtained from this method, and used in the simulations, are $n = 1.32$ and $\kappa = 1.74$. A comparison of the reflection curves for the materials that make up the inertial sensor system are shown in Figure 5.6.

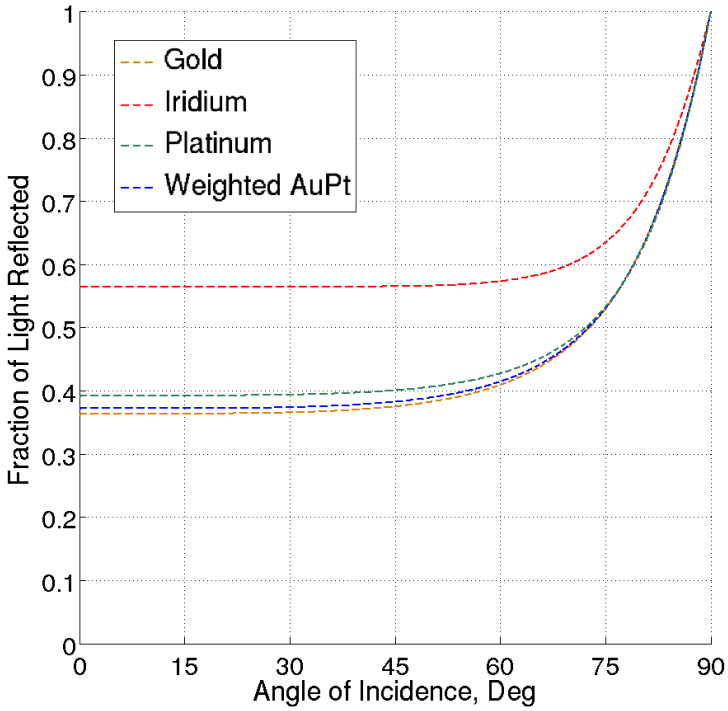

Figure 5.6: Comparison of reflectivities at 254 nm of the materials that make up the flight inertial sensor. Note that iridium has a significantly higher reflectivity than gold, which could affect the performance of the discharge system given that the iridium caging fingers were not present in the four-mass measurements.

5.1.3.2 Surface Roughness

The roughness of the various surfaces that make up the inertial sensor determine the distribution of any reflected UV light. One way of quantifying a surface's roughness is with the parameter R_a, which is the arithmetical mean roughness. It is essentially a measure of the vertical variation around a surface's mean height and is given by:

$$R_a = \frac{1}{n}\sum_{i=1}^{n} |y_i| \tag{5.1}$$

where $|y_i|$ gives the absolute distance of a point from the mean height. Estimates for the sensor surfaces R_a values are collated in Table 5.1.

Surface	Roughness
Electrodes	$\sim$ 10 nm
Housing	$\sim$ 400 nm
Test Mass Sides	$\sim$ 1 nm
Test Mass Corner Domes	$\sim$ 250 nm
Caging Fingers	$\sim$ 250 nm

Table 5.1: The R_a roughness estimates for the inertial sensor flight surfaces. Values obtained from LTP ISS Team (2009).

If a surface is very smooth it will reflect light in a purely specular way while increasing surface roughness increases the prominence of the specular lobe component, (Nayar et al., 1991). Generally, when the size of surface irregularities are small compared to the illuminating wavelength a surface is considered smooth while if they are larger than the illuminating wavelength the surface is considered rough. The Rayleigh criterion, described by Nayar et al. (1989), provides a simple definition of when a surface can be considered rough. It relates not only the incident wavelength and variation in surface height but also the angle of incidence. Generally, as the angle of incidence approaches a grazing angle reflection becomes specular. A surface is considered rough when:

$$\mathrm{H} > \frac{\lambda}{8\cos\theta} \tag{5.2}$$

where H is the height of the surface irregularities, λ is the wavelength of the light and θ is the angle of incidence. For the 254 nm UV light at normal incidence one obtains $\mathrm{H} > 31.75$ nm. With this definition the test mass sides and the electrodes would be considered smooth while the other surfaces would be considered rough. This suggests the test mass sides and electrodes reflection can be considered purely specular. Indeed this was observed experimentally with the measurements made in Chapter 4 on a gold surface representative of the electrodes. The other surfaces meanwhile can be expected to be dominated by a specular lobe, described by the parameter σ_α.

The smooth specularly reflecting gold, which covers $\sim 65\%$ of the inertial sensor surfaces, has been experimentally measured. Unfortunately, suitable samples of the remaining surfaces have not been available and it is difficult to accurately estimate σ_α values for them. These surfaces are particularly important as the illuminating UV is initially incident in these areas. Given this uncertainty, the σ_α values of the hous-

ing (σ_{eh}), test mass corners (σ_{tm}) and caging fingers (σ_{cf}) were varied between the possible extremes of completely specular and completely diffuse in order to scale any effect. It will be shown in the next section that the roughness has only a small effect on the total amount of light absorbed by either the test mass or electrode housing but rather determines how wide an area the absorbed light is distributed over. This is still significant as it determines which electric fields the emitted photoelectrons experience and therefore influences the discharging behaviour of the system.

5.1.4 Results

The ray trace was run for both the four-mass inertial sensor geometry and the flight inertial sensor geometry. As discussed, most of the model parameters were either measured or in the case of the iridium and $Au_{0.7}Pt_{0.3}$ refractive indices, took literature values. The most significant unknown parameters related to the distribution of reflected light from the non-specular housing, test mass corner and caging finger surfaces. To examine the affect these parameters have on the ray trace results they were varied between the extreme possibilities of completely specular and completely Lambertian. It should be noted that diffuse Lambertian reflection within this model is not entirely physically consistent with the way it calculates absorption and is shown merely as a reference. Within these extremes the σ_α parameter was used to describe the reflected distribution, varying between 1°, fairly specular, up to 45°, extremely diffuse. Initially all the unknown reflection parameters took the same values. In order to be consistent with the estimated R_a surface roughness values, shown in Table 5.1, a run was also performed with the slightly smoother test mass corners and caging fingers set at $\sigma_{\mathrm{tm}}, \sigma_{\mathrm{cf}} = 15°$ while the slightly rougher housing surface took the value $\sigma_{\mathrm{eh}} = 25°$. Given the uncertainty with these parameters and that these values are approximately in the middle of the possible extremes, they are considered the best educated guess. Currently, all that can be said with confidence is that the unknown surfaces will be neither completely specular nor completely diffuse. However, it will later be shown that with parameters $\sigma_{\mathrm{tm}} = 15°$ and $\sigma_{\mathrm{eh}} = 25°$ the ray trace provides results that are capable of reproducing the four-mass discharging results.

For all the results presented, 10^7 initial rays were used. It was found that this number of rays produced repeatable results and gave a reasonable runtime on a desktop machine of approximately two hours. Although it is capable of outputting the coordinates of each individual absorption point the ray trace instead stores the percentage of UV light absorbed by different regions. Aiding later analysis,

the system is split into regions where photoelectrons can be influenced by different electric fields. The six housing sides are referred to as x, y and z surfaces and sense and injection electrodes are distributed in regions across the surface. The opposite areas on the test mass are split into regions to match those on the housing with the shaft and test mass corner regions treated separately. As will be discussed, only light that is absorbed on housing surfaces facing the test mass are likely to generate photoelectrons capable of reaching the test mass. Due to this, light that is absorbed within the housing gaps or within the caging holes is considered 'wasted', as photoelectrons originating in these regions are unlikely to affect discharging. It should be noted that there is a small hole on the bottom of the hollow test mass used with the four-mass experiment. Again, any light entering the hole and absorbed within the test mass is considered 'wasted' as it would be extremely unlikely for any photoelectrons produced to be able to exit. Finally, a small percentage of the light (< 2 %) was found to escape the system through the caging finger holes. This missing light is left out of the totals as it does not contribute to discharging.

5.1.5 Four-Mass Pendulum Model

The results of the ray trace for the four-mass system are summarised in Tables 5.2 and 5.3, showing the ISUK aimed at the housing and test mass respectively. Each table shows the percentage of UV light absorbed by each region on both the electrode housing (EH) and test mass (TM). In each case a total of seven different runs were performed with the reflection distribution of the unknown surfaces varied. As one would expect the unknown surfaces do affect the results but reassuringly the total light absorbed by either the test mass or housing remains roughly the same, irrespective of the unknown reflection distributions. When the housing is illuminated just $19 - 26$ % is absorbed by housing surfaces 'useful' to discharging, while $8 - 11$ % is absorbed by the test mass. Meanwhile, when the test mass is illuminated $65 - 69$ % is absorbed by the test mass and $15 - 17$ % is absorbed by housing surfaces 'useful' to discharging. The large amount of 'wasted' light when the housing is illuminated is mainly due to light being lost within the caging hole. It seems the system geometry, the ISUK light distribution and the intrinsic surface reflectivities dominates in determining the total amounts of light absorbed. However, the reflection distributions do have a significant influence in determining over what regions the absorbed light is spread.

	All Specular		All $\sigma_\alpha = 1°$		All $\sigma_\alpha = 15°$		$\sigma_{\text{tm}} = 15°$, $\sigma_{\text{eh}} = 25°$		All $\sigma_\alpha = 25°$		All $\sigma_\alpha = 45°$		All Lambertian	
Surface	EH	TM	EH	TM	EH	TM	EH	TM	EH	TM	EH	TM	EH	TM
-X Housing Region	0.0531	0.0012	0.0465	0.0015	0.6694	0.0988	1.3114	0.1649	1.3191	0.1623	1.9355	0.1688	3.3136	0.5270
-X Sense Region 1	0.0001	0.0001	0.0000	0.0001	0.0088	0.0075	0.0120	0.0106	0.0125	0.0104	0.0125	0.0104	0.0205	0.0161
-X Sense Region 2	0.0002	0.0002	0.0005	0.0002	0.0299	0.0229	0.0739	0.0524	0.0730	0.0535	0.0981	0.0676	0.1802	0.1324
+X Housing Region	0.6680	0.0394	0.6857	0.0520	0.9252	0.0642	0.7773	0.0541	0.7748	0.0541	0.6613	0.0360	0.2404	0.0259
+X Sense Region 1	0.0010	0.0006	0.0008	0.0006	0.0071	0.0073	0.0077	0.0086	0.0067	0.0093	0.0047	0.0070	0.0033	0.0039
+X Sense Region 2	0.0004	0.0003	0.0003	0.0002	0.0018	0.0019	0.0028	0.0033	0.0030	0.0036	0.0027	0.0036	0.0025	0.0027
-Y Housing Region	0.5759	0.0148	0.5762	0.0143	0.8885	0.0432	0.7773	0.0425	0.7762	0.0410	0.6935	0.0304	0.3144	0.0268
-Y Sense Region 1	0.0001	0.0002	0.0004	0.0003	0.0062	0.0060	0.0063	0.0084	0.0071	0.0085	0.0054	0.0079	0.0049	0.0046
-Y Sense Region 2	0.0000	0.0001	0.0000	0.0000	0.0004	0.0004	0.0006	0.0007	0.0006	0.0006	0.0004	0.0006	0.0006	0.0006
-Y Injection Region 0	0.0001	0.0001	0.0001	0.0001	0.0018	0.0016	0.0025	0.0029	0.0030	0.0028	0.0025	0.0025	0.0024	0.0024
+Y Housing Region	0.0492	0.0009	0.0495	0.0017	0.5766	0.0807	1.2167	0.1373	1.2224	0.1374	1.8358	0.1509	3.1074	0.4291
+Y Sense Region 1	0.0006	0.0002	0.0006	0.0004	0.0229	0.0181	0.0557	0.0391	0.0556	0.0389	0.0808	0.0479	0.1386	0.0898
+Y Sense Region 2	0.0000	0.0000	0.0000	0.0000	0.0018	0.0021	0.0033	0.0034	0.0034	0.0035	0.0035	0.0035	0.0052	0.0052
+Y Injection Region 0	0.0001	0.0002	0.0001	0.0001	0.0111	0.0098	0.0192	0.0167	0.0198	0.0173	0.0208	0.0198	0.0344	0.0300
-Z Housing Region	12.1338	2.4518	12.0901	2.3365	13.0970	2.6422	14.0786	2.9752	14.0245	2.9709	15.0589	2.7010	12.7139	3.9568
-Z Sense Region 1	3.9741	1.6507	3.9750	1.6462	4.4842	1.8321	4.4271	1.4353	4.4154	1.4205	4.2779	0.9491	4.3818	0.9410
-Z Sense Region 2	0.0804	0.1061	0.0900	0.1171	0.1431	0.1282	0.1207	0.0966	0.1194	0.0941	0.0905	0.0612	0.0712	0.0467
-Z Injection Region 1	1.1778	0.2043	1.2723	0.1797	0.9968	0.1570	0.8947	0.1422	0.8293	0.1398	0.6798	0.1208	0.5700	0.1167
-Z Injection Region 2	0.5843	0.5873	0.8039	0.6377	0.9251	0.5163	0.8058	0.4887	0.8189	0.4929	0.6645	0.4418	0.6376	0.3921
+Z Housing Region	0.0015	0.0001	0.0010	0.0000	0.0586	0.0021	0.1035	0.0043	0.1025	0.0038	0.1069	0.0029	0.1044	0.0059
+Z Sense Region 1	0.0000	0.0000	0.0000	0.0000	0.0004	0.0003	0.0006	0.0011	0.0007	0.0010	0.0006	0.0009	0.0015	0.0015
+Z Sense Region 2	0.0000	0.0000	0.0000	0.0000	0.0001	0.0001	0.0003	0.0004	0.0002	0.0003	0.0002	0.0003	0.0003	0.0003
+Z Injection Region 1	0.0000	0.0000	0.0000	0.0000	0.0001	0.0001	0.0005	0.0001	0.0004	0.0002	0.0003	0.0001	0.0004	0.0002
+Z Injection Region 2	0.0000	0.0000	0.0000	0.0000	0.0004	0.0001	0.0007	0.0003	0.0007	0.0002	0.0006	0.0003	0.0014	0.0006
Shaft	0.0000	N/A	0.0000	N/A	0.0001	N/A	0.0003	N/A	0.0004	N/A	0.0004	N/A	0.0004	N/A
TM Corner Sphere	N/A	0.0857	N/A	0.0971	N/A	0.1403	N/A	0.3020	N/A	0.3089	N/A	0.4949	N/A	0.9175
TM Corner Region	N/A	0.3404	N/A	0.3240	N/A	0.1720	N/A	0.2994	N/A	0.3168	N/A	0.4109	N/A	0.7579
TM Caging Hole	N/A	2.2076	N/A	2.2530	N/A	2.4633	N/A	2.2885	N/A	2.4651	N/A	2.5310	N/A	2.2094
Wasted Light	72.7734	0.0000	72.5012	0.0000	67.0149	0.0034	65.1933	0.0034	65.1227	0.0047	64.4621	0.0070	62.9036	0.0090
Useful Total	19.3008	7.6921	19.5931	7.6626	22.8574	8.4184	24.6992	8.5789	24.5897	8.7577	26.2381	8.2718	25.8513	10.6429

Table 5.2: Percentage of UV absorbed by four-mass surfaces upon housing illumination. Unknown reflection properties were varied.

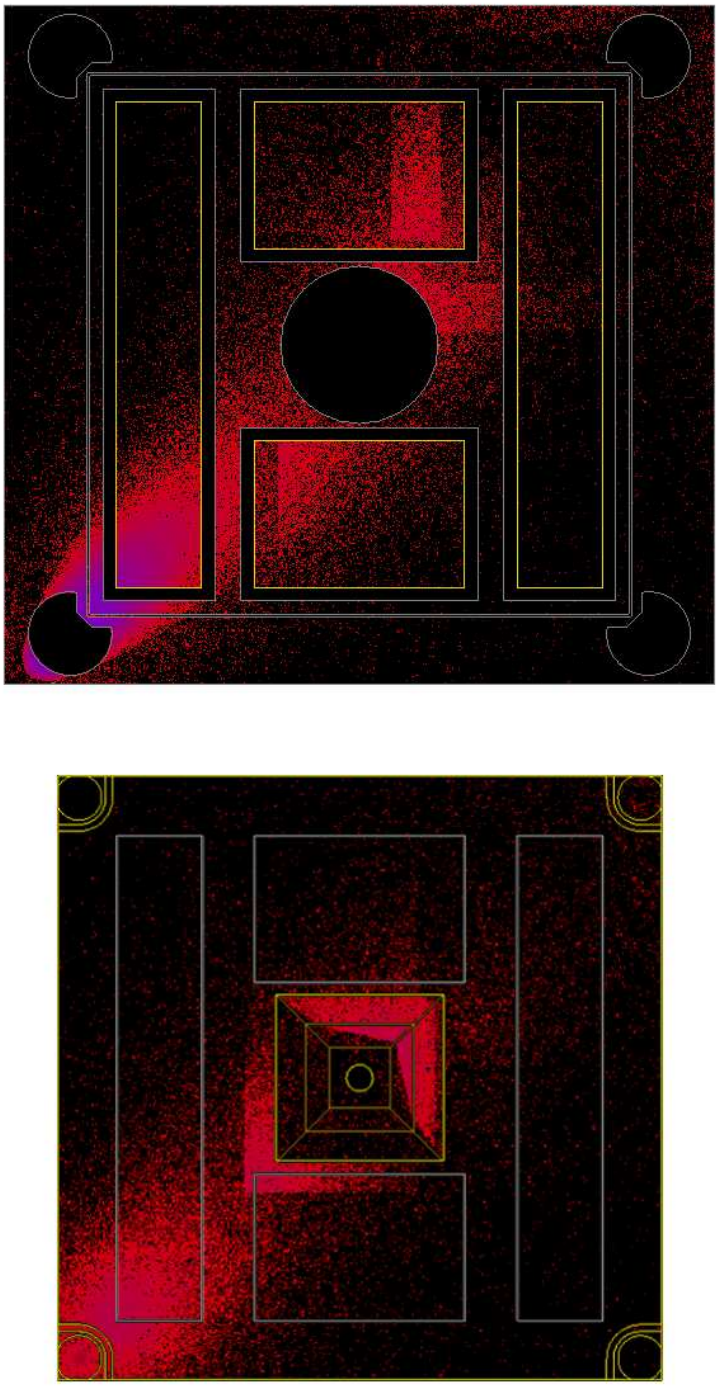

Figure 5.7: Distribution of absorbed UV light upon illuminating the four-mass electrode housing. *Top:* Absorption taking place on the housing lower z face. *Bottom:* Absorption taking place on the test mass lower z face. The test mass sides and electrodes were given purely specular properties, the test mass corner regions had a $\sigma_{\mathrm{tm}} = 15°$ and the housing had a $\sigma_{\mathrm{eh}} = 25°$. Purple represents high absorption, red low absorption and black zero absorption.

	All Specular		All $\sigma_\alpha = 1°$		All $\sigma_\alpha = 15°$		$\sigma_{\rm tm} = 15°$, $\sigma_{\rm eh} = 25°$		All $\sigma_\alpha = 25°$		All $\sigma_\alpha = 45°$		All Lambertian	
Surface	EH	TM	EH	TM	EH	TM	EH	TM	EH	TM	EH	TM	EH	TM
-X Housing Region	0.4553	0.0281	0.4600	0.0300	0.5039	0.0378	0.4444	0.0314	0.4389	0.0292	0.3538	0.0186	0.2303	0.0251
-X Sense Region 1	0.0006	0.0002	0.0009	0.0005	0.0027	0.0028	0.0033	0.0040	0.0033	0.0036	0.0023	0.0029	0.0039	0.0038
-X Sense Region 2	0.0010	0.0007	0.0010	0.0010	0.0039	0.0042	0.0030	0.0041	0.0033	0.0041	0.0018	0.0025	0.0025	0.0025
+X Housing Region	2.3999	13.1523	2.3813	13.1670	3.0284	13.3431	3.2972	13.3509	3.6098	13.3499	4.1434	13.2895	4.4732	13.8291
+X Sense Region 1	0.1440	0.1354	0.1404	0.1346	0.1109	0.0993	0.0845	0.0736	0.0821	0.0716	0.0613	0.0494	0.0588	0.0457
+X Sense Region 2	1.6204	1.2697	1.6052	1.2529	1.4468	0.8266	1.3984	0.7409	1.3963	0.7337	1.3530	0.6628	1.4234	0.7517
-Y Housing Region	0.5432	0.0285	0.5428	0.0274	0.6594	0.0401	0.5549	0.0327	0.5416	0.0303	0.4028	0.0175	0.2333	0.0202
-Y Sense Region 1	0.0003	0.0002	0.0008	0.0004	0.0034	0.0037	0.0040	0.0048	0.0035	0.0046	0.0027	0.0033	0.0038	0.0036
-Y Sense Region 2	0.0003	0.0002	0.0003	0.0003	0.0010	0.0011	0.0010	0.0013	0.0011	0.0012	0.0006	0.0007	0.0005	0.0005
-Y Injection Region 0	0.0012	0.0005	0.0007	0.0004	0.0036	0.0033	0.0033	0.0039	0.0031	0.0037	0.0020	0.0021	0.0020	0.0019
+Y Housing Region	1.7158	13.0201	1.7068	13.0339	2.1741	13.1323	2.3524	13.1237	2.6206	13.1700	3.0393	13.1342	3.4834	13.4466
+Y Sense Region 1	1.7912	1.1011	1.7882	1.0925	1.6382	0.7919	1.6106	0.7437	1.6029	0.7440	1.5691	0.7091	1.6093	0.7536
+Y Sense Region 2	0.0036	0.0016	0.0035	0.0017	0.0047	0.0047	0.0045	0.0039	0.0045	0.0045	0.0038	0.0035	0.0050	0.0047
+Y Injection Region 0	0.1193	0.1091	0.1174	0.1076	0.1154	0.0879	0.1041	0.0812	0.1035	0.0807	0.0962	0.0685	0.1020	0.0773
-Z Housing Region	5.5656	1.6988	5.5460	1.7104	5.6003	1.8775	5.9139	1.8441	5.3137	1.7804	4.5553	1.5635	4.3141	1.8775
-Z Sense Region 1	0.0450	0.0164	0.0446	0.0216	0.0631	0.0462	0.0584	0.0382	0.0587	0.0372	0.0513	0.0281	0.0542	0.0343
-Z Sense Region 2	0.3791	0.7138	0.3773	0.7074	0.4868	0.7682	0.4775	0.7658	0.4068	0.7322	0.2734	0.6729	0.1742	0.6878
-Z Injection Region 1	0.2565	0.0762	0.2570	0.0683	0.2832	0.0543	0.2711	0.0485	0.2538	0.0472	0.2213	0.0365	0.2174	0.0394
-Z Injection Region 2	0.3929	0.0574	0.3952	0.0561	0.4323	0.0861	0.4163	0.0895	0.3606	0.0803	0.2779	0.0680	0.2584	0.0859
+Z Housing Region	0.0427	0.0012	0.0436	0.0014	0.1059	0.0041	0.1123	0.0045	0.1170	0.0043	0.1134	0.0031	0.0983	0.0058
+Z Sense Region 1	0.0000	0.0001	0.0000	0.0000	0.0002	0.0002	0.0003	0.0002	0.0002	0.0003	0.0002	0.0002	0.0003	0.0002
+Z Sense Region 2	0.0001	0.0001	0.0001	0.0001	0.0007	0.0008	0.0008	0.0011	0.0009	0.0011	0.0007	0.0010	0.0014	0.0014
+Z Injection Region 1	0.0000	0.0000	0.0000	0.0000	0.0004	0.0001	0.0005	0.0001	0.0004	0.0001	0.0003	0.0001	0.0004	0.0001
+Z Injection Region 2	0.0000	0.0000	0.0001	0.0000	0.0007	0.0002	0.0007	0.0003	0.0009	0.0002	0.0006	0.0003	0.0013	0.0004
Shaft	0.0000	N/A	0.0000	N/A	0.0002	N/A	0.0004	N/A	0.0004	N/A	0.0004	N/A	0.0004	N/A
TM Corner Sphere	N/A	24.5474	N/A	24.5322	N/A	24.9012	N/A	24.9269	N/A	26.0229	N/A	27.9796	N/A	24.7268
TM Corner Region	N/A	8.7344	N/A	8.7322	N/A	8.7967	N/A	8.7965	N/A	9.2304	N/A	10.0027	N/A	8.4587
TM Caging Hole	N/A	0.1103	N/A	0.1149	N/A	0.2815	N/A	0.2937	N/A	0.2980	N/A	0.2753	N/A	0.3229
Wasted Light	16.6843	0.0001	16.7693	0.0001	16.5339	0.0030	16.6660	0.0047	15.6872	0.0040	14.4024	0.0031	17.4427	0.0048
Useful Total	15.4778	64.8034	15.4130	64.7944	16.6701	65.1958	17.1176	65.0096	16.9279	66.4657	16.5267	68.5958	16.7516	65.2075

Table 5.3: Percentage of UV absorbed by four-mass surfaces upon test mass illumination. Unknown reflection properties were varied.

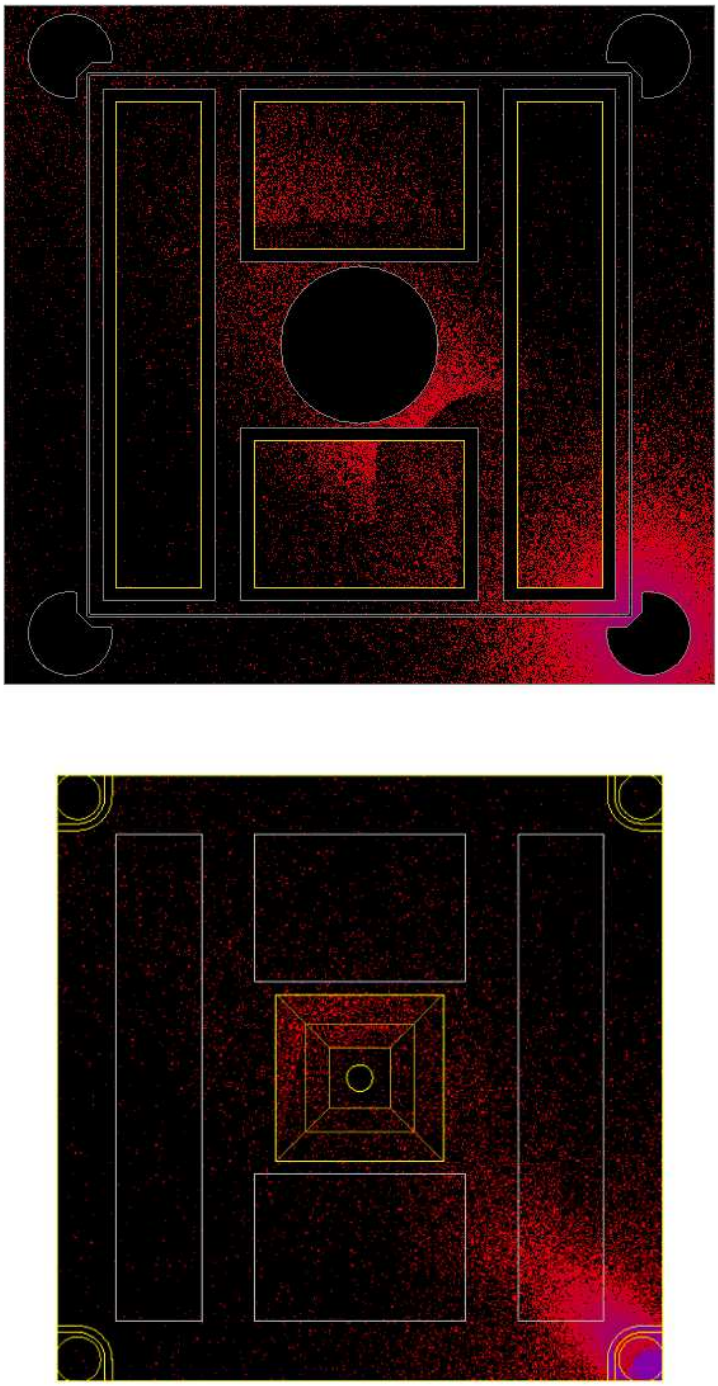

Figure 5.8: Distribution of absorbed UV light upon illuminating the four-mass test mass. *Top:* Absorption taking place on the housing lower z face. *Bottom:* Absorption taking place on the test mass lower z face. The test mass sides and electrodes were given purely specular properties, the test mass corner regions had a $\sigma_{\mathrm{tm}} = 15°$ and the housing had a $\sigma_{\mathrm{eh}} = 25°$. Purple represents high absorption, red low absorption and black zero absorption.

The ray trace also allows several general observations to be made about the four-mass discharge system, that are true whichever properties the unknown reflection distributions take. For example, a large percentage of light is effectively 'wasted', particularly when illuminating the housing where $63-73$ % of the light is absorbed within gaps and particularly the nearest caging hole. A further general observation is that upon illuminating the test mass a significant amount of light falls on the x and y faces in addition to the nominal z face. These general observations are shown clearly in Figures 5.7 and 5.8. The colour-maps show visually the distribution of absorbed UV light for the two illuminations. It is clear that neither of the illuminations are ideal and are due to the design of the inertial sensor caging mechanism changing significantly after the discharging setup was finalised.

5.1.5.1 Estimating Quantum Yields

In conjunction with the four-mass discharging results presented in Chapter 3, Section 3.4.2.3, the ray trace can be used to estimate the quantum yields of both the housing and test mass. One will recall that the apparent yield is defined as the net number of electrons exchanged with the test mass per UV photon entering the inertial sensor. For the housing illumination the maximum apparent yields were approximately $+1.03 \pm 0.02 \times 10^{-5}$ e/photon and $-2.4 \pm 0.5 \times 10^{-6}$ e/photon. Likewise, for the test mass illumination the maximum apparent yields were approximately $+8.8 \pm 0.1 \times 10^{-5}$ e/photon and $-1.7 \pm 0.1 \times 10^{-6}$ e/photon. These apparent yields are measured when the maximum photocurrent flows in one direction while the opposing photocurrent is completely suppressed. To obtain the true quantum yields, the number of photoelectrons emitted by a surface per absorbed photon, one needs to know what fraction of the total UV light is absorbed by particular surfaces. The ray trace allows these absorption fractions to be estimated.

It has been found that the absorption fractions obtained using the best educated guess parameters of $\sigma_{\mathrm{tm}} = 15^{\circ}$ and $\sigma_{\mathrm{eh}} = 25^{\circ}$ provide good results while being physically consistent with the known properties of the system. For the housing illumination, from Table 5.2, the total fraction of 'useful' light absorbed by the housing is 0.2470 and for the test mass is 0.0858. Using these values with the measured apparent yields gives a quantum yield for the housing surfaces of $9.7 \pm 2.0 \times 10^{-6}$ e/photon and for the test mass $1.20 \pm 0.02 \times 10^{-4}$ e/photon. If one does the same for when the test mass is illuminated one obtains absorption fractions of 0.6501 for the test mass and 0.1712 for the housing surfaces. These give quantum yields of $9.9 \pm 0.6 \times 10^{-6}$ e/photon for the housing and $1.35 \pm 0.01 \times 10^{-4}$ e/photon for the test mass surfaces. These quantum yield estimates include the statistical

measurement error but any systematic error in the absorption fractions is not included.

There are two things that are immediately striking about these quantum yield estimates. Firstly, the estimates obtained when either the housing or test mass are illuminated are fairly consistent with each other with the housing surfaces agreeing within experimental error and the test mass deviating by $\sim 10\,\%$. Given that the two ISUKs illuminate different corners of the sensor this suggests that not only does the test mass have fairly homogeneous properties but the properties of the housing are both homogeneous and similar to the electrodes. Secondly, these estimates confirm that the test mass is considerably more emissive than the housing surfaces with the quantum yield being $\sim 13\times$ higher.

What is also nice about these estimates is that they begin to build confidence in the simulation. The quantum yield estimates do not allow one to discriminate between the different reflection distribution parameters, as they all produce reasonable, and fairly similar results. However, they do suggest that there are no fundamental problems with the ray trace and that the total amount of light absorbed in either case is approximately correct. What is also reassuring is that the quantum yields estimated for the housing and electrodes are within the mid-range of values measured for gold at Modena, discussed in Chapter 4. The test mass however seems to show unusually high emission compared to previously measured values. The reason for this is the subject of a intense project level study.

5.1.6 Flight Model

As has been noted, there are several differences between the sensor used at the four-mass experiment and the flight system, the most significant being the presence of iridium caging fingers and the distribution of light emitted from the ISUK. The flight model ray trace allows one to examine how these differences will affect discharging. As before, the results are summarised in Tables 5.4 and 5.5, showing the ISUK aimed at the housing and test mass respectively. The corresponding colour-maps are shown in Figures 5.9 and 5.10.

The results show that when illuminating the test mass there is little change in the absorbed light distributions with the test mass absorbing $65 - 68$ % and the housing surfaces $17 - 18$ %. The similarity can also be seen in the test mass illuminated colour-map, with the main difference from the four-mass case being the caging finger absorbing $1 - 3$ % of the light. However, when illuminating the housing a significant difference is seen. While the caging finger prevents some of the light entering the caging hole, and therefore being 'wasted', the light is instead either absorbed by the finger or reflected back into the system, most likely towards the test mass. The housing surfaces absorb slightly more light than in the four-mass case, $22 - 30$ %, but the test mass absorbs up to twice as much $13 - 20$ %. The caging fingers themselves absorb $22 - 25$ %. Unfortunately, the iridium fingers are not expected to produce photoelectrons at 254 nm, with the Modena study unable to detect a measurable photocurrent from an iridium surface, Chapter 4, Section 4.3. Both the light absorbed by the caging finger and the additional light absorbed by the test mass are clearly seen in the colour-map, Figure 5.9.

Purely in terms of the UV light absorption, the flight situation is worse than the four-mass setup. However, the photoelectric properties of the surfaces will have the most significant affect on the discharging behaviour.

	All Specular		All $\sigma_\alpha = 1°$		All $\sigma_\alpha = 15°$		$\sigma_{\mathrm{tm,cf}} = 15°$, $\sigma_{\mathrm{eh}} = 25°$		All $\sigma_\alpha = 25°$		All $\sigma_\alpha = 45°$		All Lambertian	
Surface	EH	TM	EH	TM	EH	TM	EH	TM	EH	TM	EH	TM	EH	TM
-X Housing Region	0.7683	0.0857	0.7904	0.0934	1.9038	0.3221	2.0793	0.3012	2.7712	0.4025	3.5454	0.3568	5.6533	1.0274
-X Sense Region 1	0.0090	0.0063	0.0093	0.0073	0.0318	0.0262	0.0291	0.0222	0.0417	0.0342	0.0386	0.0300	0.0527	0.0427
-X Sense Region 2	0.0529	0.0242	0.0550	0.0237	0.2015	0.1158	0.1945	0.1139	0.2919	0.1600	0.2767	0.1490	0.4979	0.2874
+X Housing Region	0.8450	0.0480	0.8683	0.0637	0.9994	0.0768	0.8320	0.0610	0.8711	0.0623	0.7571	0.0404	0.3850	0.0427
+X Sense Region 1	0.0014	0.0007	0.0012	0.0006	0.0080	0.0078	0.0077	0.0098	0.0080	0.0096	0.0048	0.0077	0.0052	0.0052
+X Sense Region 2	0.0004	0.0004	0.0005	0.0003	0.0034	0.0033	0.0042	0.0049	0.0046	0.0055	0.0039	0.0050	0.0047	0.0050
-Y Housing Region	0.7948	0.0238	0.7701	0.0222	1.0041	0.0518	0.8855	0.0472	0.9481	0.0506	0.8542	0.0364	0.5134	0.0428
-Y Sense Region 1	0.0004	0.0004	0.0007	0.0006	0.0075	0.0069	0.0076	0.0090	0.0078	0.0101	0.0061	0.0086	0.0076	0.0073
-Y Sense Region 2	0.0001	0.0001	0.0000	0.0001	0.0009	0.0009	0.0012	0.0011	0.0015	0.0012	0.0009	0.0013	0.0013	0.0012
-Y Injection Region 0	0.0001	0.0001	0.0001	0.0002	0.0027	0.0023	0.0035	0.0036	0.0043	0.0045	0.0034	0.0037	0.0045	0.0044
+Y Housing Region	0.6829	0.0706	0.7225	0.0781	1.8180	0.2812	2.0131	0.2614	2.6772	0.3497	3.3736	0.3129	5.3218	0.8269
+Y Sense Region 1	0.0418	0.0171	0.0420	0.0177	0.1497	0.0856	0.1446	0.0846	0.2190	0.1140	0.2179	0.1024	0.3545	0.1735
+Y Sense Region 2	0.0029	0.0023	0.0026	0.0024	0.0113	0.0099	0.0095	0.0085	0.0137	0.0114	0.0093	0.0092	0.0178	0.0158
+Y Injection Region 0	0.0153	0.0164	0.0158	0.0160	0.0540	0.0479	0.0467	0.0442	0.0700	0.0697	0.0580	0.0588	0.1013	0.0966
-Z Housing Region	9.2269	9.0320	9.3212	8.8844	10.2160	7.2635	11.0150	7.5145	10.7611	6.4065	11.2872	4.9203	9.6798	5.8472
-Z Sense Region 1	6.3934	4.1359	6.3578	4.1211	5.5806	2.8697	5.5545	2.7128	5.2283	2.1176	4.8854	1.3716	4.9358	1.2222
-Z Sense Region 2	0.0868	0.1129	0.1020	0.1251	0.1628	0.1343	0.1448	0.1043	0.1402	0.0985	0.1110	0.0657	0.0886	0.0568
-Z Injection Region 1	1.3748	0.2466	1.5189	0.2311	1.1444	0.1936	1.0616	0.1779	0.9494	0.1704	0.7731	0.1495	0.6616	0.1483
-Z Injection Region 2	1.7953	0.8755	1.8595	0.8949	1.4875	0.6291	1.3983	0.6008	1.2399	0.5800	0.9891	0.5007	0.9181	0.4528
+Z Housing Region	0.0467	0.0016	0.0440	0.0015	0.2908	0.0120	0.2866	0.0113	0.3728	0.0151	0.3162	0.0097	0.3722	0.0219
+Z Sense Region 1	0.0001	0.0000	0.0000	0.0001	0.0020	0.0023	0.0021	0.0027	0.0029	0.0039	0.0017	0.0030	0.0049	0.0052
+Z Sense Region 2	0.0000	0.0000	0.0000	0.0000	0.0006	0.0006	0.0006	0.0005	0.0009	0.0009	0.0004	0.0006	0.0009	0.0010
+Z Injection Region 1	0.0000	0.0000	0.0000	0.0000	0.0008	0.0002	0.0012	0.0002	0.0015	0.0004	0.0011	0.0002	0.0014	0.0003
+Z Injection Region 2	0.0000	0.0000	0.0001	0.0000	0.0022	0.0007	0.0024	0.0010	0.0032	0.0014	0.0020	0.0011	0.0046	0.0017
Caging Fingers	23.0089	N/A	22.9940	N/A	22.7898	N/A	22.0512	N/A	23.4736	N/A	25.1370	N/A	21.6509	N/A
TM Corner Sphere	N/A	1.7953	N/A	1.7913	N/A	1.5573	N/A	1.6164	N/A	1.4500	N/A	1.2309	N/A	2.0554
TM Corner Region	N/A	1.9819	N/A	2.0078	N/A	1.9848	N/A	2.0481	N/A	1.7170	N/A	1.3578	N/A	1.7156
TM Caging Hole	N/A	2.0741	N/A	2.2287	N/A	2.5630	N/A	2.4625	N/A	2.5882	N/A	2.6802	N/A	2.3918
Wasted Light	34.2565	N/A	33.8632	N/A	33.6625	N/A	33.7814	N/A	33.2628	N/A	33.8024	N/A	32.1895	N/A
Useful Total	22.1392	20.5518	22.4820	20.6118	25.0835	18.2495	25.7253	18.2255	26.6302	16.4352	27.5172	13.4132	29.5886	16.4990

Table 5.4: Percentage of UV absorbed by flight surfaces upon housing illumination. Unknown reflection properties were varied.

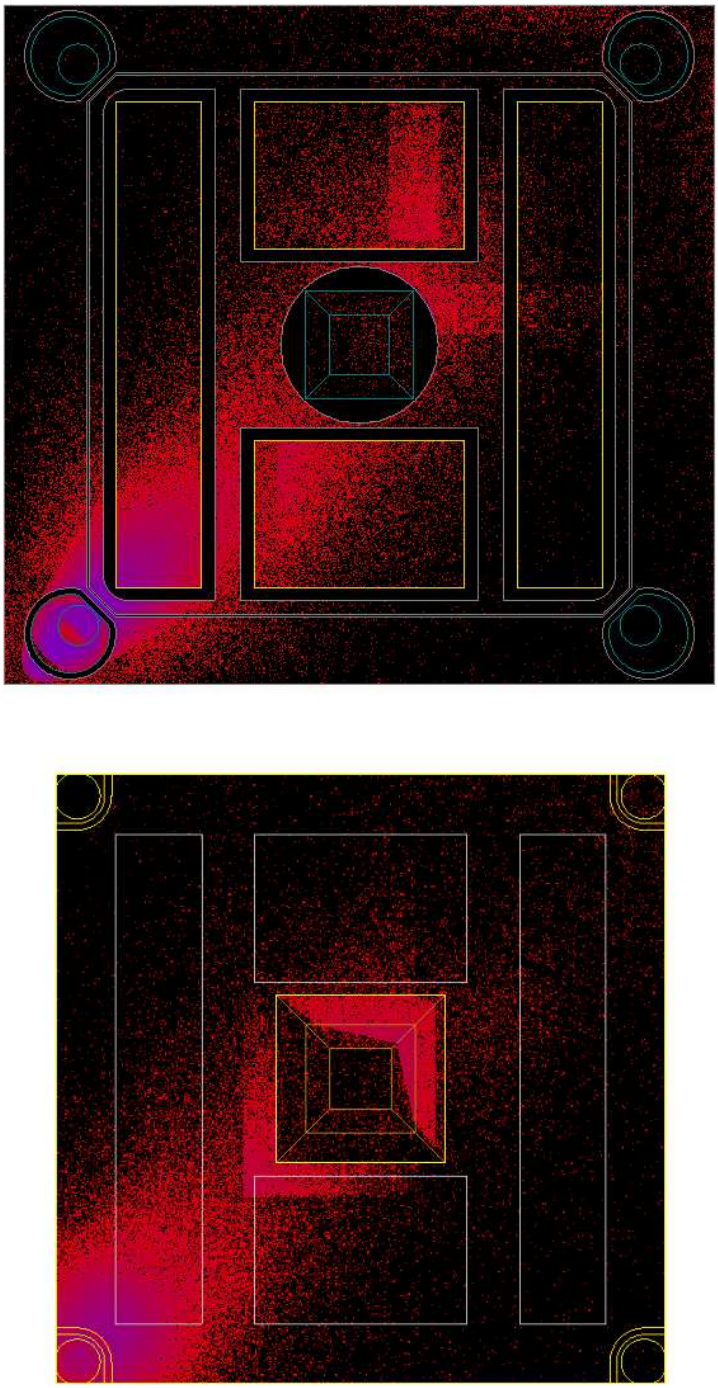

Figure 5.9: Distribution of absorbed UV light upon illuminating the flight electrode housing. *Top:* Absorption taking place on the housing lower z face. *Bottom:* Absorption taking place on the test mass lower z face. The test mass sides and electrodes were given purely specular properties, the test mass corner regions and caging fingers had a $\sigma_{\mathrm{tm}}, \sigma_{\mathrm{cf}} = 15°$ and the housing had a $\sigma_{\mathrm{eh}} = 25°$. Purple represents high absorption, red low absorption and black zero absorption.

	All Specular		All $\sigma_\alpha = 1°$		All $\sigma_\alpha = 15°$		$\sigma_{\mathrm{tm,cf}} = 15°$, $\sigma_{\mathrm{eh}} = 25°$		All $\sigma_\alpha = 25°$		All $\sigma_\alpha = 45°$		All Lambertian	
Surface	EH	TM	EH	TM	EH	TM	EH	TM	EH	TM	EH	TM	EH	TM
-X Housing Region	0.6400	0.0413	0.6457	0.0410	0.6362	0.0469	0.5614	0.0384	0.5511	0.0375	0.4652	0.0244	0.3320	0.0352
-X Sense Region 1	0.0008	0.0003	0.0011	0.0005	0.0041	0.0037	0.0046	0.0051	0.0046	0.0049	0.0035	0.0044	0.0061	0.0059
-X Sense Region 2	0.0015	0.0011	0.0013	0.0009	0.0041	0.0046	0.0039	0.0053	0.0033	0.0048	0.0021	0.0030	0.0031	0.0031
+X Housing Region	2.8738	14.0940	2.8419	14.0928	3.2072	14.1921	3.4489	14.1833	3.6009	14.1796	4.0305	14.0899	4.4438	14.6772
+X Sense Region 1	0.1701	0.1626	0.1701	0.1636	0.1278	0.1150	0.1021	0.0890	0.0972	0.0873	0.0729	0.0614	0.0750	0.0576
+X Sense Region 2	1.9669	1.3556	1.9551	1.3424	1.7722	0.9258	1.7261	0.8471	1.7075	0.8443	1.6691	0.7709	1.7471	0.8687
-Y Housing Region	0.7466	0.0370	0.7474	0.0380	0.7967	0.0483	0.6709	0.0385	0.6443	0.0365	0.5088	0.0232	0.3213	0.0278
-Y Sense Region 1	0.0006	0.0002	0.0010	0.0005	0.0051	0.0047	0.0047	0.0057	0.0050	0.0051	0.0032	0.0046	0.0051	0.0044
-Y Sense Region 2	0.0004	0.0002	0.0003	0.0004	0.0013	0.0013	0.0012	0.0013	0.0012	0.0013	0.0008	0.0007	0.0005	0.0006
-Y Injection Region 0	0.0015	0.0007	0.0009	0.0006	0.0041	0.0037	0.0044	0.0044	0.0038	0.0042	0.0022	0.0025	0.0026	0.0026
+Y Housing Region	2.1389	13.8957	2.1255	13.8820	2.3475	13.9640	2.5387	13.9469	2.6641	13.9788	2.9788	13.9109	3.5293	14.2764
+Y Sense Region 1	2.1435	1.2515	2.1429	1.2410	1.9790	0.9444	1.9451	0.9028	1.9264	0.8960	1.8960	0.8660	1.9512	0.9203
+Y Sense Region 2	0.0111	0.0075	0.0104	0.0074	0.0076	0.0066	0.0067	0.0056	0.0055	0.0053	0.0039	0.0042	0.0060	0.0056
+Y Injection Region 0	0.1743	0.1528	0.1718	0.1508	0.1481	0.1150	0.1387	0.1045	0.1336	0.1009	0.1200	0.0834	0.1319	0.0984
-Z Housing Region	4.6388	2.2269	4.6519	2.2296	4.7381	2.3751	5.0440	2.3593	4.5958	2.2639	4.0626	2.0407	3.6515	2.5093
-Z Sense Region 1	0.0630	0.0220	0.0662	0.0288	0.0866	0.0615	0.0823	0.0516	0.0822	0.0521	0.0716	0.0393	0.0782	0.0483
-Z Sense Region 2	0.3823	0.9419	0.3829	0.9460	0.4863	0.9762	0.4828	0.9769	0.4160	0.9507	0.2868	0.8924	0.2081	0.9258
-Z Injection Region 1	0.3592	0.1111	0.3574	0.0963	0.3855	0.0732	0.3660	0.0671	0.3468	0.0658	0.3123	0.0518	0.3138	0.0561
-Z Injection Region 2	0.5233	0.0716	0.5200	0.0745	0.5217	0.0997	0.5099	0.1071	0.4581	0.0988	0.3831	0.0886	0.3800	0.1167
+Z Housing Region	0.2250	0.0066	0.2291	0.0067	0.1616	0.0069	0.1648	0.0065	0.1392	0.0054	0.1213	0.0037	0.1247	0.0078
+Z Sense Region 1	0.0001	0.0000	0.0000	0.0000	0.0003	0.0003	0.0004	0.0005	0.0003	0.0005	0.0002	0.0003	0.0003	0.0003
+Z Sense Region 2	0.0002	0.0003	0.0002	0.0003	0.0014	0.0015	0.0012	0.0016	0.0010	0.0015	0.0007	0.0010	0.0016	0.0016
+Z Injection Region 1	0.0000	0.0000	0.0000	0.0000	0.0006	0.0002	0.0007	0.0002	0.0006	0.0002	0.0005	0.0002	0.0006	0.0001
+Z Injection Region 2	0.0001	0.0000	0.0001	0.0000	0.0012	0.0004	0.0015	0.0005	0.0010	0.0004	0.0008	0.0004	0.0015	0.0006
Caging Fingers	3.1675	N/A	3.1579	N/A	2.3238	N/A	2.2445	N/A	1.8995	N/A	1.4775	N/A	2.1674	N/A
TM Corner Sphere	N/A	20.8498	N/A	20.8807	N/A	21.2647	N/A	21.2813	N/A	22.1838	N/A	23.8490	N/A	21.1090
TM Corner Region	N/A	9.5657	N/A	9.5451	N/A	9.4913	N/A	9.5128	N/A	9.9567	N/A	10.7021	N/A	9.1152
TM Caging Hole	N/A	0.1637	N/A	0.1692	N/A	0.3803	N/A	0.3984	N/A	0.4051	N/A	0.3837	N/A	0.4466
Wasted Light	14.7594	N/A	14.8231	N/A	15.0113	N/A	14.9069	N/A	14.4622	N/A	13.5805	N/A	15.1704	N/A
Useful Total	17.0617	64.9602	17.0231	64.9390	17.4241	65.1073	17.8109	64.9415	17.3893	66.1711	16.9969	67.9023	17.3154	65.3210

Table 5.5: Percentage of UV absorbed by flight surfaces upon test mass illumination. Unknown reflection properties were varied.

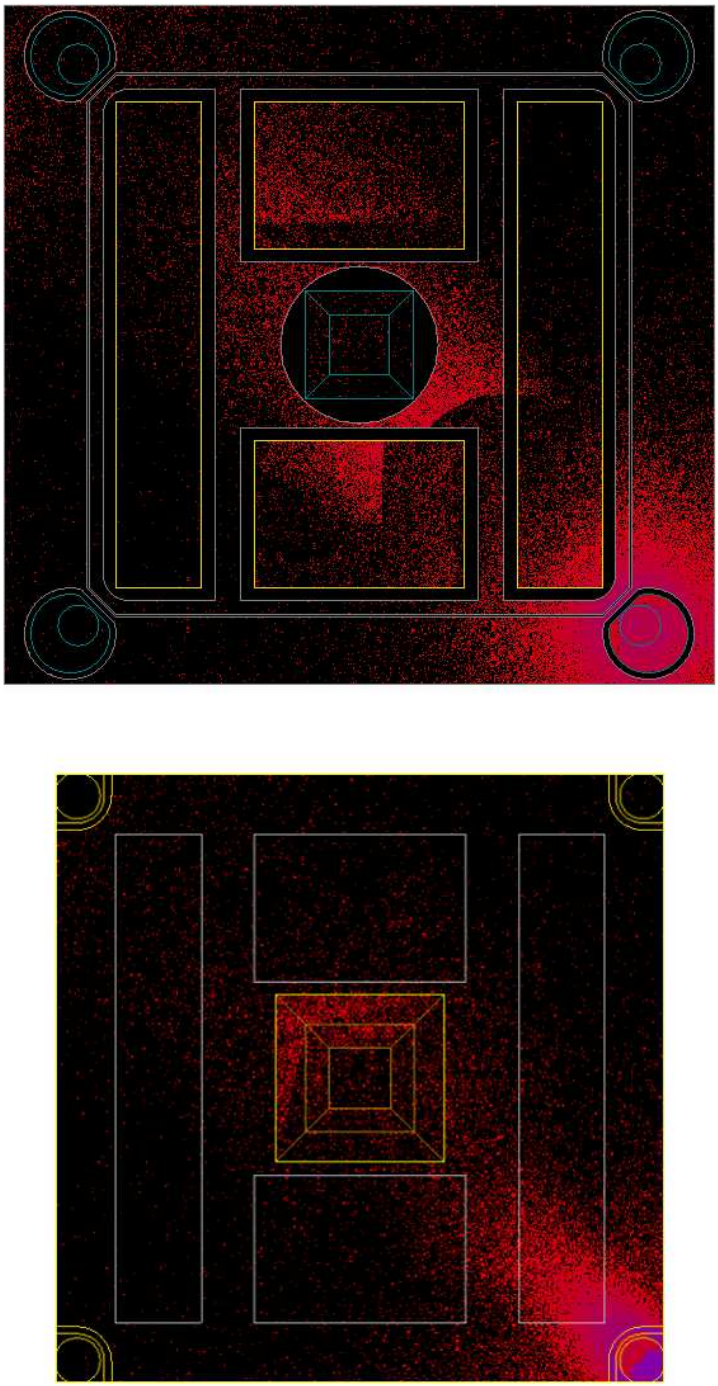

Figure 5.10: Distribution of absorbed UV light upon illuminating the flight test mass. *Top:* Absorption taking place on the housing lower z face. *Bottom:* Absorption taking place on the test mass lower z face. The test mass sides and electrodes were given purely specular properties, the test mass corner regions and caging fingers had a $\sigma_{\mathrm{tm}}, \sigma_{\mathrm{cf}} = 15^{\circ}$ and the housing had a $\sigma_{\mathrm{eh}} = 25^{\circ}$. Purple represents high absorption, red low absorption and black zero absorption.

5.1.7 Conclusions

Two Geant4 ray trace simulations have been created with inertial sensor geometries representative of both the Trento four-mass pendulum and the Pathfinder flight model. Most of the parameters that describe these systems have either taken literature values or have been experimentally measured, detailed in Chapter 4. The remaining unknown properties of the system are the reflected light distributions from the rough gold coated housing, iridium caging fingers and the test mass corner regions. While it is difficult to predict with confidence the exact form these distributions will take, their properties are constrained. Unlike the test mass sides and electrodes, the rough surfaces R_a estimates suggest they will not exhibit purely specular reflection. Instead a micro-facet model has been invoked which describes a surface with a parameter σ_α. In the future, when suitable surfaces become available the remaining unknown reflection distributions can be experimentally measured and added to the simulations. In the absence of these measurements the parameters that describe the reflection distributions of the unknown surfaces have been varied and their affect observed.

Whatever the form of the unknown reflection distributions there are some things that can be said with confidence:

- In the four-mass system, when illuminating the housing, a significant amount of light is shone directly into the caging finger recess.
- In both four-mass and flight cases, when illuminating the test mass, light is aimed directly at the complex test mass corner region.
- In both four-mass and flight cases, when illuminating the test mass, a significant amount of light unintentionally reaches the x and y faces.
- Results suggest that in terms of where the UV light is absorbed, the discharge situation will be worse in flight, mainly due to the presence of the iridium caging fingers.

The best educated guess for the reflection parameters are $\sigma_{\mathrm{tm}} = 15^\circ$ and $\sigma_{\mathrm{eh}} = 25^\circ$ and these values have been found to give reasonable and consistent four-mass quantum yield results. It will be shown in the next section that describing the unknown surfaces with these reflection parameters, and the quantum yields obtained using them, give good results for the rest of the torsion measurements. This suggests that either the reflection distributions used are close to the true situation or that any discrepancy present does not significantly affect the discharging behaviour.

5.2 Photoelectron Flow Model

A simple photoelectron flow model has been developed in MATLAB. By making several assumptions and approximations it uses the output of the ray trace to estimate the performance of the entire system, given the photoelectric properties of the individual surfaces. The photoelectron flow model's core concept is to split the inertial sensor up into adjacent pairs of regions on the test mass and electrode housing. The net flow of photoelectrons between these parallel surfaces can then be estimated, while taking into account the potential difference between the surfaces as well as the energy distribution of the emitted photoelectrons. The measurements made with the four-mass pendulum experiment, described in Chapter 3, Section 3.4, have been used to help verify the model and the performance of the flight system has then been estimated.

5.2.1 Model Approximations

The photoelectron flow model aims to provide first-order estimates of the system's performance, in a reasonable time-scale. With this in mind several approximations have been made and the number of parameters describing the system has been kept to a minimum. The first approximation is that the model treats each pair of surfaces, for example a sense electrode and its adjacent area on the test mass, as parallel plates. A uniform electric field is then assumed between the two regions with edge effects being ignored. This is probably a reasonable approximation for the main faces of the test mass but breaks down in the corner regions.

The next approximation within the model is that the photoelectrons are emitted perpendicular to the surface and are therefore confined to any initial electric field and can only reach the adjacent region. According to the literature this is probably quite a poor approximation with the photoelectrons likely being emitted with a particular angular distribution. Indeed Pei and Berglund (2002) observed a cosine distribution when illuminating 15 nm gold thin films with 257 nm UV light. It should be noted however that this experiment studied the transmitted photoelectrons from the side of the film opposite to that of illumination. Earlier work by Pauty et al. (1974) on bulk gold with 254 nm UV illumination suggests a more complex angular distribution though no photoelectrons were observed to be emitted with an angle greater than 60° from the surface normal.

The affect of a possible angular distribution in the emitted photoelectrons would be most noticeable when there is only a weak electric field present which some of the photoelectrons could escape. It can be argued that given the relatively low energy of

the photoelectrons, typically a few tenths of an eV, the electric fields dominate when determining the path of the photoelectrons and any possible angular distribution can be ignored. A similar argument can be made for photoelectrons generated within the housing gaps not being able to escape when a field is present. Even when no field is present it is unlikely an electron will be emitted with an angle large enough to be able to escape the gaps. A related approximation is that photoelectrons emitted from the corners of the main housing surfaces are treated as if they are adjacent to the test mass. Again, with increasing electric field strengths these photoelectrons final destination will be the same whether they are adjacent to the test mass or not. The main concern is whether an electron passes between the test mass and housing, or vice-versa, not which direction it takes.

Another assumption used within the model is that the photoelectrons can traverse the gaps before the time varying electric fields vary significantly. This is a fairly good approximation given that the photoelectron energies are of the order of ~ 0.1 eV, having typical velocities of $\sim 2 \times 10^5$ ms^{-1}. This means that approximate crossing times for the largest gaps of 4 mm are around 20 ns, much smaller than the time period of the fastest AC fields used for sensing, 10000 ns. Therefore during the time a photoelectron is propagating within the system it experiences quasi-static electric fields.

In an effort to use as few parameters as possible to describe the system the photoelectric properties of the test mass are assumed to be uniform as well as those of the housing and electrodes. It is not unreasonable that the photoelectric properties could have varied between surfaces or even across a single surface. However, as in the previous section it has been found that the four-mass results can be adequately fit with uniform properties. Also following on from the previous section, the output from the ray trace using $\sigma_{\mathrm{tm}} = 15^\circ$ and $\sigma_{\mathrm{eh}} = 25^\circ$ reflection parameters have been used in all the following analysis.

5.2.2 Photoelectron Energy Distributions

As discussed in Chapter 4, Section 4.3.4, the emitted photoelectrons have a distribution of energies but its precise form is unclear, though it seems approximately triangular. With this in mind a fairly general triangular function has been used to describe the distribution in photoelectron energies, shown in Figure 5.11.

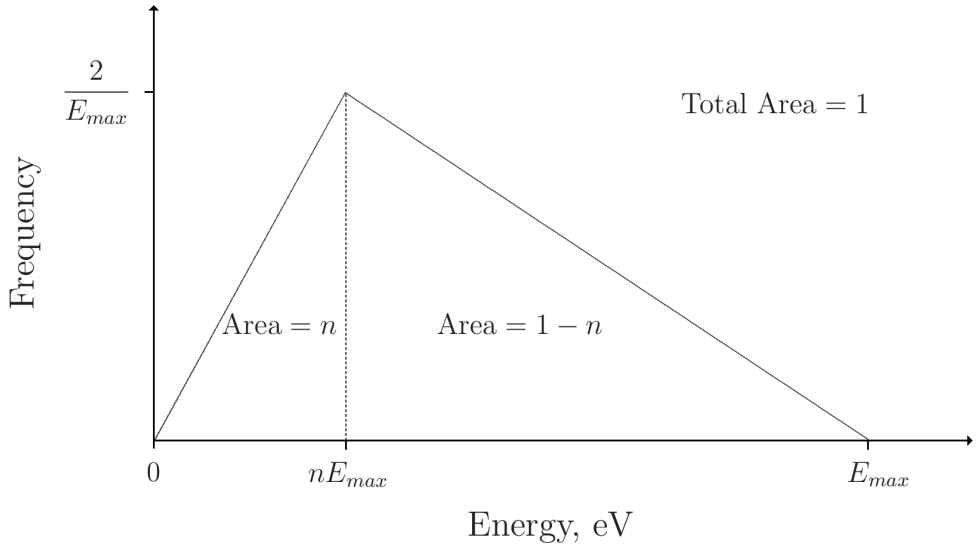

Figure 5.11: The triangular distribution used to model the energy of the emitted photoelectrons.

The triangular distribution is described with just two parameters, E_{max} and n. The parameter E_{max} is the maximum energy in eV a photoelectron can have which is given by $4.88 - \phi$, where ϕ is the work function. The parameter n defines at what fraction of E_{max} the triangular distribution peaks. The triangular distribution is defined by two linear equations:

$$f(E) = \begin{cases} 0 & \text{if } E < 0 \\ \frac{2E}{nE_{max}^2} & \text{if } 0 < E \leq nE_{max} \\ \frac{2}{E_{max}(1-n)} - \frac{2E}{E_{max}^2(1-n)} & \text{if } nE_{max} < E < E_{max} \\ 0 & \text{if } E > E_{max} \end{cases}$$

Within the model one assumes that the photoelectrons are emitted perpendicularly towards an adjacent surface. Only a certain fraction of the photoelectrons have sufficient energy to overcome a given retarding potential difference between the two surfaces, V. This fraction, $F(V)$ can be obtained by integrating the triangular distribution and considering the four possible situations:

$$F(V) = \begin{cases} 1 & \text{if } V < 0 \\ 1 - \frac{V^2}{nE_{max}^2} & \text{if } 0 < V \leq nE_{max} \\ \frac{1}{(1-n)}\left(1 - \frac{2V}{E_{max}} + \frac{V^2}{E_{max}^2}\right) & \text{if } nE_{max} < V < E_{max} \\ 0 & \text{if } V > E_{max} \end{cases}$$

In the first case the potential difference does not oppose the photoelectrons at all, therefore they all make it across the gap. In the middle two cases the potential difference means only a certain fraction of the photoelectrons have sufficient energy to overcome it. In the final case the potential difference is so large that none of the photoelectrons have enough energy to overcome the opposing potential.

5.2.3 Model Routine

Before the photoelectron flow model is run the user needs to specify several settings and parameters. First, a ray trace file needs to be chosen which contains the percentage of light each surface absorbs for a given illumination. For all the results presented here the file produced with the unknown reflection distributions of $\sigma_{\text{tm}} = 15°$ and $\sigma_{\text{eh}} = 25°$ were used. The user then needs to specify both the quantum yields and work functions of all the surfaces. Here all the test mass surfaces take the same values as do all the housing and electrode surfaces. Similarly, the parameter n which describes the photoelectron energy distribution needs to be given.

Both the AC and DC voltages applied to the injection and sense electrodes can be defined, with the number of times per period the AC biases are sampled also chosen. For the results presented here the 100 kHz AC injection bias was sampled 128 times per period. Finally the user chooses the UV power of the light entering the system, typically 6 nW, and the number of seconds the lamp is turned on. If necessary the test mass can also be given an initial charge. The model then runs in the following sequence:

- The size of the smallest time step is calculated, given by the fastest AC time period divided by the number of times it should be sampled.
- The maximum number of photoelectrons each surface can emit during a time step is calculated, given the percentage of light each surface absorbs, the total intensity of light entering the system and the quantum yield of each surface.
- The model then enters a loop for the number of seconds the lamp is turned on, progressing one time step at a time.
- At each time step the instantaneous test mass potential is calculated using Equation 3.4, described in Chapter 3:

$$V_{TM} = \frac{q}{C_T} + \sum_i \frac{C_i \delta V_i}{C_T}$$

- The instantaneous potential difference between each housing surface and the test mass is then calculated, while considering any voltages applied to the electrodes.
- For each pair of surfaces the fraction of photoelectrons flowing in either direction, given the instantaneous potential difference, is calculated for the current time step.
- A total net flow of photoelectrons towards or away from the test mass then alters the charge on the test mass for the next time step.
- The time, test mass potential, test mass charge and net yield is read out.
- The run finishes when the sum of the time steps is equal to the length of time the lamp was specified on.

5.2.4 Results

A photoelectron flow model was created for both the four-mass and the flight case. They are identical in operation with only small differences in the surfaces they consider, for example the shaft or caging fingers. In order to verify the performance of the four-mass model it was used to reproduce the measurements made at the torsion pendulum, discussed in Chapter 3. Given, the fairly simplistic nature of the models it was decided to only specify the system parameters to one decimal place. Of the six unknown parameters, the work functions and quantum yields of the test mass and housing were well constrained with only the two n parameters having scope to be varied. The run times ranged from a few minutes to several hours, depending on the property being determined.

5.2.4.1 Four-Mass Pendulum Model

The quantum yields of the test mass and housing surfaces had been heavily constrained, independently of the photoelectron flow model, as discussed in Section 5.1.5.1. One will recall that the two illuminations produced fairly consistent results, suggesting homogeneous surface properties. For the results discussed here the mean values of the quantum yields obtained previously were used. The quantum yield for the test mass was taken as 1.3×10^{-4} e/photon and 9.8×10^{-6} e/photon for the housing and electrodes. Based on the four-mass measurements the work functions could realistically only take certain values with the test mass work function being constrained between 3.4 and 3.9 eV and the housing and electrodes between 4.2 and

4.7 eV. It was found by manually varying these parameters that values of 3.8 eV and 4.5 eV, for the test mass and housing respectively, gave the best results. As one might expect, the work function of the more emissive test mass is considerably lower than the housing. Finally the parameter n, which describes the shape of the photoelectrons energy distribution, was found to give the best results when it took the value 0.2 in all cases. It should be kept in mind that the parameters need to be consistent for all the measurements and both illuminations.

Figure 5.12 shows how the simulated apparent yield measurements compare to those obtained at the four-mass experiment, previously discussed in Chapter 3, 3.4.2.3. All apparent yield measurements were taken with an injection voltage of 0.054 V at 100 kHz AC and show how the net yield of the system varies with the test mass potential, for both illuminations. The apparent yield measurements also demonstrated the effect of the different photoelectric parameters. The quantum yields determine the values reached at the asymptote plateaus, the work functions determine the point at which these plateaus are reached and the parameter n determines the shape of the slope between the two plateaus.

The results shown in Figure 5.12 show good qualitative and fairly good quantitative agreement between simulated and measured behaviour. The biggest quantitative difference comes at around zero test mass potential with the housing illumination. Nevertheless, the agreement between the simulated and measured data is surprisingly good considering the simplicity of the model and the number of steps involved in arriving at an answer.

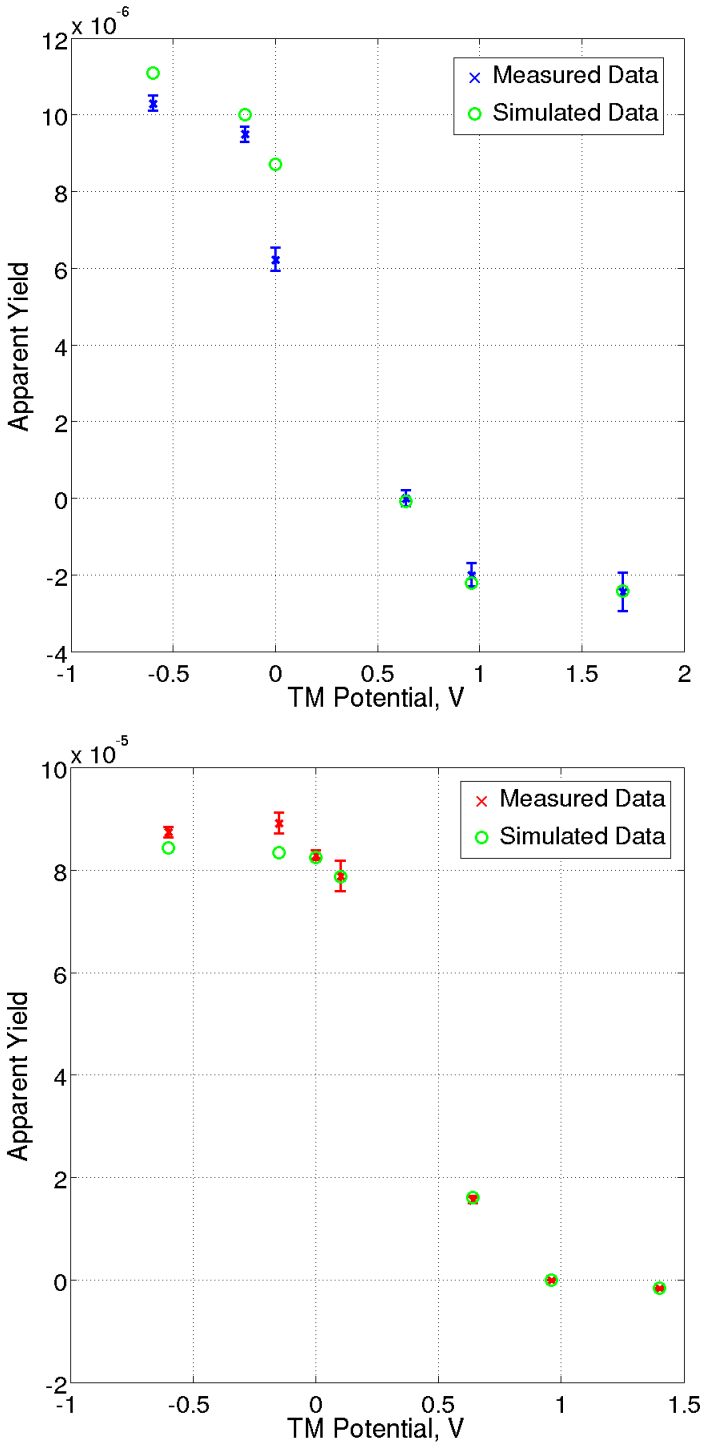

Figure 5.12: The simulated and measured apparent yields at different test mass potentials, for both illuminations. *Top*: Illuminating electrode housing. *Bottom*: Illuminating test mass.

Figure 5.13 shows the equilibrium potential the test mass reaches when the amplitude of the injection bias is varied for both illuminations with no applied DC biases. Again, the simulated results show good qualitative and fairly good quantitative agreement between simulated and measured behaviour. It should be noted that the nominal behaviour of the system would be for a negative test mass equilibrium potential to be reached upon electrode housing illumination. The fact that it does not is due to a combination of non-optimal illumination of the electrode housing and the test mass having a quantum yield more than an order of magnitude greater than the housing.

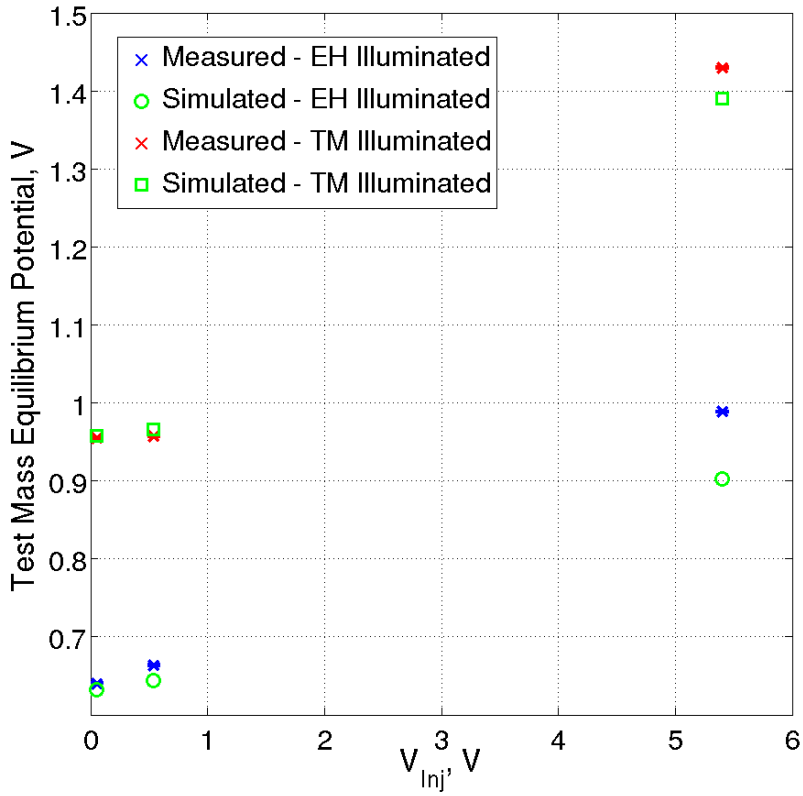

Figure 5.13: The simulated and measured equilibrium potential reached with 100 kHz AC injection voltages of 0.054, 0.54 and 5.4 V. While qualitatively the simulated results are good there is some quantitative disagreement, particularly at 5.4 V.

The excellent quantitative agreement of the results at 0.054 V between simulation and measurement should be emphasised. As shown in Figure 5.13 the experimentally measured test mass equilibrium potential was 0.641 ± 0.001 V when the housing was illuminated and 0.955 ± 0.001 V for the test mass illumination. The compares to simulated results of 0.632 V and 0.958 V respectively.

Finally, one will recall the technique of applying appropriate DC biases in order to charge the test mass negatively when illuminating the housing. It was shown at the four-mass experiment that the test mass potential could be brought down to -0.614 ± 0.001 V. This involved using a 0.054 V, 100 kHz AC injection bias and +4.5 V applied to all the x sense electrodes, +5.0 V to all the y sense electrodes and +4.5 V to just the upper z sense electrodes. Using the same settings the simulation reached an equilibrium potential of -0.595 V. The good agreement in this result is particularly pleasing as it relies on the accurate modelling of different biases being applied in different regions.

While the simulated results are generally very good there are some discrepancies. This is not surprising given the simplicity of the model and likely can be explained by a combination of two weaknesses. Firstly, although the UV ray trace can approximately predict the total amount of light absorbed by either the test mass or housing, the exact distribution in absorbed UV light is still uncertain. To predict this with confidence one requires measurements of the reflection profiles of the rough surfaces. As the distribution in absorbed light determines which electric fields emitted photoelectrons are influenced by, this affects the discharging behaviour. It should be noted that the distributions currently predicted with $\sigma_{\mathrm{tm}} = 15°$ and $\sigma_{\mathrm{eh}} = 25°$ do not seem far off the true properties given the subsequent good agreement with the measured discharge properties. Possible evidence for this theory is the fact that the model has trouble fitting the results at large applied injection bias. This could suggest the amount of UV absorbed within the injection electrode regions is out, though not by a large amount.

The second weakness in the simulation, and possibly the more likely cause of the discrepancies, is that it assumes that the photoelectrons only travel between adjacent surfaces. This is a good approximation when potential differences are large, greater than the photoelectron energies in eV, as the resulting electric fields dominate the photoelectron trajectories. However, when the potential differences are small, less than the energy of the photoelectrons in eV, the likely cosine distribution in the direction of emitted photoelectrons would allow some of them to cross into different regions. In the case of photoelectrons emitted from the housing, when the potential differences are small some would miss the test mass altogether. In addition, some photoelectrons emitted within the gaps could reach the test mass. Possible evidence for this theory is the fact that the model has trouble fitting the results when the the test mass potential is near zero and the housing is illuminated.

5.2.4.2 Flight Model

A photoelectron flow model was also created for the flight system. As was shown in Section 5.1.6, the UV light distributions within the sensor are different in the flight case, mainly due to the presence of the iridium caging fingers. The ray trace results for the test mass illumination are very similar to the four-mass situation but for the housing illumination they are worse as the test mass absorbs more reflected light. To see the effect this may have on discharge performance, the flight simulation was run assuming the photoelectric properties of the surfaces are the same as those in the four-mass sensor. This is likely a very poor assumption, as will be discussed, but allows the affect of the UV distributions to be observed. Based on the measurements at Modena, Chapter 4, the iridium caging fingers were assumed to give zero emission at 254 nm, while the uncoated $Au_{0.7}Pt_{0.3}$ corner domes were given the same photoelectric properties as the gold.

The equilibrium potential the test mass reaches when the 100 kHz AC injection bias is 0.054 V and no DC biases are applied was found to be 0.770 V and 0.957 V, for the housing and test mass illuminations respectively. This shows no change from the four-mass simulation for the test mass illumination and an increase for the housing illumination. A similar increase was found when DC biases were applied to the electrodes and the housing illuminated. With +4.5 V applied to all the x sense electrodes, +5.0 V to all the y sense electrodes and +4.5 V to just the upper z sense electrodes, the test mass potential was found to be −0.563 V. This is encouraging as even with the absorption distributions becoming worse with the flight housing illumination, it is still possible to charge the test mass negatively.

Of course this brief analysis of the flight situation ignores the fact that the photoelectric properties of the surfaces could be completely different in the flight sensor. The Modena measurements appear to show a large variation in properties for nominally identical surfaces. However, the four-mass measurements seem to show homogeneous properties for the test mass and housing. Also, the housing and electrodes seem to have similar properties even though they were coated separately. There has been a suggestion that the baking out of the four-mass system while in vacuum acted to stabilise and homogenise the surface properties, which was not done in a controlled way at Modena. If the photoelectric properties of the flight surfaces are significantly different the discharge behaviour could be completely changed, possibly for the worse. The worst case scenario would be that bipolar discharging were impossible, irrespective of the applied DC biases. Efforts are being made to not only minimise the chance of the flight system being worse but actually improve on the four-mass performance. These efforts will be discussed in the next section.

5.2.5 Conclusions

A simple photoelectron flow model has been developed for both the four-mass and flight system to simulate the discharging performance. It uses the output from the UV ray trace and a set of three parameters to describe the photoelectric properties of each surface. By considering the electric fields present it allows several properties of the system as a whole to be calculated. Using the ray trace results generated with $\sigma_{\mathrm{tm}} = 15°$ and $\sigma_{\mathrm{eh}} = 25°$ it has been shown that with a small set of parameters, that are consistent and physically realistic, the four-mass results can be reproduced. The parameters used to reproduce the four-mass results were a test mass quantum yield of 1.3×10^{-4} e/photon, a work function of 3.8 eV and an energy distribution parameter $n = 0.2$. The housing and electrodes had a quantum yield of 9.8×10^{-6} e/photon, a work function of 4.5 eV and an energy distribution parameter $n = 0.2$.

The ability of the photoelectron flow model to reproduce the behaviour observed at the four-mass experiment is encouraging and also builds further confidence in the UV ray trace. The simulation results show that the four-mass measurements are consistent with homogeneous surface properties but that the test mass is $\sim 13\times$ more emissive than the housing and electrodes. Interestingly, given that the separate housing and electrode surfaces appear to have the same properties it seems that the test mass is the odd one out. This may suggest that the test mass gold coating has some form of contamination which is not present with the housing or electrodes.

To improve the photoelectron flow model would take a considerable change in approach. Ideally, one would track each individual photoelectron through the system which would be emitted with a randomly sampled angular distribution. The time dependant electric fields within the sensor would also need to be accurately predicted and taken into account. Geant4 has the capability for such a model but a simulation of this complexity would be extremely time consuming to run.

5.3 Studying Possible Solutions

As has been discussed in the preceding chapters, the performance of the flight charge management system for Pathfinder is currently uncertain. To summarise, testing with the four-mass system has revealed an inability under nominal operational conditions to achieve bi-polar discharge. In all previous discharge testing no such problem was observed. Further analysis of the measurements and simulation of the four-mass system suggest the cause is a more than an order of magnitude difference in surface quantum yields. Ray tracing simulations also suggest that this problem is accentuated by non-optimal illumination of the housing, where a large fraction of light is either wasted or unintentionally reflected onto the test mass. Fortunately, bi-polar discharging has been demonstrated with the four-mass system but only using applied DC biases, which is not ideal. It is however possible that the properties of the flight system could conspire to prevent even this being accomplished. Such uncertainty in performance is clearly unacceptable for a vital flight system and great effort has been made to understand the cause of the problem and mitigate its affect. This endeavour is ongoing but at this stage of the project any solution has to work with the existing flight hardware. The following describes some of the options being considered.

The large asymmetry between the housing and test mass quantum yields is the most significant contributing factor to the anomalous discharging problem. Measurements carried out at Modena, in addition to work in the literature, suggest the quantum yield is extremely sensitive to surface contamination. This contamination could occur during the gold coating procedure, handling or just through exposure to air. The effects appear to be highly variable, difficult to predict and while baking-out a surface causes the quantum yield to vary the few measurements made seem to result in inconsistent changes. Even with these uncertainties, the test mass used at the four-mass facility appears to have an unusually high quantum yield, even after bake-out. It appears to be higher than any previously measured surface and the search for a source of possible contamination continues. At the time of writing a new test campaign has just begun at the Institut fur Technische Thermodynamik, Stuttgart. The aim is to study the affect of temperature on the quantum yield and perform measurements in a more controlled way than possible at the Modena facility. Clearly, it would alleviate the problem if the photoelectric properties of all the sensor surfaces could be reliably made uniform.

A promising possibility to solve the bi-polar discharge problem is through the use of hotspots. This idea is at an early stage but would involve intentionally con-

taminating a small spot on an illuminated surface so as to greatly increase the quantum yield. As opposite corners of the sensor are used for test mass or housing illumination, reflected light would be less of a problem. The plan is to test contaminated gold surfaces at Institut fur Technische Thermodynamik and if they are found to be suitable further testing can be carried out at the four-mass setup with the UV ray trace being used to identify the optimal location of the hotspot.

An idea that has been discounted was to add a $10-100$ nm layer of gold to the tip of one of the ISUKs, creating a mini-cathode. Jiang et al. (1998) demonstrated transmissive quantum yields of $\sim 10^{-4}$ e/photon with a 15 nm gold layer at 254 nm. Such a layer would have been applied to either an ISUK aimed at the test mass, where the electrons would flow directly towards it, or an ISUK aimed at the housing where an electric field could sweep the electrons towards the test mass. However, at this thickness approximately 40% of the UV would also be transmitted through the gold layer and into the system. With the transmissive quantum yield presumably as difficult to control as the reflective quantum yield one could find oneself in the same situation as one started with, that being the cathode and housing having a much lower quantum yield than the test mass.

A reasonable possibility that would greatly improve the flight housing illumination situation would be to gold coat the iridium caging fingers. This would be relatively easy to implement as long as care was taken not to coat the small hemispherical depression that will be in direct contact with the test mass, minimising the chance of gold pealing away during decaging. Not only would the gold surfaces produce photoelectrons, which the iridium does not at 254 nm, but the amount of UV reflected back on to the test mass would also be significantly reduced due to gold's lower reflectivity. Currently with the uncoated iridium fingers the UV ray trace predicts approximately 26% of useful light being absorbed by the housing and 18% for the test mass, for housing illumination. An initial crude simulation performed with entirely gold coated fingers predicts approximately 54% of useful light being absorbed by the housing, including fingers, and just 14% by the test mass. The true amount of useful light absorbed by the caging fingers would be slightly less as the uncoated recesses have not been considered, but gold coating the fingers would certainly offer a significant improvement overall.

The final idea is to adapt the ISUK tip pointed at the housing in such a way as to redirect the light towards a more advantageous location. For example, if the sense electrode regions absorbed a large percentage of the light entering the system discharging could be reliably manipulated via the application of DC biases. There are several possible ways of redirecting the light but any method has to work with

the existing ISUK and must be contained within the confined hole it enters through. The most promising method seems to be to slice the ISUK fibre tip at a particular angle, refracting the light in the desired direction. Again, the UV ray trace would play an important role if this idea were to be pursued.

5.4 Summary

The development and testing of a UV ray trace and a photoelectron flow model has been presented. The UV ray trace provides estimates of the distribution of UV light upon illumination of either the housing or test mass. While the majority of the ray trace parameters have been measured, or take literature values, the exact reflection distribution from several surfaces is still unknown. However, their properties are constrained by their predicted R_a values and for reasonable reflection parameters the distribution of absorbed UV light do not vary significantly. By taking $\sigma_{tm} = 15°$ and $\sigma_{eh} = 25°$ for the unknown surfaces it has been shown that one can obtain reasonable and consistent four-mass quantum yield results. Purely in terms of illumination, the flight UV ray trace also suggests that the discharging situation will be worse in the flight system, due to the position of the iridium caging fingers.

The photoelectron flow model is able to reproduce the four-mass results with a fairly small set of parameters. It has been shown that the four-mass measurements can be reproduced with a test mass quantum yield of 1.3×10^{-4} e/photon, a work function of 3.8 eV and an energy distribution parameter $n = 0.2$. The housing and electrodes had a quantum yield of 9.8×10^{-6} e/photon, a work function of 4.5 eV and an energy distribution parameter $n = 0.2$. The explanation for the non-conformant behaviour of the four-mass discharging system appears to be that the test mass is $\sim 13\times$ more emissive than the housing surfaces. The problem is accentuated by the non-optimal illumination of the housing due to the position of the caging finger recess.

Given the uncertainties related to the photoelectric properties of the surfaces there is currently no guarantee of how the flight discharge system will behave. There is ongoing work examining the best way to proceed with several options being explored. Both the UV ray trace and photoelectron flow model will play an important role in finding a solution. As the UV ray trace is improved and refined it can be used to aid the design of the LISA discharge system. This will help to prevent similar problems reoccurring while optimising the absorption percentages.

Chapter 6

Towards LISA

Introduction

Following the production of the flight Charge Management System for Pathfinder, attention is turning to improvements that can be made for LISA. During the course of this thesis the strong dependence of the inertial sensors surface properties on the performance of the discharge system has been highlighted. The design of the LISA discharge system must aim to minimise the effect of these highly variable and difficult to control surface properties. Possible solutions to this challenge have been discussed in Chapter 5, Section 5.3, but these solutions are restricted in that they have to work with the existing Pathfinder system. The design for LISA on the other hand can address these issues from the beginning, leading to several new possibilities. For example, technological advances since the Pathfinder system was first developed have made using a solid state UV light source a viable option. Ultra-Violet Light Emitting Diodes (UV-LEDs) are a promising technology that offers several advantages over the currently employed mercury lamps. Initial work has began at Imperial College London to assess the possibility of using UV-LEDs within the Charge Management System for LISA. This chapter presents work carried out to study the UV-LEDs spectral properties under a variety of operating conditions and also discusses how they can be used to mitigate the effect of surface properties on discharge performance.

6.1 UV-LEDs

In the last few years LED technology has developed and matured to a point where devices with peak output in the ultra-violet region have become commercially avail-

able. The world's sole commercial manufacturer of sub-350 nm LEDs is Sensor Electronic Technology, Inc. and they currently supply LEDs with a nominal peak wavelength down to 240 nm as well as devices peaking at 255 nm, comparable to the mercury lamps which have a spectral line at 254 nm. These UV-LEDs have the potential to replace the mercury lamps in the Charge Management System for LISA.

There are many advantages to using UV-LEDs as they are smaller, lighter and consume less power then the mercury lamps. They also offer a superior dynamic range and can be supplied with an optical fibre directly coupled to the device offering an efficient method to collect and channel the light to the inertial sensor. According to their data sheet the 255 nm LEDs have a typical optical power of $\sim 200\ \mu W$ at 25 °C and 20 mA drive current (Sensor Electronic Technology, Inc., 2011), which is far in excess of the nW optical power levels required for discharging. Furthermore, unlike the lamps they do not require a high voltage to drive them and can be run either continuously or in a pulsed mode. The benefits of a pulsed mode with regards the discharging system will be discussed in detail in Section 6.5.1.

The LEDs consist of a structure of AlGaN layers grown on a sapphire substrate via a patented chemical vapour deposition process. The mixing ratio of Al and Ga within the $Al_xGa_{1-x}N$ alloy determines the peak wavelength of the LED with increased Al content and reduced Ga leading to a minimum attainable peak wavelength of ~ 230 nm, (Hirayama, 2005). The LED chip itself is hermetically sealed in a TO-39 package, with a choice of a flat window or lens front. Figure 6.1 shows a nominally 255 nm peak LED next to a potted mercury vapour lamp, as used for Pathfinder.

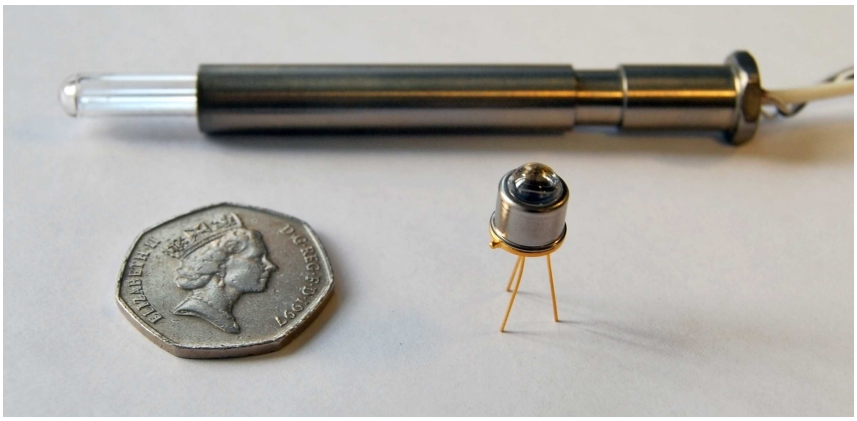

Figure 6.1: Photograph of a nominally 255 nm peak UV-LED with a ball lens in a TO-39 package. A potted mercury vapour lamp, almost identical to those which will be used for Pathfinder, is also shown.

While mercury lamps are a very mature technology with a space heritage, UV-LEDs will require extremely thorough testing and qualification before they can be used. This will include examining their general electrical properties and spectral stability, lifetime testing as well as space qualification tests for radiation hardness, vibration and performance at varying temperature and under vacuum. A group at Stanford University have already begun this process for nominally 255 nm LEDs provided by Sensor Electronic Technology, Inc. They have been running lifetime tests on two LEDs, one in a nitrogen environment the other in a 10^{-7} torr vacuum, for 19000 and 8000 hours respectively, (Sun et al., 2009). They state the LEDs have shown no degradation in output during this time, but there is a slight discrepancy in the drive settings they provide. The LED in the nitrogen environment is pulse driven at 2 mA, with a 10% duty cycle and at a 1 kHz rate. This contradicts an earlier paper (Sun et al., 2006a) that states the drive current as 1 mA, possibly suggesting that they have had to increase the drive current to maintain the same optical output as the LED has decayed. The same paper also mentions 'Preliminary lifetime testing' lasting 6 weeks prior to the continuous measurements commencing, the details of which are not given. Additionally the Stanford group have made measurements before and after exposing two different 255 nm LEDs to 63 MeV protons to a total fluence of 2×10^{12} protons cm^{-2}, again the LEDs apparently showed no degradation in output, (Sun et al., 2009).

6.2 Spectral Measurements

Like the 254 nm spectral line from the mercury lamps, the UV-LEDs peak wavelength corresponds to a photon energy that is close to the work function of gold. As has been shown in previous chapters, within this regime the photoelectric behaviour is extremely sensitive to the relationship between the surface properties and the illuminating radiation. It is therefore vital to understand the spectral properties of the UV-LEDs as they act to determine the discharging behaviour of the system. In addition to the UV-LEDs intrinsic spectrum there is evidence in the literature that suggests the spectral properties could vary with operating temperature, drive current and age.

An LED produces light when an electron from the valence band obtains enough energy to cross the forbidden band gap and reach the conduction band. When the electron relaxes back to the valence band a photon is emitted with a wavelength, λ, related to the band gap of the semiconductor, E_g, by $E_g = hc/\lambda$, where h is the Planck constant and c is the speed of light in a vacuum. The structure of the band

gap is determined by the composition of the semiconductor and can be engineered to give a particular emission spectrum. This spectrum is temperature dependent as the magnitude of E_g varies due to increased inter-atomic spacing within the semiconducting crystal as the temperature rises. The size of the effect depends on the materials used but generally the peak wavelength position increases with increasing temperature and the spectrum also broadens, (Varshni, 1967; Johnston, 2010). The source of current dependence on an LEDs emission spectrum is more complicated but also depends on the LED composition. Generally, increased drive current increases the junction temperature leading to similar thermal effects but some semiconductor crystals can have piezoelectric properties leading to lattice strain with applied electric field. This strain in turn alters the band gap and thus the emission spectrum, (Mukai et al., 1998).

Reynolds et al. (1991) describes a study of two LED spectra varying with temperature. One LED had a nominal peak wavelength of 660 nm (Red) while the other peaked at 950 nm (Infra-Red) and shifts of 5.5 nm and 7.8 nm were found over a temperature range of 0 to 50 °C. Mukai et al. (1998) examines the effect of both operating temperature and current on a range of diodes. For diodes with peak wavelengths at 525 nm (green) and 475 nm (blue) no variation was observed with temperatures between 30 and 80 °C but a significant variation of $\sim$ 25 nm was seen for both LEDs between 5 and 80 mA. They also show results for a 640 nm (Red) LED which did not vary with current but varied by $\sim$ 25 nm between 30 and 80 °C. Interestingly the same paper describes measurements made on three separate LEDs peaking at 370, 375 and 380 nm (Ultra-Violet). The LED at 380 nm showed a variation of a few nm with both temperature and current over the same range as previously stated. The LEDs at 370 and 375 nm meanwhile showed no variation with current but a shift of $\sim$ 8 nm between 30 and 80 °C. Reifegerste and Lienig (2008) studied a range of LEDs between 502 and 563 nm (green to yellow) from a variety of manufacturers and various material compositions. While varying temperature and current they observed shifts up to $\sim$ 10 nm. Finally, Zhang et al. (2005) presents measurements for a 277 nm (Ultra-Violet) LED with a similar AlGaN composition to the ones studied here. While varying the current between 1 and 50 mA a small increase of $\sim$ 0.5 nm in the peak wavelength was observed and the FWHM increased from 9.3 to 9.5 nm. The measurements were performed at room temperature but it is not stated if the device was actively temperature controlled.

With these findings in mind I carried out a series of measurements on a nominally 255 nm LED, described previously, in order to determine its spectrum and any dependence on temperature, current and possibly age.

6.2.1 Experimental Setup

The measurements presented here were made with a Acton VM-502 monochromator from Princeton Instruments, (Princeton Instruments, 2011). It consists of a reflective diffraction grating mounted within a $34.3 \times 31.0 \times 25.9$ cm chamber which has three entrance slits, adjustable with micrometer screws. One of these entrances was sealed off with a flange, one acted as the entrance slit and the other the exit slit. For the measurements performed here both slits were set at 1.9 mm, which was found to give a good compromise between increased signal but reduced resolution. The grating's rotational position was controlled via an external motor with six different speed settings and its position displayed on a mechanical dial. The readout dial was in angstroms but a significant offset was introduced after the drive belt was replaced. This was compensated for by taking several calibration measurements with a mercury vapour lamp, Section 6.2.2. The light source being studied was set back 20.0 cm from the entrance slit at the end of a 7.0 cm diameter vacuum pipe. This added distance combined with the slit acted to collimate the light source. Upon entering the chamber the light was reflected from the diffraction grating towards the exit slit at an angle given by the grating equation:

$$d\left(\sin\left(\theta_i\right) + \sin\left(\theta_m\right)\right) = m\lambda \tag{6.1}$$

where d is the distance between grating elements, m is the diffraction order integer (positive or negative), θ_i is the angle of incidence, θ_m is the angle of the diffraction order m and λ is the wavelength of the light. The diffracted light was detected on the other side of the exit slit by a custom built circuit which employed a OPT301 integrated photodiode and amplifier with an additional 1 GΩ gain resistance, (Burr-Brown, 1994). The circuit was powered by a 15 V desktop power supply and its output was fed into a PC via a Keithley 2000 multimeter through a RS-232 cable. The data was recorded by a custom written LabVIEW program and saved to an ASCII file. Figure 6.2 shows the response curve for the photodiode and it was applied during data analysis of all measurements. This was achieved by fitting a 15^{th} order polynomial to the response data to allow the relative response at a particular wavelength to be calculated and applied.

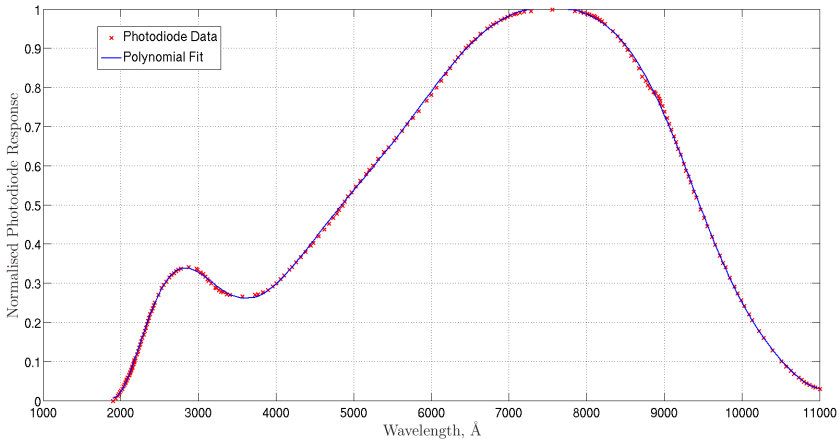

Figure 6.2: The OPT301 photodiode response data was taken from the components data sheet (Red) and a 15^{th} order polynomial (Blue) was fitted to allow the variation with wavelength to be calculated. Data taken from (Burr-Brown, 1994).

For the UV-LED measurements a custom designed mount was manufactured, Figure 6.3. The UV-LED was inserted in a tight fitting aluminium block with thermal grease being used to ensure good contact. Four screws within the block held the UV-LED in place and a thermistor was embedded both above and below to monitor the temperature. The aluminium block was then attached to one side of a 9.0×9.0×3.8 mm Peltier using thermal epoxy, with the other side of the Peltier being attached to a copper heat sink. The heat sink was then screwed onto a micrometer platform mounted on the spectrometer which allowed the UV-LEDs position to be aligned with the entrance slit. The Peltier was driven with a commercially available temperature control circuit, (SuperCool, 2005), with the two thermistors providing a feedback loop. The temperature control circuit was supplied with software that allowed the aluminium block temperature to be set via a PC and automatically maintained at ±0.01 °C. Once the UV-LED was mounted on the spectrometer a fin was attached to the protruding copper heat sink to aid heat exchange with the air. The UV-LED being studied was powered by a current limited desktop power supply with a multimeter being used as an independent monitor.

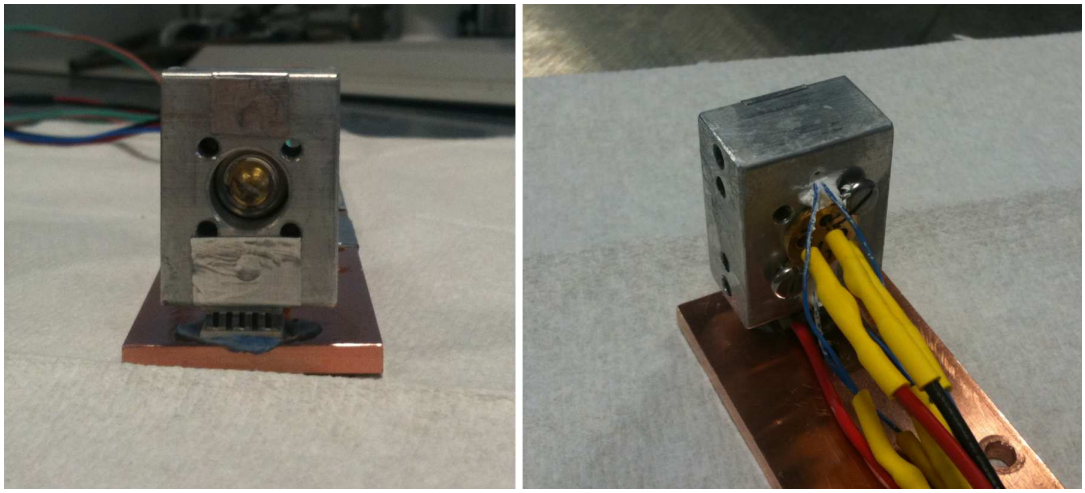

Figure 6.3: Photographs of the UV-LED mount block sitting on top of the Peltier. The other side of the Peltier is in contact with the copper heat sink, both being held in place with thermal epoxy. The UV-LED mount block has two thermistors embedded in it to monitor temperature, coated in white thermal grease.

The spectral measurements made with both the calibrating mercury lamp and the nominally 255 nm UV-LED followed the same procedure. With the light source mounted, the motor was turned on and would rotate the diffraction grating at a constant rate. The photodiode data collection program would then be started which would proceed to take readings at a constant rate. After scanning through the spectrum the data collecting would be stopped. Crucially, the reading on the spectrometer dial was recorded at the exact moment data taking was started and stopped, allowing a linear scale to be applied to the recorded data. Great care was taken to ensure that the motor speed and data collection rate were constant and consistent between runs. This included timing each measurement and taking readings with the grating rotating either clockwise or anticlockwise to check for consistency. Each UV-LED measurement was made over a range of 1000 Å and took 1512.8 ± 0.8 s, with 2006 ± 3 individual readings. A diagram of the spectrometer setup is shown in Figure 6.4.

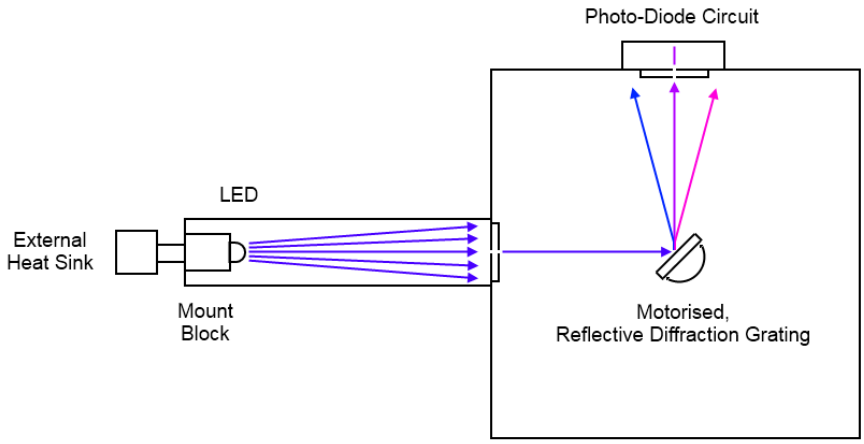

Figure 6.4: A diagram of the spectrometer setup showing the position of the various components. While measurements were being taken the entire system was light sealed, with aluminium tape covering any joints.

Air causes low attenuation of light from 2200-5500 Å, only $\sim$ 0.2 % is lost at 2500 Å traversing 1.0 m of air at standard temperature and pressure, (Baum and Dunkelman, 1955). It was therefore intended that all the measurements would be performed in air and as such the UV-LED mount and photodiode electronics were not designed to operate under vacuum, though the spectrometer itself can be used in this way. During some early calibration measurements using a mercury vapour lamp it was noticed that the intensity of the 2537 Å spectral line fell in intensity with time. This was accompanied by a strong smell of ozone when the sealed spectrometer was opened and it was then realised that the spectral emission at 1849 Å was generating ozone via photodissociation interactions with H_2O and O_2 in the air, (Creasey et al., 2000). O_3 is highly attenuating between 2000-3000 Å, with peak absorption at $\sim$ 2550 Å, (Inn and Tanaka, 1953). Although this was unlikely to have caused a problem for the UV-LED spectrum the spectrometer chamber was sealed from the outside atmosphere and flooded with nitrogen for all further measurements. The intensity of the 2537 Å spectral line was no longer seen to reduce with time.

6.2.2 Mercury Spectrum

Before measurements of the UV-LED could be made the spectrometer needed to be accurately calibrated. This was achieved using a mercury pencil lamp, similar to those which are used in flight for Pathfinder, run from a desktop power supply. The

spectral line wavelengths for elemental mercury are well studied in the literature, (Reader, 1996). Sansonetti et al. (1996) additionally gives the relative intensities of the lines, specifically for a mercury pencil lamp. The spectra of the mercury pencil lamp was measured using the procedure previously described and the six strongest lines between 2400 Å and 3200 Å were compared to the literature, Figure 6.5. As expected the 254 nm line dominates being around forty times more intense than the second strongest line with the measured FWHM for the single spectral lines being 30.3 ± 0.6 Å. This gives some indication of the spectrometer resolution given the actual spectral line widths should be less than ~ 0.1 Å. All the relative line positions are consistent with the literature and their relative intensities are in fair agreement.

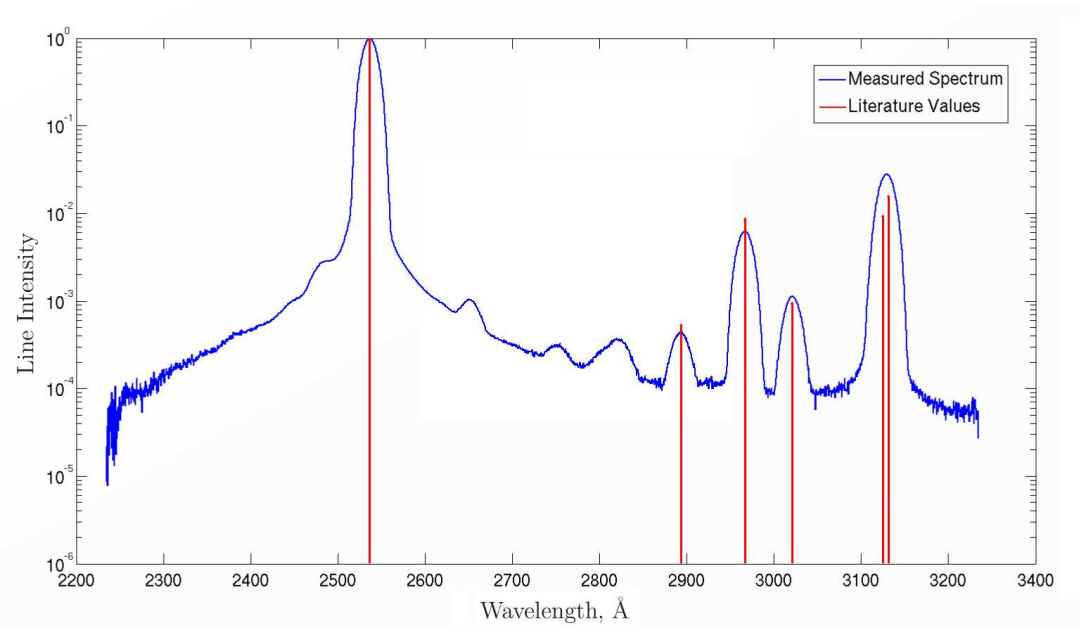

Figure 6.5: A comparison between the measured mercury pencil lamp spectrum and the six strongest lines given by Sansonetti et al. (1996). All the lines have been normalised with respect to the 254 nm line. The measured spectrum required a 2564.1 Å linear offset to fit the literature positions.

The mercury lamp spectrum was measured several times during the UV-LED study to ensure consistency. By considering the three strongest single lines for each measurement a mean offset for the spectrometer dial was calculated as 2564.1 ± 1.6 Å. The offset is large and close to 254 nm due to the dial being roughly aligned with the central maxima when the drive belt was replaced. This offset is corrected for in all presented spectra.

6.3 Results

6.3.1 255 nm LED Spectrum

The typical electro-optical properties of the nominally 255 nm UV-LED are given by its data sheet, (Sensor Electronic Technology, Inc., 2011). The data provided by SET are general electrical characteristics as well as a rather crude spectral measurement. The peak wavelength of the UV-LEDs is given as 255 ± 2 nm, with a typical FWHM of 12 nm, at 25 °C and 20 mA drive current. As a comparison, a measurement was made with the spectrometer under the same conditions and is compared to the filtered 254 nm spectral line used by the Pathfinder Charge Management System in Figure 6.6.

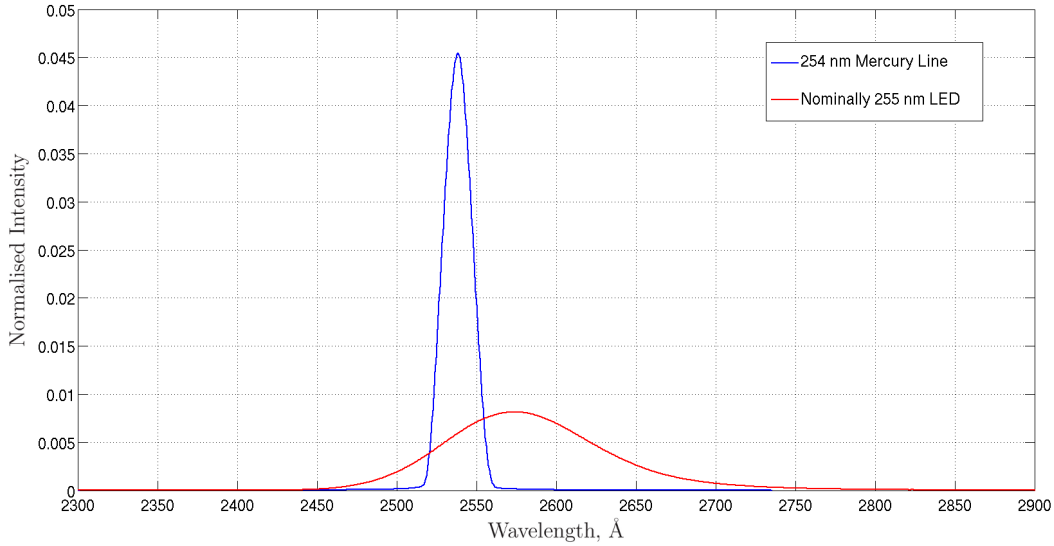

Figure 6.6: A comparison between the filtered 254 nm spectral line used in the Pathfinder Charge Management System and the nominally 255 nm UV-LED spectrum, taken at 25 °C and 20 mA. Both have been normalised so as to have areas equal to one. Note the actual peak wavelength measured here was 2575.6 ± 1.6 Å.

For this measurement the peak wavelength was found to be 2575.6 ± 1.6 Å, with a FWHM of 112.2 ± 0.4 Å, in fair agreement with the data sheet. As expected, the UV-LED spectrum is broader than that of the filtered 254 nm mercury line.

6.3.2 Operating Temperature

In order to study the effect of operating temperature on the optical properties of the UV-LED the LED mount block was held at a given temperature while the

spectrum was measured. All the temperature spectra were obtained while driving the UV-LED with a current of 20 mA. Two thermistors embedded within the LED mount showed a measured temperature variation across the block of between 0.1 and 0.5 °C, on opposite sides of the LED. The thermistor furthest from the Peltier was used as the temperature reference by the automated control software. The data sheet recommended -30 and 55 °C as the minimum and maximum operating temperatures. Measurements were made with the nominally 255 nm LED at 50, 40, 30, 20, 10, 0 and -7.5 °C, which was the minimum temperature that could be reached with the UV-LED being driven at 20 mA in this setup. The results are shown in Figure 6.7.

As expected, the results show an inverse relationship between operating temperature and UV-LED output with an increase of $\sim$ 40 °C roughly halving the LED output. Further analysis of the spectra demonstrates that the peak position shows no significant variation within the experimental limit of $\pm$1.6 Å. A small variation in the FWHM of the spectra is observed with an increase of $\sim$ 7.0 Å seen over the temperature range studied.

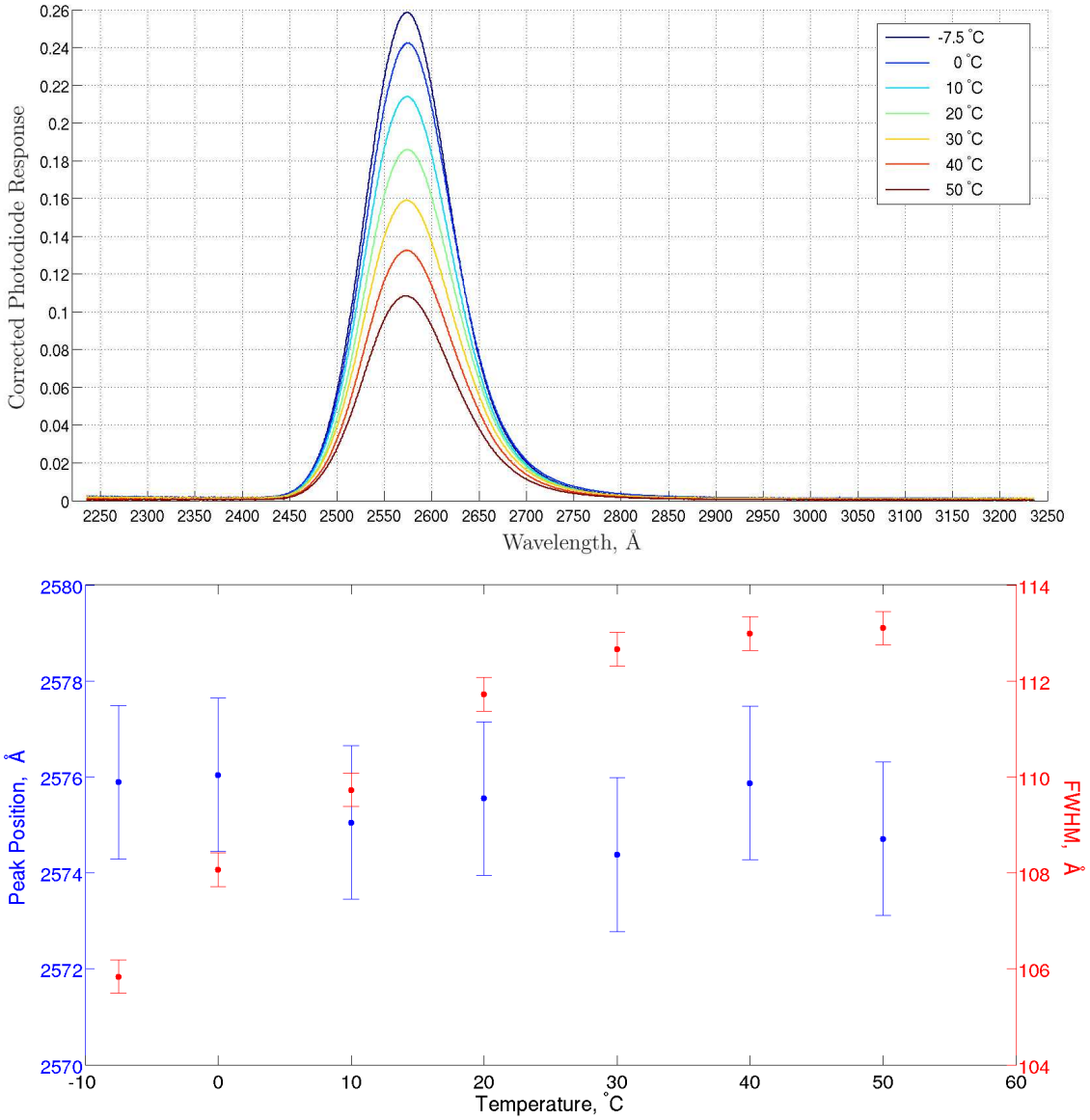

Figure 6.7: *Top:* Spectra from the nominally 255 nm UV-LED with varying operating temperature. All spectra were measured with a 20 mA drive current. *Bottom:* The peak position and FWHM of each spectrum measured. There appears to be no significant change in peak position while a small change in the FWHM is observed.

6.3.3 Operating Current

The effect of the drive current on the UV-LED spectra was studied in a similar way to that of temperature. This time the UV-LED was held at a constant 10 °C while the current was varied. The data sheet recommended a maximum DC drive current of 30 mA and measurements were made at 30, 25, 20, 15, 10, 5 and 1 mA, which was the lowest current setting that a clear spectrum could still be observed. The results are shown in Figure 6.8.

As shown in the data sheet, the UV-LED demonstrates a linear relationship between drive current and optical output above 5 mA. Like the previous temperature measurements, the spectra show no significant variation in peak position within the experimental limit of ±1.6 Å. Likewise, the FWHM of the spectra show no significant variation with the very small increase observed possibly due to the increased current heating the junction.

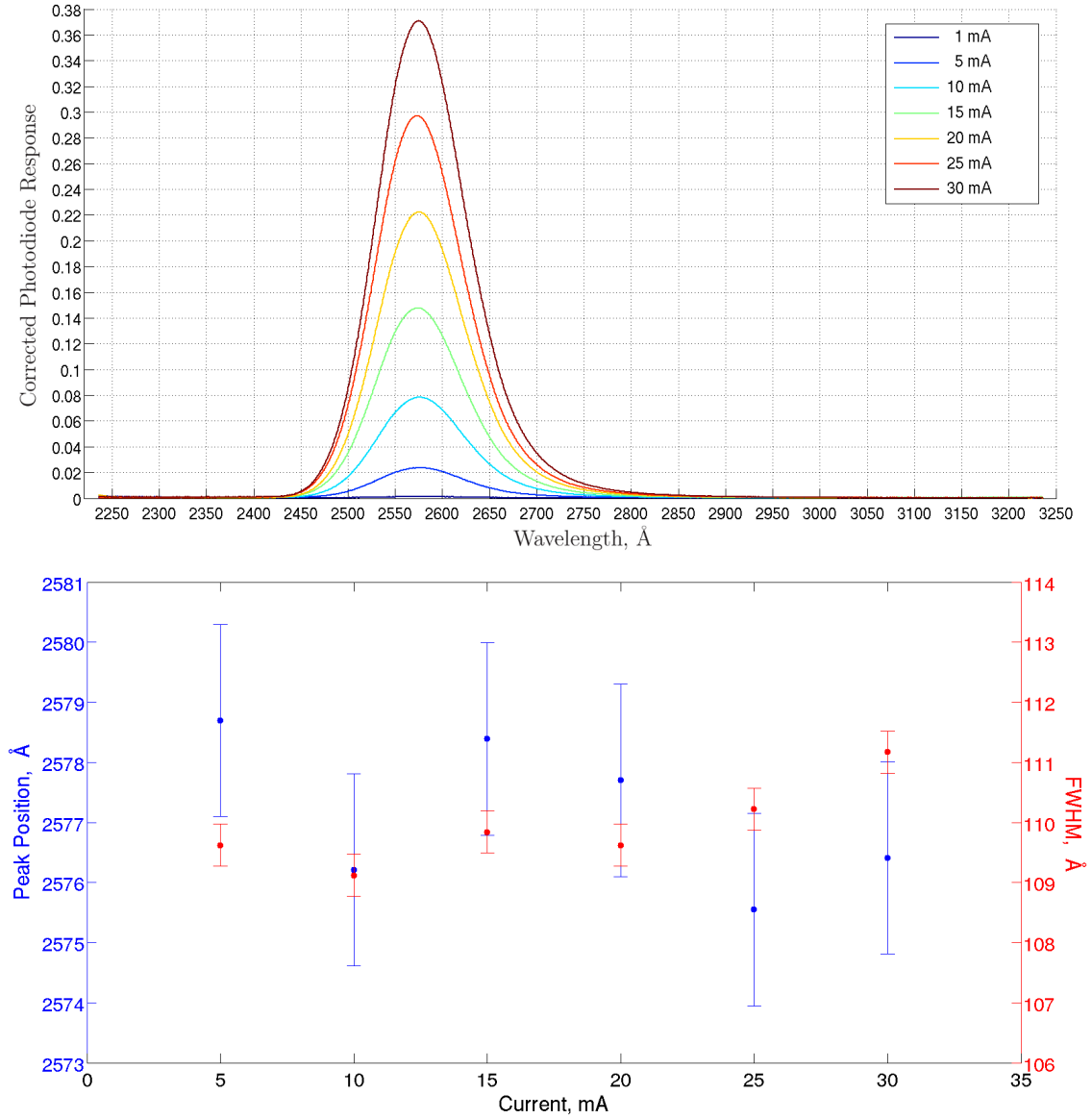

Figure 6.8: *Top:* Spectra from the nominally 255 nm UV-LED with varying operating current. All spectra were measured at a 10 °C operating temperature. *Bottom:* The peak position and FWHM of each spectrum measured. There appears to be no significant change in peak position or the FWHM observed.

6.3.4 Ageing

While studying the UV-LED spectra it became apparent that the output was decaying with time. This was unexpected as the UV-LED was always operated within data sheet recommended limits and they were thought to have long lifetimes. Fortunately, a log had been kept detailing at what temperature and current the UV-LED had been run and for how long. This allowed the effect to be studied from the first time the UV-LED had been turned on. Following the constant temperature and current measurements, described previously, the UV-LED was run continuously for approximately two weeks at 10 °C with a 20 mA drive current, while still mounted in the spectrometer, in order to study the effect further. Spectra were measured intermittently during this time until the output had fallen to $\sim 50\%$. By multiplying the drive current by the amount of time run at that current the cumulative runtime of the UV-LED was compared to its output for its entire history. The results are shown in Figure 6.9, with the data scaled to the first reading.

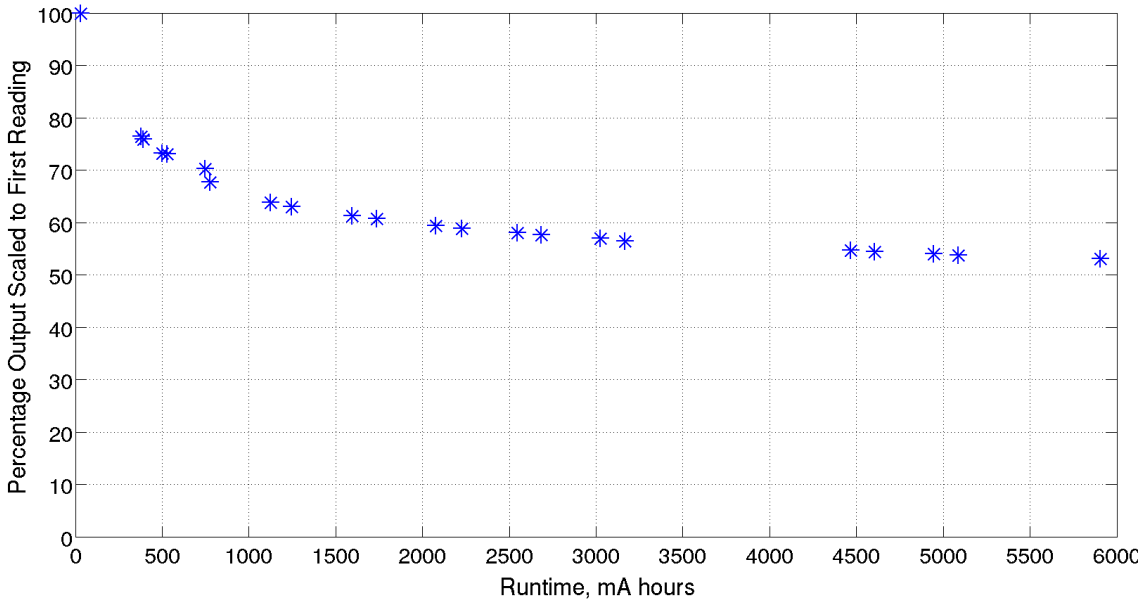

Figure 6.9: The decay in UV-LED output with runtime. The output was calculated from the spectral measurements and scaled to the first reading. All measurements were made at 10 °C with a 20 mA drive current. During the first $\sim$ 750 mAh the UV-LED was run at a range of currents and temperatures in between being measured, while after this it was run continuously at 10 °C with a 20 mA drive current.

As can be seen, the UV-LED showed a steep decline in output during the first $\sim$ 1000 mAh of operation, dropping by $\sim$ 30%. The output then became more

stable, falling only $\sim 10\%$ during the following 5000 mAh. These observations seem to be consistent with a study by Zhang et al. (2005) that describes work with a similar AlGaN 280 nm UV-LED. During preliminary reliability tests they observed a 30% reduction in output during the first 600 mAh but 'remained constant for the rest of the test', over 6000 mAh at 20 mA.

Further study of the literature revealed that for similar AlGaN 280 nm UV-LEDs DC drive currents of above 10 mA are considered high. Both Gong et al. (2006) and Sawyer et al. (2008) study the degradation mechanisms in the 280 nm UV-LEDs by driving them at 20 mA in order to accelerate the ageing processes. The decay in the optical power that they present is of the same form as was observed in the 255 nm UV-LEDs. It appears that the UV-LED observed here suffered from accelerated LED degradation due to high electrical stress. The same studies also show that one would not expect the UV-LED degradation to scale linearly with operating current or temperature. For example an LED run at 20 mA for 1 hour would be expected to decay more than an LED run at 1 mA for 20 hours. Also, the higher the operating temperature the more rapid the decay is expected to be. This may explain why very little degradation has been observed in the much longer lifetime testing performed by Sun et al. (2009), which has operated at around 1 mA with a 10% duty cycle for over two years, or approximately 2000 mAh.

The accelerated ageing of the UV-LED described here does allow any potential spectral variation to be observed as it decays. As the UV-LED degrades its composition or structure must change which could potentially effect the emission spectrum. At the drive settings required for LISA, $\sim$ 1 mA for continuous discharging, the rate of degradation would be much lower but over the course of several years of operation, or if an increased output were required to counter increased charging due to a large coronal mass ejection, could become significant. The spectra measured as the UV-LED decayed are shown in Figure 6.10. As with the previous tests, no significant change in the spectral properties was observed.

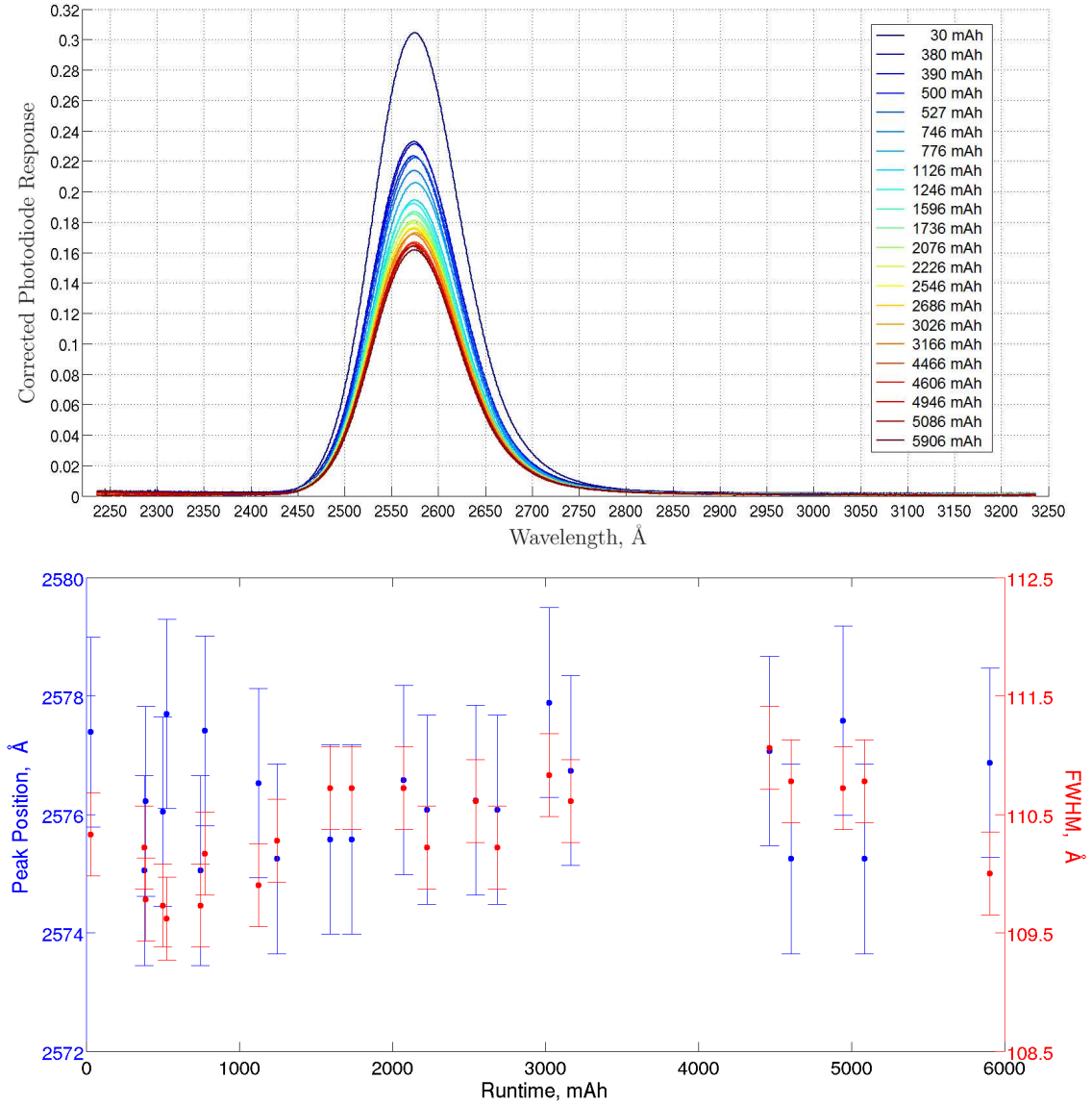

Figure 6.10: *Top:* Spectra from the nominally 255 nm UV-LED with increasing age. All spectra were measured at a 10 °C operating temperature and 20 mA drive current. *Bottom:* The peak position and FWHM of each spectrum measured. There appears to be no significant change in peak position or the FWHM observed.

6.4 Conclusions

A UV sensitive spectrometer has been setup and calibrated in order to study the spectral properties of a nominally 255 nm peaked UV-LED.

- The nominally 255 ± 2 nm UV-LED studied had a measured peak wavelength of 257.6 ± 0.1 nm.
- Its spectrum had a measured FWHM of 11.2 nm, at 25 °C and 20 mA drive current.
- A small variation in the FWHM of $\sim$ 0.7 nm was observed when operated between -7.5 and 50 °C.
- No significant variation in spectral properties were observed with DC drive currents between 1 and 30 mA.
- When driven at currents greater than $\sim$ 10 mA, the UV-LED's output decayed by $\sim$ 30% during the first $\sim$ 1000 mAh of operation.
- The UV-LED's output then stabilised, falling only $\sim$ 10% during the following 5000 mAh.
- No significant variation in spectral properties were observed due to output degradation.
- Overall the UV-LED was found to be very spectrally stable with no significant variation in peak wavelength with operating temperature, drive current or age.

Following commissioning of the UV spectrometer it is now ready to be used in future measurements. For example, checking for spectral variation between individual devices or devices from different batches. It can also be used to check for spectral variation following space qualification testing, especially after exposure to radiation.

6.5 Discussion

6.5.1 Mitigating the Effect of Surface Properties

The use of UV-LEDs as the light source for the Charge Management System on board LISA offers two potential ways in which to mitigate the effect of surface properties on discharging performance. Firstly, by using a light source that produces higher energy photons one can move further away from the work function of the illuminated material. This not only increases the quantum yield but should also reduce the sensitivity to any surface contamination. While this effect will be fairly small for the nominally 255 nm devices our group has also recently procured several nominally 240 nm UV-LEDs where the effect could be more significant. At 240 nm the photons have an energy of 5.2 eV which is the work function of pure gold. It is important to keep in mind though that a trade off between the two UV-LEDs will have to be made. As the wavelength is reduced the optical fibres used to transport the light become increasingly opaque. This effect is amplified as the lower wavelength light also damages the fibres, increasing their opacity further. This is why the output from the mercury lamps has to be filtered and the 1849 Å mercury line not used in the Pathfinder system. It should also be noted that according to the data sheet, the same drive settings with the nominally 240 nm UV-LEDs produce an optical output around ten times less than the 255 nm devices, (Sensor Electronic Technology, Inc., 2011).

While the 255 nm UV-LEDs driven with a DC current could simply replace the existing mercury lamps, and this remains an option, one of the biggest advantages of using them would be to reduce the affect of surface properties by driving them with a high frequency AC current. As explained in previous chapters a 5.4 V, 100 kHz AC bias is applied to the injection electrodes within the inertial sensor. This in turn creates a ~ 0.61 V AC bias on the test mass. Syncing a pulse driven UV-LED with this injection bias would therefore offer a huge advantage. By adjusting the phase of the UV-LED pulses the device would only illuminate the sensor when the potential differences between the test mass and housing surfaces were favourable to the direction of discharge. Any photocurrents produced in the opposite direction by reflected light would be heavily suppressed. Indeed, if the pulse width were short enough, the phase optimal and the maximum photoelectron energy less than the potential difference of any illuminated surfaces, it could be completely stopped. This final stipulation is another reason why it would be undesirable to make the illuminating wavelength too low.

It is clear that pulsing the UV-LEDs in this way would elegantly solve the

problems caused by differences in the surface quantum yields. Not only that, but it would also provide a level of redundancy as shifting the phase of the pulses by 180° would also reverse the direction of the photocurrent by only allowing the photoelectrons produced by the reflected light to flow. This would allow a single UV-LED to discharge in both directions, if required, by simply adjusting the phase. Being able to adjust both the phase and the amplitude of the UV-LED pulses would also increase both the dynamic range and the resolution the discharging system is capable of. Furthermore, discharging would be more efficient then in a DC system where during half of the injection cycle the electric fields act against the desired discharge direction. This means less total UV light is needed to produce the same rate of discharge leading to less power consumption and longer device lifetimes.

Before such a scheme can be implemented for LISA the high frequency capabilities of the UV-LEDs need to be studied. A group at Stanford University have already demonstrated discharging at 1 kHz (Sun et al., 2006a) and 10 kHz (Sun et al., 2006b) using the 255 nm UV-LEDs. Our group aims to create a similar system but capable of syncing with the 100 kHz injection bias present within the inertial sensor, possibly with a 240 nm UV-LED. Once the new UV-LED drive electronics have been designed and built lifetime testing can begin in a temperature controlled vacuum system that has already been setup. In addition to this our group at Imperial is developing a simplified sensor geometry, in vacuum, capable of testing various discharging properties. A further step towards LISA will be to use the ray tracing simulation developed for Pathfinder to optimise the illumination properties. This will depend on the type of light source chosen as well as the drive method but will greatly help in the design for LISA and prevent some of the problems that have arisen during Pathfinder's development.

Chapter 7

Conclusion

The detection and study of gravitational waves will open a new observational window on the Universe. Of particular interest are low frequency gravitational waves as they are thought to be produced by a diverse range of astrophysical sources. The Laser Interferometer Space Antenna, or LISA, is an ambitious future mission that aims to study these waves by placing an interferometer in space. The key to LISA's success will be in its ability to accurately measure the sub-atomic variation in proper distance between pairs of isolated, distant test masses. Such a task poses huge scientific and technical challenges and has prompted a technology demonstration mission, LISA: Pathfinder. One of the goals for Pathfinder is to study sources of test mass acceleration noise which could mask the weak gravitational wave signal. Test mass charging is one such source of noise and the capability of the Charge Management System to control the level of free charge on the isolated test masses will be important to the success of both Pathfinder and LISA.

This thesis included a description of the radiation monitor that will be flown on board Pathfinder. The monitor will help characterise the radiation environment responsible for test mass charging by measuring both the rate and energy spectra of the incident ionising radiation. Simulations aided the analysis of the successful proton beam testing with the flight model radiation monitor hardware.

The production of the flight Charge Management System was described as well as testing of the system at the Trento torsion pendulum facility. While initial tests with the single-mass pendulum were successful, later measurements with the four-mass setup exhibited anomalous behaviour. In an effort to gain a better understanding of discharging performance several individual properties of the system were measured. These included the photoelectric properties of the various surfaces within the inertial sensor, the reflectivity of gold at 254 nm and the distribution of the UV light emitted from the ISUKs that deliver the light.

These experimentally measured properties were then incorporated into simulations of both the four-mass and flight discharging systems. The simulations showed that due to the introduction of additional caging features, discharging illumination is no longer optimal. In addition, the simulations confirmed that the anomalous four-mass behaviour can be explained by a large asymmetry in the quantum yields of the housing and test mass surfaces. The simulations found that the quantum yield of the test mass was 1.3×10^{-4} e/photon while for the housing only 9.8×10^{-6} e/photon. The cause of such a large asymmetry is under continuing investigation but is likely due to some level of surface contamination. It was also shown that from an illumination perspective the situation will be worse in the flight system due to the presence of the iridium caging fingers. There remains several possibilities to ensure the Charge Management System returns to optimal performance and these are being actively pursued. The simulations will aid this ongoing effort.

Finally, work was presented on initial testing of UV-LEDs as a potential new source of light for the LISA discharge system. The UV-LEDs were shown to be spectrally stable with varying operating temperature, drive current and age. The possibility of using these devices in pulsed mode offers a promising way of alleviating the dependence of discharge performance on the photoelectric properties of individual surfaces.

References

Abramovici, A., Althouse, W. E., Drever, R. W. P., Grsel, Y., Kawamura, S., Raab, F. J., Shoemaker, D., Sievers, L., Spero, R. E., Thorne, K. S., Vogt, R. E., Weiss, R., Whitcomb, S. E., and Zucker, M. E.: 1992, *Science* **256(5055)**, pp. 325

Adams, G. P., Rochester, G. K., Summer, T. J., and Williams, O. R.: 1987, *Journal of Physics E: Scientific Instruments* **20(10)**, 1261

Alloway, D. M., Hofmann, M., Smith, D. L., Gruhn, N. E., Graham, A. L., Colorado, R., Wysocki, V. H., Lee, T. R., Lee, P. A., and Armstrong, N. R.: 2003, *The Journal of Physical Chemistry B* **107(42)**, 11690

Antonucci, F., Cavalleri, A., Dolesi, R., Hueller, A., Perreca, S., Vitale, S., and Weber, W. J.: 2010, *Test-Mass Discharging Test Campaign on TM3 with the Four-Test-Mass Torsion Pendulum*, S2-UTN-TN-3080 Issue 1.0, University of Trento

Antonucci, F., Cavalleri, A., Dolesi, R., Perreca, S., Vitale, S., and Weber, W. J.: 2011, *Charge Measurements on TM3 After Bake-Out*, S2-UTN-TN-3083 Issue 2.0, University of Trento

Araújo, H., Wass, P., Shaul, D., Rochester, G., and Sumner, T.: 2005, *Astroparticle Physics* **22(5-6)**, 451

Armstrong, J. W.: 2006, *Living Reviews in Relativity* 9(1)

Armstrong, J. W., Estabrook, F. B., and Tinto, M.: 2003, *Classical and Quantum Gravity* **20(10)**, S283

Armstrong, J. W., Iess, L., Tortora, P., and Bertotti, B.: 2003, ApJ **599**, 806

Arun, K. G., Babak, S., Berti, E., Cornish, N., Cutler, C., Gair, J., Hughes, S. A., Iyer, B. R., Lang, R. N., Mandel, I., Porter, E. K., Sathyaprakash, B. S., Sinha, S., Sintes, A. M., Trias, M., Broeck, C. V. D., and Volonteri, M.: 2009, *Classical and Quantum Gravity* **26(9)**, 094027

Astone, P., Ballantini, R., Babusci, D., Bassan, M., Bonifazi, P., Cavallari, G., Chincarini, A., Coccia, E., D'Antonio, S., Emilio, M. D. P., Fafone, V., Foffa, S., Gemme, G., Giordano, G., Maggiore, M., Marini, A., Minenkov, Y., Modena, I., Modestino, G., Moleti, A., Pallottino, G. V., Parodi, R., Pizzella, G., Quintieri, L., Rocchi, A., Ronga, F., Sturani, R., Terenzi, R., Torrioli, G., Vaccarone, R., Vandoni, G., and Visco, M.: 2008, *Classical and Quantum Gravity* **25(11)**, 114048

Aude, M., Barret, P., Lopez, M., and Malandit, O.: 2002, *Hamamatsu Photodiodes (DPD-S8576) - Report E01P1435*, Evaluation Report, Serma Technologies, `http://www.serma.com`

Bajpai, R. P., Kita, H., and Azuma, K.: 1976, *Japanese Journal of Applied Physics* **15(11)**, 2083

Baker, J. G., McWilliams, S. T., van Meter, J. R., Centrella, J., Choi, D.-I., Kelly, B. J., and Koppitz, M.: 2007, *Phys. Rev. D* **75(12)**, 124024

Barish, B. C.: 2000, *Advances in Space Research* **25(6)**, 1165

Baum, W. A. and Dunkelman, L.: 1955, *J. Opt. Soc. Am.* **45(3)**, 166

Bishop, N. and Maharaj, S.: 2002, *General Relativity and Gravitation*, World Scientific

Bouwman, R. and Sachtler, W. M. H.: 1970, *Journal of Catalysis* **19(2)**, 127

Bradaschia, C., Fabbro, R. D., Virgilio, A. D., Giazotto, A., Kautzky, H., Montelatici, V., Passuello, D., Brillet, A., Cregut, O., Hello, P., Man, C., Manh, P., Marraud, A., Shoemaker, D., Vinet, J., Barone, F., Fiore, L. D., Milano, L., Russo, G., Aguirregabiria, J., Bel, H., Duruisseau, J., Denmat, G. L., Tourrenc, P., Capozzi, M., Longo, M., Lops, M., Pinto, I., Rotoli, G., Damour, T., Bonazzola, S., Marck, J., Gourghoulon, Y., Holloway, L., Fuligni, F., Iafolla, V., and Natale, G.: 1990, *Nuclear Instruments and Methods in Physics Research Section A: Accelerators, Spectrometers, Detectors and Associated Equipment* **289(3)**, 518

Brown, W. R., Kilic, M., Hermes, J. J., Allende Prieto, C., Kenyon, S. J., and Winget, D. E.: 2011, ApJL 737

Buhler, P., Ljungfelt, S., Mchedlishvili, A., Schlumpf, N., Zehnder, A., Adams, L., Daly, E., and Nickson, R.: 1996, *Nuclear Instruments and Methods in Physics Research Section A: Accelerators, Spectrometers, Detectors and Associated Equipment* **368(3)**, 825

Burr-Brown: 1994, *Integrated Photodiode and Amplifier - OPT301*, Data sheet, Burr-Brown, `http://www.burr-brown.com/`

Camp, J. and Cornish, N.: 2004, *Annual Review of Nuclear and Particle Science* **54**, 525

Cañizares, P., Conchillo, A., García-Berro, E., Gesa, L., Grimani, C., Lloro, I., Lobo, A., Mateos, I., Nofrarias, M., Ramos-Castro, J., Sanjuán, J., and Sopuerta, C. F.: 2009, *Classical and Quantum Gravity* **26(9)**, 094005

Carbone, L., Cavalleri, A., Dolesi, R., Hoyle, C. D., Hueller, M., Vitale, S., and Weber, W. J.: 2005, *Classical and Quantum Gravity* **22(10)**, S509

Carbone, L., Ciani, G., Dolesi, R., Hueller, M., Tombolato, D., Vitale, S., Weber, W. J., and Cavalleri, A.: 2007, *Phys. Rev. D* **75(4)**, 042001

Cavalleri, A., Ciani, G., Dolesi, R., Heptonstall, A., Hueller, M., Nicolodi, D., Rowan, S., Tombolato, D., Vitale, S., Wass, P. J., and Weber, W. J.: 2009a, *Classical and Quantum Gravity* **26(9)**, 094017

Cavalleri, A., Ciani, G., Dolesi, R., Hueller, M., Nicolodi, D., Tombolato, D., Wass, P. J., Weber, W. J., Vitale, S., and Carbone, L.: 2009b, *Classical and Quantum Gravity* **26(9)**, 094012

Ciddor, P. E.: 1996, *Appl. Opt.* **35(9)**, 1566

Creasey, D. J., Heard, D. E., and Lee, J. D.: 2000, *Geophys. Res. Lett.* **27(11)**, 1651

Cutler, C. and Thorne, K. S.: 2002, *An Overview of Gravitational-Wave Sources*, World Scientific

Danzmann, K. and Rüdiger, A.: 2003, *Classical and Quantum Gravity* 20(10)

Dettmann, J., Reitz, G., and Gianfiglio, G.: 2007, *Acta Astronautica* **60(1)**, 17

E. E. Huber, J.: 1966, *Applied Physics Letters* **8(7)**, 169

Eastman, D. E.: 1970, *Phys. Rev. B* **2(1)**, 1

Efstathiou, G. and Gratton, S.: 2009, *Journal of Cosmology and Astroparticle Physics* **2009(06)**, 011

Folkner, W. M., Hechler, F., Sweetser, T. H., Vincent, M. A., and Bender, P. L.: 1997, *Classical and Quantum Gravity* **14(6)**, 1405

Gair, J. R., Barack, L., Creighton, T., Cutler, C., Larson, S. L., Phinney, E. S., and Vallisneri, M.: 2004, *Classical and Quantum Gravity* **21(20)**, S1595

Ghatak, A. and Thyagarajan, K.: 1998, *An Introduction to Fiber Optics*, Cambridge University Press

Gong, Z., Gaevski, M., Adivarahan, V., Sun, W., Shatalov, M., and Khan, M. A.: 2006, *Applied Physics Letters* **88(12)**, 121106

Gottfried, J. M., Schmidt, K. J., Schroeder, S. L. M., and Christmann, K.: 2003, *Surface Science* **536(1-3)**, 206

Haynes, W. and Lide, D.: 2010, *CRC Handbook of Chemistry and Physics*, Taylor & Francis Group

Hirayama, H.: 2005, *Journal of Applied Physics* **97(9)**, 091101

Hobbs, G.: 2011, in D. F. Torres & N. Rea (ed.), *High-Energy Emission from Pulsars and their Systems*, p. 229

Hughes, S. A. and Thorne, K. S.: 1998, *Phys. Rev. D* **58(12)**, 122002

Inn, E. C. Y. and Tanaka, Y.: 1953, *J. Opt. Soc. Am.* **43(10)**, 870

Jiang, X., Berglund, C. N., Bell, A. E., and Mackie, W. A.: 1998, *Journal of Vacuum Science and Technology* **16(6)**, 3374

Johnson, P. B. and Christy, R. W.: 1972, *Phys. Rev. B* **6(12)**, 4370

Johnston, A.: 2010, *Reliability and Radiation Effects in Compound Semiconductors*, World Scientific, Page 102

Knoll, G.: 1979, *Radiation detection and measurement*, Wiley

Landau, L.: 1944, *Collected Papers of L. D. Landau*, Pergamon Press

Laser Components Ltd: 2011, *Specification Document for SiC Photodiode Model Series JEC 0.1S*, Data sheet, Laser Components Ltd, `http://www.lasercomponents.co.uk`

Levin, A. and Moisan, C.: 1996, *Nuclear Science Symposium* **2**, 702

Lobo, A., Nofrarias, M., Ramos-Castro, J., Sanjuan, J., Conchillo, A., Ortega, J. A., Xirgu, X., Araujo, H., Boatella, C., Chmeissani, M., Grimani, C., Puigdengoles, C., Wass, P., García-Berro, E., García, S., Martínez, L. M., and Montero, G.: 2006, in S. M. Merkovitz & J. C. Livas (ed.), *Laser Interferometer Space Antenna: 6th International LISA Symposium*, Vol. 873 of *American Institute of Physics Conference Series*, pp 522–528

LTP ISS Team: 2009, *ISS EH and TM Requirement Specification*, S2-CGS-RS-3001, Carlo Gavazzi Space

McKenna-Lawlor, S., Rusznyak, P., Buchman, S., Shestople, P., and Thatcher, J.: 2003, *Nuclear Instruments and Methods in Physics Research Section A: Accelerators, Spectrometers, Detectors and Associated Equipment* **498(1-3)**, 220

Meyer, P., Ramaty, R., and Webber, W. R.: 1974, *Journal of Applied Physics* **27(10)**, 23

Mohammadzadeh, A., Evans, H., Nieminen, P., Daly, E., Vuilleumier, P., Buhler, P., Eggel, C., Hajdas, W., Schlumpf, N., Zehnder, A., Schneider, J., and Fear, R.: 2003, *Nuclear Science* **50(6)**, 2272

Moyal, J. E.: 1955, *Philosophical Magazine* **46**, 263

Mukai, T., Yamada, M., and Nakamura, S.: 1998, *Japanese Journal of Applied Physics* **37(Part 2, No. 11B)**, L1358

NASA: 2011, `http://science.gsfc.nasa.gov/663/research/`

Nayar, S., Ikeuchi, K., and Kanade, T.: 1989, *Surface Reflection: Physical and Geometrical Perspectives*, CMU-RI-TR-89-07, Robotics Institute, Pittsburgh, PA

Nayar, S., Ikeuchi, K., and Kanade, T.: 1991, *Pattern Analysis and Machine Intelligence* **13(7)**, 611

Palik, E. and Ghosh, G.: 1998, *Handbook of Optical Constants of Solids*, Academic Press

Pauty, F., Matula, G., and Vernier, P. J.: 1974, *Journal of Applied Physics* **45(10)**, 1203

Pei, Z. and Berglund, C. N.: 2002, *Japanese Journal of Applied Physics* **41(Part 2, No. 1A/B)**, L52

Pells, G. P. and Shiga, M.: 1969, *Journal of Physics C: Solid State Physics* **2(10)**, 1835

Poenaru, D. and Greiner, W.: 1997, *Experimental Techniques in Nuclear Physics*, Walter de Gruyter

Princeton Instruments: 2011, *Acton VM Series*, Data sheet, Princeton Instruments, `http://www.princetoninstruments.com`

Reader, J.: 1996, *VizieR Online Data Catalog* 6016

Reale, C.: 1970, *Infrared Physics* **10(3)**, 173

Reifegerste, F. and Lienig, J.: 2008, *Journal of Light & Visual Environment* **32(3)**, 288

Reynolds, K. J., De Kock, J. P., Tarassenko, L., and Moyle, J. T. B.: 1991, *British Journal of Anaesthesia* **67(5)**, 638

Rochester, G. K., Sumner, T. J., and Shaul, D. N. A.: 2003, *LISA CMS: Discharge Tests On Dummy Proof Mass*, Technical report, Imperial College London, GKR/SMART/7

Ruiter, A. J., Belczynski, K., Benacquista, M., and Holley-Bockelmann, K.: 2009, *The Astrophysical Journal* **693(1)**, 383

Sansonetti, C. J., Salit, M. L., and Reader, J.: 1996, *Appl. Opt.* **35(1)**, 74

Sathyaprakash, B. S. and Schutz, B. F.: 2009, *Living Reviews in Relativity* **12**, 2

Saville, G. F., Platzman, P. M., Brandes, G., Ruel, R., and Willett, R. L.: 1995, *Journal of Vacuum Science and Technology* **13(6)**, 2184

Sawyer, S., Rumyantsev, S., and Shur, M.: 2008, *Solid-State Electronics* **52(6)**, 968

Schulte, M.: 2007, *Effects of the Angle of Incidence of the UV on the Current Emitted by Relevant Surfaces*, S2-ICL-TN-3010 Issue 2, Imperial College London

Schutz, B. and Ricci, F.: 2010, *ArXiv e-prints*

Sensor Electronic Technology, Inc.: 2011, *Deep UV LED Technical Catalogue*, Data sheet, Sensor Electronic Technology, Inc., `http://www.s-et.com`

Seoul Semiconductor Ltd: 2006, *Specification Document for UV LED Model Series T9B25**, Data sheet, Seoul Semiconductor Ltd, `http://www.socled.com`

Sesana, A., Volonteri, M., and Haardt, F.: 2009, *Classical and Quantum Gravity* **26(9)**, 094033

Shaul, D. N. A., Araújo, H. M., Rochester, G. K., Sumner, T. J., and Wass, P. J.: 2005, *Classical and Quantum Gravity* **22(10)**, S297

Shaul, D. N. A., Sumner, T. J., Araujo, H. M., Rochester, G. K., Wass, P. J., and Lee, C. G.-Y.: 2004, *Classical and Quantum Gravity* **21(5)**, S647

Silva, C.: 2010, *Ph.D. thesis*, University of Coimbra

Silva, C., da Cunha, J. P., Chepel, V., Pereira, A., Solovov, V., Mendes, P., Neves, F., and Lopes, M. I.: 2007, *Nuclear Instruments and Methods in Physics Research Section A: Accelerators, Spectrometers, Detectors and Associated Equipment* **580(1)**, 322 , Proceedings of the 10th International Symposium on Radiation Physics - ISRP 10

Silva, C., da Cunha, J. P., Pereira, A., Chepel, V., Lopes, M. I., and Solovov, V.: 2009, *Reflectance of Polytetrafluoroethylene (PTFE) for Xenon Scintillation Light*, Review arXiv:0910.1056, University of Coimbra

Simpson, J. A.: 1983, *Annual Review of Nuclear and Particle Science* **33(1)**, 323

Stroeer, A. and Vecchio, A.: 2006, *Classical and Quantum Gravity* **23(19)**, S809

Sun, K.-X., Allard, B., Higuchi, S., Goh, A., Gill, D., Buchman, S., and Byer, R.: 2006a, *AIP Conference Proceedings* **873(1)**, 215

Sun, K.-X., Buchman, S., Allard, B., Williams, S., and Byer, R. L.: 2006b, *Classical and Quantum Gravity* **23(8)**, S141

Sun, K.-X., Leindecker, N., Higuchi, S., Goebel, J., Buchman, S., and Byer, R. L.: 2009, *Journal of Physics: Conference Series* **154(1)**, 012028

SuperCool: 2005, *Peltier Control Module - TC-XX-PR-59*, Data sheet, SuperCool, `http://www.supercool.se`

Sylvestre, J. and Tinto, M.: 2003, *Phys. Rev. D* **68(10)**, 102002

The Geant4 Collaboration: 2003, *Nuclear Instruments and Methods in Physics Research Section A: Accelerators, Spectrometers, Detectors and Associated Equipment* **506(3)**, 250

The Geant4 Collaboration: 2006, *Nuclear Science* **53(1)**, 270

The IPTA Collaboration: 2010, *Classical and Quantum Gravity* **27(8)**, 084013

The LIGO Collaboration: 2009, *Reports on Progress in Physics* **72(7)**, 076901

The LISA Collaboration: 2011, *LISA - Unveiling a Hidden Universe.*, Assessment Study Report - Yellow Book, ESA

The VIRGO Collaboration: 2010, *Journal of Physics: Conference Series* **203(1)**, 012074

Thèye, M.-L.: 1970, *Phys. Rev. B* **2(8)**, 3060

Turner, J.: 2007, *Atoms, Radiation, and Radiation Protection*, Wiley-VCH

Varshni, Y. P.: 1967, *Physica* **34(1)**, 149

Vernier, P., Pauty, M., and Pauty, F.: 1969, *AVS* **6(4)**, 743

Wass, P. J., Araujo, H., Boatella, C., Chmeissani, M., Hajdas, W., Lobo, A., Puigdengoles, C., and Sumner, T.: 2006a, *AIP Conference Proceedings* **873(1)**, 225

Wass, P. J., Araújo, H. M., Shaul, D. N. A., and Sumner, T. J.: 2005, *Classical and Quantum Gravity* **22(10)**, S311

Wass, P. J., Carbone, L., Cavalleri, A., Ciani, G., Dolesi, R., Hueller, M., Rochester, G., Schulte, M., Sumner, T., Tombolato, D., Trenkel, C., Vitale, S., and Weber, W.: 2006b, *AIP Conference Proceedings* **873(1)**, 220

Wass, P. J., Cavalleri, A., Antonucci, F., Weber, W. J., and Dolesi, R.: 2010, *First Results of Charge Measurements with the EH FM Replica*, S2-UTN-TR-3001 Issue 1.2, University of Trento

Weber, J.: 1960, *Phys. Rev.* **117(1)**, 306

Weber, W. J., Tombolato, D., and Hueller, M.: 2006, *Experimental Results from Torion Pendulum Testing of the LTP Charge Management System*, S2-UTN-TN-3038 Issue 1, University of Trento

Weisberg, J. M. and Taylor, J. H.: 2005, *ASP Conf. Ser.* **328**, 25

Weiss, R.: 1972, *Electromagnetically Coupled Broadband Gravitational Antenna*, Technical report, MIT

Zhang, J., Hu, X., Lunev, A., Deng, J., Bilenko, Y., Katona, T. M., Shur, M. S., Gaska, R., and Khan, M. A.: 2005, *Japanese Journal of Applied Physics* **44(10)**, 7250